

UNIVERSITA' DEGLI STUDI DI VERONA

DIPARTIMENTO DI

Scienze Chirurgiche Odontostomatologiche e Materno-Infantili

SCUOLA DI DOTTORATO DI

Scienze della Vita e della Salute

DOTTORATO DI RICERCA IN

Scienze cardiovascolari

Con il contributo di

Università degli Studi di Verona

CICLO /ANNO XXXIV/2018

TITOLO DELLA TESI DI DOTTORATO

Video Kinematic Evaluation: new insights on the cardiac mechanical function

S.S.D. MED/23

Coordinatore: Prof. Giuseppe Faggian

Firma _____

Tutor: Prof. Giovanni Battista Luciani

Firma _____

Co-Tutor: Prof. Michele Miragoli

Firma _____

Dottorando: Dott. Francesco Paolo lo Muzio

Firma 

Quest'opera è stata rilasciata con licenza Creative Commons Attribuzione – non commerciale
Non opere derivate 3.0 Italia . Per leggere una copia della licenza visita il sito web:

<http://creativecommons.org/licenses/by-nc-nd/3.0/it/>



Attribuzione Devi riconoscere una menzione di paternità adeguata, fornire un link alla licenza e indicare se sono state effettuate delle modifiche. Puoi fare ciò in qualsiasi maniera ragionevole possibile, ma non con modalità tali da suggerire che il licenziante avalli te o il tuo utilizzo del materiale.



NonCommerciale Non puoi usare il materiale per scopi commerciali.



Non opere derivate —Se remixi, trasformi il materiale o ti basi su di esso, non puoi distribuire il materiale così modificato.

Video Kinematic Evaluation: new insights on the cardiac mechanical function

Francesco Paolo lo Muzio

Tesi di Dottorato

Verona, **GIORNO DEPOSITO PIATTAFORMA ONLINE**

ISBN **CODICE**

Index

SOMMARIO	1
ABSTRACT	2
INTRODUCTION	3
Ventricular Pressure-Volume Relationship	3
<i>PV-loop diagram</i>	4
<i>End-systolic pressure-volume relationship</i>	7
<i>End-diastolic pressure-volume relationship</i>	7
<i>Myocardial energetics</i>	8
<i>Right Ventricle PV-loop</i>	9
Cardiovascular Imaging	12
<i>Echocardiography</i>	12
<i>Motion mode</i>	15
<i>Doppler echocardiography</i>	16
<i>Tissue doppler imaging</i>	16
<i>Transesophageal echocardiography</i>	18
<i>Echocardiographic assessment of the right ventricle</i>	19
<i>Nuclear cardiology</i>	21
<i>Cardiac PET</i>	22
<i>Computed tomography</i>	23
<i>Cardiac magnetic resonance imaging</i>	23
<i>Technical aspects</i>	25
<i>Contrast agents</i>	27
<i>CMR is the gold standard for congenital heart disease</i>	29
<i>Strain</i>	30
<i>Tissue tracking for strain measurement</i>	30
<i>Speckle tracking echocardiography</i>	32
<i>CMR-strain</i>	33
<i>Basics of the heart video kinematic assessment</i>	35
<i>Cardiac kinematics during open chest surgery</i>	40

Video Kinematic Evaluation	47
<i>Image processing and definition of the parameters</i>	48
From cardiac syncytia to the beating heart	49
<i>Validation of Energy</i>	49
<i>Validation of Force</i>	50
<i>Validation via computer model</i>	51
In Vivo experimentation	55
<i>Ischemia-reperfusion rat heart model</i>	55
<i>Coronary artery bypass graft surgery</i>	57
<i>Vi.Ki.E.'s frequency relationship</i>	59
Advantages and disadvantages	59
Electromechanical dyssynchrony	60
<i>Electromechanical dyssynchrony in patients and therapy</i>	63
<i>Electromechanical delay assessment</i>	66
Global excitation-contraction coupling with Vi.Ki.E.	72
METHODS	73
Experimental protocol for the CMR studies	73
Vi.Ki.E. studies: Animal protocol	77
Vi.Ki.E. studies: Clinical protocol	80
STATISTICAL ANALYSIS	82
Statistical analysis in the CMR studies	82
<i>Intra- and inter-reproducibility of CMR-FT global strain parameters in pigs</i>	82
<i>Correlation between CMR-FT global strain parameters and invasive hemodynamics</i>	82
<i>CMR-based quantification of myocardial energetics under different inotropic states</i>	83
Statistical analysis in the Vi.Ki.E. studies	83
<i>Vi.Ki.E.'s frequency relationship</i>	83
<i>Vi.Ki.E. assessment of the right ventricle in Tetralogy of Fallot patients</i>	83
<i>Timing of pulmonary valve replacement is a key factor in determining recovery of the right ventricle in ToF</i>	84
<i>Vi.Ki.E. based supervised machine learning classifiers to support decision-making during surgery</i>	84
RESULTS	86

Intra- and inter-reproducibility of CMR-FT global strain parameters in pigs – Attachment 1	86
Correlation between CMR-FT global strain parameters and invasive hemodynamics – Attachment 2	91
CMR-based quantification of myocardial energetics under different inotropic states – Attachment 3	97
Vi.Ki.E.’s frequency relationship – Attachment 4	102
Vi.Ki.E. assessment of the right ventricle in Tetralogy of Fallot patients - Attachment 5 .	106
Timing of pulmonary valve replacement is a key factor in determining recovery of the right ventricle in ToF – Attachment 6	112
Vi.Ki.E. based supervised machine learning classifiers to support decision-making during surgery – Attachment 7	120
Work in progress: global excitation-contraction coupling with Vi.Ki.E.	129
CONCLUSIONS	132
New perspectives on the left ventricle assessment	133
Video Kinematic Evaluation of the right ventricle	135
REFERENCES	139
AKNOWLEDGEMENTS/RINGRAZIAMENTI	161
ATTACHMENTS	163

Sommario

L'attività meccanica del cuore gioca un ruolo importante nel governare e regolare la funzionalità cardiaca sia in condizioni fisiologiche che patologiche. Storicamente, il ventricolo sinistro è stato considerato il principale regolatore del mantenimento di una normale emodinamica cardiaca e per tale ragione è stato studiato maggiormente sia in condizioni fisiologiche che in patologie congenite e acquisite. Negli ultimi decenni si è osservato un maggiore interesse da parte di clinici e scienziati riguardo il ruolo del ventricolo destro nel determinare una efficiente funzionalità cardiaca e nella prognosi in diverse condizioni patologiche. Ciononostante, non sarebbe corretto distinguere l'attività dei singoli ventricoli in quanto sono in costante interazione condividendo il setto interventricolare, diversi fibre miocardiche ed essendo circondati dal pericardio. Conseguentemente, alterazioni della funzionalità di un ventricolo possono alterare l'attività dell'altro. Tale interazione persiste anche in seguito la rimozione del pericardio a causa di pericardite costrittiva o durante chirurgia a cuore aperto. Durante un intervento a cuore aperto, solo l'attività meccanica del ventricolo destro è valutata qualitativamente dall'esperienza del chirurgo e del cardiologo. Ciò è dovuto ad un'assenza di una tecnica di "imaging" intraoperatoria capace di valutare la sua complessa geometria e funzione. Infatti, è interessante notare come la maggior parte delle tecniche di imaging disponibili siano definite per la valutazione del ventricolo sinistro e che il parametro di frazione di eiezione sia il più usato e affermato. Però tale parametro è una misura della funzionalità sistolica globale e perciò non è in grado di indentificare regioni miocardiche compromesse e la meccanica di contrazione.

Per tali ragioni, nuovi approcci potrebbero rivelarsi utili nello studio dell'attività meccanica di entrambi i ventricoli permettendo di raggiungere una più completa valutazione della funzione meccanica cardiaca.

In questa tesi ho applicato diverse modalità della risonanza magnetica per studiare l'attività meccanica del ventricolo sinistro ed utilizzato una nuova tecnica di imaging, sviluppata con il mio contributo, per la valutazione della meccanica del ventricolo destro durante operazioni a cuore aperto.

Abstract

The cardiac mechanical function plays a critical role in governing and regulating its performance under both normal and pathological conditions.

The left ventricle has historically received more attention in both congenital and acquired heart diseases and was considered as the mainstay of normal hemodynamics. However, over the past few decades, there has been increasing recognition of the pivotal role of the right ventricle in determining functional performance status and prognosis in multiple conditions. Nonetheless, the ventricles should not be considered separately as they share the septum, are encircled with common myocardial fibers and are surrounded by the pericardium. Thus, changes in the filling of one ventricle may alter the mechanical function of its counterpart. This ventricular interdependence remains even after the removal of the pericardium because of constrictive pericarditis or during open chest surgery. Interestingly, during open chest surgery, only the right ventricle mechanical activity is visually checked by the surgeon and cardiologist due to the absence of an intraoperative imaging technique able to evaluate its complex function. Noteworthy, most of the imaging techniques available to clinicians are established for the assessment of the left ventricle, with the ejection fraction being the most used parameter. However, this value is a measure of global systolic function which comes short in identifying regional myocardial impairment and the mechanical contraction. Therefore, new approaches are needed to deeply investigate the mechanics of both ventricles and correctly assess the cardiac mechanical performance.

In this thesis, I studied the mechanical function of the left ventricle through different modalities of cardiac magnetic resonance and employed an innovative imaging technique for the assessment of the right ventricle mechanical function during open chest surgery.

Introduction

Ventricular Pressure-Volume relationship

Otto Frank originally described the cardiac cycle and ventricular properties through the window of the pressure–volume (PV) loop in 1895. Suga and Sagawa introduced methods for real-time measurements in *ex vivo* blood-perfused hearts, which generated research that culminated in unparalleled understanding of ventricular mechanics and energetics. The introduction of the PV catheter by Baan et al facilitated *in vivo* studies[1-3].

The PV analysis can elucidate pathophysiological mechanisms of heart failure (HF), myocardial and valvular heart diseases as well as monitoring the effects of therapeutic interventions[4-8].

Clinical PV acquisition is made with a 4–7 F PV catheter containing 12 equidistant electrodes and a solid-state pressure sensor in the middle of the array (Inca, CD Leycom) as portrayed in Figure 1.

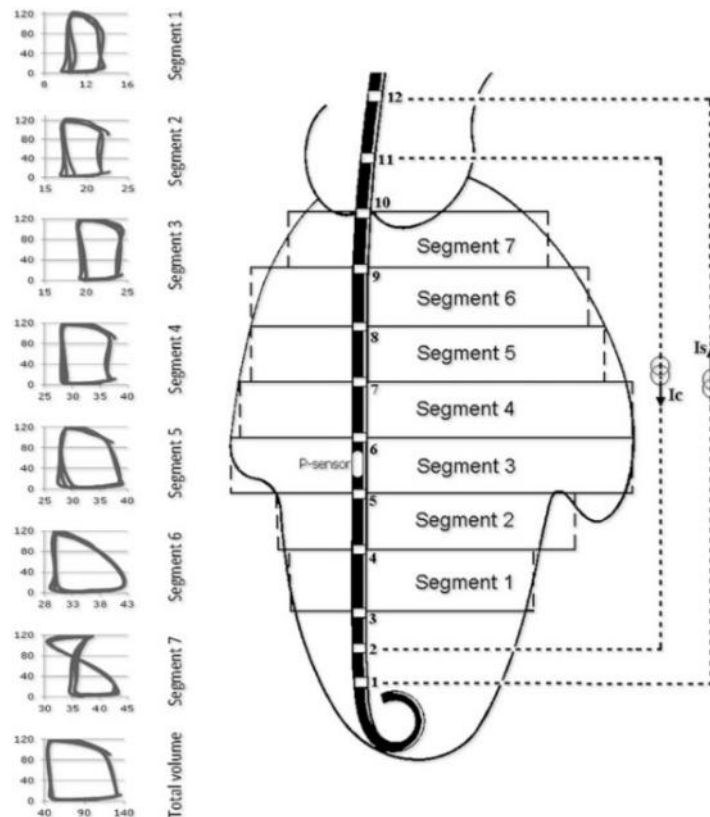


Figure 1. Schematic representation of the conductance catheter positioning with segmental pressure-volume loops displayed on the left. Segment 1 corresponds to the apex, while segment 7 to base. In physiological condition, segments 1 to 6 display an upright rectangular shape,

whereas segment 7 displays a “figure-8” outline because is partially in the aorta. The calculation of the total volume is performed with summation of segments 1 to 6. From Bastos et al.[9]

The catheter placement could be trans-aortic or trans-septal with the tip usually in the LV apex with the most proximal electrode above the aortic or mitral valve. Briefly, an electrical current (I) between distal and proximal electrodes create an electrical field. Since blood is partially conductive, the voltage decreases across each successive pair of electrodes. The voltage drop between two adjacent electrodes (V_i) is inversely related to:

- the cross-sectional area (A_i) of a hypothetical cylindrical segment defined at the level of the electrodes,
- the distance between electrodes (D)
- blood resistance (ρ) as measured by the Inca system.

The segmental volume between an adjacent pair of electrodes ($Vol_{i,est}$) is estimated by:

$$Vol_{i,est} \approx A_i \times D \approx I \times \rho \times D^2 / V_i$$

where V_i is directly measured.

The first method of volume calibration relies on immediate pre-procedure measurements of LV end-diastolic volume (V_{ed}) and stroke volume (SV) or ejection fraction (EF) taken from echocardiography, computed tomography, or cardiac magnetic resonance imaging. This concept assumes that chamber dimensions remained constant between the time of imaging acquisition and the time of invasive PV measurement.

A second and more accurate method can be drawn from a combination of hypertonic saline infusion into the pulmonary artery or right atrium and thermodilution to assess SV[10].

PV loop diagram

Ideally, the PV loop in a normal LV is rectangular or trapezoidal, depicting the four phases of the cardiac cycle as described in Figure 2: isovolumetric contraction (from point A to B), ventricular ejection (from point B to C),

isovolumetric relaxation (from point C to D), and diastolic (passive) filling (from point D to A).

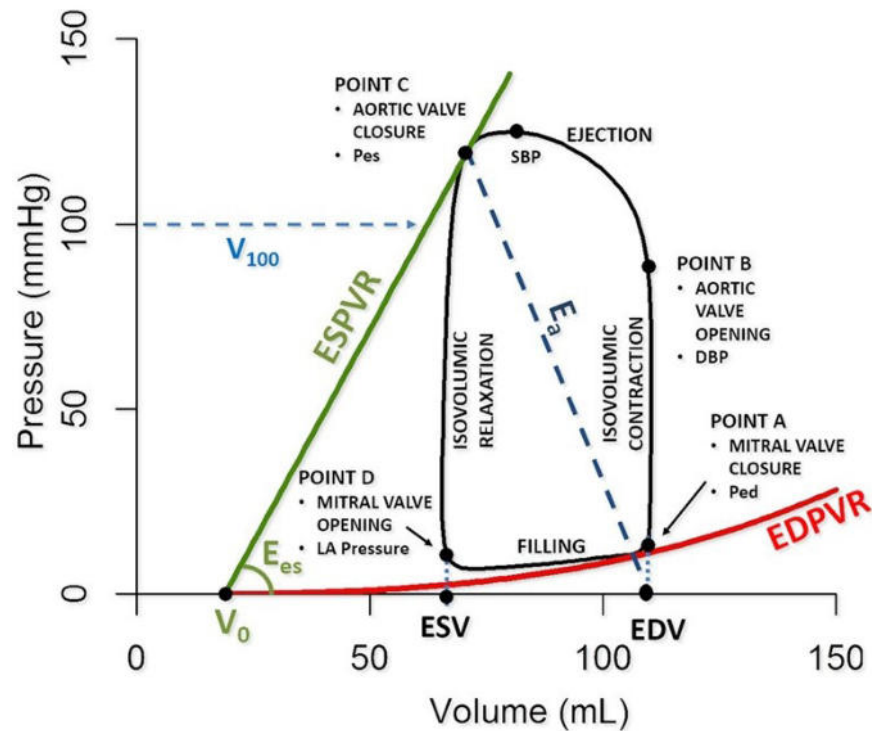


Figure 2. The standard LV pressure-volume loop configuration. The shape of the loop is rectangular, and four phases can be distinguished (in counterclockwise direction): isovolumetric contraction (from point A to B), ventricular ejection (form point B to C), isovolumetric relaxation (from point C to D) and diastolic filling (from point D to A). Four points (from A to D) are highlighted in the diagram corresponding to the mitral and aortic valves opening and closing. The green and red lines represent the end-systolic and end-diastolic PV relationships (ESPVR and EDPVR, respectively). Different parameters are displayed in the graph and are explained in the main text. From Bastos et al[9].

Five pressure points are displayed on the y-axis: the peak pressure at end systole (end-systolic pressure, P_{es}), the maximum pressure against the arteries during systole (systolic blood pressure, SBP), the pressure at which the aortic valve opens during systole (diastolic blood pressure, DBP), the pressure within the left ventricle following the completion of diastolic filling just prior to systole (left ventricular end-diastolic pressure, P_{ed}) and the left atrial pressure (LA). The stroke volume (SV, the width of the PV-loop) is defined as the difference between end-systolic and end-diastolic volumes highlighted on the x-axis (ESV and EDV, respectively). The ratio of ventricular P_{es} over SV, represented by the blue dashed diagonal connecting EDV and P_{es} , is the effective arterial

elastance (E_a). The end-systolic pressure-volume relationship (ESPVR), represented with green straight line, describes the maximal pressure that can be developed by the ventricle at any given volume. The end-systolic elastance (E_{es}) is the slope of the ESPVR and represents a load independent index of myocardial contractility. The end-diastolic relationship (EDPVR), represented with the red curved line, describes the passive properties of the myocardium. Finally, the ESPVR-extrapolated volume at 100 mmHg (V_{100}), considered as a surrogate index of contractility, is displayed in light blue.

Both ESPVR and EDPVR characterize LV systolic and diastolic properties (Figure 3). Classically, measurement of these relationships requires transient modulations of preload (i.e. inferior caval vein occlusion) or afterload (e.g. hand grip maneuver).

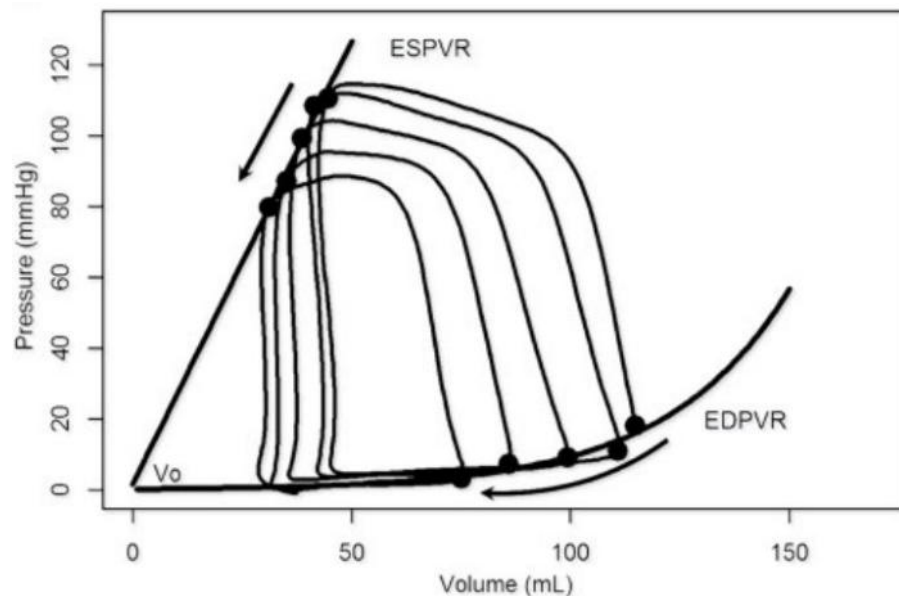


Figure 3. Representation of vena cava occlusion to change preload and determine the end-systolic and end-diastolic relationships (ESPVR and EDPVR, respectively) by linear regression. From Bastos et al[9].

Single-beat algorithms simplify PV analysis by estimating ESPVRs and EDPVRs from a single steady-state PV loop tracing and further relying on measurements of arterial systolic and diastolic pressures, SV, EF, pre-ejection time period, and total systolic period that are obtained with the conductance catheter.

End-systolic pressure-volume relationship

The ESPVR is approximately linear (Figure 3) in the physiological range of end-systolic pressures (P_{es}) and volumes (V_{es}). It is characterized by a slope (end-systolic elastance, E_{es}) and a volume axis intercept V_0 such that:

$$P_{es} = E_{es} \times (V_{es} - V_0)$$

E_{es} represents the peak chamber elastance during a beat and reflects ventricular chamber mechanical properties when the maximum number of actin-myosin bonds is formed. E_{es} increases with positive inotropism (e.g. dobutamine) and sympathetic activation, but decreases with negative inotropism (e.g. beta-blockers, calcium channel blockers), dyssynchrony, and myocardial ischaemia or infarction. E_{es} is a relatively load-independent measure of LV contractility[2,4,11]. Increased contractility occurs when changes in E_{es} and V_0 result in a leftward and/or upward ESPVR shift.

End-diastolic pressure-volume relationship

Contrary to ESPVR, the EDPVR is non-linear (Figure 3). The EDPVR reflects the passive mechanical properties of the LV chamber, when all actin-myosin bonds are uncoupled. Accordingly, the EDPVR is determined by the size, orientation and mass of myocytes and extracellular matrix. Therefore, fibrosis, ischaemia, oedema, myocyte remodeling, and hypertrophy affect the EDPVR. Its slope (dP/dV) estimates LV chamber stiffness and is load-dependent. To note, compliance can also be calculated from the PV-loop as it is the mathematical inverse of stiffness (dV/dP). The LV volume at 30 mmHg on the EDPVR (V_{30}) reflects compliance (Figure 4A) and would suggest remodeling (rightward shift of the EDPVR) or diastolic dysfunction (leftward shift of the EDPVR). V_{30} increases in HF with reduced EF and decreases in restrictive and hypertrophic cardiomyopathies[4]. Ventricular performance is also highly influenced by the rate of relaxation (or lusitropy) (Figure 4B). The rate of pressure decay during isovolumetric relaxation is characterized by an exponential time constant of decay (τ), or the time for pressure to fall by 50% ($t_{1/2}$), reflecting the average rate of cross-bridge uncoupling within the myocytes. A normal value of τ is ~20–30 ms and impaired relaxation, caused for example by LV hypertrophy or ischaemia, prolongs τ (e.g. 70–100 ms).

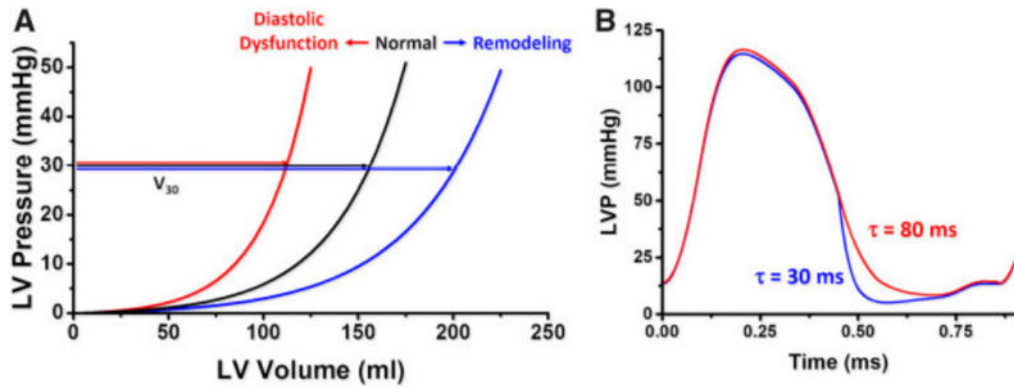


Figure 4. Graphs representing the importance of the end-diastolic pressure-volume relationship and the rate of relaxation. **A.** V_{30} is the left ventricular (LV) volume at a pressure of 30 mmHg and reflects compliance. A shift to the left suggests diastolic dysfunction (red), whereas a shift to the right (blue) suggests ventricular remodeling. **B.** Impaired active relaxation delays the pressure decay (in red) increasing the time constant of delay (τ) in early diastole compared to physiological condition (in blue). From Bastos et al[9].

Myocardial energetics

The myocardial energetics that can be derived from a PV loop are portrayed in Figure 5.

The total LV mechanical energy per beat is indexed by the PV area (PVA), which is the sum of the SW (i.e. the area within the PV loop, or the heart external work) and the residual potential energy (PE) stored in the myocardium (internal work) at the end of contraction ($PVA = SW + PE$).

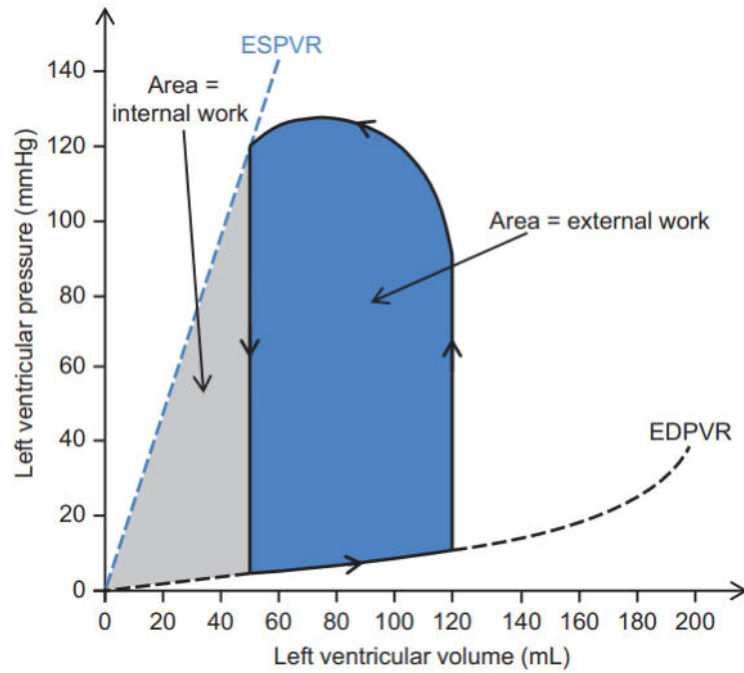


Figure 5. The integration of the area inside the PV loop (blue area) is defined as the external work or stroke work (SW). The grey area next to the PV loop and between the ESPVR, the isovolumic contraction and begin of the EDPVR is defined as the internal work or potential energy (PE). The sum of the two areas defines the heart mechanical energy (PVA). Chambers et al[12].

Clinically, SW is estimated by the product of SV and mean arterial pressure (MAP) during ejection ($SW \approx SV \times MAP$). Stroke work (or external work) represents the energy required to propel blood across the vasculature. PE (or internal work) is the remaining energy stored in the myofilaments at the end of systole that is not dissipated as external work. The PVA was found to correlate linearly with the myocardial oxygen consumption per beat (MVO_2). Total MVO_2 includes the basal metabolism, intracellular calcium cycling involving the sarcoplasmic reticulum (both independent of PVA) and cross-bridge cycling (directly proportional to PVA). When multiplied by HR, PVA represents total power output. Total power output is useful in evaluating the effects of inotropes and different classes of mechanical circulatory support devices as they affect cardiac metabolism during ischaemia and cardiogenic shock.

Right ventricle PV loop

Over the past few decades, there has been increasing recognition of the role of the right ventricle (RV) in determining functional performance and prognosis

in multiple conditions[13]. In the past, most of the works investigating the right ventricle in different diseases and at exercise were performed by imaging alone which evaluate its performance by means of SV or right ventricular ejection fraction[14-16]. Although the clear advantages of noninvasive approaches as magnetic resonance and speckle-tracking echocardiography in the measurement of regional myocardial mechanics[17,18], their disadvantage is the evaluation of right ventricular function in relation to its preload and afterload, and thus, cannot be considered a proper quantification of its function.

Therefore, as described for the LV, some parameters calculated from the PV loop can be more insightful in the assessment of the right ventricular function[19].

In Figure 6 is portrayed the PV-loop of the RV after vena cava occlusion (multiple loops).

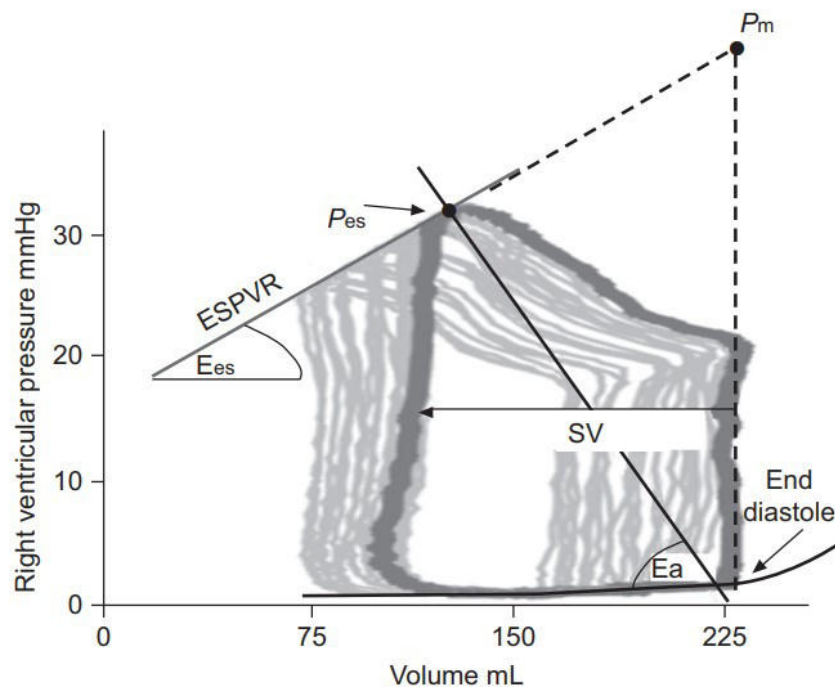


Figure 6. Schematic representation of the right ventricle PV-loop and the main parameters. Compared to the left ventricle, the shape of the right ventricle PV-loop is trapezoidal. The measurable parameters are defined with the same methods described for the left ventricle. From Vonk-Noordegraaf and Westerhof[20].

The pressure–volume loop of the RV is, in general, more of a trapezoidal shape than the more rectangular shape of the left ventricle, probably because of the very compliant pulmonary tree.

Starting at end-diastole the loop consists of four phases: isovolumic contraction, ejection, isovolumic relaxation and filling phase. The area within the loop is the SV . The line connecting the end-systolic pressure–volume points is the ESPVR. Its slope, E_{es} , is a measure of systolic ventricular function (contractility) and is a generally accepted load-independent characterization of the cardiac pump. To calculate the ESPVR, and thus E_{es} , the best approach is the occlusion of the vena cava but it is often not practical or desirable. Therefore, as shown for the LV, methods have been developed to obtain E_{es} from measurement of right ventricular pressure (catheterization) and volume (MRI) of a single beat[21,22], making it a practical method to obtain a load-independent functional characterization of the right heart. The slope of the line connecting end-diastolic volume and end-systolic pressure (P_{es} , closely related to mAOP) is called arterial elastance (E_a) but is actually close to pulmonary vascular resistance over heart period. The ratio E_a/E_{es} is a measure of ventriculo-arterial coupling. With the single beat method, the maximal isovolumic pressure (P_m) is determined and thus E_{es} is calculated as $(P_m - P_{es})/SV$.

The EDPVR determines filling and thus cardiac output (CO) but a straight-line approach is not sufficiently accurate. Therefore, several descriptions of the curved diastolic EDPVR have been proposed with different approximation but none are generally accepted.

Although PV loop analysis provides the most comprehensive measurement available for both hemodynamics and cardiac function, it is not routinely performed because pressure can only be reliably obtained by invasive catheterization, unlike volumes that can be calculated noninvasively by different imaging techniques[23,24]. Nevertheless, noninvasive techniques such as echocardiography or MRI still refer to PV loop as a benchmark of comparison for the assessment of the cardiac mechanical function.

Cardiovascular imaging

Echocardiography

Echocardiography is the cornerstone of most cardiac imaging techniques. The absence of ionizing radiation or potentially toxic contrast agent administration is particularly advantageous when repeated evaluations are required. Physicians and/or specialist technicians can acquire and interpret core images in real time without the need of complex postprocessing, making the delivery of echocardiography services more flexible than other cardiac imaging techniques. The most common ways to perform echocardiography are the Transthoracic (TTE) and Transesophageal (TEE).

The creation of an image in echocardiography involves the production of an ultrasound wave by a piezoelectric crystal placed in the transducer[25]; the wave travels through the tissue in a straight line until it meets an interface between two media with different acoustical properties. In this case it will be reflected with an energy directly proportional to the difference in acoustical impedance (Figure 7).

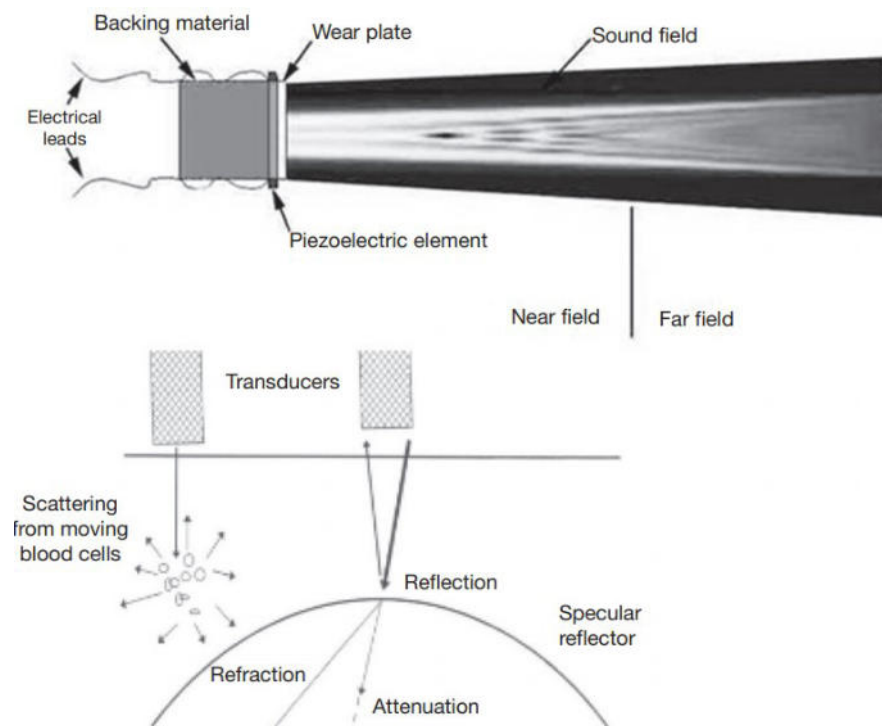


Figure 7. Schematic representation of the principles of Echocardiography. The ultrasound waves are emitted from the transducer, reflected by the tissue, and then received by transducer

which converts them to electrical signals via a piezoelectric element and generates an image. From Daly, Abbasi and Kwong [26].

The reflected wave is converted back to an electrical signal by the piezoelectric element and is used to create the image displayed[26]. By calibrating the ultrasound for the velocity of sound in the medium under examination, the time it takes for the wave to leave and return to the transducer can be converted into distance allowing accurate measurements of cardiac dimensions. These are the principles for the so-called B(Brightness)-mode echocardiography, the most common form of two-dimensional (2D) ultrasound imaging.

Modern equipment uses phased array principles in which multiple ultrasound elements are used to form the ultrasound beam, and their sequence and direction controlled electronically.

Lower frequency beams with longer wavelength have low resolution but better penetration, which represents the ability to transmit sufficient energy into the chest to produce a satisfying image. Conversely, high-frequency transducers have higher resolution but low penetration and may not be able to pass through thick chest walls in larger humans and are, instead, used in children. The placement and angulation of the transducer allows for standardized acquisition's views[27] of the heart to interrogate the great vessels, valves, and blood flow characteristics and allows the qualitative and quantitative assessment of ventricular volumes, wall thickness, mass, and function[25] (Figure 8). The views reported below refers to TTE only.

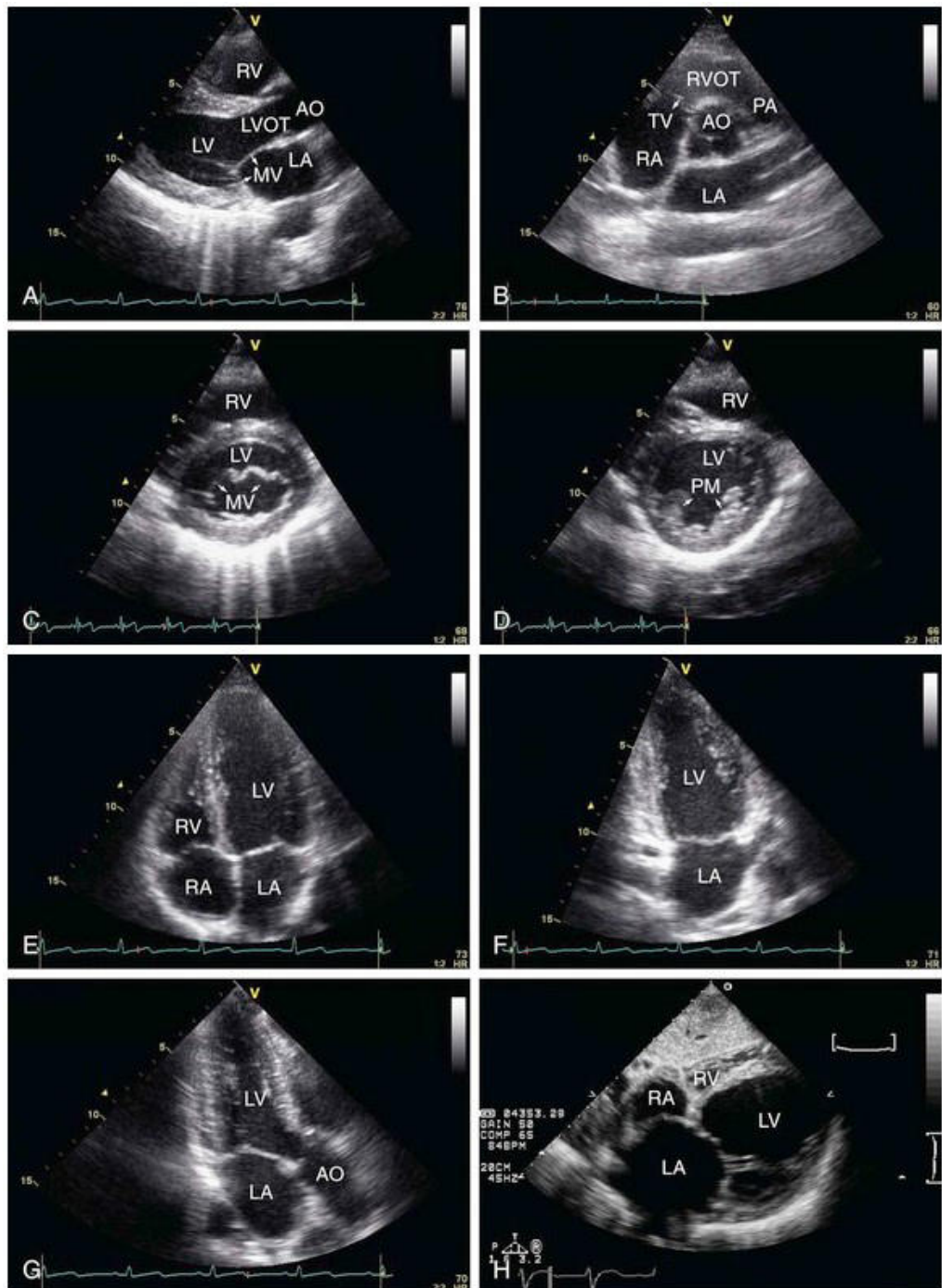


Figure 8. Views for transthoracic echocardiography: A through D: Images from the parasternal position. A: long axis view. B: short axis view. C: short axis view of basal left ventricle with the mitral valve open. D: short axis view of left ventricle. E, F, and G: images from the apex. E: apical four-chamber view. F: two-chamber view. G: three-chamber view. H: subcostal view. The chambers and structures highlighted are the following: AO, aorta; ASC Ao, ascending aorta; DESC Ao, descending aorta; LV, left ventricle; LVOT, LV outflow tract; MV, mitral valve; PA, pulmonary artery; PM, papillary muscles; RV, right ventricle; RVOT, RV outflow tract; TV, tricuspid valve. From <https://radiologykey.com/echocardiography-3/>

However, despite the advances in technology, image quality remains challenging[26] especially in individuals who are difficult to scan because of their physique or poor echocardiographic windows due to rib anatomy or hyper-inflated lungs.

Motion mode

M-(motion)mode is a one-dimensional image with time displayed on the horizontal axis. It is characterized by an extremely high temporal resolution as the sampling rate could be 1000 pulse/s or higher. The probe can be swept in a sector from the apex to the base of the heart to gain highly accurate recordings of the amplitude and rate of motion of the cardiac structures (Figure 9).

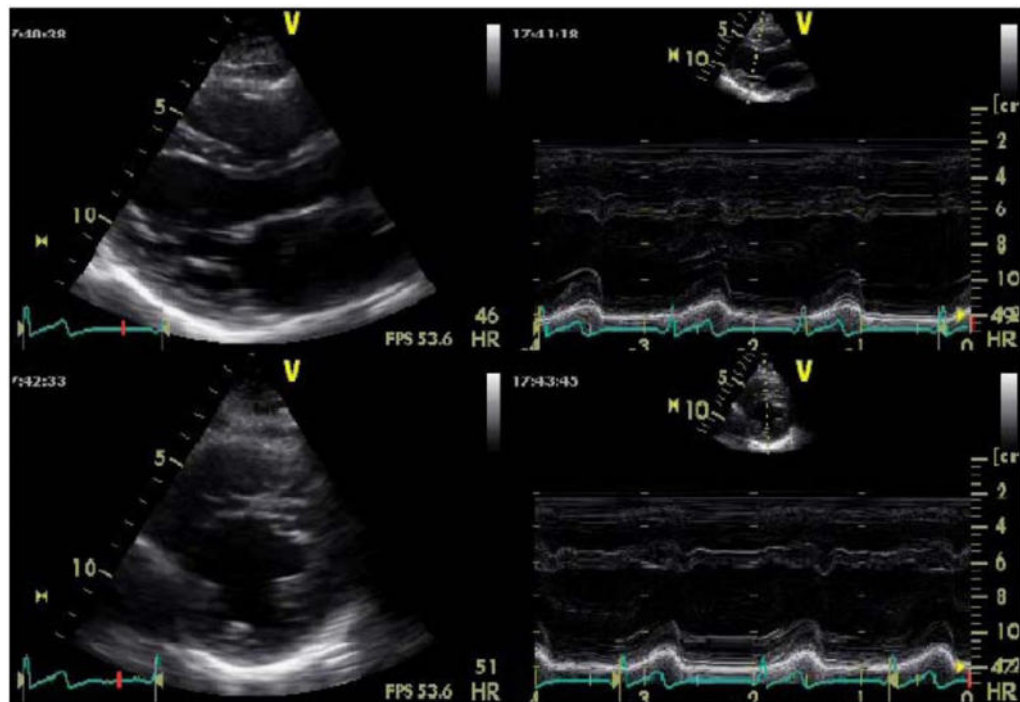


Figure 9. Representative images of M-mode from the parasternal long-axis view (upper panels) and short axis view (bottom panels). From Daly, Abbasi and Kwong[26].

M-mode echocardiography is used to evaluate the ventricle through calculation of the ejection fraction, although in most cases this is complemented by additional information on diastolic function, filling pressures, and measures of myocardial strain.

Doppler echocardiography

Doppler echocardiography is the principal ultrasound technique used in the clinical routine to obtain hemodynamic information. The Doppler effect refers to the observed differences in reflected and transmitted frequencies when the target is moving. When an object (e.g., blood) reflecting ultrasonic energy is moving toward the transducer, the reflected frequency (f_r) is greater than the transmitted frequency (f_t). Once the Doppler frequency and the angle (θ) between the plane of the ultrasound beam and the moving target are known, it is possible to calculate the velocity of the moving target as following:

$$V = \frac{f_r \times \text{constant}}{2f_t(\cos\theta)}$$

where V is the velocity of the blood cells, and the *constant* is the velocity of sound.

Pulsed wave or continuous Doppler[28,29] may be used to calculate flow velocities depending on whether it is required to measure velocity at a particular point along the ultrasound beam or to record high velocities. Doppler techniques are critical for the evaluation of valvular lesions, shunts, and other physiological measurements such as the measurement of diastolic function. Using Doppler and a modification of the Bernoulli equation, which relates the difference in pressure across a stenosis to a difference in velocities, it is possible to accurately assess the gradient across stenotic valves and LV outflow tract obstruction or estimate right ventricle RV systolic pressure. Combining Doppler data (velocity-time integral) with dimensions obtained from 2D or M-mode images, it is also possible to estimate CO and calculate left to right shunts.

Tissue doppler imaging

Tissue Doppler imaging (TDI) for echocardiographic evaluation of myocardial function was first described in 1989[30]. It is designed to characterize low velocity-high amplitude signals from myocardial motion[30] that are obtained by inverting the low pass filter (used in traditional Doppler) to a high pass filter.

Pulsed wave TDI measures the peak longitudinal myocardial velocity from a single segment but has to be performed ‘online’. On the contrary, color tissue doppler imaging (CTDI) is performed ‘offline’ and can interrogate velocities from multiple sites simultaneously[29]. However, as CTDI measures the mean peak velocity, its values are ~25% lower than pulsed wave Doppler[31] and, thus, the two methods are not interchangeable.

In Figure 10A-B is displayed the standard TDI signal over a cardiac cycle which is characterized by three peaks: a positive systolic peak and two negative diastolic peaks.

The positive systolic wave (s’ velocity, Sa or Sm) represents the myocardial contraction. The negative waves represent the early diastolic myocardial relaxation (e’ velocity, Ea or Em) and active atrial contraction in late diastole (a’ velocity, Aa or Am).

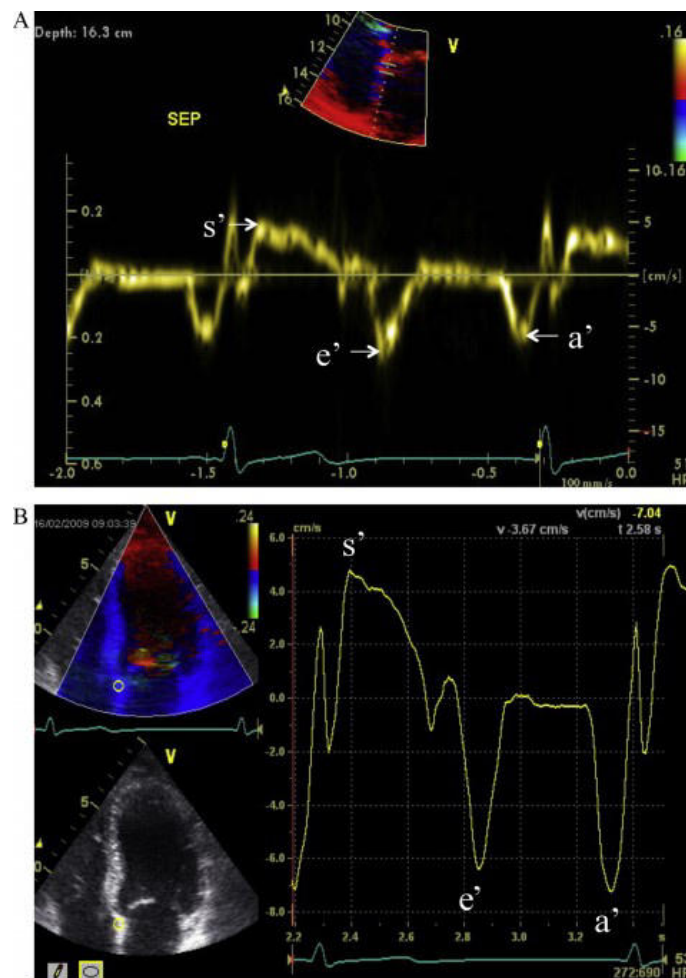


Figure 10. Standard Tissue doppler imaging (TDI) acquisition. **A:** pulsed wave imaging recording from the apical four chamber view sampling from the mitral valve. **B:** color doppler imaging recording from the apical four chamber view sampling from the mitral valve. In both

panel is displayed the typical TDI signal over a cardiac cycle highlighting its three waves. The s' represents the myocardial contraction, the e' is the early diastolic myocardial relaxation and the a' represents the active atrial contraction. From Krishna Kadappu and Thomas[32].

TDI measurements are reported in different cardiac conditions where it has been validated as a marker of LV systolic dysfunction[33,34], diastolic dysfunction[35,36], LV dyssynchrony[37], right ventricular[38] and atrial function[39].

However, TDI is limited by its inability to differentiate active myocardial contraction from the tethering effects of adjacent myocardium, thus lacking site specificity[32,40]. The major disadvantage of TDI is its angle dependency as it has been reported that if the angle of incidence exceeds 15 degrees there is ~4% underestimation of velocity[41]. Moreover, echocardiographic quantification of the RV function is under-reported because of the difficulty in accurate evaluation due to its retrosternal position, making imaging more challenging. Similar to the LV, pulsed TDI velocities of RV demonstrate a base to apex gradient with lateral RV s' being greater than the LV lateral s' velocity[42].

Transesophageal echocardiography

TEE involves the placement of the ultrasound probe in the esophagus to acquire cardiac images. It usually requires conscious sedation and is associated with complications related to both sedation and intubation. Although more invasive, it offers improved image quality over TTE particularly for posterior structures such as the left atrium, mitral valve, and pulmonary veins. It is also useful for imaging the ascending and descending aorta and proximal portions of the great vessels. Improved image quality is possible for two reasons: the proximity of the structures studied without interposition of the pulmonary or parietal structures and the high resolution of the transducers used. TEE allows for assessment of chamber size and function and Doppler assessment of valvular function, including calculation of stenotic lesions or quantification of regurgitation in a similar manner to transthoracic. The placing and the angulation of the probe allow to evaluate different structures of the heart. The main views are the upper esophageal (UE), midesophageal (ME) four-chamber,

the ME short- and long-axis, and the transgastric (TG). In Figure 11 are portrayed all the 20 different views that can be obtain with TEE[43-45].

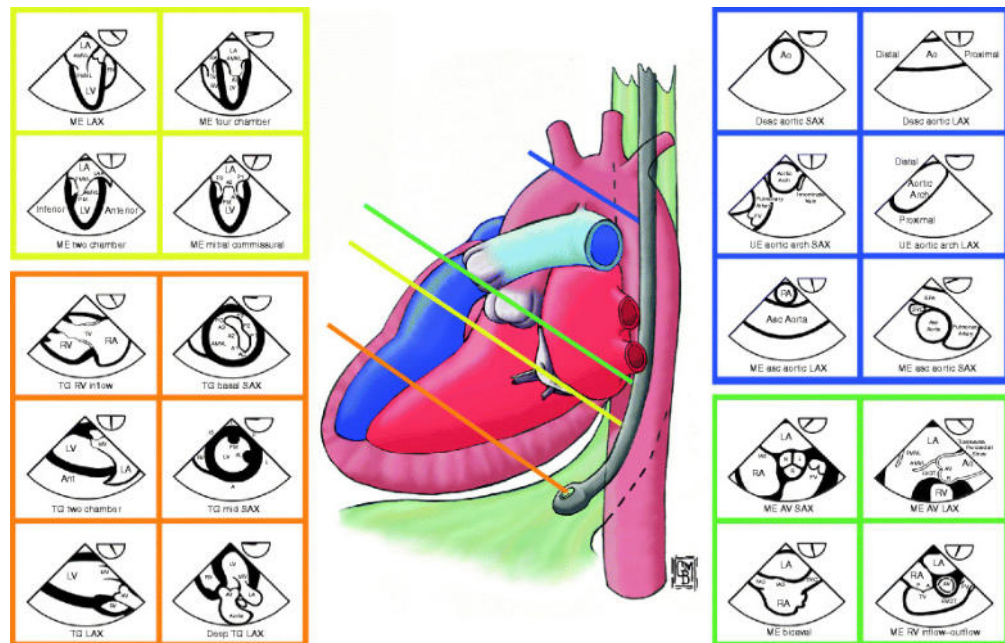


Figure 11. The standard views for transesophageal echocardiography: midesophageal (ME), upper esophageal (UE) and trans gastric (TG). In this representation, the views are grouped by the structures interrogated following a color scheme. Blue: ME and UE views, in either long-axis (LAX) or short-axis (SAX), able to evaluate different regions of the aorta (ascending, descending and the arch). Green: ME views able to evaluate the aortic valve (AV), right ventricle inflow and outflow tract (RVOT), and bicaval view. Yellow: ME views able to evaluate the left ventricle (LV) and mitral valve in LAX, SAX, two-chamber or commissural views. Orange: TG views able to evaluate the LV, RV, and AV for spectral Doppler alignment in the two-chamber, SAX or LAX views. From Vegas[43].

Echocardiographic assessment of the right ventricle

The evaluation of the LV function can be performed through TEE with all the methods described up to this point. On the contrary, the assessment of global RV function it is a more complicated task.

Because of its irregular shape, acquisition of multiple images might be necessary to fully define chamber size and shape. Several methods have been described to measure RV volume and function. First, maximal short-axis and mid short-axis measurements of RV chamber size can be made in a single-plane[24]. Second, application of the multiplane method or modified Simpson's rule can be used to determine RV volume[46]. Third, investigators have

estimated RV volume from summation of smaller geometric volumes using models of an ellipsoid, a prism, and a pyramid[47]. Finally, right ventricular end-diastolic and end-systolic measurements can be measured by planimetry, and the ejection fraction could be measure via fractional area change[24]. However, due to the difficulty to acquire good quality images of its complex geometry and given the intricacy and potential inaccuracies of all the cited methods, quantitative assessment of RV is rarely performed in clinical TEE practice[48,49] and especially during surgical procedures.

Nuclear Cardiology

The development of both scintillation camera in 1958 and radiotracers paved the road for the evolution of nuclear cardiology[50,51] as a discipline. Initial applications included imaging of radiotracers circulating through different cardiac chambers in real time for detection of intracardiac shunts followed by the measurements of regional myocardial perfusion and regional ventricular function. Current applications range from the assessment of myocardial volumes and function to myocardial perfusion, metabolic imaging and infarct imaging.

Nuclear cardiology imaging techniques rely on the principle of radioactive decay. This refers to the spontaneous transformation of an unstable atomic nucleus into a lighter one, with the release of radiation in the form of alpha particles (α), beta particles (β), gamma rays (γ), or other particles. For human diagnostic purposes, gamma rays and positrons (PET) are preferred as these are associated with less damaging biological effects. The rate of decay of radioactive substances is measured in terms of their half-life ($T_{1/2}$), the time needed for half the nuclei in a sample of a radioactive substance to undergo radioactive decay. Radiotracers used in medical diagnostics ideally have a relatively short half-life to ensure minimization of the radiation dose to the patient.

Briefly, the process consists in selecting a specific radiolabeled agent to reflect the spatial and temporal distribution of a particular body function or metabolism. The radiotracer decays by emitting gamma rays or positrons which are detected by a gamma camera or PET camera. The distribution of the radioactive tracer is inferred from the detected gamma rays (or positrons) and mapped as a function of time and/or space. Nowadays, almost all nuclear cardiology studies are performed using single-photon emission computed tomography (SPECT)[52]. This is a tomographic imaging technique that uses gamma rays emitted from an injected radiopharmaceutical to depict the distribution of the radiotracer within the body acquiring the data as a 3D volume.

The gamma rays emitted from the patient are collimated, namely, they must pass through a lead structure with multiple holes or a pinhole collimator

ensuring that only gamma rays traveling as parallel as possible to the main beam of energy will be transmitted to the detection crystals. Those rays interact through the photoelectric effect energy with the release of light scintillations which are converted by photomultiplier cells to electrical energy. The latter can then be processed through position and summation circuits and a pulse wave analyzer to create an image useful for diagnostic purposes.

In PET imaging, positrons and electrons collide causing the formation of two high-energy photons that move in opposite directions from each other. Then, they are recorded and counted by detectors only if they hit them at the same time, thereby producing high-resolution 3D images.

For SPECT myocardial perfusion study, the most performed nuclear cardiology evaluation, after injection of the radiotracer (either at resting or stress), the patient sits or lies on a table with single or multiple detector heads rotating around the chest and must remain stationary for between 12 and 25 min during the acquisition. Patient motion during the study is one of the many potential sources of artifact in nuclear imaging. Although algorithms have been developed to correct for motion in a craniocaudal direction, horizontal motion is more difficult to correct for and the optimal strategy remains to prevent, as far as possible, patient motion.

Cardiac PET

The electrical collimation unique to PET yields high spatial resolution and high-count density images. The technique is intrinsically 3D with spatial resolution almost ten times superior to SPECT and stress and rest perfusion protocols are generally shorter than SPECT. PET can measure both blood flow and metabolic rates of a variety of energy substrates and this characteristic is particularly useful in research applications. These inherent advantages combine to provide better diagnostic accuracy, in terms of both sensitivity and specificity, in PET myocardial perfusion imaging than SPECT. Finally, there are many positron-emitting tracers available to evaluate specific aspects of myocardial tissue function. In clinical practice, cardiac PET imaging is commonly used for complex cases where myocardial viability and hibernation are in play.

However, PET has different limitations as its high cost, radiation burden, limited spatial resolution, and the complexity in acquisition and analysis of the data.

Computed tomography

Cardiac computed tomography[53,54] (CT) has evolved rapidly over the past two decades to encompass many important clinical applications including the assessment of congenital heart disease, ventricular volumetric and functional analysis, valvular disease, preoperative cardiac and thoracic surgical planning, and disorders of the aorta and great vessels.

The basic principle of CT involves the passage of a thin x-ray beam through the patient's body at many angles allowing generation of cross-sectional images. The x-ray transmission is collected by a detector array and digitized into pixels of known dimensions. The grayscale information in individual pixels is determined by the attenuation of the x-ray beam by tissues of different densities -for example, the bone, muscle, fat, blood, or air- defined with reference to the value for water in units known as Hounsfield units. Differences in brightness between points of the image are determined by the physical density of the tissue/fluid imaged and the absorption of the x-ray beam. Calcium is bright white, air is black, and the blood and muscle are varying shades of gray. Iodinated contrast may be added to highlight vascular structures.

CT scanners used for cardiac imaging use either a rotating x-ray source with a circular stationary detector array (spiral or helical CT) or a rotating electron-beam CT.

Cardiac Magnetic Resonance imaging

Having excellent spatial and temporal resolution, unrestricted tomographic fields, and no exposure to ionizing radiation, CMR provides morphological and functional information relevant to a broad array of cardiovascular diseases. This is the reason why it is considered the gold standard for cardiac imaging.

MRI is based on imaging of protons (spins) in the body[55] which behave like tiny magnets. When a patient is placed inside the CMR scanner within a static

magnetic field (called β_0), spins either align with or arrange opposite to the main direction of β_0 . The magnetization of the summed spins (aligned and opposing) forms a net magnetization vector aligned along the longitudinal axis (z-axis) of the magnet. In addition to lining up with β_0 , spins also precess at a frequency ω_0 (known as the Larmor frequency). The Larmor frequency is proportional to β_0 : $\omega_0 = \gamma\beta_0$ where γ is the gyromagnetic ratio (a constant for hydrogen for a given field strength).

In an imaging magnet, three orthogonal sets of gradient coils are placed so that a slight linear alteration in the strength of β_0 can be created in each of the x, y, and z directions. As a result, magnetic spins precess at frequencies according to their locations along each of the three orthogonal axes and they can be selectively excited by specific radiofrequency (RF) pulses. To create a magnetic resonance image, an RF pulse with a frequency matched to the Larmor frequency of the magnetic spins will excite magnetic spins of interests to a higher energy state. This leads to transition of the net magnetization vector from the z-axis onto the x-y plane.

The magnitude of the vector onto the x-y plane will determine the amount of signal generated, which is received by a set of surface coils. To imaging a specific slice plane through the body, the magnetic gradient causes a spread of Larmor frequencies perpendicular to a prescribed slice plane. The RF pulse will then only excite the slice plane with magnetic spins precessing at frequencies matching the frequency bandwidth of the RF pulse. The absorbed electromagnetic energy will be released by two coexisting mechanisms: longitudinal magnetization recovery and transverse magnetization decay.

Longitudinal magnetization recovery corresponds to the exponential rate of recovery of the longitudinal component (z-direction) of the magnetization vector, characterized by a time constant, T_1 , which is defined as the time to recover 63% of the original longitudinal magnetization vector. T_1 is a physical characteristic of tissue and is affected by the field strength of the scanner. T_1 characterization therefore allows generation of images that reflect the differences of T_1 between tissue types.

The transverse magnetization decay results from interaction between neighboring spins (or spin-spin interaction) leading to exponential loss of the transverse component of the net magnetization vector, defined by the time

constant T_2 . T_2 is tissue-specific and is defined as the time to lose 63% of the transverse magnetization. Unlike T_1 , T_2 values are less related to the field strength of the scanner.

With the application of magnetic field gradients in any of the three orthogonal directions, the magnetic resonance signal can carry spatial localization information, produced by encoding steps known as slice select, phase encoding, and frequency encoding. The information regarding the magnetic resonance signal is stored in a data matrix called the k-space, which undergoes 2D-inverse Fourier transformation to form an image.

Technical aspects

CMR employs a range of strategies to overcome technical difficulties caused by the cardiac, respiratory, or blood flow motions[56]. To reduce blurring from cardiac motion, many CMR techniques fractionate the image to acquire data only within a narrow window of the cardiac cycle (known as segmented approach). Currently, patient breath-holding remains the most common method to contain respiratory motion during CMR data acquisition. Finally, by rapidly acquiring data of an entire image within a cardiac cycle, single-shot imaging and real-time cine imaging (continuous acquisition of single-shot images) can overcome both respiratory and cardiac motions at the expense of reduced temporal and spatial resolutions.

One of the main advantages of CMR is the possibility to interrogate the heart in different angles (the views displayed in Figure 12) enabling a comprehensive view of the heart geometry and identification of specific anatomical features.

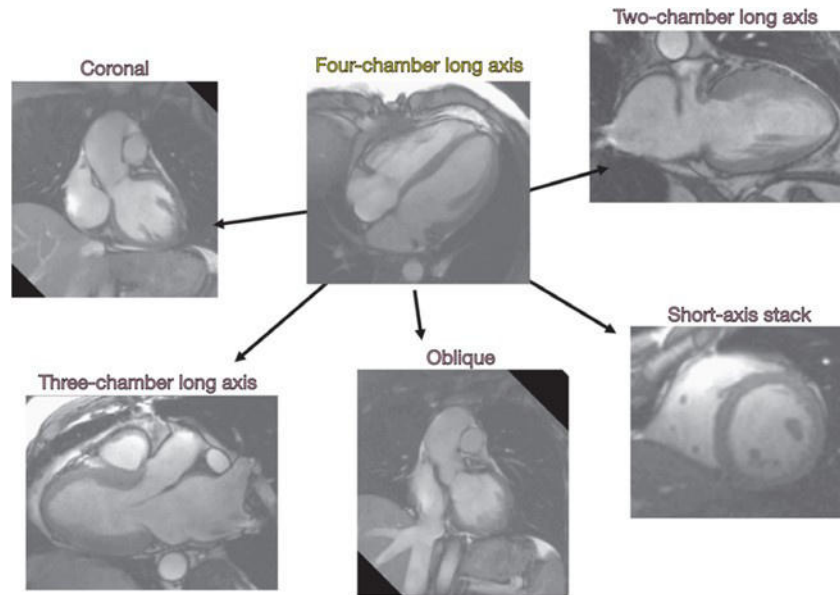


Figure 12. The planes of views of CMR imaging. Traditionally, CMR functional analysis uses the standard echocardiographic planes including the four-, three- and two-chamber long axis views and short axis views. From Daly, Abbasi and Kwong[26].

Cine CMR is the modality that serves as a reference standard for quantifying ventricular volumes. Among the cine techniques, the steady-state free precession (SSFP) is commonly the technique of choice. It can acquire a cine movie at a high temporal resolution of 30–45 ms during a breath-hold of <10 s thus capturing the whole heart in motion volumetrically for 3-5 min.

The most available technique developed to quantify intramyocardial motion is line tagging. Tagging assesses myocardial strain by marking the myocardium with parallel dark lines or a grid so that myocardial deformation can be visualized or quantified. Circumferential and radial strain can also be calculated and displayed with a color-coded scale (Figure 13).

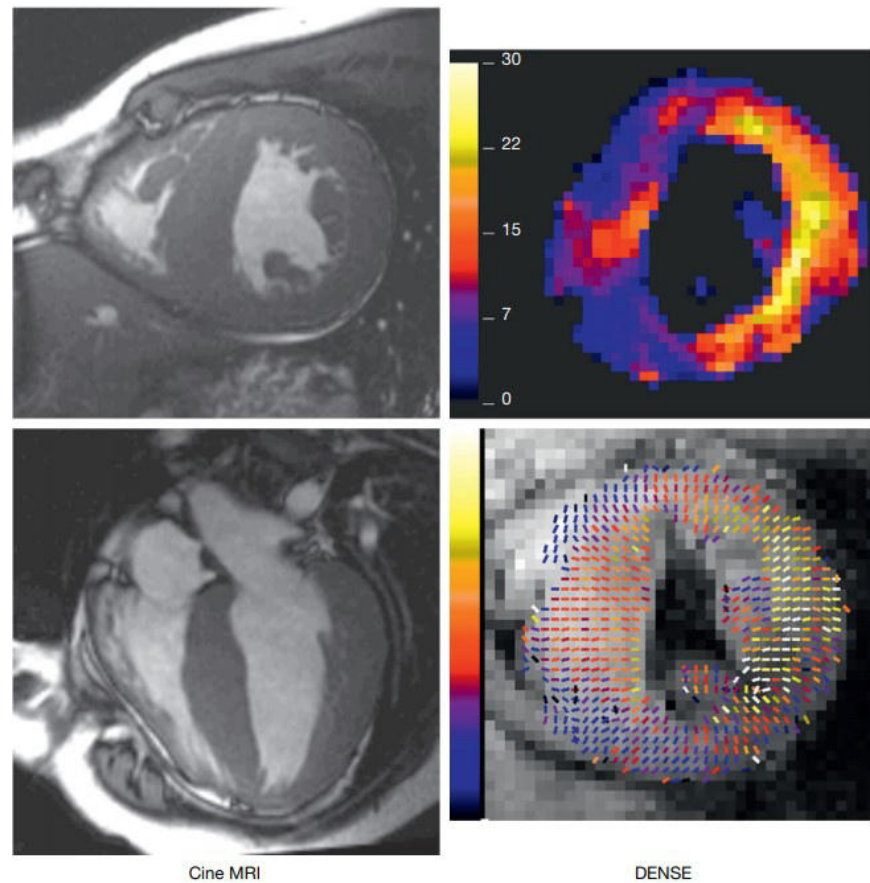


Figure 13. Cine cardiac magnetic resonance to detect intramyocardial motion. Left panels: cine steady-state free precession imaging used to qualitative assess wall motion. Right panels: quantitative assessment of wall motion with displacement encoding with stimulated echoes (DENSE) technique. From Daly, Abbasi and Kwong[26].

Contrast agents

Currently, only gadolinium-based contrast agents (GBCAs) are used clinically. When injected as an intravenous bolus, GBCA takes 15–30 s transit through the cardiac chambers and blood vessels (first-pass phase) before it diffuses into the extracellular space. At ~10–15 min after injection, a transient equilibrium between contrast washing-in into the extracellular space and washing-out to the blood pool is reached. Myocardial perfusion CMR and most magnetic resonance angiography are performed during the first-pass phase, whereas late gadolinium enhancement images are obtained during the equilibrium phase. Briefly, as the human body is composed for around 70% of water, the best choice for a contrast agent is a water-soluble one and Gadolinium is a water-soluble chelated agent laying in the intravascular space and permeating the

interstitial space of the tissue except brain (Figure 14). A healthy tissue will display different Gadolinium concentration compared to a pathological one due to the different kinetics. Moreover, pathological myocardium has larger interstitial space because of a loss of intact myocardium in infarcted/scarred hearts[55]. Therefore, because Gadolinium is a contrast agent that shortens the T_1 of the proton spins, an abnormal myocardium will show signal enhancement on MRI images[56].

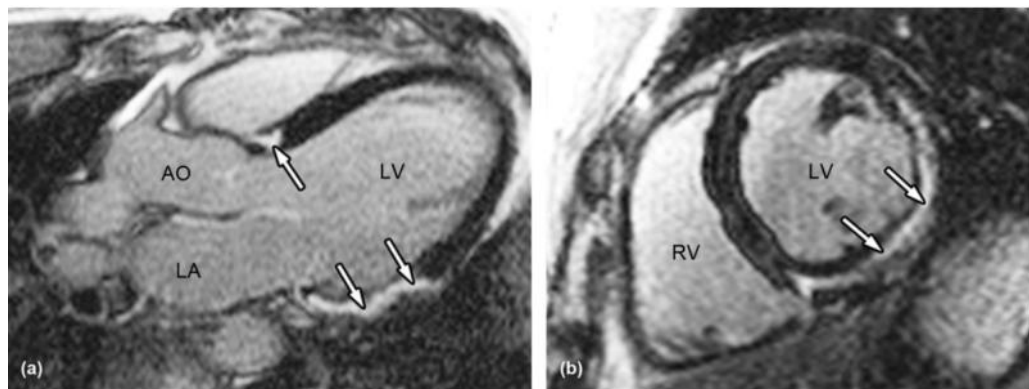


Figure 14. Late gadolinium enhancement (LGE) imaging in a patient with cardiac sarcoidosis. Left panel: three-chamber view. Right panel: short axis view. White arrows: foci of dense gadolinium accumulation. Ao, aorta; LV, left ventricle; LA, left atrium; RV, right ventricle. From Daly, Abbasi and Kwong[26].

For diffuse fibrosis assessment, the modified Look-Locker inversion-recovery sequence (known as MOLLI) is commonly used and often acquired in breath holding in a basal and a mid-ventricular short-axis view, before and after contrast administration[57] (Figure 15).

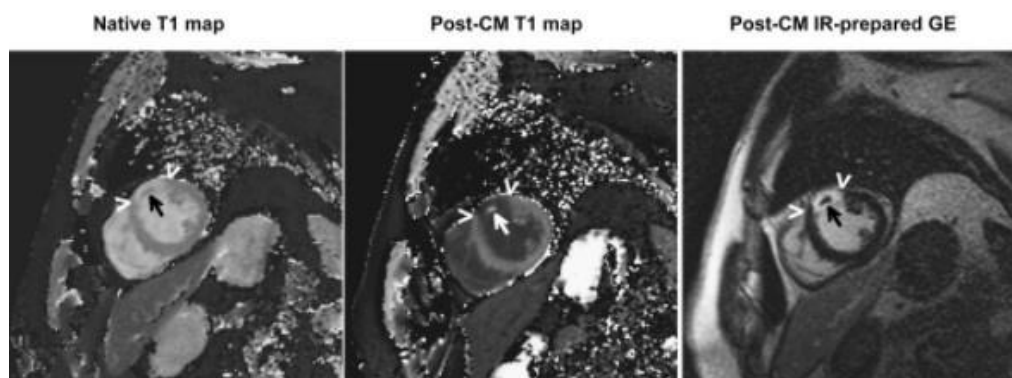


Figure 15. Pre- and post-contrast (CM, contrast medium) short-axis T_1 maps and corresponding conventional inversion recovery-(IR)-prepared gradient echo (GE) in a patient with acute anteroseptal myocardial infarction. The extent of infarcted region is highlighted by arrowheads, while the arrows indicate the “hypo-enhanced core” phenomenon. From Messroghli et al[57].

Compared to the T_1 mapping technique described by Wacker et al[58,59], MOLLI images have a higher matrix (240×151 vs. 128×80) despite their lower acquisition time (191 vs. 230 ms) and hold higher dynamic signal range due to the use of an inversion pulse instead of a saturation pulse.

CMR is the gold standard for congenital heart disease

CMR offers tomographic imaging in any orientation or angle, making it the ideal study for morphological assessment of the heart in congenital heart disease[55].

While infants and children generally have acceptable acoustic windows for echocardiographic imaging, these windows become more limited with body growth or chest wall deformations as these patients approach adulthood, creating an important role for CMR. Additionally, the lack of ionizing radiation by CMR allows for repeat evaluations without fear of aggregate radiation exposure (as it occurs with CT scan).

CMR provides a noninvasive alternative to echocardiography and diagnostic catheterization in assessing patients presenting with evidence of right-sided volume overload or when the detection of shunting is inconclusive. CMR can determine the presence of septal defects, their location, and their suitability for transcatheter closure in addition to providing important information about right heart size and function

Finally, conotruncal anomalies such as tetralogy of Fallot (TOF) are a common referral to CMR in young adults. In patients being planned for surgical repair of TOF, CMR allows for evaluation of the sources of pulmonary blood flow (including pulmonary arterial, aortopulmonary collateral, and ductus-arterial sources) in the presence of RV outflow obstruction. In addition, CMR allows for the quantitation of the severity of infundibular or pulmonary stenosis, assessment of RV function, and evaluation for coexisting anomalous coronary artery.

Strain

The term ‘strain’ is used to describe local shortening, thickening, and lengthening of the myocardium as a measure of regional LV function.

The strain tensor has six components, three of them providing the shortening along the three orthogonal axes (x, y, z), and three shear strain numbers providing the skew in the x–y, x–z, and y–z planes. By dividing the myocardium into many cubes, the complex and detailed deformation can be described by one strain tensor for each small element at each time during the cardiac cycle[60]. However, this description is too detailed for practical use in routine echocardiography assessment where it is only required a limited number of parameters representing the average deformation within a segment of the myocardium.

Therefore, it is more convenient to use an internal coordinate system aligned with the three cardiac axes (longitudinal, circumferential, and radial), and to measure both shortening and elongation in the three directions through the cardiac cycle referring to the size at the time of the QRS-complex. If we denote L_t as the segment length along one of these directions at any time t in the cardiac cycle and L_0 as initial length, 1D strain is defined as: $\varepsilon_t = \frac{L_t - L_0}{L_0}$

This is also called Lagrange strain and it is measured by the distance between two material points in the myocardium both following the motion during contraction and relaxation. Noteworthy, positive strain represents elongation whereas negative strain is shortening. Strain (ε_t) in the myocardium can be measured by TDI, speckle-tracking echocardiography (STE) or CMR.

Tissue tracking for strain measurements

Generally, the initial step is to recognize the key cardiac events: end-diastole (ED) and end-systole (ES).

Definition of ED and ES has been reported to have a major influence on the accuracy of strain measurements, up to the point that changing either ED or ES by only four frames can significantly impact strain values by as much as 20–40% relative changes[61].

The second step is the definition of a region of interest encompassing the myocardial wall by semi-automatic contouring of the endocardial and epicardial borders either in ED or in ES or both. Segmentation is a critical step as it defines the set of points that will be tracked, introducing variability depending on the user and the segmentation algorithm[62]. Finally, the region of interest is tracked throughout the cardiac cycle, and strain curves are computed, possibly post-processed. These concepts are portrayed in Figure 16.

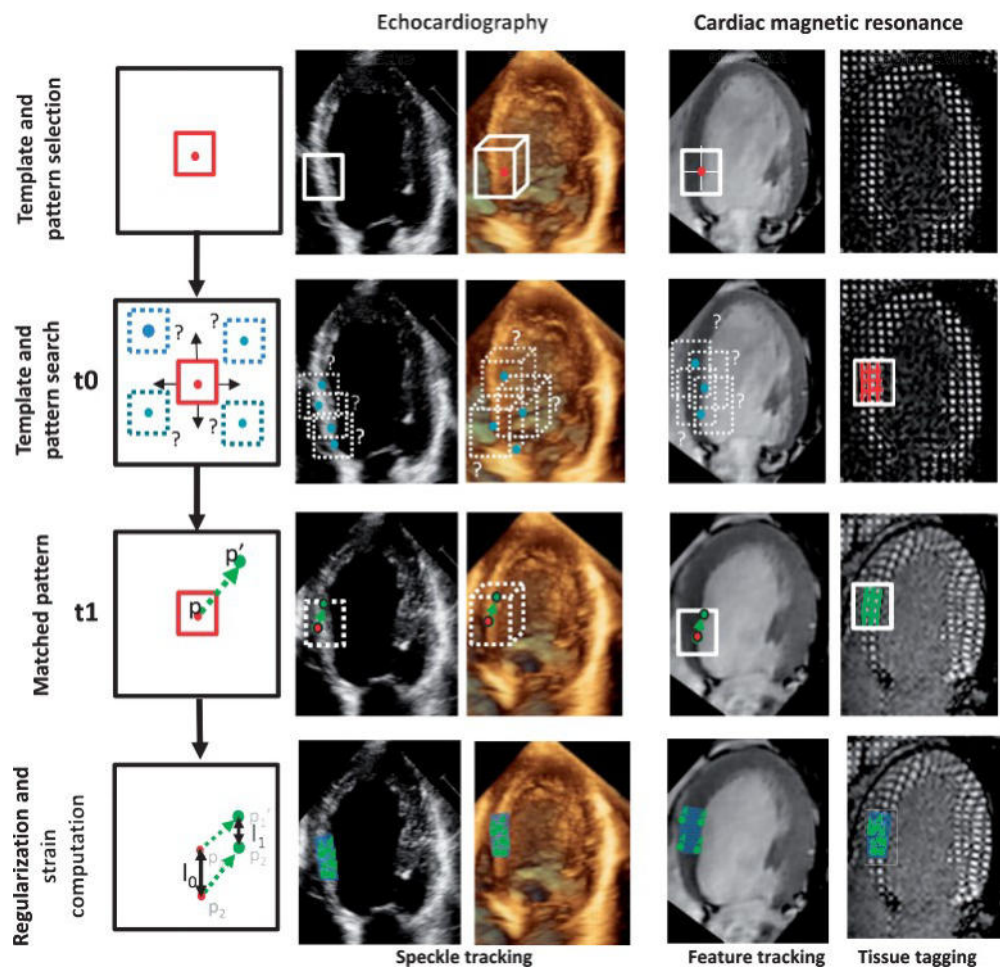


Figure 16. The principles of tissue tracking in three different techniques: echocardiography, cine-CMR and CMR-Tagging (from left to right). The first step is the identification of specific and stable characteristics in the image. In cardiac imaging it is used the speckled pattern of echocardiographic images, the anatomical features recognized in cine-CMR images or by exploiting tissue magnetization in CMR-tagging. These patterns will be followed over time frame-by-frame by different algorithms (i.e. the flowchart on the left) searching the most probable pattern. From Amzulescu et al[63].

The algorithms used to measure strain apply spatial and temporal smoothing to regularize the results and reduce the noise, which can affect the measurement

robustness in two ways: by missing significant localized abnormalities in the case of spatial smoothing or by masking rapid events in case of temporal smoothing[64,65]. Moreover, as strain is computed from the spatial derivatives of the displacement, different regularization strategies can dramatically affect the range of deformation values computed from the displacement field when considering single material points or small regions. Therefore, parameters based on local estimates are more prone to variability than those based on an integrative combination. In fact, it is known that global strains are more stable and reliable than segmental strains. For block-matching algorithms, the most used method for strain measurement, the size of the search region must be carefully tuned[64]. In general, solving for displacements between short distance regions is challenging and may explain why radial strain (computed on the small distance between endo- and epicardium) is usually less reliable than longitudinal and circumferential strains[66] which are computed over larger regions.

Speckle tracking echocardiography

STE is an alternative technique that analyzes motion by tracking natural acoustic reflections and interference patterns within an ultrasonic window. It is currently the most widespread technique to quantify myocardial deformation[67], mainly because it can be performed on conventional B-Mode images, assuming that the quality is sufficient.

It utilizes the phenomenon in which natural acoustic markers in greyscale ultrasound images form interference patterns (known as ‘speckles’) within myocardial tissue. These patterns are quite stable over the short time between two consecutive frames. An image processing algorithm tracks user-defined regions of interest composed of blocks of ~20–40 pixels, a process known as block matching, containing stable unique and identifiable speckles. This process is repeated for all frames through the cardiac cycle to produce a 2D displacement curve for each point in the myocardium. Subsequently, strains are calculated from each LV segment in circumferential, longitudinal, or radial directions[68].

Speckle-tracking-derived strain is independent of LV morphology and is more reproducible and less affected by intra- and inter-observer variability than tissue Doppler methods. Noteworthy, the measurements are still angle dependent because radial strain has opposite polarity of longitudinal and circumferential strains. Therefore, with increasing deviation from the major axis, there will be progressive reduction in absolute strain. Due to the low spatial resolution in the lateral direction, the best strain performance is always achieved in the direction of the ultrasound beam. This is the reason why most laboratories record LV strain in the long axis and use global longitudinal strain -calculated as the average from all segments- as a measure of global LV function. Technically, good recordings can be achieved along any axis, but interpretation of radial and circumferential strains are complicated by substantial transmural non-uniformity in the normal LV.

Furthermore, similar to all measures of myocardial shortening, systolic strain is load dependent and thus blood pressure should be considered when interpreting measurements of strain[69].

CMR-strain

Myocardial deformation can also be assessed from CMR images following a similar general workflow to that of STE. CMR tagging[68,70] magnetically labels different regions in the myocardium by creating, prior to image acquisition, locally induced perturbations of the magnetization with selective RF saturation planes resulting in dark lines. When the saturation pulses are applied in two orthogonal planes, the resulting tagging pattern forms a grid of intrinsic tissue markers known as tags. Because the magnetization is a property of the tissue, the tag lines move along with the tissue in which they are created during contraction. Thus, tracking the tag deformation allows direct evaluation of the myocardial deformation or strain.

CMR tagging has been widely accepted as the reference standard imaging modality for strain quantification after extensive validation in vitro[71] and in vivo[72-74] and has allowed the development of the first models of normal and abnormal myocardial motion in humans[75]. The main advantage of tagging is that deformation is directly measured by physical properties of the tissue. Yet,

CMR tagging also has certain limitations. Tagged images have low temporal resolution reaching at the best 20–30 frames/heartbeat. Furthermore, tag deposition in the beginning of systole starts after detection of R wave and introduces a delay of approximately 30 ms, thus, tag deposition may not be exactly at the beginning of cardiac contraction potentially leading to underestimation of strain especially at high heart rates. The spatial resolution of tags, as well as the ratio of tag spacing to slice thickness, are also important factors for reliable strain measurements. For this reason, the accuracy of strain estimates from CMR tagging is lower at the endocardial border and in thin-walled regions of the LV, and CMR tagging estimates essentially mid-wall rather than endocardial strain. Finally, tagging requires dedicated acquisition sequence and time-consuming post-processing using specific software.

Basics of the heart video kinematic assessment

Kinematics is the branch of mechanics concerned with the description of the motion of objects without referencing the forces that caused them to move[76]. The structural alterations undergone by the heart during each beat are complex and nonlinear such that its displacements are finite rather than infinitesimal due to variations not only in geometry but also in position.

In 1980 Meier et al[77] developed a video approach to assess the mechanical function of the heart employing the theoretical framework of kinematics, laying the foundation of its use to derive both regional and global quantitative description of cardiac movement.

In their work, the authors implanted three small radiopaque markers in the right ventricular free wall in the midventricle of dog hearts defining a triangle with centroid S (Figure 17).

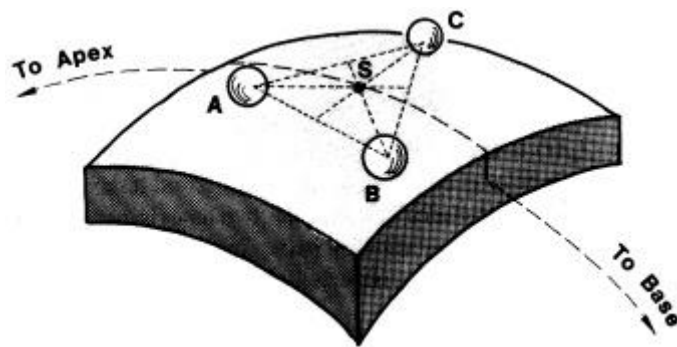


Figure 17. Configuration of the radiopaque markers (the spheres denoted with the letters A, B C) implanted in the epicardium of an *in situ* dog heart defining a triangle with centroid (S). The two arrows represent the primary plane in the local coordinate system. From Meier et al[77].

To set up the local coordinate system they created planes similarly to the ones defined in geography where a terrestrial meridian is the curve of intersection with the earth's surface of a plane passing through both poles. Therefore, they defined the poles by implanting one radiopaque marker at the apex of the left ventricle and another one at the root of the aorta (the base of the heart). By taking the centroid S of the triangle as the given point on the heart, they established the epicardial meridian as the plane bisecting the heart (Figure 18) and its perpendicular vector m .

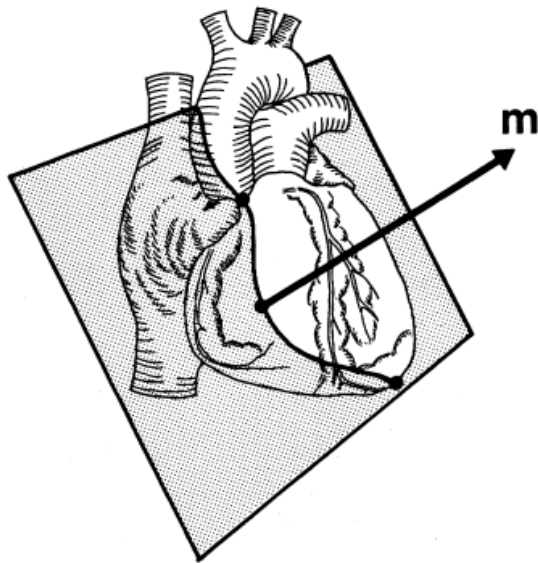


Figure 18. The bisecting plane defined by the two radiopaque markers (represented by the black dots) implanted at the apex and base of the heart and by the centroid of the epicardial triangle. The black arrow represents the perpendicular vector (m). From Meier et al[77].

Next, they established the plane tangential to the epicardial triangle marker and its perpendicular vector n (Figure 19).

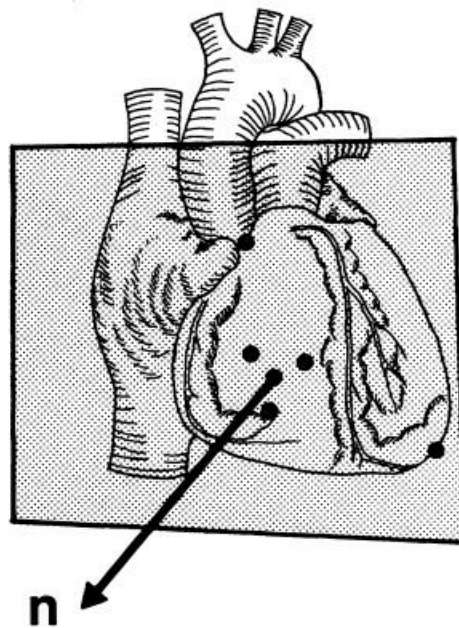


Figure 19. The epicardial tangential plane spanned by the closely spaced epicardial markers and their centroid (black dots). In the figure is represented the two poles at apex and the base also represented by black dots. The black arrow represents the perpendicular vector (n). From Meier et al[77].

Finally, the line of intersection between the bisecting and epicardial tangential planes defines the tangent vector v which is the cross product of the vectors m

and n (Figure 20). The vector u is obtained as the cross product of the vectors v and n and is also tangential to the epicardium. Therefore, the local epicardial coordinate system can now be defined by the local vectors, with the origin in the centroid S , in the directions of u and v .

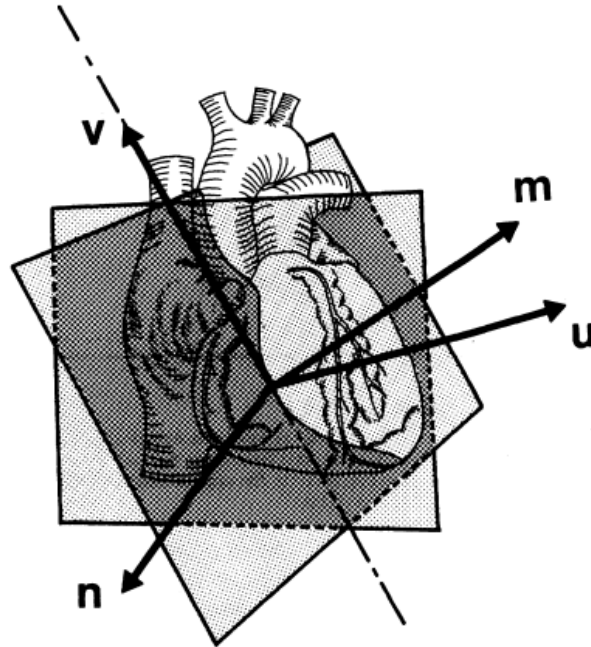


Figure 20. Representation of the local epicardial coordinates system defined by the intersection of the bisecting and epicardial tangential planes. The vectors m and n are perpendicular to the bisecting and epicardial tangential planes, respectively. The vector v is obtained from the cross product between these two vectors. The vector u is obtained by the cross product of the vectors v and n . From Meier et al[77].

With this set up and considering the triangle as a marker, they recorded videos of the *in situ* beating heart at 75 fps and developed a program to extract the coordinates to determine the tensor, calculate eigenvalues, eigenvectors, and the rotation angle[77]. This program takes as references the positions of the five radiopaque markers (one at the apex, one at the base and three at the midventricle) in late diastole.

They also defined that considering the heart's reference configuration at end diastole, when the epicardial region is stretched (during relaxation) in the direction of an eigenvector the associated eigenvalue is positive, whereas when it is shrunk (during contraction) the associated eigenvalue is negative. Moreover, given that the regional deformation in the right ventricular free wall

is homogeneous only at the epicardium, they defined the parameter of wall thickening as an eigenvalue of the stretch tensor.

In Figure 21 are displayed the calculated eigenvalues (Λ_1 and Λ_2) of the local coordinate systems and the derived eigenvalue of wall thinning Λ_3 against the right ventricular pressure (RV_p) measured with a transducer catheter inserted in the ventricle over two cardiac cycles. As it can be noted, the variation of the eigenvalues occurs almost at the same moment of the rise in pressure in the right ventricle and the highest percentage of change was the wall thickening.

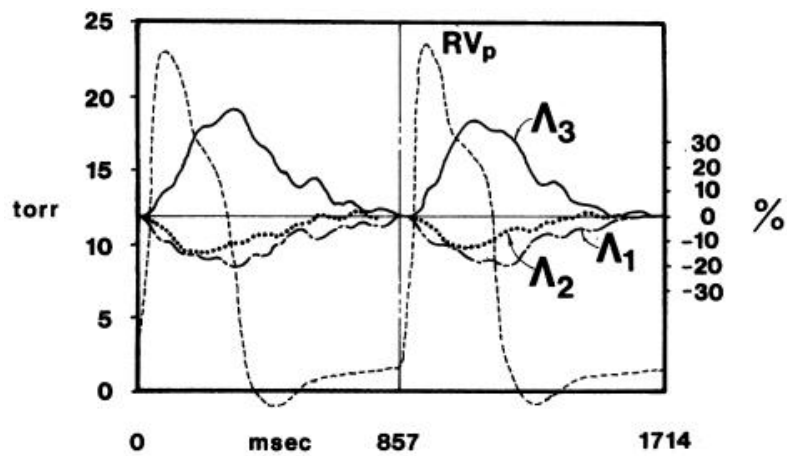


Figure 21. The local coordinate systems eigenvalues (Λ_1 and Λ_2) of the marker triangle and the derived eigenvalue of wall thickening plotted against (Λ_3) the right ventricular pressure (RV_p) during two cardiac cycles. From Meier et al[77].

In conclusion, was the first to present a kinematic approach to evaluate the cardiac mechanical function and because the marker motion is referenced with respect to its own anatomical landmarks (the five radiopaque markers defining the organ coordinate system), their method is valid to compare the results of different hearts.

Later, McCulloch et al[78] aimed to study the regional epicardial deformations in the left ventricle using the kinematic framework. They employed a similar approach described by Meier et al by suturing triplet of markers in an equilateral triangle configuration in six different regions of the left ventricle of dog's hearts (Figure 22).

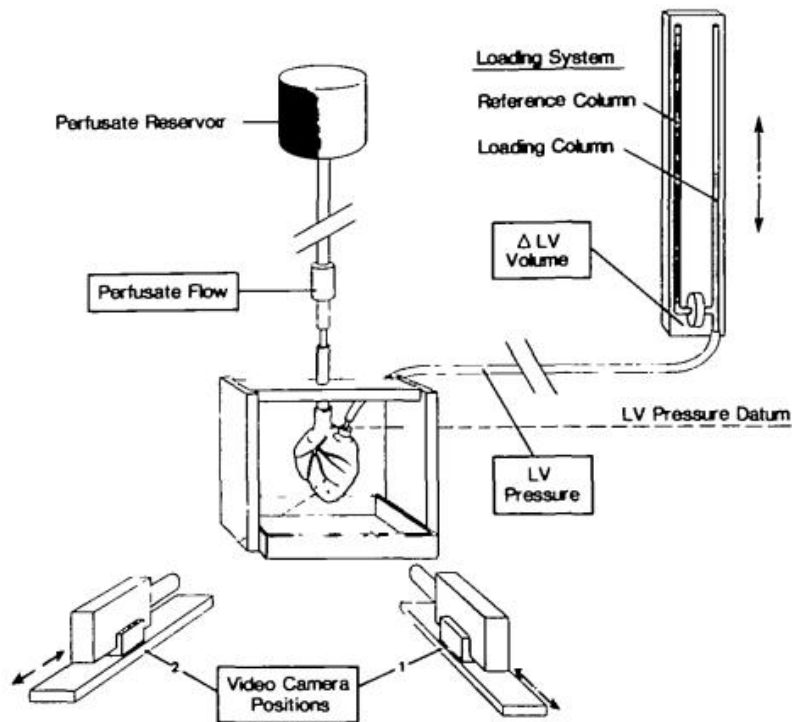


Figure 22. Schematic representation of the experimental recording system showing the heart supported by a special cannula assembly at the center of the biplane video camera arrangement. From McCulloch et al[78].

Each marker consisted of two fine silk threads sutured in a small cross to the epicardium. The marker triplet at the anterior midventricle was selected as the control region, the other triplets were placed at posterior midventricle, anterior base, posterior base, anterior apex, and posterior apex of the left ventricle.

The three-dimensional positions of the epicardial markers were reconstructed from the biplane video recordings using the computer-aided technique developed by McCulloch et al in a previous work[78].

The displacements were analyzed using the homogeneous strain theory described by Meier et al obtaining a complete description of local epicardial deformations independent of the orientation of the marker triangle.

In this case, the local coordinate system was defined as follows: the longitudinal axis was formed by the intersection of the marker plane with the vertical plane containing the axis of the aortic cannula and passing through the centroid, while the local circumferential axis was perpendicular to the longitudinal one and in the plane of the three markers.

Their results show that their approach was able to show the heterogeneities of stretches and wall thinning over the whole left ventricle and at different loading conditions (Table 4 from McCulloch et al[78]). They also showed as example the trends of the major and minor stretches and the wall thinning at different loading condition in three different regions of the left ventricle: anterior midventricle, posterior base and posterior apex (Figure 23).

At the anterior midventricle, both major and minor stretches and wall thinning increased linearly with a rise in volume. The same trend was obtained at the posterior base for the three strains, but the values reached were higher at the anterior midventricle. Finally, at the posterior apex both major and minor stretches increased linearly with rise in volume, while the wall thinning reached lowest values compared to the other regions and displayed a non-linear trend.

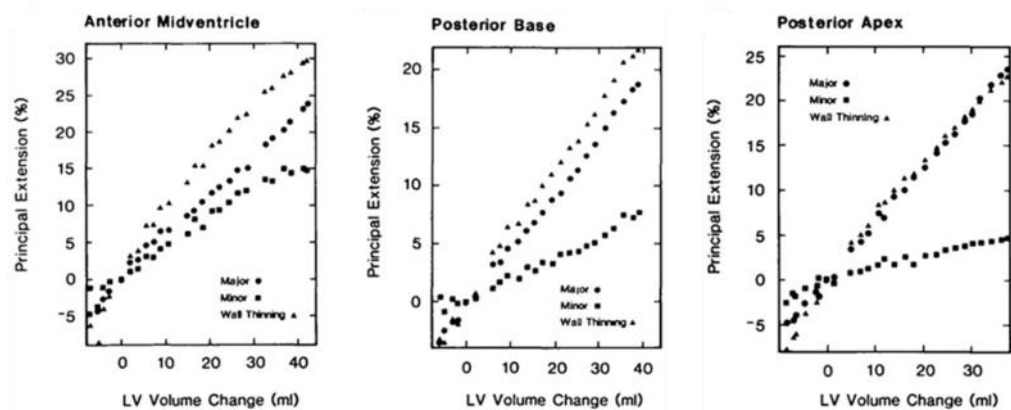


Figure 23. Major, minor and wall thinning strains in three different regions of the left ventricle at increasing loading conditions. Modified from McCulloch et al[78].

This study not only confirmed that strains are heterogeneous throughout the heart but also showed that kinematic parameters of epicardial deformation correlates well with changes in volume.

Cardiac kinematics during open-chest surgery

Successful open-chest surgery requires accurate monitoring and measurement of myocardial mechanical function during the procedure as the movement, deformation, and contractility of both ventricles are indexes of the heart

condition[79,80]. As explained in Chapter “*Echocardiography*”, the clinicians usually used TEE to assess the left ventricular function, while they only visually check the right ventricle. Although the great experience surgeons have built throughout their careers, a method capable to quantify the kinematics of the right ventricle could improve the outcome of the procedure and possibly the prognosis.

Solitani et al[81] developed an optical approach to quantify the mechanical function of the right ventricle during open chest surgery base on Digital Image Correlation (DIC) which calculates the deformation by tracking the movement of points of interest[82]. Usually, a random speckle pattern with high contrast is typically applied onto the ventricle surface and one or more cameras are used to acquire images of the beating heart. Then, by sub-dividing the images into smaller sets, each deformed state image is compared to a reference image when the heart is in a non-deformed state (end-diastole).

In Figure 24 is displayed the DIC setup where the two cameras were installed above the surgery table framing the patient’s chest from an angled view. Complying with the strict regulations inside the operating room, calibration was done after surgery by placing the calibration plate approximately at the position of the heart during the procedure. The results were then transferred to the surface of the heart numerically using an iterative procedure developed by Hokka et al during coronary artery bypass graft surgery monitored with DIC[83].



Figure 24. Representation of the video cameras position in the operating room. Modified from Solitani et al[81]

In Figure 25 is displayed the speckle pattern applied by the surgeon in three different stages of the operation: i) the native stage, when images were obtained after pericardium suspension, ii) weaning stage, recorded after surgical repairs, and iii) drug stage, whose video recordings occurred after a theophylline bolus (minutes after the weaning stage).

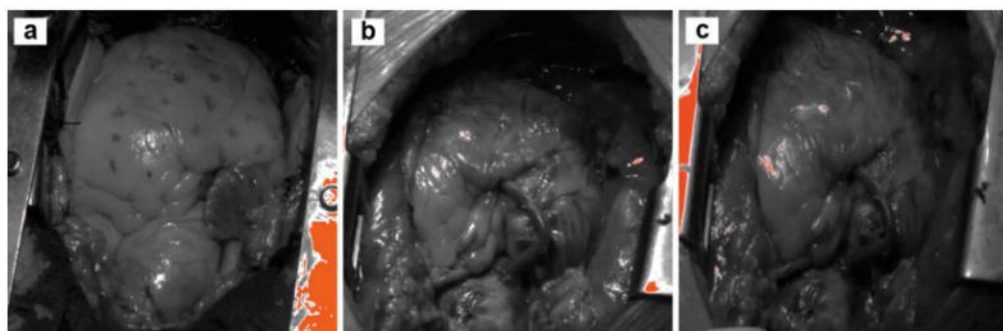


Figure 25. Representative images of the speckle pattern applied by the surgeons in (a) native stage (after pericardium suspension), (b) weaning stage (after surgery), and (c) drug stage (after theophylline bolus). From Solitani et al[81].

The recorded images were processed and analyzed using the Davis software v8.3 by LaVision where vector displacement is always determined from two

consecutive images (Figure 26). Moreover, to alleviate the gradual accumulation of errors during the analysis of a long sequence of images, the displacement was processed for each cardiac cycle individually and then using the software to join them together.

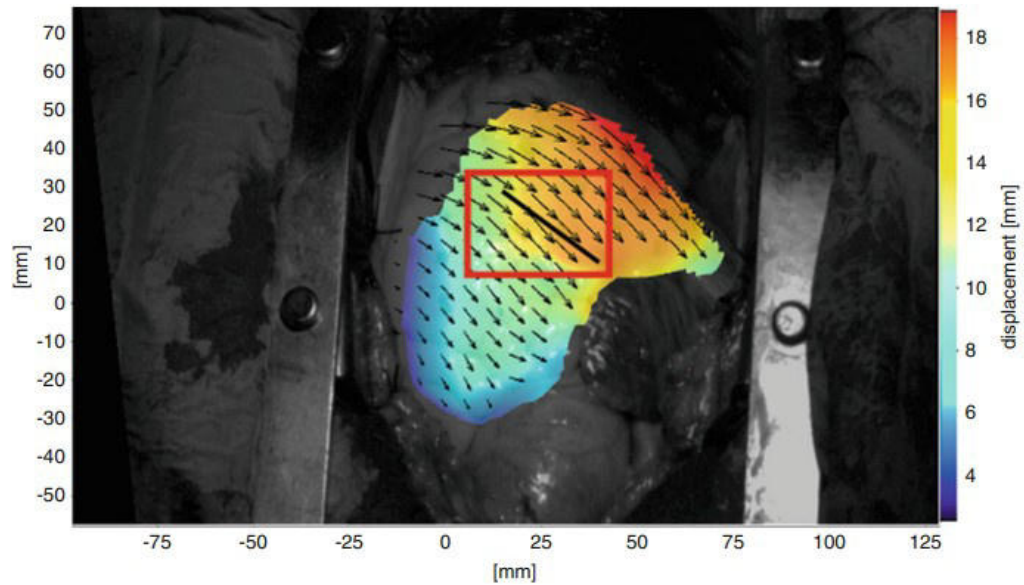


Figure 26. A representative image of the heart with displacement vectors (arrows) heatmap (different colors). The black line represents the length and direction of the virtual extensometer, while the red rectangle represents the region of the interest (specified from the user) from which strain data was extracted. From Solitani et al[81].

In Figure 27 are displayed representative results of the maximum and minimum principal strains for each recording stage. To note that a positive value is obtained during relaxation while a negative value is obtained during contraction because of the selection of the reference frame in end-diastole.

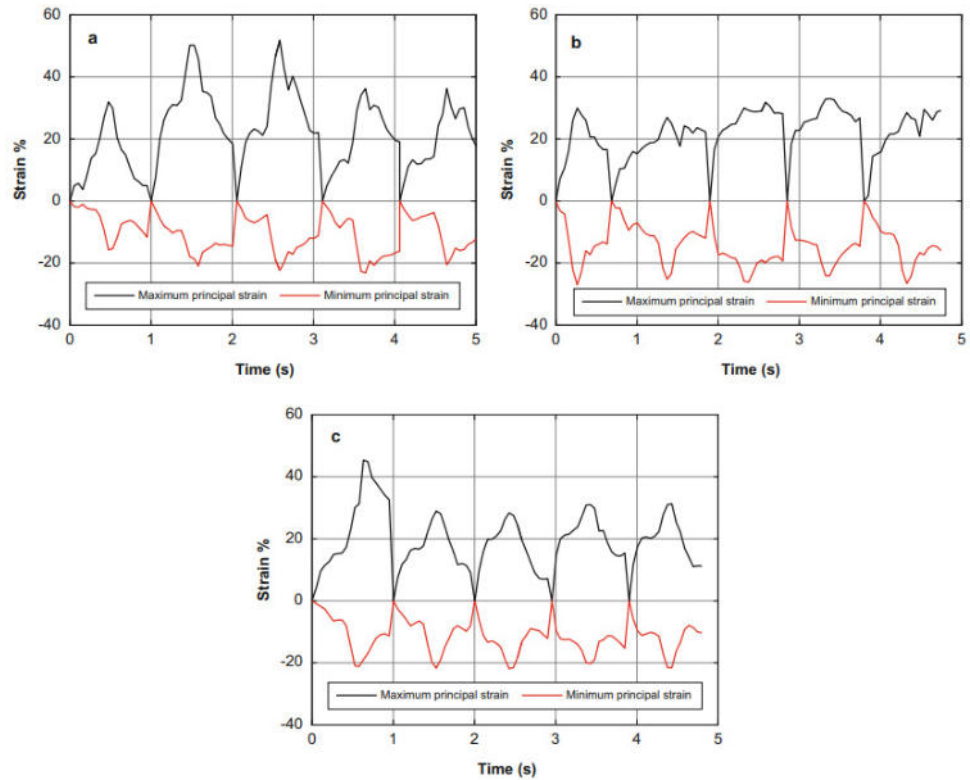


Figure 27. Representative graphs displaying the percentage of both maximum (black line) and minimum (red line) principal strains in the three recording stages: **(a)** native stage, **(b)** weaning stage, and **(c)** drug stage. From Solitani et al[81].

As it can be noted, the strains parameters are similar in values but shows different trends possibly because of the underlying condition of the heart.

In Figure 28 are displayed the overall vector length (V_{lenght}) and its three components along the x , y and z axes for each stage.

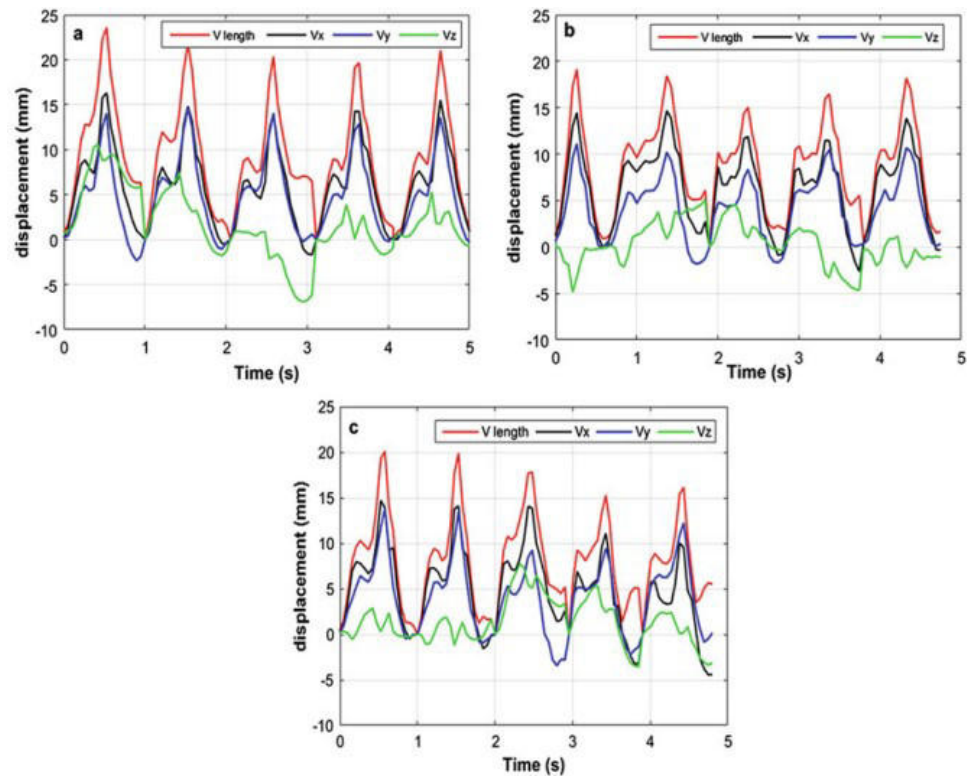


Figure 28. Representative graphs showing the overall vector length (V_{length}) and its three components (V_x , V_y , and V_z) for each recording stage: **(a)** native stage, **(b)** weaning stage, and **(c)** drug stage. From Solitani et al[81].

It can be noted that, in each recording step, V_x and V_y retains the same regular shape varying their values between the cardiac cycles (as expected because of the beat-to-beat variability). However, V_z displays a completely different behavior compared to the other components. Apart from the native stage (Figure 28 a), where it can be somewhat detected a pattern, notwithstanding the high variance in each beat, in the other stages (Figure 28 b-c) the displacement in the z dimension did not have a regular shape and vastly fluctuate.

These results are very interesting as they show the possibility to monitor the right ventricle during open chest surgery employing a video kinematic analysis. However, the approach has different limitations.

One of them is the authors did not perform any correlation with other clinically relevant techniques to demonstrate if DIC held possible prognostic value. Moreover, the quality of the results depends on various factors such as the contrast pattern on the heart's surface which can be applies with spray or graphite particles on biological materials[84,85]. However, none of these

methods is applicable because toxic materials as graphite cannot be used on the human heart during the surgical procedure. Although the presence of non-toxic, biocompatible inks (e.g., methylene blue), the surface of the heart is wet, which hampers the possibility to use sprays for the desired pattern. Moreover, as showed in Figure 25 c, applying the required pattern in the late stage of the surgery was difficult than in the native stage.

Finally, another important factor is the perpendicularity of the cameras with respect to the heart surface. In fact, according to the estimations by Hijazi et al. and Hiddadi et al[86,87], misalignments as small as 2° can lead to high strain errors and that they are linearly proportional to the amount of out of plane displacement, respectively.

Video Kinematic Evaluation (Vi.Ki.E.)

Vi.Ki.E. is a video-based and contactless technique invented, customized and tested through a collaboration between University of Pavia, University of Verona, and University of Parma. It can provide cardiac kinematic data that can be adapted for both basic and clinical research. This innovative technique is able to extract kinematic parameters from videos of beating cardiomyocytes and hearts, displaying video-cardiograms and trajectories of the cardiac cycle[88-91]. At the time of writing, *in vivo* Vi.Ki.E. consists of a high-speed 2D-camera (200 fps in humans, 500-to-1000 fps in animals) placed above the open chest recording videos of the beating heart. The online tracking software Video Spot Tracker (VST, Computer Integrated Systems for Microscopy and Manipulation, CISMM, UNC Chapel Hill, NC, USA) allows to place a virtual marker on the first frame of the video and to track the spatial-temporal coordinates x , y and t of that marker in each frame (Figure 29).

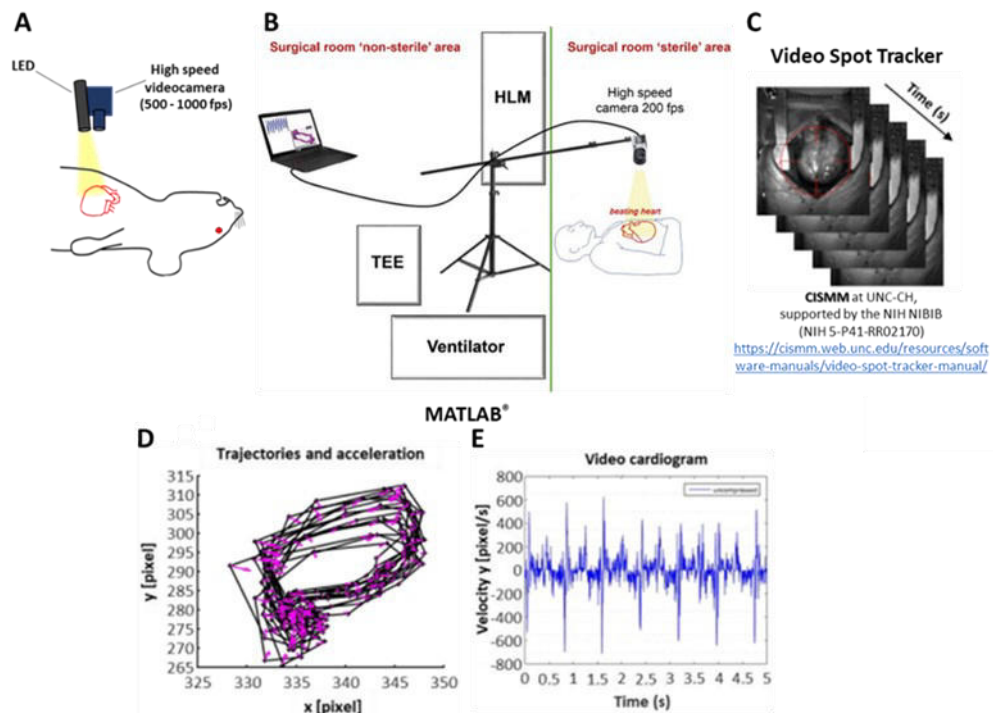


Figure 29. Schematic representation of Vi.Ki.E. workflow. **A:** video camera position during animal experimentation. A LED is placed perpendicularly to the exposed heart to create a light spot that will be used in post processing. **B:** tripod and video camera positions during open chest surgery as described from Rozzi and Lo Muzio et al[89]. **C:** sequence of acquired images analyzed with Video Spot Tracker. The red circle represents the virtual marker positioning on the light spot created either with the LED (in animals) or the scialytic lamp (in human). **D:** the trajectories of the marker in a representative recording. The pink arrows represent the

instantaneous velocity between two consecutive frames. **E**: the so-called video cardiogram, namely, the velocities along one axis of the tracked movement. **D** and **E** are modified from Fassina and Rozzi et al[88].

Then a custom algorithm implemented with MATLAB Programming Language (The MathWorks, Inc., Natick, MA, USA), analyzes these coordinates, computes the displacement along x and y axes, draws the marker trajectories and calculates the parameters showed in Table 1.

Parameter name	Formula	Physiological meaning
Displacement (pixel)	$U = dx$	Marker displacement between 2 consecutive video frames: it estimates the instantaneous movement of the cardiac tissue and builds the marker trajectory.
Velocity (pixel/s)	$v = dx/dt$	Marker velocity between 2 consecutive video frames: it estimates the instantaneous motility or contractility of the cardiac tissue and builds the marker trajectory.
Kinetic energy (pixel ² /s ²)	$E = \frac{1}{2}v^2$	Marker kinetic energy between 2 consecutive video frames: it estimates the consumption of ATP to generate the cardiac movement.
Frequency (Hz)	$f = \text{beat number} / \text{video duration}$	Contraction frequency calculated from the cardiac beats identified.
Acceleration (pixel/s ²)	$a = dv/dt$	Marker acceleration between 2 consecutive video frames: it estimates the instantaneous variation of the motility of the cardiac tissue and builds the marker trajectory.
Force (N)	$F = ma$	Cardiac force moving the mass m .

Table 1. Table displaying the basic parameters of the Vi.Ki.E. technique, their definition physiological interpretation. From Fassina and Rozzi et al[88].

Images processing and definition of the parameters

The approach and the algorithm at the base of the Vi.Ki.E. technique were postulated by professor Lorenzo Fassina (University of Pavia) in a study where he aimed to investigate the kinematic and dynamic parameters to assess the cardiac syncytia movement[92]. Previous studies used variations of pixel intensity to measure beat frequency[93], analysis of negative and positive total pixel intensity to identify beats[94] or contour extraction and shape descriptor methods to calculate the contraction[95]. In his work he used the displacement and the velocity vector field. Briefly, videos of beating cardiac myocytes were processed by VST recording, frame by frame, the spatial-temporal coordinates x, y (both measure in pixel), and t (seconds). Then, for each virtual marker and frame, the displacement (pixel), velocity (pixel/seconds), and acceleration (pixel/seconds²) vectors were calculated and plotted. Because the active phases of the movement of the syncytium involve both contraction and relaxation[96], the kinetic energy was defined as: $E = \frac{1}{2} A \frac{B}{NM} \sum_{i=1}^N \sum_{j=1}^M |v_{i,j}|^2$

where $v_{i,j}$ is the velocity of the marker i in the frame j , M is the total number of video frames, N is the total number of markers, A is the constant related to the tissue mass, and B is the constant derived from the linear relation between the units meter and pixel in a video. If the video camera and the cell/heart positions are not changed during the experiment there is no need to know the mass or the A constant because they are the same in each video. The same occurs for the video metrics or the B constant. Therefore, the normalized mean kinetic energy E_{norm} in a discrete video is defined as: $E_{norm} = \frac{E}{\frac{1}{2}AB} = \frac{1}{NM} \sum_{i=1}^N \sum_{j=1}^M |v_{i,j}|^2$ (measured in pixel²/seconds²)

The contraction force was calculated with the Hamiltonian mechanics in which the energy is the sum of the potential and kinetic energy. By assuming plentiful metabolic resources for a homogeneous production and distribution of ATP, the related potential energy for the contraction movement could be posited as a constant in time and space. Therefore, following the Hamiltonian mechanics and the abovementioned assumption that the mass is constant, the contraction force in a discrete video is defined as: $F_{mean} = \frac{1}{AB} \frac{1}{NM} \sum_{i=1}^N \sum_{j=1}^M |F_{i,j}|^2$ (measured in pixel/seconds²)

Further details can be found in the work of Fassina et al[92].

From cardiac syncytia to the beating heart

Through the collaboration between University of Parma and University of Verona, we tested if the algorithm developed by professor Fassina was suitable to study the kinematics of beating hearts in both basic research (rat) and experimental clinical research. Therefore, the first steps were to validate the parameters of energy and force.

Validation of Energy

The Energy parameter was validated by acquiring videos of the periodic motion of a pendulum oscillating for small displacements (Figure 30).

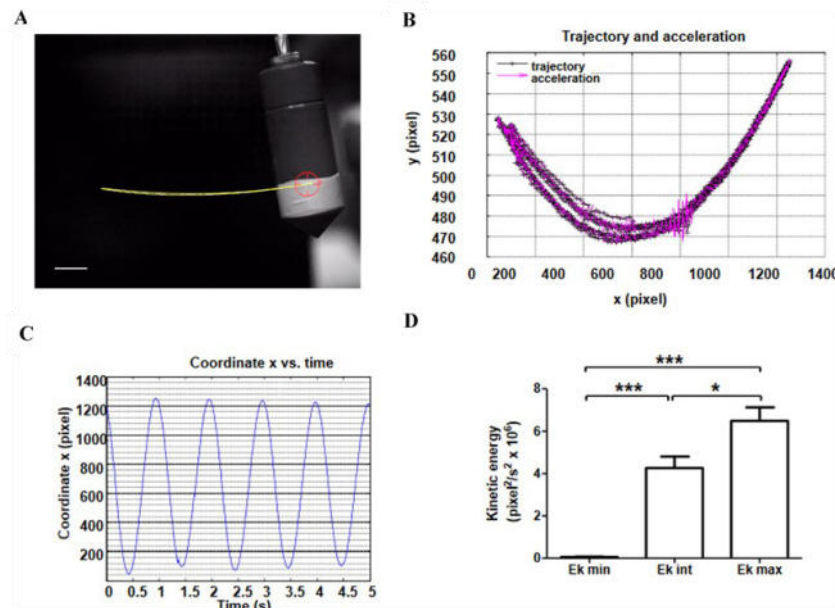


Figure 30. Validation of the Energy parameter. **A:** frame of the videorecording showing the tracking of a pendulum by Video Spot Tracker. Yellow line, pendulum trajectory. Red circle, virtual marker. **B:** Vi.Ki.E. trajectories of the tracked pendulum. **C:** Video cardiogram showing the marker displacement along the x coordinate. **D:** histogram for the kinetic energy at the highest, intermediate and lowest position of the pendulum ($E_{k \text{ min}}$, $E_{k \text{ int}}$, $E_{k \text{ max}}$, respectively). * $p < 0.05$, *** $p < 0.001$. Modified from Fassina and Rozzi et al[88].

The pendulum (mass of 200 g) was connected to an arm by a 21.5 cm not-stretchable string and the motion was acquired at 200 fps for five seconds. The video marker was placed onto a white area of the pendulum and displayed: the trajectories, the coordinate x vs. time and the kinetic energy at the highest, intermediate and lowest positions. As expected, the marker movement was an arc and when the coordinate x was displayed vs. time, it drew a periodic wave. The kinetic energy was measured for five consecutive frames in the three aforementioned positions and was nearly 0 at the highest position ($h = 17$ cm) and maximal at the lowest position ($h = 11.5$ cm).

Validation of Force

The Force validation was made by anchoring a spherical object of known mass (0.035 g, diameter = 3 mm) onto epicardial surface in three different rat hearts (Figure 31).

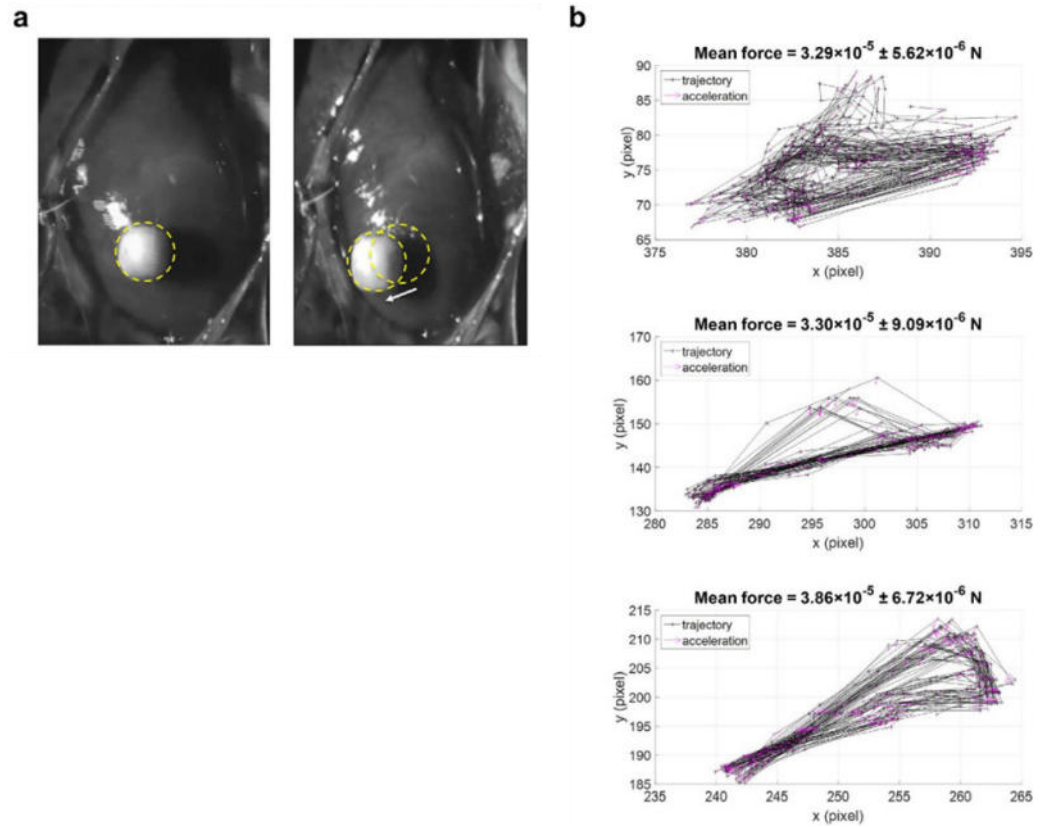


Figure 31. Validation of the Force parameter. **(a)** Position of the spherical mass used during the protocol at the beginning of systole (left) and diastole (right), respectively. The white arrow represents the displacement vector between the two phases. **(b)** Trajectories and acceleration of the spherical mass in three rat hearts with the calculated average contraction force displayed on the top of each panel. Data are expressed as mean \pm SEM. Modified from Fassina and Rozzi et al[88].

This setting allowed to switch from a description of the parameter in terms of pixel acceleration (pixel/s^2) to the International System of Units and to calculate the contraction force (N) moving the mass. In all three rats the Force was about the same, suggesting that every cardiac cycle, even if in different animals, exerts a well-conserved force of contraction. We also observed, for every beat, a well-conserved contraction-relaxation trajectory which was similar to a hysteresis loop due to the intrinsic viscoelastic properties of the myocardium.

Validation via computer model

We evaluated the effectiveness of our algorithm on data obtained from numerical simulations based on the cardiac electro-mechanical coupling (EMC)

model. We modified the model incorporating a transmural ischemic region of $1 \text{ cm} \times 1 \text{ cm}$ with the following parameters.

The intra (i)- and extra (e)- cellular conductivity coefficients of the Bidomain model, along (l) and across (t) the fiber direction, were $\sigma_{il} = 3$, $\sigma_{el} = 2$, $\sigma_{it} = 0.31525$, $\sigma_{et} = 1.3514$, all in $\text{m}\Omega\text{-1cm-1}$. The parameters of the strain energy function were the same of the original paper[97] apart the bulk modulus, which amounted to 200 kPa. The extracellular potassium concentration was increased from 5.4 mM to 8 mM; the maximal conductance of the INa and ICaL currents was decreased of 25%; the parameters of the IKATP current were modified as in Colli-Franzone et al[98] for ischemia stage 2. From the mechanical point of view, ischemic conditions were modeled by reducing the active tension and passive tissue stiffness of 10% and 25% with respect to their normal values, respectively.

The excitation process was initiated by stimulating three endocardial anterior apical sites and one endocardial posterior apical site, mimicking an idealized Purkinje network. Two simulations were performed, one for a healthy tissue (HEALTH) and one for a tissue with a transmural ischemic region (ISCH). In both cases three beats were simulated, at a basic cycle length of 500ms.

Figure 32 shows the epicardial distributions of transmembrane and extracellular potentials computed in the HEALTH and ISCH simulations, during the plateau phase of the heartbeat (ST segment, $t = 120\text{ms}$). The ISCH transmembrane potential distribution showed a minimum in the ischemic region, whereas the ISCH extracellular potential distribution showed a maximum (ST elevation), in correspondence of the ischemic region.

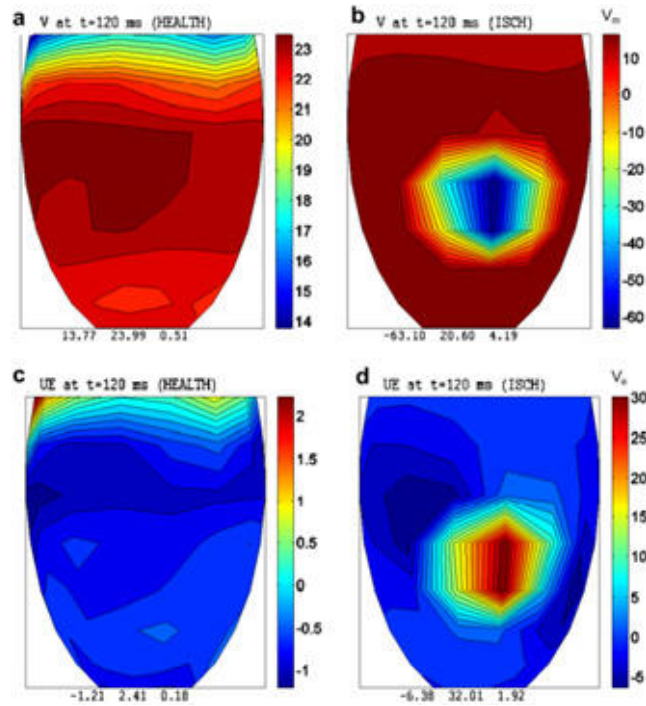


Figure 32. Representation of the numerical simulation of both epicardial transmembrane and extracellular potential distributions. **a:** Epicardial transmembrane potential (V) 120 ms after stimulation in the simulated healthy tissue condition (HEALTH). **b:** V distribution 120 ms after the stimulation in the simulated tissue with transmural ischemia (ISCH). **c:** extracellular potential distribution (UE) 120 ms after stimulation in HEALTH. **d:** UE distribution 120 ms after stimulation in ISCH. The numbers at the bottom of each panel represent the minimum value, the potential step, and the maximum value, respectively, for both V and UE distributions. Modified from Fassina and Rozzi et al[88].

The kinematic evaluation applied to the experimental data was also validated on both the simulated healthy and ischemic tissue (Figure 33).

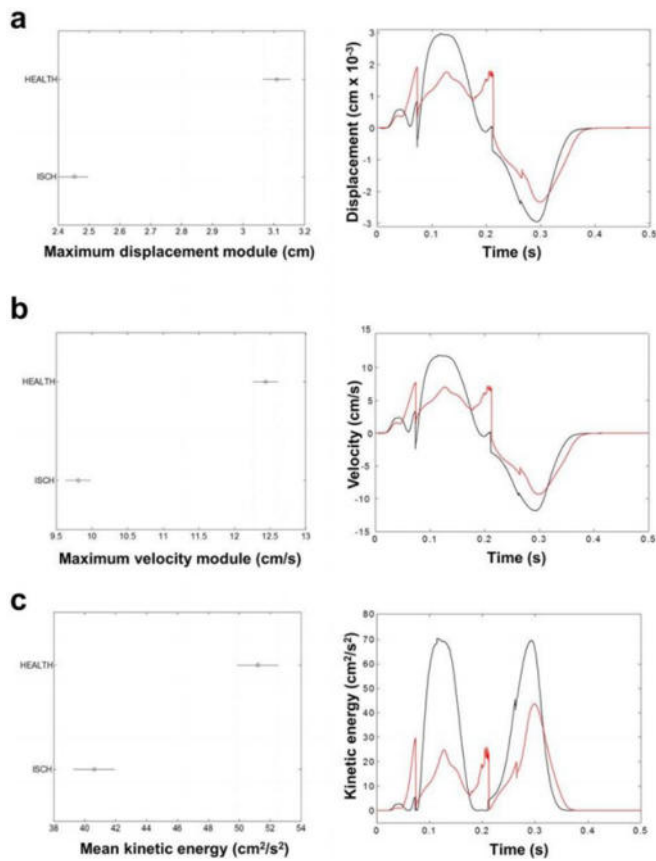


Figure 33. Vi.Ki.E. parameters in a simulated ischemic heart. **a:** Left panel, maximum displacement module averaged across 48 healthy (HEALTH) and 48 ischemic (ISCH) sites. The horizontal bars are the 95% confidence intervals for the differences between means according to one-way ANOVA and LSD (Least Significant Difference) post hoc test. There is a statistically significant difference between the means with non-overlapping bars. Right panel, comparison of the displacement over time between healthy (black) and ischemic (red) for a single sample site. **b:** Same as **a** for the maximum velocity module. **c:** Same as **a** for the mean kinetic energy. Modified from Fassina and Rozzi et al[88].

Figure 33 reports that ischemia decreased of about 20% in: i) the maximum displacement module (Figure 33 a), ii) the mechanical behavior of the cardiac tissue with a reduction of the maximum velocity module (Figure 33 b) and iii) the mean kinetic energy (Figure 33 c).

In conclusion, these theoretical and experimental findings validated the use of our technique and its kinematic parameters as indices of cardiac mechanical performance.

In vivo experimentation

Ischemia reperfusion rat heart model

We acquired videos of 1s in six rat hearts at 500 fps before an acute cardiac ischemia/reperfusion injury model[99] (Figure 34). First, the beating heart was recorded in normal condition (HEALTH) followed by anterior descending coronary ligation. The surgical needle was left within the performed knot to enable the removal of the ligation without damaging the tissue. After the ligation, two more videos were recorded each after 6 minutes in the ischemic (ISCH) and, after removal of the ligation, in the reperfusion conditions (REP).

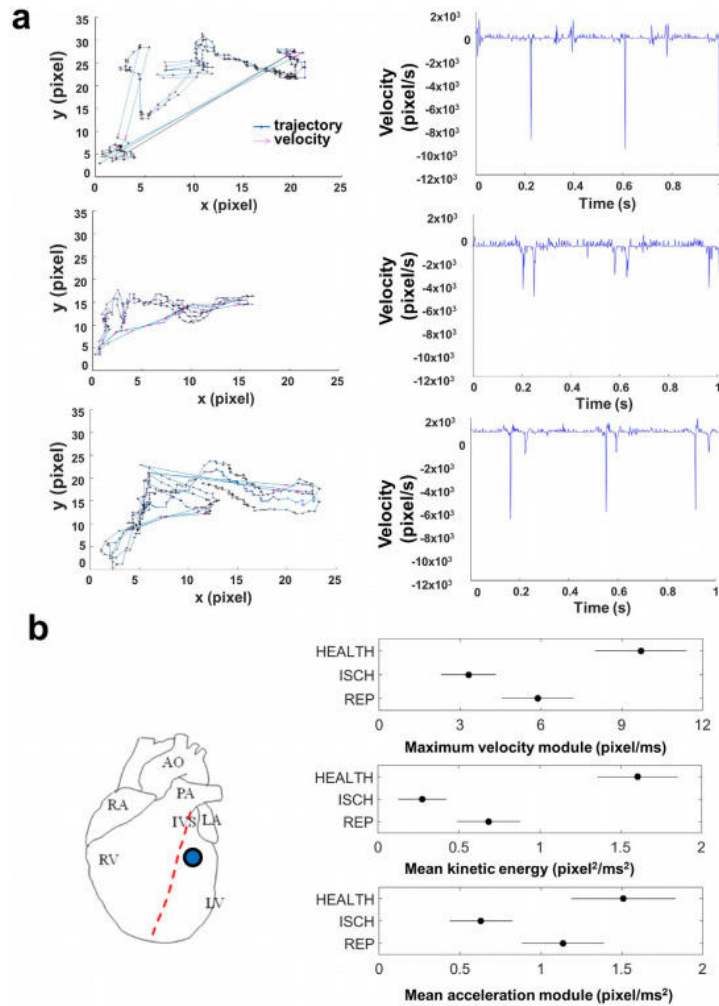


Figure 34. Vi.Ki.E. assessment during an ischemia/reperfusion protocol in rats (n=6). **a:** Left column, trajectories and velocities measured from a recording of 1 s acquired at 500 fps during an ischemia/reperfusion protocol. Top panel: healthy tissue. Middle panel: ischemic tissue. Bottom panel: reperfusion tissue. Right column, marker velocities over time in the three conditions: healthy (top), ischemic (middle) and reperfusion (bottom). **b:** Left panel,

representative position of the virtual marker (blue circle) on the rat heart. The marker radius was 20 pixel and it was placed on the tissue underneath the coronary ligation. Right panel, the kinematic parameters of maximum velocity module (top), mean kinetic energy (middle), and mean acceleration module (bottom) measured in the healthy (HEALTH), ischemic (ISCH) and reperfused (REP) condition. The horizontal bars are the 95% confidence intervals for the differences between means according to one-way ANOVA and LSD (Least Significant Difference) post hoc test. From Fassina and Rozzi et al[88].

We placed the virtual marker on the well-defined region beneath the ligation (Figure 34, left panel) and extracted data where the ischemic tissue turned from deep red to trans-lucid white as a sign of a nearly complete coronary occlusion. Like the computer model simulations, our imaging technique captured that the brief ischemia clearly corrupted the mechanical performance of the ischemic region in terms of trajectories, video cardiograms and kinematic parameters (Figure 34, right panel), while the reperfusion caused significant improvements of those parameters. We found that the maximum velocity module was significantly reduced during ischemia from 9.71 ± 3.09 pixel/ms to 3.32 ± 1.05 pixel/ms ($p < 0.05$ vs. healthy tissue), whereas after 6 min of reperfusion, this parameter was significantly higher (5.88 ± 1.95 pixel/ms, $p < 0.05$ vs. ischemic tissue, $p < 0.05$ vs. healthy tissue).

We observed an analogous behavior for the mean kinetic energy. Specifically, it significantly decreased during ischemia from 1.60 ± 0.68 pixel²/ms² to 0.27 ± 0.11 pixel²/ms² ($p < 0.05$ vs. healthy tissue) whereas, after 6min of reperfusion, this parameter showed significantly higher and more physiological values (0.68 ± 0.16 pixel²/ms², $p < 0.05$ vs. healthy tissue).

The mean acceleration module significantly decreased during ischemia from 1.51 ± 0.84 pixel/ms² to 0.63 ± 0.16 pixel/ms² ($p < 0.05$ vs. healthy tissue) whereas after 6 min of reperfusion, this parameter showed significantly higher values (1.14 ± 0.22 pixel/ms², $p < 0.05$ vs. ischemic tissue).

In addition, the mean frequency of contraction was also decreased in the ischemic condition compared to the healthy one (from 4.08 ± 1.81 Hz to 3.64 ± 0.45 Hz, $p = ns$) and did not change after reperfusion.

Coronary artery bypass graft surgery

Following the testing and validation of our technique in both computer and rat models, we then moved to experimental medicine by recording the hearts of patients undergoing coronary artery bypass graft (CABG) surgery. In detail, we recorded and analysed videos of 10 CABG patients and the results were the following.

In average, the coronary occlusion of the 10 patients was $86.1 \pm 2.5\%$. For all hearts, we selected a video marker (radius= 20 pixel) onto the epicardial surface beneath the region where CABG was performed. We performed video recordings for each patient at chest opening (after pericardium opening) and before chest closing (after protamine sulphate infusion). The TEE assessment (Figure 35) showed a significant improvement for the mean ejection fraction (EF%, from 31.75 ± 4.80 to 46.70 ± 2.60 , $p=0.004$) and a not significant increment for the mean fractional shortening (FS%, from 38.40 ± 6.10 to 50.27 ± 2.50 , $p=0.08$).

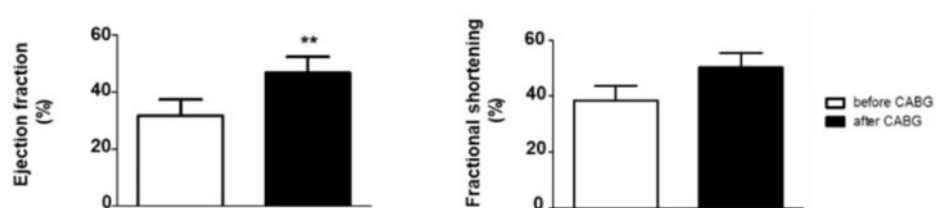


Figure 35. TEE assessment in our CABG population (n=10) through the ejection fraction and fractional shortening parameters. White, assessment before surgery. Black, evaluation after surgery. ** $p < 0.01$. From Fassina and Rozzi et al[88].

With our method, we observed significant changes for the acceleration module ($p=0.02$) and an improvement for the other three parameters (although not significant) (Figure 36).

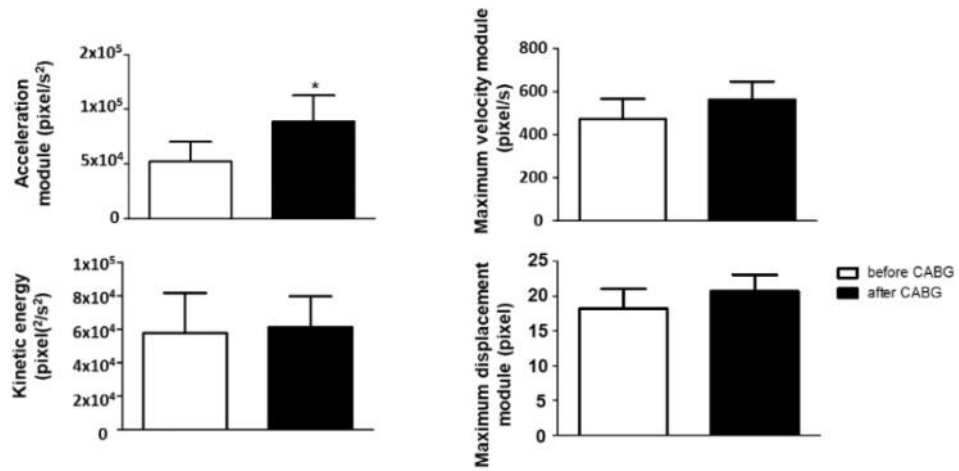


Figure 36. Vi.Ki.E. parameters in our CABG population (n=10). White, assessment before surgery. Black, evaluation after surgery. * p < 0.05. From Fassina and Rozzi et al[88].

However, when we evaluated the individual patient's outcome, it stood out that patient #3, despite increased acceleration module, denoted a substantial reduction in the other three parameters in line with the other patients. Interestingly, patient #6 denoted an increment in all kinematic parameters (Figure 37).

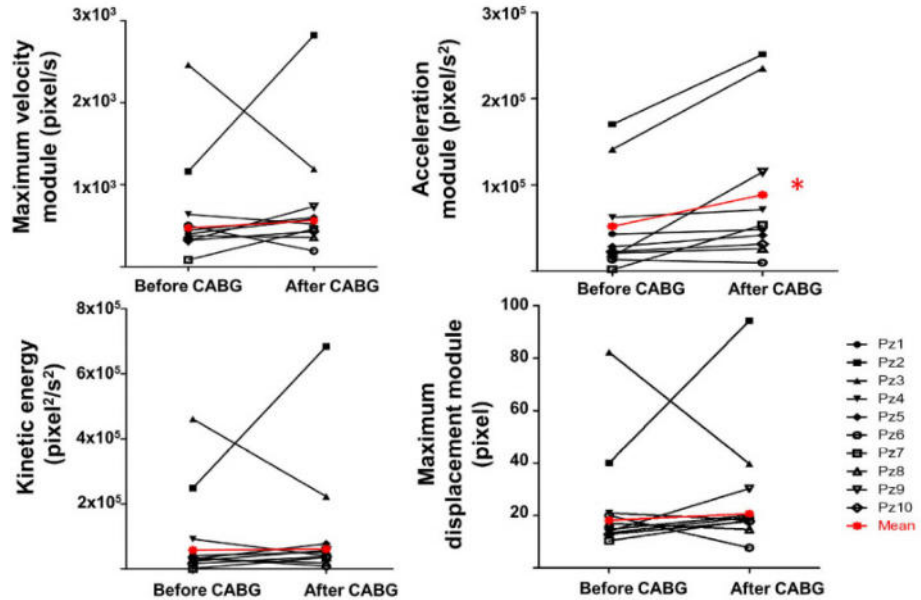


Figure 37. Single patient Vi.Ki.E.-assessment before and after surgery in our CABG population (n=10). From Fassina and Rozzi et al[88].

The results showed that the local cardiac kinematics before and after CABG were extremely variable possibly depending on the volume of ischemic region, age, gender, weight, lifestyle, and medical records (i.e., when coronary

occlusions have been detected). In fact, there is clinical evidence supporting the concept that all patients undergoing CABG have different degrees of myocardial stunning[100], which occasionally requires inotropic support after surgery (i.e., patient #3), but not signs of myocardial infarction.

In conclusion, our parameters must be interpreted considering the pathology under analysis. In the case of the CABG patients, our results find a plausible explanation in the Frank-Starling mechanism which asserts that a decrease in ventricular preload is followed by a reduction of both force and energy consumption[101]. Therefore, our kinematic parameters denote an improvement of the cardiac performance because the heart is less fatigued and, from this perspective, we can conclude that the Vi.Ki.E. results are in line with TEE as emphasized by the increased ejection fraction after surgery.

Vi.Ki.E. 's frequency relationship

Being based on kinematic, the frequency at which the heart is beating can influence the movement of the heart and thus the path (trajectory) and displacement at the base of all Vi.Ki.E. parameters. Therefore, we performed a study on both male and female rat hearts to assess how our parameters behaved at increasing frequency of stimulation (from BCL 390 ms to 160 ms). More details are provided in the Result section “*Vi.Ki.E. 's frequency relationship*” and in *Attachment 4*. Briefly, we observed an increase of our parameters following the increase in frequency of contraction in both male and female rats. However, we also observed, after BCL 230 ms, a different mechanism of adaptation at increasing frequency of stimulation between male and female, possibly related to sex hormones.

Advantages and disadvantages

While several imaging techniques are present for post-operative evaluation of cardiac function (e.g., CT-scan, MRI), only TEE can directly assist surgeons during open-chest surgery assuring an assessment of good-prognosis before closing the chest. However, as already described in the appropriate section, TEE has several limitations as it requires essential operator skills and provides

qualitative and quantitative data (with low reproducibility) only about the left ventricle function with low spatial and temporal resolution. Moreover, its parameters are usually calculated offline with an appropriate software.

On the contrary, the Vi.Ki.E. technique is not invasive and is able to assess the RV -the only ventricle exposed in open chest surgery- in real time with high spatial and temporal resolution. However, the kinematic evaluation performed from a single camera is not suited to study the movement in the z-axis resulting in a bidimensional analysis of a three-dimensional phenomenon.

At the time of writing, the Vi.Ki.E. technique lacks correlations with other techniques commonly used in the assessment of the cardiac function.

Electromechanical dyssynchrony

The contraction-relaxation process within a cardiomyocyte is mainly mediated by Ca^{2+} . The release of Ca^{2+} after electrical activation induces the contraction of the cardiomyocyte, a process known as excitation—contraction coupling[96]. The Ca^{2+} influx through sarcolemmal voltage-dependent channels triggers the Ca^{2+} release from the sarcoplasmic reticulum (SR) in a process known as Ca^{2+} induced- Ca^{2+} release. This increase in cytosolic Ca^{2+} activates the myofilaments that induces cell shortening. To allow cell relaxation, Ca^{2+} is extracted from the cytosol, mainly by the SERCA pump into the SR, and by the $\text{Na}^+/\text{Ca}^{2+}$ exchanger to the extracellular space[96]. In cardiomyocytes, coordinated Ca^{2+} release from the SR determines cellular contraction. Ca^{2+} -induced Ca^{2+} release is regulated locally in subcellular microdomains as demonstrated in some studies providing quantitative evidence for regional differences in the subcellular regulation of Ca^{2+} release[102]. Moreover, Cordeiro et al finely demonstrated there are important differences in calcium homeostasis and mechanical function among the epicardial, endocardial and midmyocardial unloaded cells. Although the three cell types have distinct electrical characteristics, the intrinsic differences in excitation-contraction coupling are needed to synchronize contraction across the ventricular wall[103].

Areas of delayed Ca^{2+} release were related to regional absence of t-tubules and regional differences in Ca^{2+} re-uptake during diastole were also reported[104]. In the study of Hohendanner et al, heterogeneities in the sarcomere

relaxation/re-lengthening time were found which was correlated with the local $[Ca^{2+}]$ decay time. These findings indicate that dyssynchrony of the decay of cytosolic $[Ca^{2+}]$ contributes to dyssynchronous intracellular sarcomere re-lengthening. The increased dyssynchrony in intracellular $[Ca^{2+}]$ decay and sarcomere re-lengthening may impair cardiomyocyte function[104]. All these findings demonstrate the existence of functional heterogeneities within healthy cardiac cells and suggest that they may play an important role under pathological conditions.

The electromechanical delay (EMD) was described as a time elapse between the onset of muscle electrical activation and onset of force production, reflecting both electrochemical processes (i.e. synaptic transmission, propagation of the action potential, excitation-contraction coupling) and mechanical processes[105-109]. In the heart, EMD is a function of the myocyte's intrinsic latent period between membrane depolarization and myofilament activation in the excitation-contraction process[103], but is also dependent on the local myofiber mechanical loading conditions[110].

Experimental observations have shown that EMD is non-uniform, highly dependent on the electrical activation sequence and that there are differences between apex and base[111-113]. In 2004, Ashikaga et al. showed that EMD at a specific location during sinus rhythm (SR) was different from that during epicardial pacing and larger on the epicardium than on the endocardium at a single location[112]. Finally, Ashikaga et al. demonstrated that during transmural electrical propagation, EMD was longer in the late-activated region than at the corresponding stimuli site.

The first computational study to assess the 3D distribution of EMD was by Usyk and McCulloch[114]. In this study, the authors employed an electromechanical model of the normal canine ventricles to determine the 3D EMD distribution during sinus rhythm and following LV pacing. With this model, the authors demonstrated that EMD may be both positive and negative, indicating that myofiber shortening may precede electrical activation in the whole heart. The computational study by Gurev et al[115]. provided a thorough analysis of the 3D-EMD distribution in the normal rabbit heart and its dependence on the loading conditions. Simulations of electromechanical activity during sinus rhythm and LV epicardial pacing were conducted and compared to determine

the effect of electrical activation pattern on the 3D distribution of EMD (Figure 38).

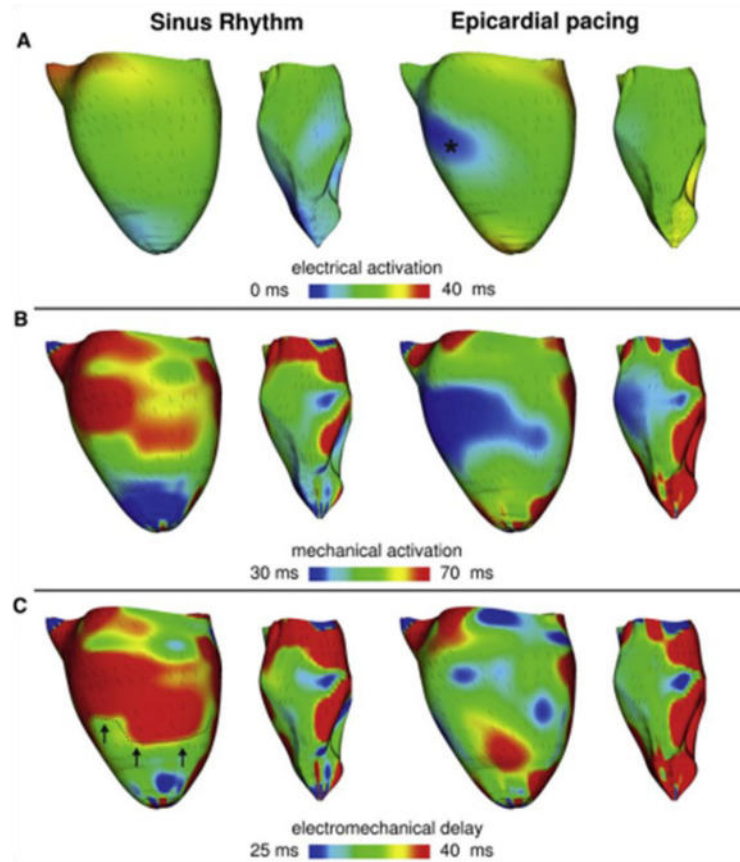


Figure 38. Electrical activation times (A), mechanical activation times (B), and EMD (C) during SR and EP. Each panel display LV lateral view of epicardium (left) and endocardium (right). (Lines) Fiber direction. Modified from Gurev et al[115].

The simulation results revealed that the 3D distribution of EMD was heterogeneous and depended on the electrical activation sequence. Moreover, the distributions were markedly different for sinus rhythm and epicardial pacing. During sinus rhythm, the delay was longer at the epicardium compared to the endocardium and longer at the base compared to the apex. Following epicardial pacing, the distribution was markedly different: the posterior wall exhibited longer EMD compared to the anterior wall. Mechanistic analysis of the electromechanical behavior revealed that the late-depolarized regions were characterized with significant myofiber pre-stretch. The condition of pre-stretch arises either because the early-depolarized regions passively stretch those depolarized later or because, in the later phases of isovolumic contraction, the active tension developed by the late-depolarized regions is insufficient to result

in shortening. This pre-stretch, in turn, delayed myofiber shortening onset and resulted in longer EMD.

Electromechanical dyssynchrony in patients and therapy

Patients with heart failure and decreased function frequently develop uncoordinated contraction because of dyssynchrony which further decreases systolic function and cardiac efficiency and worsens morbidity and mortality[116,117]. Most of the patients with dilated cardiomyopathy have conduction delays such as left bundle branch block[118,119] (LBBB) and the resulting contractile dyssynchrony generates marked regional heterogeneity of myocardial work[120] with the early-stimulated regions having reduced load and the late activated ones having a higher load[121,122] (Figure 39A). Displacement of blood volume from early- to late-regions and back to early activated sites results in a net decline in ejected stroke volume[123]. These shifts occur when differences in muscle activation are greatest between early and late contracting zones, during isovolumic contraction and at late systole into early relaxation (Figure 39B). The global effect assessed by pressure-volume relations reveal a rightward shift of the ESPVR and a decline of both stroke volume and stroke work (Figure 39C).

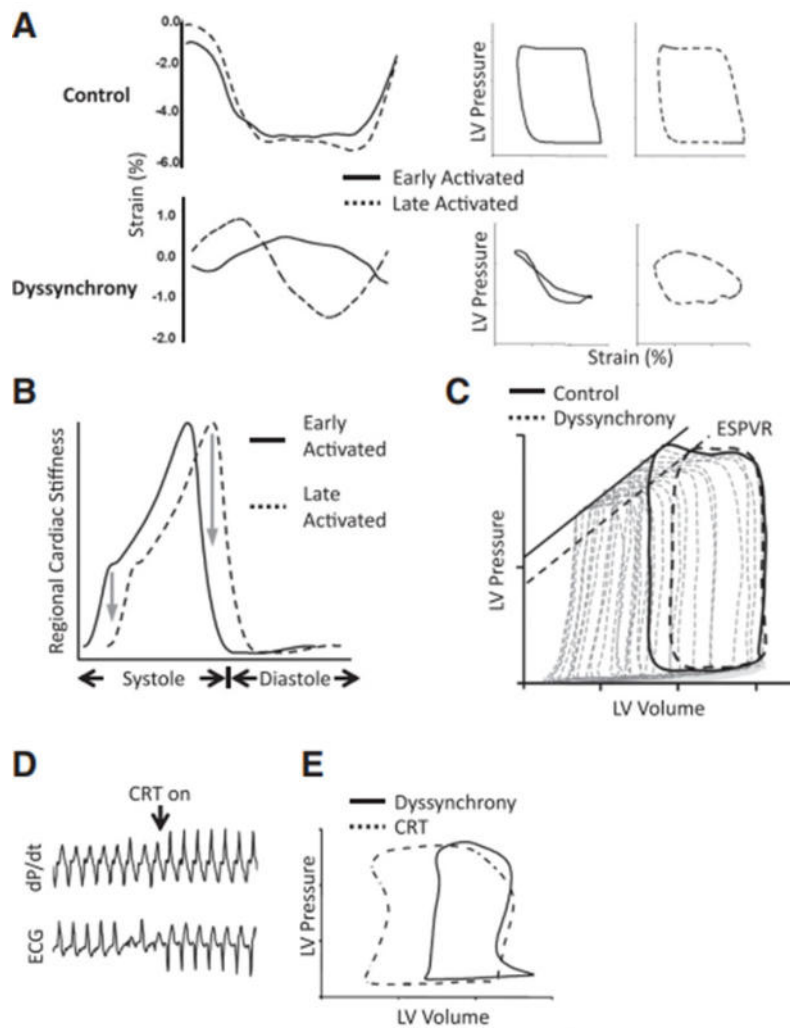


Figure 39. **A:** Left, strain plots vs time for control and dyssynchronous dogs in both the early- and the late-activated regions. As it can be noted, the late activated region is stretched early in the cardiac cycle, while the early-activated region is stretched later. Right, pressure–strain loops for the early- and late-activated regions. From Chakir et al[123]. **B,** Time-varying elastance plots for the early- and late-activated regions highlighting the time difference between them. **C,** PV loops in control and dyssynchronous right ventricle during pacing. The ESPVR relationship shifts rightward in dyssynchrony, indicating reduced function. **B** and **C,** are both from From Spragg and Kass[124]. **D,** Cardiac resynchronization therapy (CRT) has an almost instantaneous effect on function, improving rate of pressure rise (dP/dt) within a single beat. From Spragg and Kass[124]. **E,** CRT also improves the global function, shown via PV loops, reversing the negative changes observed in **C.** From Kass et al[125]. The whole figure is modified from Jonathan A. Kirk and David A. Kass[126].

In the mid- 1990s, the cardiac resynchronization therapy (CRT) was developed: a pacemaker-based treatment to restore mechanical synchrony by electrically activating both right and left sides of the heart[125,127,128]. CRT typically

involves electric pre-excitation of the right ventricular septum or apex and the left ventricular free wall.

CRT is the only clinical treatment that can both acutely and chronically improve cardiac systolic function while also increasing cardiac work and improving long-term survival in patients with an history of dyssynchrony.

Using the biventricular pre-excitation mode of CRT, it occurs an improvement of the ventricular systolic performance (Figure 39D) and an increase of its ejection (Figure 39E). The improvements are achieved without an increase in myocardial oxygen consumption indicating a recovery of the ventricular efficiency[129,130].

Heterogeneities of wall stress, contractility, fibrosis, or other abnormalities can also impact electromechanical association and, thus, lead to uncoordinated contraction which can exacerbates EMD in the late activated regions[110,131]. Furthermore, wall motion can appear dyssynchronous even when electric activation is normal because of regional heterogeneity of myocardium function[132]. For example, dyssynchrony can occur with pulmonary hypertension because of higher right ventricle wall stress[133-135]. Therefore, heart failure is not the only condition when dyssynchrony can arise.

Pulmonary right ventricular dysfunction and occasional failure are associated with many congenital disease, most predominantly postoperative Tetralogy of Fallot[136] (ToF). Right bundle branch block (RBBB) is the most frequent cause of electromechanical impaired coordination in repaired ToF patients and congenital heart disease in general[137,138]. Moreover, these patients can experience RV volume overload that, together with other factors, results in RV dysfunction and adverse clinical outcomes[139,140].

In postoperative ToF, RV dyssynchrony has been associated with decreased RV ejection fraction, mechanical inefficiency, and impaired exercise capacity. In the work of Janoušek et al[141], patients with congenital heart disease and RBBB benefitted from CRT by decreasing QRS duration (a QRS>150ms is commonly a sign of heart failure[142]), eliminating RBBB morphology, increasing the RV maximum rate of systolic pressure rise, the pulmonary artery velocity time integral, and RV filling time.

Electromechanical delay assessment

The difficulty to reliably identify responders to CRT may be due to incomplete understanding of the complex electromechanical interaction required to achieve the functional synchronization in the heart to pump blood.

Different groups have used different methodologies to study the electromechanical coupling in vivo in both animal and clinical studies.

One of the first approach to evaluate the extent of dyssynchrony was to use STE[143,144].

For example, Hui et al[145] and Yim et al[146] adopted STE to study the mechanisms of the RV dyssynchrony in a cohort of ToF patients after repair.

Their method to calculate dyssynchrony in the RV consisted in acquiring the strain curves of the basal lateral and midseptal segments and to calculate the difference in the time-to-onset and the time-to-peak between the two segments. The time of RV systole was defined as the time interval from QRS onset to pulmonary valve closure and the parameters of electromechanical dyssynchrony were calculated with the Q-wave onset on the ECG as a reference (Figure 40).

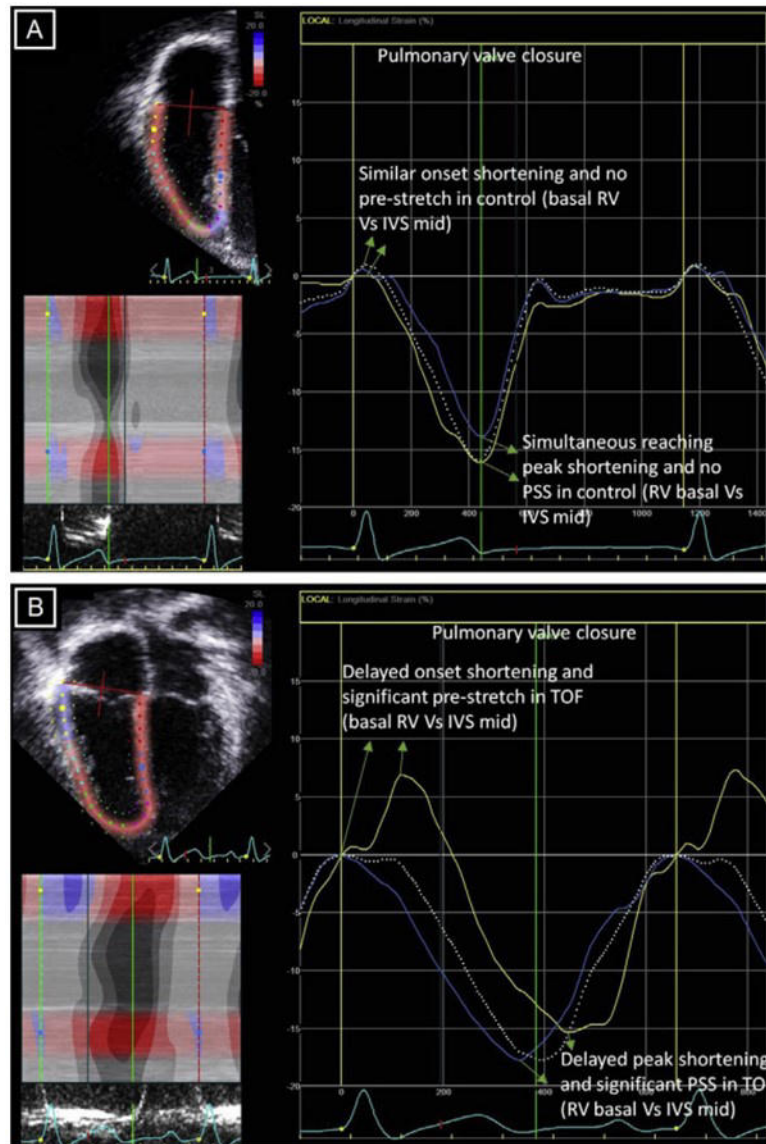


Figure 40. RV segmental strain curves using echocardiographic speckle-tracking showing examples of a control subject **A:** and a patient after TOF repair. **B:** Strain curves in the control subject are synchronous with no significant differences in time between basal lateral (yellow curve) and midseptal (blue curve) segments. By comparison, it can be noted that the patient after TOF repair shows early septal activation with prestretch and late contraction post systolic stretch (PSS) of the RV basal lateral segment (yellow curve). The dotted white curve represents the average strain of six RV segments, which is automatically provided by the software. From Yim et al[146].

They reported that dyssynchrony manifested as a right-sided septal/apical flash and is characterized by early septal activation with late contraction and postsystolic shortening of the RV basal lateral wall.

However, STE cannot measure the dyssynchrony with precision because of its low temporal resolution (50-70 fps) and therefore cannot be used to consistently

identify patients who may benefit from CRT. Moreover, this approach does not measure the electromechanical delay as the difference between the mechanical and the electrical onsets but as time-to-peak of shortening. Consequently, ECG and echocardiographic measurements do not allow accurate quantification of local electromechanical delay times and their parameters are not reliable representative of the global dyssynchrony either.

An interesting method was described by Kroon et al[147] using the 3D NOGA mapping system[148] in a small cohort of HF patients where a 7Fr deflectable-tip mapping catheter was employed and inserted in the LV via a retrograde aortic approach from the femoral artery. Unipolar electrograms (UEGs) and catheter tip trajectories were recorded at 100-200 LV endocardial locations and were aligned using the simultaneously recorded 12-lead surface ECG. This data was processed offline with a custom MATLAB algorithm where the local times of depolarization were extracted from the UEGs while the catheter tips trajectories were converted to local shortening. Moreover, the system can reconstruct the 3D morphology of the LV (Figure 41).

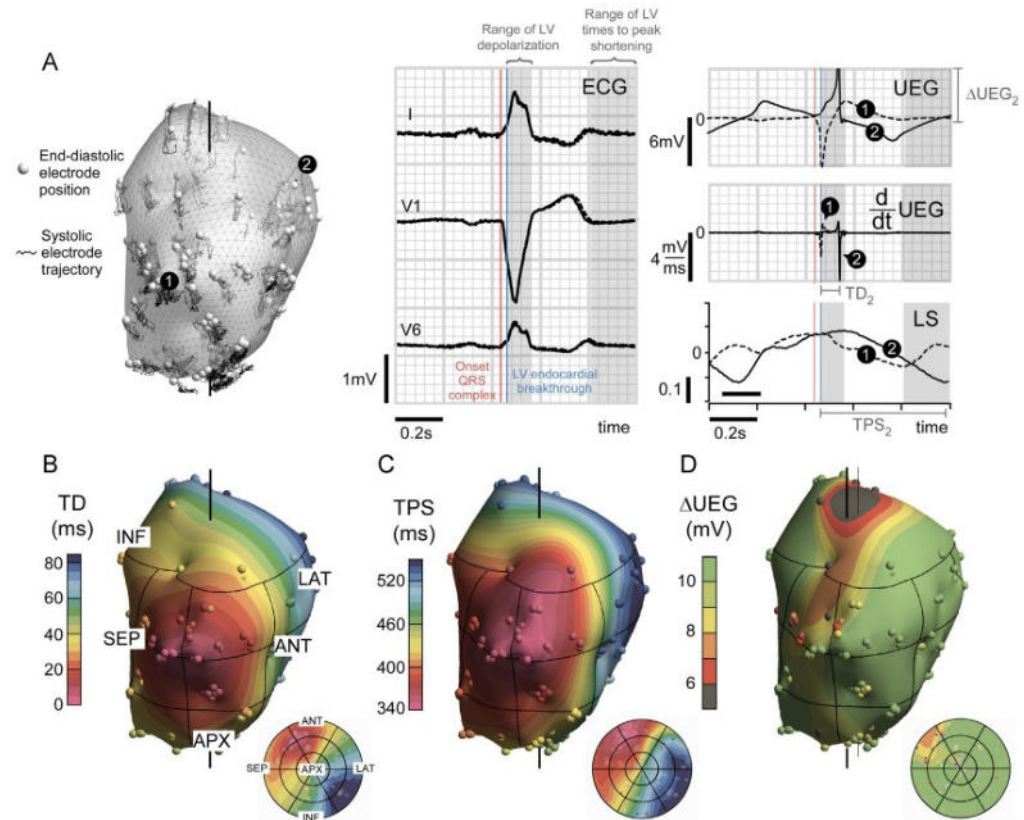


Figure 41. A: Offline end-diastolic geometrical reconstruction, systolic trajectory of electrode positions, body surface electrocardiograms (ECG). and unipolar intracardiac electrograms

(UEG) recorded in patient 1. Signals are shown for an early depolarized ❶ and a late ❷ depolarized region. Unipolar voltage amplitude (Δ UEG), depolarization time (TD), and time to peak shortening (TPS) for the late activated region are highlighted. **B**: Reconstructed TD map. **C**: Reconstructed map of times to peak shortening (TPS). **D**: Map of amplitude of unipolar electrograms (Δ UEG). Timing in B and C is expressed relative to left ventricular. From Kroon et al[147].

In their study, the electromechanical delay was defined as the difference in time between the local peak shortening and depolarization. The time from the region with earliest peak in LS to that with the latest peak was used as measure for LV mechanical dyssynchrony.

The authors emphasized more on a global rather than a local assessment of dyssynchrony because the electromechanical delay parameter was highly variable possibly because of tissue heterogeneities or other abnormalities present in HF. However, the interval between the time of depolarization and time-to-peak shortening was similar to those observed by speckle tracking echocardiography[149]. Lastly, the authors found that the relationships between time of depolarization and time-to-peak shortening had a large slope implying that mechanical dyssynchrony was more pronounced than electrical dyssynchrony as also observed by other groups[110,111].

As it can be evinced from the studies with STE, the main difficulty in the in vivo evaluation of dyssynchrony through imaging techniques is their temporal resolution which is not sufficient to reliably assess the electromechanical activity of the heart. Nevertheless, Provost et al[150] proposed an ultrasound-based imaging technology, named Electrical Wave Imaging (EWI), capable to map the electromechanical activity in all four heart chambers at a very high temporal resolution (500 fps). This temporal resolution cannot be achieved by full view speckle tracking techniques (33 fps), although its resolution can be increased up to 70-90 fps at the expense of a very narrow field of view (preventing spatial assessment). Apart from the high temporal and spatial resolutions, one of the EWI main advantages is its high translatability being based on a clinical ultrasound scanner[151].

The other characteristic of EWI is that it uses RF-based cross-correlation at that frame rate, which is an estimation method that can be up to ten times more

accurate than brightness mode-based speckle tracking[152]. The EWI workflow is portrayed in Figure 42.

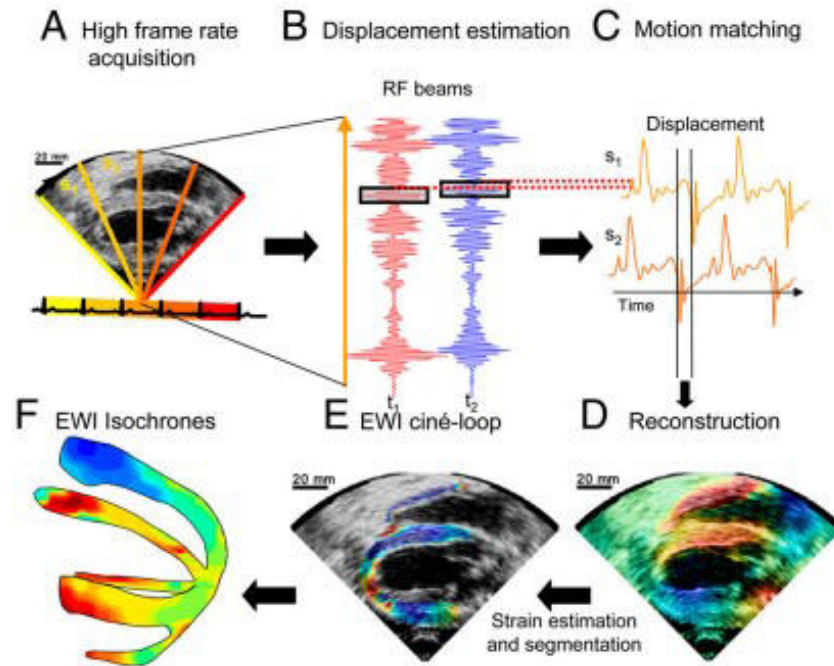


Figure 42. Block diagram of the EWI technique. **A:** A full view of the two ventricles is first divided in partially overlapping sectors, which are imaged at separate heartbeats. **B:** High-precision displacement estimation between two consecutively acquired RF beams (t_1 , t_2) is then performed using very high-frame-rate RF speckle tracking. **C:** A region of the heart muscle, common to two neighboring sectors, is then selected. By comparing the temporally varying displacements measured in neighboring sectors (s_1 , s_2) via a cross-correlation technique, the delay between them is estimated. **D:** A full-view cine loop of the displacement overlaid onto the B mode can then be reconstructed with all the sectors in the composite image synchronized. **E:** The heart walls are then segmented, and incremental strains are computed to depict the EW. **F:** By tracking the onset of the EW, isochrones of the sequence of activation are generated. From Provost et al[150].

The authors showed that their methodology was able to map the electromechanical activity in *in vivo* dogs with high accuracy in both sinus rhythm and following epicardial pacing. In fact, it can be noted that the electromechanical wave (EW), represented by the isochrones, followed the electrical events on the standard ECG (Figure 42, top panel). Moreover, they found a strong correlation between the EW onset and the electrical activation onset whose slope was similar to the ones obtained by other groups[153-155] (Figure 43, bottom panel). This finding suggests that EWI can precisely map the electrical activation sequence *in vivo*.

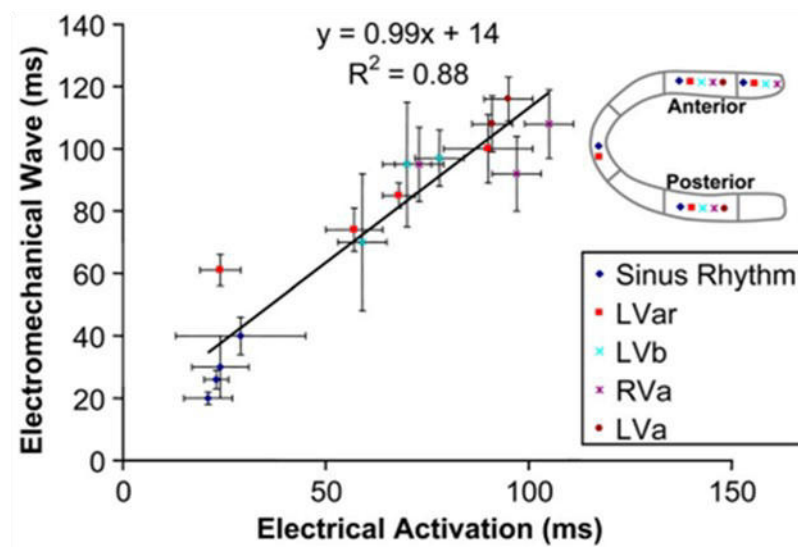
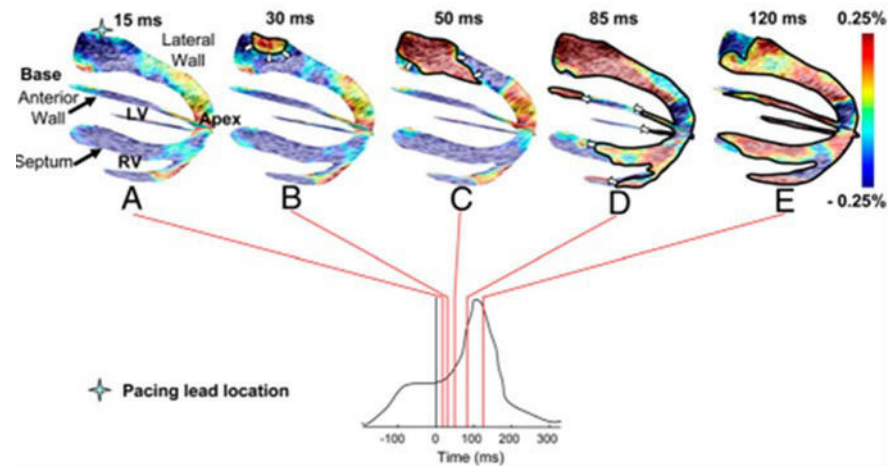


Figure 43. Top panel: Propagation of the electrical wave (EW) when paced from the lateral wall, near the base. Activated regions are traced at (A) 15 ms, (B) 30 ms, (C) 50 ms (D) 85 ms, and (E) 120 ms and indicated on the (F) ECG; the solid black line corresponds to the pacing stimulus at 0 ms. From A to C, the EW propagates from the basal part of the lateral wall toward the apex. In D a transition from lengthening to shortening is observed rather than a transition from thinning to thickening. From D to E, in the anterior wall, the EW propagates from both the base and apex. The scale shows interframe strains. **Bottom panel:** Electrical and electromechanical activation times after pacing and in sinus rhythm in four different heart segments in the posterior and anterior walls, as indicated in the legend. A strong correlation was observed ($R^2=0.88$) with a slope of 0.99 (indicating a direct correlation). Modified from Provost et al[150].

However, the authors obtained this correlation only in the imaging plane selected in the proximity of the region defined by the electrode locations to reduce the artifacts on the ultrasound image generated by the pacing. Therefore, their relationship concerned only the heart segments in the regions studied.

The most accurate approach to evaluate the global relationship between the electrical and the mechanical activity would be to compare the maps of electrical and electromechanical activation times, which is, without saying, challenging because of the 2D nature of the technique.

Global excitation-contraction coupling with Vi.Ki.E.

The Vi.Ki.E. technique could be used to measure the electromechanical delay in both basic and experimental clinical research by simultaneously acquiring both ECG and video.

As described extensively, the main difficulty in measuring the electromechanical delay is that methods used to assess the cardiac electrical activity typically ignore the cardiac motion, while on the other hand, the cardiac mechanical function is assessed with methods characterized by low temporal resolution that ignore the electrical activation. Instead, our technique for the assessment of the mechanical activity is characterized by a high temporal resolution, capable to acquire videos up to 1000 fps in the laboratory setting and at 200 fps in the operating room.

Furthermore, as highlighted in the Introduction section “*Video Kinematic Evaluation*”, there is a lack of intraoperative techniques able to assess the electromechanical function of the RV during open-chest surgery. Finally, because ca. 30% of patients undergoing CRT are not responders, our methodology could have an impact on the patients’ outcome by providing data to surgeons on the extent of dyssynchrony.

Methods

Experimental protocol for the CMR studies

Female Landrace swine (n=10, 51±10 Kg) were fasted overnight with free access to water, and then sedated and intubated on the day of the experiment. Anaesthesia was continued with fentanyl, midazolam, ketamine and pancuronium as needed. The anesthesia regimen included low-dose isoflurane to obtain a deeper sedation and stabilize hemodynamics without impacting much on systemic vascular resistance (SVR). Animals were ventilated (Cato, Dräger Medical, Lubeck, Germany) with a FiO₂ of 0.5, an I: E-ratio of 1:1.5, the positive end-expiratory pressure was set at 5 mmHg and a tidal volume of 10 ml/Kg. The respiratory rate was continuously monitored and adjusted to maintain an end-expiratory CO₂ partial pressure between 35 and 45 mmHg. Body temperature was monitored and maintained at 38°C during the entire protocol.

Under fluoroscopic guidance, all animals were instrumented with a floating balloon catheter in the right atrium as well as in the coronary sinus (Arrow Balloon Wedge-Pressure Catheters, Teleflex Inc, Wayne, Pennsylvania USA). To avoid CMR-artefacts, the balloon-tip was cut before introducing the catheters in the vessel. Respiratory gases (PM 8050 MRI, Dräger Medical), heart rate (HR), and invasively derived arterial blood pressure were continuously monitored (Precess 3160, InVivo, Gainesville, Florida, USA) via a sheath access surgically prepared in the internal carotid artery. Systolic blood pressure (SBP), diastolic blood pressure (DBP) and mean aortic pressure (mAoP) were invasively measured throughout the entire protocol via this access. SVR was calculated as follows:

$$SVR_{mmHg/L} = \frac{\text{Mean Arterial Pressure (MAP)} - \text{Right Atrial Pressure}}{\text{Cardiac Output (CO)}}$$

Cardiac power output (CPO) and Ees were calculated using the following formulas:

$$CPO = \frac{CO \times mAoP}{451}$$

$$Ees = \frac{LVP_{sys}}{V_{LVP_{max}} - V_0}$$

where:

$$LVP_{sys} = \frac{2}{3}SBP + \frac{1}{3}DBP$$

$$V_{LVP_{max}} = End - Systolic Volume$$

$$V_0 = 0$$

as described by Kelly et al[156].

After baseline measurements, two pharmacological steps were performed: dobutamine-stress (Dob) and verapamil-induced (Ver) cardiovascular depression. Dob was titrated aiming at a 25% HR increase compared to baseline values, while Ver was given as single 2.5 mg bolus, aiming at a 25% decrease of cardiac index (CI). CI was continuously assessed online via a Swan-Ganz catheter in the pulmonary artery (Edwards Lifesciences CCO connected to Vigilance I, Edwards Lifesciences, Irvine, California, USA). In case CI was not decreased as much as 25%, we proceeded with a further bolus of Verapamil. In the CMR investigation, after the first bolus, stroke volume was estimated via short-axis (SAX) cine imaging after reaching a hemodynamic steady state. Between the different steps of the protocol there was a washout period of 30 min. At each step, CMR images were acquired in the SAX, two-chamber (2Ch), three-chamber (3Ch) and four-chamber (4Ch) views. All CMR images were acquired in a supine position using a 3 T CMR scanner (Ingenia, Philips Healthcare, Best, The Netherlands) with an anterior- and a built-in posterior coil element (30 coil overall).

All animals were scanned using identical comprehensive imaging protocol. Cine images were acquired using ECG-gated bSSFP cine sequence in three LV long-axis (2Ch, 3Ch, 4Ch) planes. The ventricular 2Ch and 4Ch planes were used to plan stack of SAX slices covering the entire LV.

The following imaging parameters were used: repetition time (TR)=2.9 ms, echo time (TE)=1.45 ms, flip angle=45°, measured voxel size=1.9×1.9×8.0 mm³, reconstructed voxel size 1.0×1.0×8mm³, and 40 cardiac phases.

All images were analyzed offline using a commercially available software (Medis Suite, version 3.1, Leiden, The Netherlands) and View Forum in accordance with a recent consensus document for quantification of LV function using CMR[23]. A numeric code was assigned to the acquired images and, thus, the observers were blinded to the treatment.

On SAx view, the outline of the endocardial border of the LV was manually traced on all slices. Volumes were computed by Simpson method of disks summation, whereby the sum of cross-sectional areas was multiplied by slice thickness (8 mm). The LV ejection fraction was calculated using the Simpson method. The LV outflow tract, papillary muscles and trabeculation were included as LV volume. The ascending aorta was delineated in all the images to perform flow calculation in the corresponding velocity-encoded phase images. The average flow velocity was multiplied by the area of the vessel and integrated over one cardiac cycle to obtain SV. Then, CO is indirectly calculated as the product of SV and HR. Finally, CI is calculated as the CO divided by the body surface area (BSA) of each swine.

The strain analysis was performed including 2Ch, 3Ch, 4Ch cine images, and 3 preselected mid-ventricle slices from the SAx stack. The epicardial contours drawn with QMass (version 8.1, Medis Medical) were transferred to QStrain RE (version 2.0, Medis Medical). Then, the tissue tracking algorithm detected both epicardial and endocardial margins over the whole cardiac cycle. The long axis cine images were used to calculate the global longitudinal strain (GLS), whereas the Sax images were used to calculate both global circumferential and radial strains (GCS and GRS, respectively).

GLS, GCS and GRS were indexed for the invasively measured mAoP adapting the formula from Rhea et al.[157]:

$$\frac{\text{Global Strain} \times \text{mAoP}}{\text{avg}(\text{mAoP})}$$

where avg(mAoP) was the average of the mAoP measured at each protocol step (baseline, Dob and Ver).

Meridional wall stress was calculated via the following formula by Reichek et al.[158]:

$$LV \text{ wall stress} = \frac{0.334 \times LVP_{sys} \times LVESD}{PWT \times [1 + PWT/LVID]}$$

where LVESD=left ventricular end-systolic diameter and PWT=posterior wall thickness measured by averaging three separate measurements in the basal short axis sequence.

GLS, GCS and GRS were indexed for the calculated wall stress as described by Reichek et al[158] for each protocol step (baseline, Dob and Ver):

$$\frac{\text{Global Strain} \times LV \text{ wall stress}}{\text{avg}(LV \text{ wall stress})}$$

External myocardial power (EMP) defines the power needed to pump blood against a given afterload at the left ventricle outflow tract (LVOT).

$$EMP = (MAP + \text{mean}\Delta P_{AV}) \times CO$$

The mean Δ PAV is the mean pressure gradient across the aortic valve. In our animal model, EMP is nearly equivalent to the concept of both cardiac power output and circulatory power[159] due to the absence of aortic valve stenosis and regurgitation.

The power required by the LV myocardium to perform contraction during systole is defined as internal myocardial power (IMP).

$$IMP = \frac{V_{wall} \times \sigma_{wall}}{t_{CS}}$$

where V_{wall} is the myocardial wall volume, σ_{wall} is the peak systolic wall stress, and t_{CS} is the left ventricular systolic contraction time.

Finally, the myocardial efficiency was defined as the ratio between IMP and EMP.

The described methods refer to the following Results: “*Intra- and inter-reproducibility of CMR-FT global strain parameters in pigs*”, “*Correlation between CMR-FT global strain parameters and invasive hemodynamics*” and “*CMR-based quantification of myocardial energetics under different inotropic states*”. Further information can be found in the *Attachment 1,2,3*, respectively.

Vi.Ki.E. studies: animal protocol

The study population consisted of 12 Sprague Dawley rats (5 males and 7 females). Rats, 6 months old weighting 250-275 g, were anesthetized with 0.20 mg/kg ip of a mixture of tiletamine hydrochloride and zolazepam hydrochloride (Zoletil; Virbac S.r.l., Carros, France) + 0.15 mg/kg ip medetomidine hydrochloride (Domitor; Orion Corporation, Espoo, Finland). The heart was exposed through a median thoracotomy and suspended in a pericardial cradle under artificial ventilation (RoVent[®] Small Animal Ventilator, Kent Scientific, CT, USA). Body temperature was maintained constantly at 37°C with heath lamp radiation and further doses of anesthetic were administered when needed during the experiment. The heart was stimulated with a cathodal suprathreshold train of stimuli at different basic cycle length (BCL) by driving the right atrium with a silver electrode (0.05 mm) with one end connected to a stimulus generator (SIU-102, Warner Instruments CT, USA) and the other hooked to the atrial auricle appendage. The stimulus generator was triggered by a function generator (Aim-TTi TG310, RS Components, Milano, IT).

Videos were acquired with a spatial resolution of 1280 × 1024 pixel and at 500 fps for two seconds at each BCL. The camera (Baumer HXC13, Baumer Italia S.r.l., Milano, Italy) was connected with full CameraLink[®] interface to a frame grabber acquisition board PCIe 1433 (National Instruments, Assago, Italy) and placed at ca. 20 cm above the heart. The camera was equipped with a macro-objective Kowa Industrial Lenses LM35XC, F=1:2.0, f=35 mm, picture size 13.8-18.4 mm (RMA Electronics, Hingham, MA, USA). The acquisition board was integrated into a Workstation HP Z220 (Crisel Instruments, Roma, Italy) with 24 GB RAM and the acquisition software was custom made in LabVIEW 2013 Visual Programming Language (National Instruments, Assago, Italy). The acquired videos were analyzed with the Vi.Ki.E. technique as described in the Introduction section “*Video Kinematic Evaluation*”. Further details are provided in the Attachment 4.

One more Sprague-Dawley rat was used to develop the protocol portrayed in Figure 44 to evaluate the electromechanical activity of the heart with Vi.Ki.E.

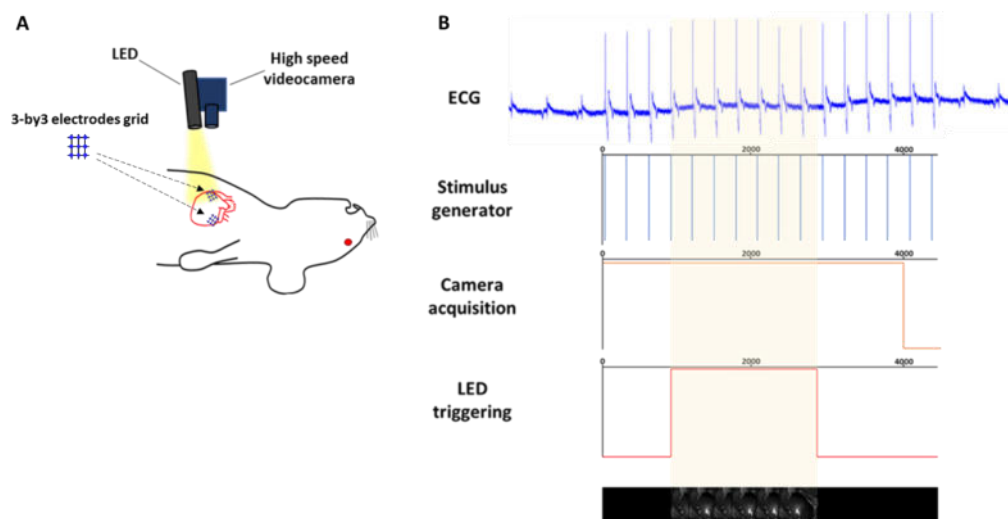


Figure 44. Schematic representation of the protocol for the assessment of the global electromechanical coupling with Vi.Ki.E. **A:** Representation of the camera and LED positions above the rat's heart during experimentation. The LED is used to create a light spot on the epicardial surface that will be used in post processing. **B:** schematic representation to simultaneously acquire the signals for the electromechanical delay measurement. The graph on the top displays the ECG acquired during experimentation. The second graph represents the ventricular stimulation performed via a stimulus generator. The third graph displays the starting and ending point of the video acquisition. The graph on the bottom represents the LED triggering via the stimulus generator program. Finally, the images on the bottom are a graphical representation of the whole process. The time, displayed on the x-axis, is in milliseconds. The yellow shaded rectangle encompassing the signals represents the period that will be used in post-processing.

In detail, after median sternotomy and heart exposure, a custom-made silver electrode array (3×3 electrodes, resulting in 1mm resolution square mesh) is placed on the epicardial surface to perform ventricular stimulation. Moreover, a LED is placed perpendicularly to the heart in order to create a “light-spot” which will be used to track the cardiac movement in postprocessing as described in the Introduction section “*Video Kinematic Evaluation*” (Figure 44A). Because of the time needed to create the memory space in which the images will be downloaded, the simultaneous acquisition of both Vi.Ki.E. and ECG is challenging. To solve this problem, I created the protocol displayed in Figure 44B.

In detail, the first signal to be acquired is the ECG which can be recorded continuously. The video recording starts slightly after and requires approximately five seconds to create the memory space in the computer. To note that during this time the LED is still turned off. On the sixth second, the ventilator is switched off to prevent breathing motion artifacts and the epicardial pacing is started via a stimulus generator (Multi Channel Systems MCS GmbH,

Baden-Württemberg, Germany). The stimulus generator's program was designed to stimulate at a BCL of 260 ms and switch on the LED from the fourth stimulus for a total of two seconds.

In post-hoc analysis, two seconds will be extracted from the ECG trace starting from the fourth epicardial stimulation which corresponds to the LED triggering. In the videorecording, the first frame in which the light is on corresponds to that stimulus and, consequently, only the following two seconds will be used for the Vi.Ki.E. analysis.

Following the described protocol, we are sure that in those two seconds both electrical (ECG) and mechanical (Vi.Ki.E.) functions were acquired simultaneously as displayed in Figure 45.

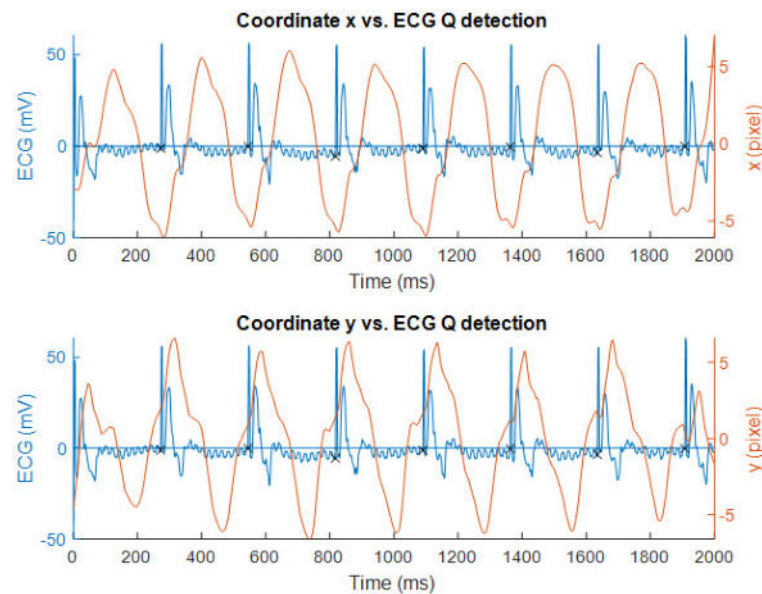


Figure 45. Superimposition of the ECG signal with the Vi.Ki.E. coordinates acquired with the above-described protocol in a control Sprague-Dawley rat. The “x” marker on the ECG signal represents the onset of the electrical activity which corresponds to the epicardial ventricular stimulation.

To measure the electromechanical delay in sinus rhythm, I adapted the above-described protocol implementing a subthreshold train of stimuli (not recording ventricular beats) and simultaneously acquiring both ECG and Vi.Ki.E. recordings using the same approach.

Vi.Ki.E. studies: clinical protocol

The study was approved by the Institutional Review Board (# 847CESC Protocol # 13371), and all patients signed an informed consent. Between November 2016 and November 2018, a total of 12 consecutive patients aged 27.1 ± 19.1 years undergoing pulmonary valve replacement (PVR) 22.1 ± 13.2 years after ToF repair were enrolled.

The selection criteria for the study were:

- i. PR after transannular patch repair of ToF with pulmonary stenosis;
- ii. symptomatic patients with severe PR or asymptomatic patients with evidence of progressive severe RV dilatation or dysfunction[160];
- iii. PVR using stented bioprostheses;
- iv. feasibility of PVR normothermic cardiopulmonary bypass on the beating heart.

The latter criterion was introduced to eliminate the influence of intraoperative myocardial ischaemia on postoperative cardiac kinematics.

Patients with associated septal defects, aortic valve or root disease, pulmonary artery branch stenosis or acquired coronary artery disease were excluded from this study. The entire population underwent preoperative MRI.

All surgical procedures were performed by 1 surgeon (G.B.L.) via repeat median sternotomy, using aortic and bicaval cannulation, under normothermic (36°C) cardiopulmonary bypass on the beating heart. Video kinematic recordings were focused on the apical trabecular component of the right ventricle, in line with previous evidence showing this portion as the one taking most of the chronic volume overload[161].

Video recordings of the beating heart, at 200 fps and with a spatial resolution of 1280×1024 , were acquired by placing a high-speed camera (Basler acA1300-200um USB 3.0 with the ON Semiconductor PYTHON 1300 CMOS sensor, Ahrensburg, Germany, equipped with Edmund Optics 6-mm compact fixed focal length lens, Barrington, NJ, USA) approximately at 0.45 m above the patient during open-chest surgery. In detail, four videos of 5 s each were recorded before and after PVR (pre-PVR and post-PVR, respectively) for each patient. The pre-PVR time point was at chest opening after freeing pericardial

adhesions, whereas the post-PVR recording was performed 30 min after protamine sulfate was administered. In the post-PVR recording, care was taken to re-establish the same hemodynamic conditions observed in the pre-PVR recording, including central venous pressure, systolic arterial blood pressure, heart rate and ventilator settings.

The camera and the tripod were sterilized before entering the operating room and between every recording.

The videos were analyzed with the Vi.Ki.E. technique as described in the Introduction section “*Video Kinematic Evaluation*”.

The first 6 patients in this series were the object of a pilot study designed to assess the safety and efficacy of the Vi.Ki.E. technique, please see the Results section “*Vi.Ki.E. assessment of the right ventricle in Tetralogy of Fallot patients*” and *Attachment 5* for further details.

The entire ToF population was the object of two other works described in the Results sections “*Timing of pulmonary valve replacement is a key factor in determining recovery of the right ventricle in ToF*” and “*Vi.Ki.E. based supervised machine learning classifiers to support decision-making during surgery*”. Further details are provided in the *Attachment 6* and *7*, respectively.

Statistical analysis

Statistical analysis in the CMR studies

Here are reported the statistical methods used for each study described in the Results section where the CMR technique was employed.

Intra- and inter-reproducibility of CMR-FT global strain parameters in pigs

Data were analyzed using IBM SPSS Statistics version 23.0 (IBM Corp. Released 2015. IBM SPSS Statistics for Windows, Version 23.0. Armonk, NY: IBM Corp) for Windows. Figures were made with GraphPad Prism version 8 and Microsoft PowerPoint.

The Shapiro–Wilk test was used to determine whether the data were normally distributed, and the nonparametric variables were compared using the Wilcoxon test. One-way ANOVA for repeated measurements was used to analyze data between groups at different inotropic states. Post-hoc testing was performed by Tukey’s test. A p-value < 0.05 was considered significant.

Inter- and intra-observer reproducibility was quantified using intra-class correlation coefficient (ICC) and Bland–Altman analysis and the following metrics were employed[64]: agreement was considered excellent for ICC>0.74, good for ICC 0.60–0.74, fair for ICC 0.40–0.59, and poor for ICC<0.40.

Correlation between CMR-FT global strain parameters and invasive hemodynamics

Data were analyzed by Sigmastat (Version 4.0, Systat Software, Inc., Cranes Software, Karnataka, India) and SPSS version 23.0 (IBM Corp. Released 2015. IBM SPSS Statistics for Windows, Version 23.0. Armonk, NY: IBM Corp). Figures were made with GraphPad Prism version 8 and Microsoft PowerPoint. The correlation between CMR-FT strain and hemodynamic data was evaluated by linear regression analysis. The three experimental conditions were included as a regressor in the linear regression model. To assess whether the linear regressions were significantly different, we employed a custom MATLAB script comparing the slopes, intercepts via t-test and the correlation coefficients via Fisher’s r-to-z transformation followed by z-test, as described by Weaver

and Wuensch[162]. Data between groups at different inotropic states were analyzed by one-way ANOVA for repeated measurements. Post-hoc testing was performed by Tukey's test. A p-value < 0.05 was considered significant.

CMR-based quantification of myocardial energetics under different inotropic states

Data were analyzed using Stata 15.1 (StataCorp, College Station, TX, USA) and GraphPad 8.0.2 (GraphPad Software, Inc., La Jolla, CA, USA).

Data distribution was tested using Shapiro–Wilk and Shapiro–Francia tests. Wilcoxon signed rank test was used to assess differences between baseline and the two pharmacological steps. The correlations between the indexed CMR parameters of IMP, EMP, myocardial efficiency, and the hemodynamic parameters of CPO and LVEF were assessed by linear regression analysis. A p-value < 0.05 was considered significant.

Statistical analysis in the Vi.Ki.E. studies

Here are reported the statistical methods used for each study described in the Results section where the Vi.Ki.E. technique was employed.

Vi.Ki.E.'s frequency relationship

The program GraphPad v.6.0 (GraphPad Software, Inc., La Jolla, CA, USA) was used for the statistical analysis while Microsoft PowerPoint was used to make the graphs.

The normality of the data was assessed with the Kolmogorov-Smirnov test. Kruskal Wallis test and 2-way ANOVA were performed. A p-value < 0.05 was considered significant.

Vi.Ki.E. assessment of the right ventricle in Tetralogy of Fallot patients

The program GraphPad v.6 (GraphPad Software, Inc., La Jolla, CA, USA) was used for analysis and results display. The normality of the data was assessed with the Kolmogorov–Smirnov test. The Student's t-test with Welch's

correction and cumulative distribution with the Kolmogorov–Smirnov test were performed. A p-value < 0.05 was considered significant.

Timing of pulmonary valve replacement is a key factor in determining recovery of the right ventricle in ToF

The program SPSS version 26 (IBM, Armonk, NY, USA) was used for the statistical analyses and GraphPad v.6 (GraphPad Software, Inc., La Jolla, CA, USA) was used to display the results. The Pearson correlation was performed to evaluate the correlation between the before surgery kinematic parameters and preoperative RVEDVi measured by MRI. The median value of 147 ml/m² was used to separate our ToF population in two groups (< 147 ml/m² for group 1 and > 147 ml/m² for group 2). The normality of the data for each parameter was assessed with the Kolmogorov–Smirnov test. A two-way ANOVA for repeated measures with ‘time’ as the within-subject factor (2 levels: Pre-PVR and Post-PVR) and ‘group’ as the between-subject factor (2 levels: group 1 and group 2) was performed. A post hoc analysis was conducted using the Student’s t-test with a Bonferroni correction for multiple comparisons where necessary. The Wilcoxon matched pairs signed-rank test or the paired t-test was used only for the parameters for which the two-way ANOVA for repeated measures could not be performed. A p-value < 0.05 was considered significant.

Vi.Ki.E. based supervised machine learning classifiers to support decision-making during surgery

The data was analyzed with GraphPad v.6 (GraphPad Software, Inc., La Jolla, CA, USA) and the graphs were made by Microsoft PowerPoint.

To calculate the minimum number of patients necessary to perform the study on ToF, we used the formula by Armitage et al[163] to evaluate the 95% confidence interval for the disease’s prevalence. Following their formula, the amplitude (D) of that confidence interval is established a priori and with $Z(\sigma/2) = 1.96$. Knowing that the ToF prevalence is circa 1/3500 live births[164] and establishing a D = 2%, the minimum number of patients that should be enrolled is $N > 10.97$.

The normality of the distribution of the data for each kinematic parameter was investigated with the Kolmogorov–Smirnov test. Consequently, the Mann–Whitney test was performed to investigate any difference between before and after surgery. A p-value < 0.05 was considered significant.

Results

Intra- and inter-reproducibility of CMR-FT global strain parameters in pigs – Attachment 1

Myocardial strain is an effective method for the assessment of the regional myocardial function and deformation. In particular, CMR tissue tracking is a comparable approach to the highly validated speckle tracking echocardiography for the measurement of strain parameters[165].

Among the different techniques available to clinicians for the assessment of the LV mechanics, a relatively novel method is CMR-FT. This technique has been validated against myocardial tagging for the assessment of regional myocardial motion in humans[166,167]. Although CMR-FT is standardized in humans[168-170], displaying an excellent intra- and inter-reproducibility, there is scarce literature on translational animal models and a lack of reproducibility studies.

Therefore, the following results aimed to assess the degree of reproducibility of CMR-FT global strain parameter under various inotropic states.

The experimental, image acquisition and analysis protocols of this study are described in the Methods section “*Experimental protocol for the CMR studies*”.

In Table 2 are displayed the global strain parameters obtained by two independent investigators.

Measurements obtained by two observers (inter-observer level)		
	First observer	Second observer
BL (%)		
GLS	-26.1 ± 5	-25.1 ± 4
GCS	-32.7 ± 8	-30.4 ± 6
GRS	73.3 ± 9	51.5 ± 17
Dob (%)		
GLS	-45.1 ± 11*	-40.6 ± 7*
GCS	-55.1 ± 12	-54.7 ± 10*
GRS	103.0 ± 20	101.8 ± 14*
Ver (%)		
GLS	-20.8 ± 6 [†]	-17.3 ± 5* [†]
GCS	-18.6 ± 4 [†]	-21.0 ± 6* [†]
GRS	53.9 ± 10 [†]	29.1 ± 9* [†]
Measurements obtained by one observer (intra-observer level)		
	First measurement	Second measurement
BL (%)		
GLS	-26.1 ± 5	-23.3 ± 4
GCS	-32.7 ± 8	-31.0 ± 8
GRS	73.3 ± 9	71.7 ± 19
Dob (%)		
GLS	-45.1 ± 11*	-45.6 ± 9*
GCS	-55.1 ± 12	-53.3 ± 11*
GRS	103.0 ± 20	87.9 ± 36
Ver (%)		
GLS	-20.8 ± 6 [†]	-16.5 ± 3* [†]
GCS	-18.6 ± 4 [†]	-16.9 ± 5* [†]
GRS	53.9 ± 10 [†]	30.3 ± 13* [†]

Table 2. Comparison of CMR-FT global strain parameters in different inotropic states. The table reports the measurements obtained by one observer (intra-observer level) and those collected by two observers (inter-observer level). All the investigators measured the global strain parameters twice and the average values were used for the analysis. GLS, global longitudinal strain. GCS, global circumferential strain. GRS, global radial strain. BL, baseline. Dob, Dobutamine. Ver, Verapamil. Data is presented as mean ± SD. *p-value<0.05 versus BL; [†]p-value<0.05 versus Dob. From Faragli et al[171].

As it can be noted, there were no differences between GLS, GCS and GRS at BL either between the two investigators or number of measurements. After Dob, both observers obtained a significant increase of GLS, but only the second observer assessed the same increase for both GCS and GRS. At the intra-observer level, Dob determined an increase in GLS and GCS. After Ver, both investigators observed a significant decrease of all global strain parameters, highlighting the cardiovascular depression obtained by Verapamil administration. Interestingly, only the second observer measured a significant reduction of GLS, GCS and GRS compared to both BL and Dob steps.

In Table 3 are displayed the intra- and inter-observer reproducibility assessment for the global strain parameters.

	Parameter	Steps	Mean difference \pm SD	Limits of agreement	ICC (95% CI)
Inter-observer variability	GLS	BL	-1.0 \pm 3.0	-6.9 to 4.8	0.88 (0.57-0.97)
		Dob	-4.5 \pm 10.0	-24.1 to 15.1	0.60 (-0.35 to 0.89)
		Ver	3.5 \pm 4.2	-4.7 to 11.7	0.79 (0.10-0.95)
	GCS	BL	-2.2 \pm 7.6	-17.2 to 12.6	0.66 (-0.21 to 0.92)
		Dob	-0.4 \pm 11.5	-23.0 to 22.2	0.51 (-0.23 to 0.87)
		Ver	2.4 \pm 3.4	-4.3 to 9.2	0.61 (-0.40 to 0.90)
	GRS	BL	21.7 \pm 11.6	-0.9 to 44.5	0.80 (0.21-0.95)
		Dob	1.2 \pm 29.6	-56.9 to 59.3	-1.60 (-9.47 to 0.35)
		Ver	24.7 \pm 12.6	0.1 to 49.4	0.24 (-2.03 to 0.81)
Intra-observer variability	GLS	BL	2.8 \pm 2.9	-2.8 to 8.5	0.81 (0.41-0.95)
		Dob	-0.4 \pm 7.3	-14.8 to 14.0	0.87 (0.45-0.96)
		Ver	4.3 \pm 4.3	-4.1 to 12.7	0.75 (0.01-0.94)
	GCS	BL	1.7 \pm 1.5	-1.3 to 4.7	0.98 (0.77-0.99)
		Dob	1.8 \pm 3.4	-4.8 to 8.4	0.97 (0.89-0.99)
		Ver	1.6 \pm 1.4	-1.1 to 4.4	0.95 (0.36-0.99)
	GRS	BL	-1.5 \pm 12.7	-26.4 to 23.3	0.79 (0.15-0.94)
		Dob	-15.1 \pm 31.1	-76.0 to 45.8	0.62 (-0.50 to 0.90)
		Ver	-23.6 \pm 15.7	-54.4 to 7.2	0.14 (-2.43 to 0.78)

Table 3. Calculation of both intra- and inter-observer reproducibility for the global strain parameters. Results are reported as mean differences \pm SD. In the table are also displayed the limits of agreement and the intraclass correlation coefficient (ICC) based on the 95% confidence interval. From Faragli et al[171].

We obtained an excellent inter-observer reproducibility for GLS during both BL and Ver steps (ICC of 0.88 and 0.79, respectively), while it was only good during Dob (ICC of 0.60). A good reproducibility was observed for GCS during both BL and Ver (ICC of 0.66 and 0.61, respectively), while it was fair during Dob (ICC of 0.51). The GRS displayed an excellent reproducibility during BL (ICC of 0.80) but a poor one during both Dob and Ver (ICC of -1.60 and 0.24, respectively).

The intra-observer analysis showed an excellent reproducibility throughout the experimental protocol for both GLS and GCS (ICC \geq 0.75 for all inotropic states), while GRS displayed an excellent reproducibility during BL (ICC of 0.79), a good one during Dob (ICC of 0.62) and a poor one during Ver (ICC of 0.14).

In Figure 46 and Figure 47 are displayed the Bland–Altman plots demonstrating the inter- and intra-observer reproducibility for the global strain parameters during BL, Dob and Ver steps.

The Bland-Altman plot describe the agreement between two quantitative measurements[172]. On the y-axis is displayed the difference between the two paired measurements (the global strain parameter assessed by either one or two observers), while on the x-axis is displayed the average of the two measurements. The straight line represents the mean difference (also known as

bias) and the dashed line outlines the 95% (calculated as ± 1.96 SD) confidence interval of that value. A low value for the mean difference and a narrow confidence interval indicates a good reproducibility.

As it can be noted, we obtained a good inter-observer (Figure 46a-c) and intra-observer (Figure 47a-c) reproducibility for GLS in both BL and Ver, whereas it was poor during Dob. GCS displayed a good inter-observer reproducibility during Ver (Figure 46f), an excellent intra-observer reproducibility in all inotropic states (Figure 47d-f), but a poor inter-observer reproducibility in both BL and Dob (Figure 46d-e). Finally, GRS showed a moderate inter- and intra-observer reproducibility in both BL and Ver (Figure 46g and i; Figure 47 g and i, respectively), while it displayed bad reproducibility for both inter- and intra-observer reproducibility during BL (Figure 46 h and Figure 47 h, respectively).

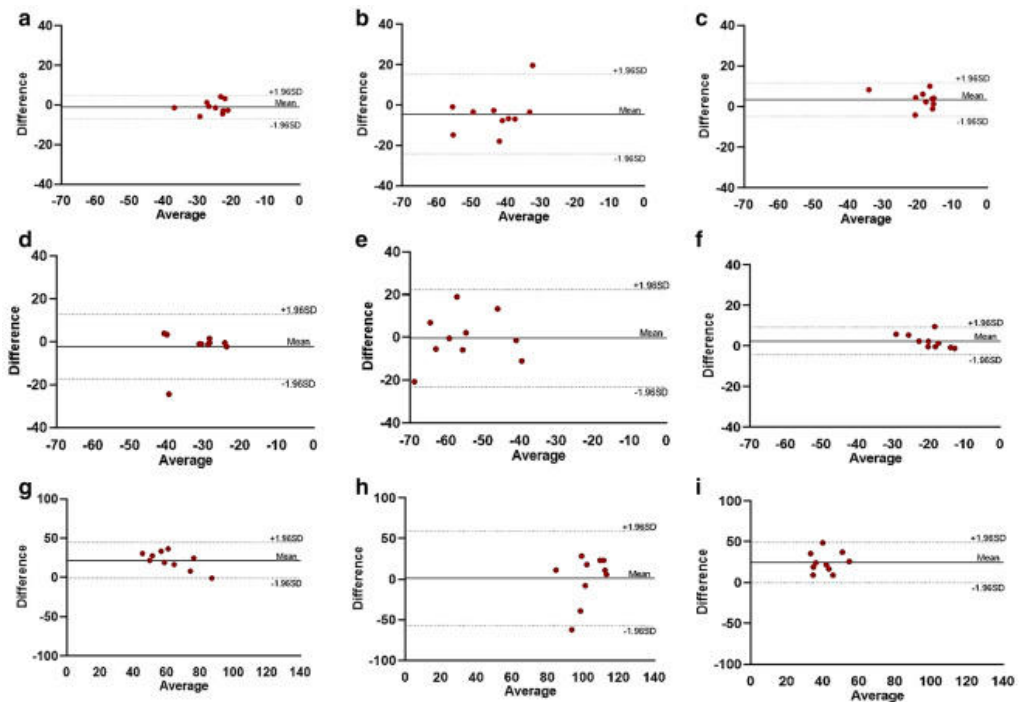


Figure 46. Bland–Altman plots for inter-observer reproducibility of global strain values. In the top row is displayed the inter-observer reproducibility of global longitudinal strain during BL (a), Dob (b) and Ver (c) steps. Middle row (d-f): same as the top row but for the global circumferential strain. Bottom row (g-i): same as the middle row but for global radial strain. Dots represent the animals (n=10). On the y-axis is displayed the difference between the measurements performed by two observers. On the x-axis is displayed the average of the two measurements. The two dashed lines represents the 95% limits of agreement. From Faragli et al[171].

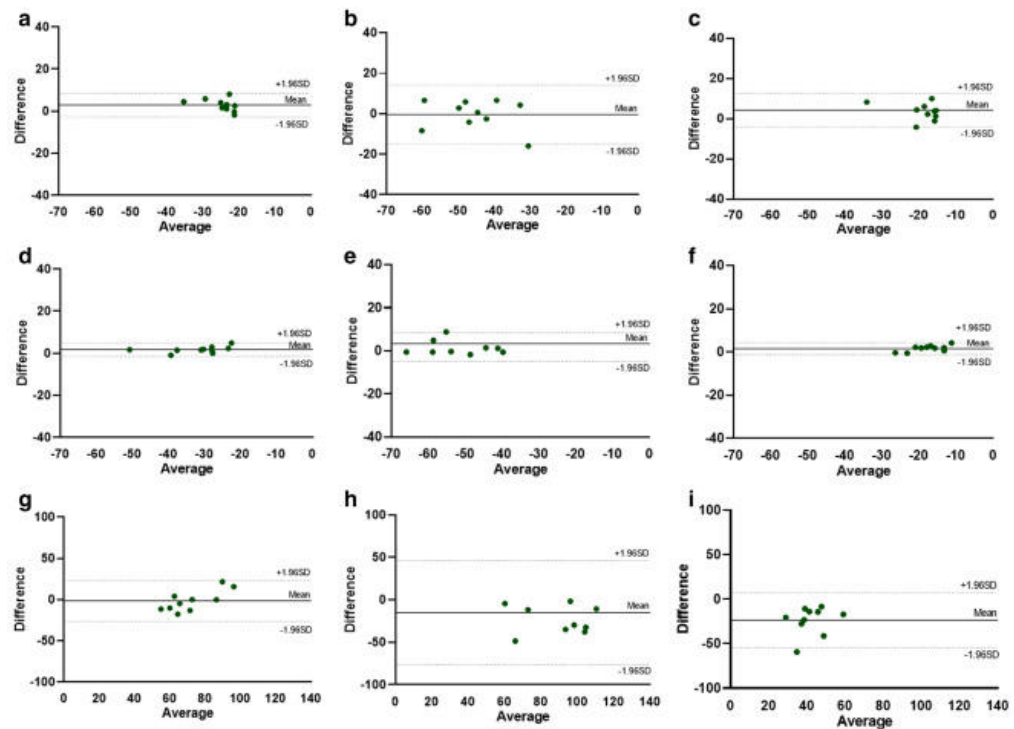


Figure 47. Bland–Altman plots for intra-observer reproducibility of global strain values. In the top row is displayed the intra-observer reproducibility of global longitudinal strain during BL (a), Dob (b) and Ver (c) steps. Middle row (d-f): same as the top row but for the global circumferential strain. Bottom row (g-i): same as the middle row but for global radial strain. Dots represent the animals (n=10). On the y-axis is displayed the difference between the measurements performed by two observers. On the x-axis is displayed the average of the two measurements. The two dashed lines represents the 95% limits of agreement. From Faragli et al[171].

In conclusion, good to excellent inter-observer reproducibility was found for both GLS and GCS, whereas GRS, displayed to be the most variable between repeated measurements. The weak reproducibility of GRS is in accordance with previous studies[173-176] as well as the higher reproducibility of both GLS and GCS[168,177]. Moreover, it can be noted that dobutamine infusion is detrimental to both intra- and inter-observer reproducibility (except for GCS) possibly because of the higher heart rate. This outcome finds explanations in the low temporal resolution of MRI and, thus, the low quality of the images acquired, as it was reported in other studies[178,179]. On the contrary, at lower heart rates (both BL and Ver) the reproducibility was higher for all the strain values.

Correlation between CMR-FT global strain parameters and invasive hemodynamics – Attachment 2

LV ejection fraction is the most used parameter to measure global systolic function in routine clinical practice, but falls short in identifying regional myocardial impairment and the mechanical contraction of the heart[180,181]. Therefore, strain imaging has recently emerged as a valid alternative to quantify myocardial LV deformation, promisingly showing an effect on the prognosis of different cardiovascular pathologies[182-186].

CMR strain imaging is a widely recognized technique to quantify myocardial deformation[186-188]. However, it is still unclear to what extent LV systolic strain relates to hemodynamic parameters under various inotropic states. Therefore, the results of the following study aimed to investigate this correlation measuring LV global strain parameters via CMR-FT in swine under different inotropic states.

The experimental, image acquisition and analysis protocols of this study are described in the Methods section “*Experimental protocol for the CMR studies*”. The global strain and indexed global strain values measured at different inotropic states are displayed in Table 4.

	Baseline	Dobutamine	Verapamil
(A)			
GLS (%)	- 23 ± 4	- 45 ± 9*	- 16 ± 3* [§]
GCS (%)	- 31 ± 8	- 53 ± 10*	- 17 ± 5* [§]
GRS (%)	72 ± 19	88 ± 36	30 ± 12* [§]
(B)			
GLSi (%)	- 23 ± 4	- 45 ± 10*	- 16 ± 4* [§]
GCSi (%)	- 30 ± 8	- 52 ± 8*	- 16 ± 5* [§]
GRSi (%)	71 ± 19	84 ± 23	30 ± 13* [§]
(C)			
GLSw (%)	- 23 ± 5	- 44 ± 10*	- 16 ± 3* [§]
GCSw (%)	- 31 ± 9	- 52 ± 13*	- 17 ± 17* [§]
GRSw (%)	71 ± 20	90 ± 54	35 ± 27* [§]

Table 4. (A) Global strain parameters measured via CMR-FT. GLS, global longitudinal strain. GCS, global circumferential strain. GRS, global radial strain. (B) GLS, GCS and GRS indexed for mean aortic pressure (i). (C) GLS, GCS and GRS indexed for meridional wall stress (w). *p<0.05 vs Baseline; §p<0.05 vs Dobutamine. From Faragli et al[189].

The linear regression analysis between global strain and hemodynamic parameters showed interesting results (Figure 48). A moderate correlation against CPO (Figure 48, top panel) was obtained for both GLS and GCS ($r^2=0.58$ and $r^2=0.52$, respectively), whereas a poor one was observed for GRS ($r^2=0.28$). A similar trend (Figure 48, middle panel) was observed for both GLS and GCS against CI ($r^2=0.62$ and $r^2=0.55$, respectively), with GRS still performing the worst ($r^2=0.33$). Finally, a moderate correlation (Figure 48, bottom panel) was obtained for both GLS and GCS vs Ees ($r^2=0.58$ and $r^2=0.58$, respectively), while a poor one was observed for GRS ($r^2=0.30$).

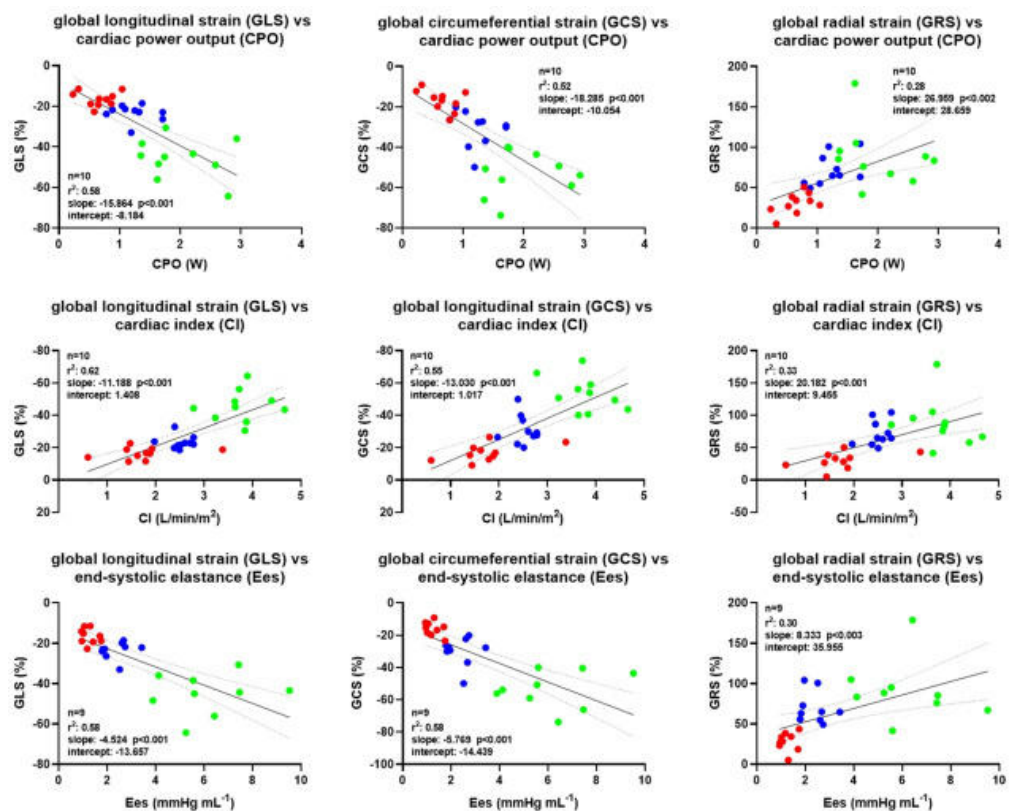


Figure 48. Correlation between global strain and invasive hemodynamics parameters. Top panels, linear regression analysis between global longitudinal strain (GLS), global circumferential strain (GCS), global radial strain (GRS) and cardiac power output (CPO). Middle panels, linear regression analysis between GLS, GCS, GRS and cardiac index (CI). Bottom panels, linear regression analysis between GLS, GCS, GRS and end-systolic elastance (Ees). Dots represents the single animal, whereas the color highlights the inotropic state. Blue: baseline. Green: dobutamine. Red: verapamil. The parameters (n , r^2 , slope, p -value and y -intercept) of each regression are displayed inside the graphs. From Faragli et al[189].

To reduce the load-dependency of the strain measurements, global strain values were indexed for both mAoP and meridional wall stress as described in the Methods section “*Experimental protocol for the CMR studies*”. Indexing CMR-FT global strain parameters for mAoP or wall stress improved the ability of CMR-derived strain parameters to reflect hemodynamic alterations, as highlighted by the increased correlations (higher r^2 value) with CPO, CI and Ees (Figure 49 and Figure 50).

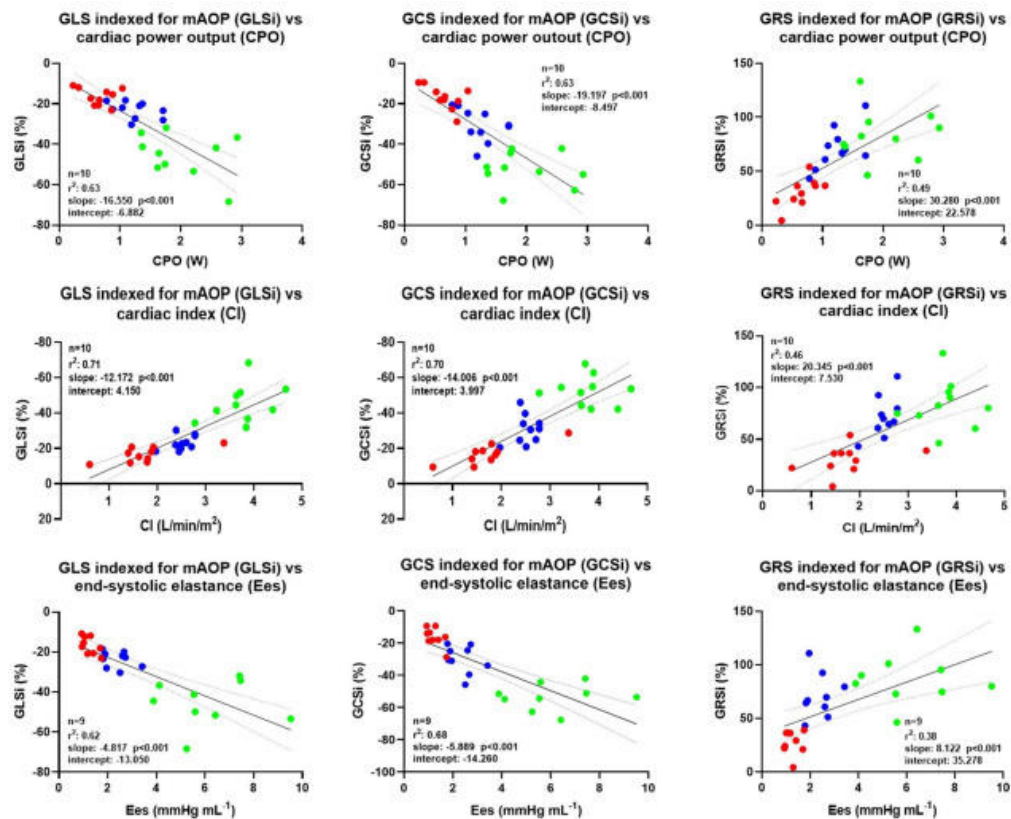


Figure 49. Correlation between global strain and invasive hemodynamics parameters after indexing for mean aortic pressure (mAoP). Top panels, linear regression analysis between global longitudinal, circumferential, and radial strains indexed for mAoP (GLSi, GCSi, GRSi, respectively) against cardiac power output (CPO). Middle panels, linear regression analysis between GLSi, GCSi, GRSi and cardiac index (CI). Bottom panels, linear regression analysis between GLSi, GCSi, GRSi and end-systolic elastance (Ees). Dots represents the single animal, whereas the color highlights the inotropic state. Blue: baseline. Green: dobutamine. Red: verapamil. The parameters (n , r^2 , slope, p -value and y -intercept) of each regression are displayed inside the graphs. From Faragli et al[189].

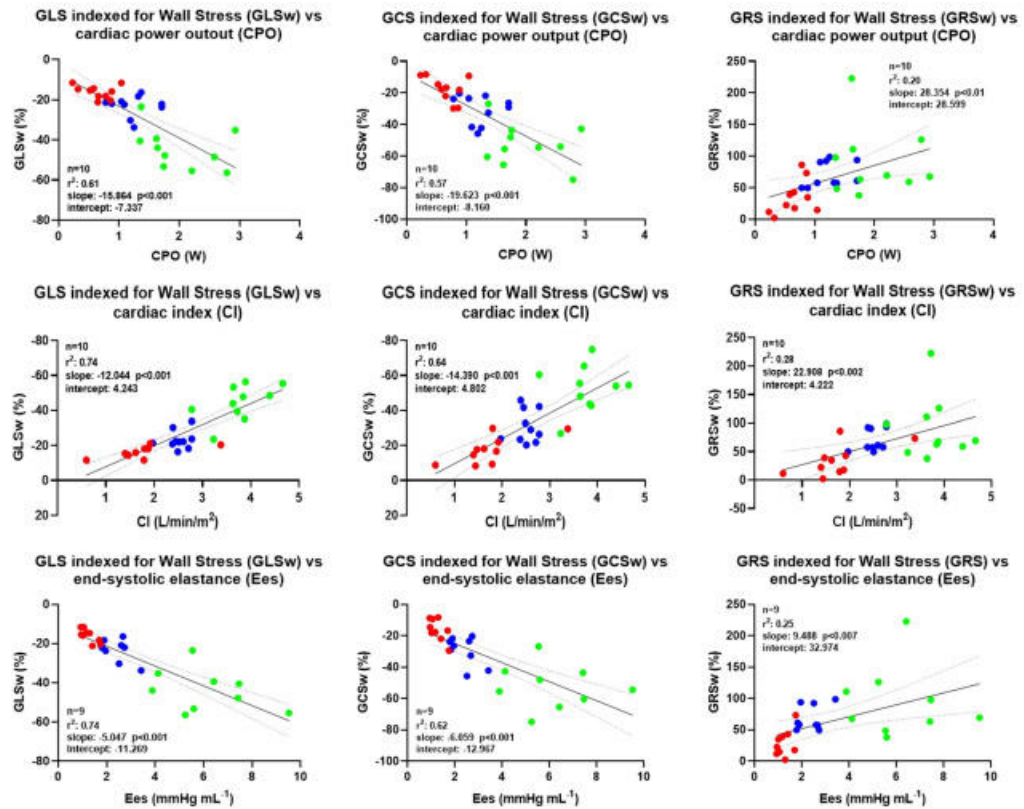


Figure 50. Correlation between global strain and invasive hemodynamics parameters after indexing for wall stress. Top panels, linear regression analysis between global longitudinal, circumferential, and radial strains indexed for wall stress (GLSw, GCSw, GRSw, respectively) against cardiac power output (CPO). Middle panels, linear regression analysis between GLSw, GCSw, GRSw and cardiac index (CI). Bottom panels, linear regression analysis between GLSw, GCSw, GRSw and end-systolic elastance (Ees). Dots represents the single animal, whereas the color highlights the inotropic state. Blue: baseline. Green: dobutamine. Red: verapamil. The parameters (n , r^2 , slope, p -value and y -intercept) of each regression are displayed inside the graphs. From Faragli et al[189].

To investigate to what extent LV global strain reflects hemodynamic alterations, we plotted the relative change of both these parameters during the experimental protocol (Figure 51).

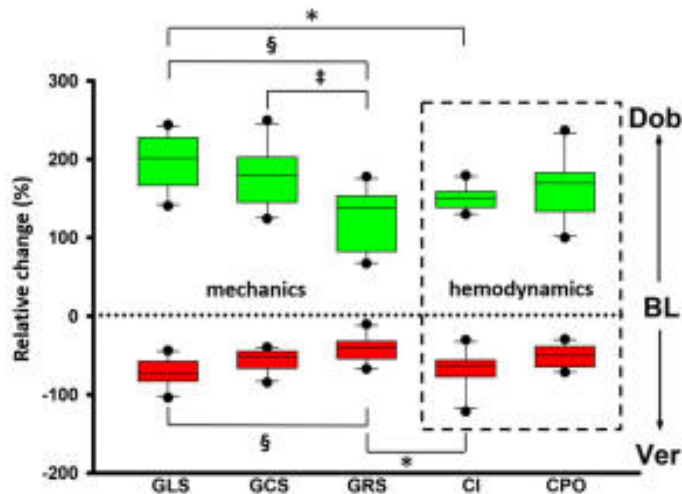


Figure 51. Relative change (%) of global strain and hemodynamic parameters from baseline to dobutamine or verapamil condition. Baseline (BL) condition is represented by the dashed horizontal line. The relative change was calculated as the difference between measurements (mechanics or hemodynamics) during Dobutamine (Dob, green boxes) or Verapamil (Ver, red boxes) and values at BL. * $p < 0.05$ vs CI, § $p < 0.05$ vs GLS, ‡ $p < 0.05$ vs GCS. From Faragli et al[189].

The overall impact of Dobutamine and Verapamil on both mechanical and hemodynamic parameters was comparable. The two exceptions were the relative change of GLS during the Dobutamine-stress phase (higher than that of CI), and the relative change of GRS during the cardiovascular depression induced by Verapamil (higher than that of CI).

Previous studies on the reproducibility of CMR-derived global strain parameters showed that radial strain was the least replicable and accurate measurement[173-175,190]. In our previous study[171] on the intra- and inter-reproducibility of global strain parameter (Results section “*Intra- and inter-reproducibility of CMR-FT global strain parameters in pigs*”), we showed that measurements at baseline were good to excellent (ICC 0.60–0.74 and ICC>0.74, respectively) for all parameters, but that only GLS and GCS displayed good reproducibility during both dobutamine and verapamil steps. Therefore, the higher relative change obtained for GRS during Verapamil administration should be handled carefully.

In conclusion, CMR-FT strain mostly reflects the hemodynamic changes following our experimental protocol. In detail, GLS and GCS showed the best

correlations with the invasively measured hemodynamic parameters. Moreover, the degree of correlation increased when both GLS and GCS were indexed for either mAoP or wall stress to manage their load-dependency. On the contrary, GRS showed the worst correlation with the hemodynamic parameters that did not improve when indexed for either mAoP or wall stress.

Therefore, CMR-FT showed to be a promising tool to characterize LV hemodynamics in patients with varying degrees of LV dysfunction.

CMR-based quantification of myocardial energetics under different inotropic states – Attachment 3

As described in depth in this thesis, the most common parameters used in routine clinical practice to assess the cardiac function are the ejection fraction, stroke volume/stroke work or global longitudinal strain. Although their main advantage is the non-invasive measurement, each parameter has a considerable margin of error and, more importantly, is strongly load dependent.

Calculating the mechanical work of the ventricle would require continuous measurement of the force and wall curvature of the LV, which is extremely difficult even under experimental conditions. Instead, pressure is commonly used as a surrogate for force, and the mechanical energy of the LV (or RV) is classically described as the sum of the area within the PV-loop and the potential energy stored in the myocardium[12]. However, this simplification does not account for the influence of chamber size on wall stress and, therefore, may be flawed when comparing ventricles of substantially different sizes.

An old concept to assess the cardiac function is the mechanical efficiency, which was developed on early observations that an increase in cardiac work was accompanied by an increase in oxygen uptake[191].

Mechanical efficiency is defined as the ratio between the external myocardial power (EMP) required to maintain blood flow against systemic vascular resistance and the internal myocardial power (IMP) required by the LV myocardium[159,192,193]. This proportion has drawn the attention of researchers and clinicians as it was found to be associated to myocardial performance and myocardial remodeling[194,195] in patients with cardiac diseases such as valvular heart disease[196,197] and failure[198]. Moreover, mechanical efficiency has the potential to provide insight into myocardial physiology and its tolerance in different inotropic states as it can be altered by changes in hemodynamic conditions.

Recently, PET was suggested for the assessment of this parameter[197,199], but its use is limited to specific clinical indications and includes exposure to ionizing radiation.

The aim of this work was to evaluate myocardial power and efficiency via a recently proposed CMR-based approach[159] in swine under stress and ischemic conditions.

The hemodynamic, anatomical, and functional parameters measured via CMR and considered in this study are displayed in Table 5. The complete hemodynamic dataset was previously described in the Results section “*Intra- and inter-reproducibility of CMR-FT global strain parameters in pigs*”, but briefly a significant increase of HR, mean aortic pressure, CPO and LVEF was obtained after Dob while a significant decrease was observed during Ver. As it can be noted, significant differences for systolic blood pressure were observed in pigs after dobutamine and verapamil, while for diastolic blood pressure we observed a not significant increase after dobutamine but a significant decrease after verapamil.

Subjects (n = 10)	BL	Dob	Ver	p-value (BL vs. Dob)	p-value (BL vs. Ver)
sBP (mmHg)	108 (101–117)	136 (127–147)	87 (78–106)	0.007	0.005
dBP (mmHg)	79 (60–87)	84 (57–97)	58 (50–66)	0.646	0.012
Myocardial mass/BSA (g/m ²)	41 (34–52)	41 (34–52)	41 (34–52)	–	–
Myocardial volume (ml)	38 (32–50)	38 (32–50)	38 (32–50)	–	–
SV _{flow} (ml)	57 (44–80)	52 (45–78)	42 (47–53)	0.386	0.005
CO _{flow} (L/min)	5.6 (4.8–6.5)	6.0 (4.6–8.0)	3.9 (3.1–4.9)	0.220	0.013
Distensibility aorta ascendens (10 ⁻³ mmHg ⁻¹)	11.2 (7.7–14.8)	9.7 (6.1–14.6)	5.5 (4.2–7.7)	0.721	0.017
Distensibility aorta descendens (10 ⁻³ mmHg ⁻¹)	7.0 (4.4–9.6)	6.7 (4.5–8.6)	4.9 (1.5–7.0)	0.721	0.139
External myocardial power (W/m ²)	1.3 (1.1–1.6)	2.3 (1.6–3.1)	0.8 (0.5–0.9)	0.005	0.005
Internal myocardial power (W/m ²)	5.9 (4.6–8.5)	7.5 (6.9–9.0)	5.8 (4.7–8.8)	0.241	0.878
Myocardial efficiency (%)	21 (15–27)	31 (20–44)	10 (8–13)	0.059	0.005

Table 5. Table showing the hemodynamic, geometrical, and functional parameters assessed via CMR in baseline, dobutamine and verapamil. BSA, body surface area; BL, baseline; Dob, dobutamine; Ver, verapamil; sBP, systolic blood pressure; dBP, diastolic blood pressure; SV, stroke volume; CO, cardiac output. Data are presented as median and interquartile range. Modified from Faragli and Alogna et al[200].

Concerning the quantification of the heart power (Figure 52), we observed a significant increase for EMP after dobutamine and a significant decrease following verapamil infusion. There were no significant changes in IMP during our protocol. The myocardial efficiency, calculated as the ratio between EMP and IMP, showed an increasing trend after dobutamine and a significant decrease after verapamil.

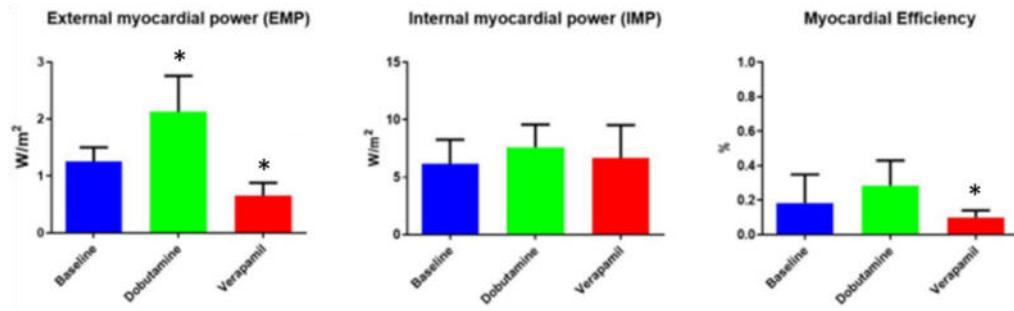


Figure 52. External myocardial power (EMP), internal myocardial power (IMP) and myocardial efficiency at baseline and after dobutamine and verapamil. Data are presented as mean \pm SD. * $p < 0.05$ vs. baseline. Modified from Faragli and Alogna et al[200].

To investigate the degree of correlation between the heart power parameters and invasively measured hemodynamic parameters, we performed a linear regression analysis between EMP, IMP, and myocardial efficiency and both CPO and LVEF (Figure 53).

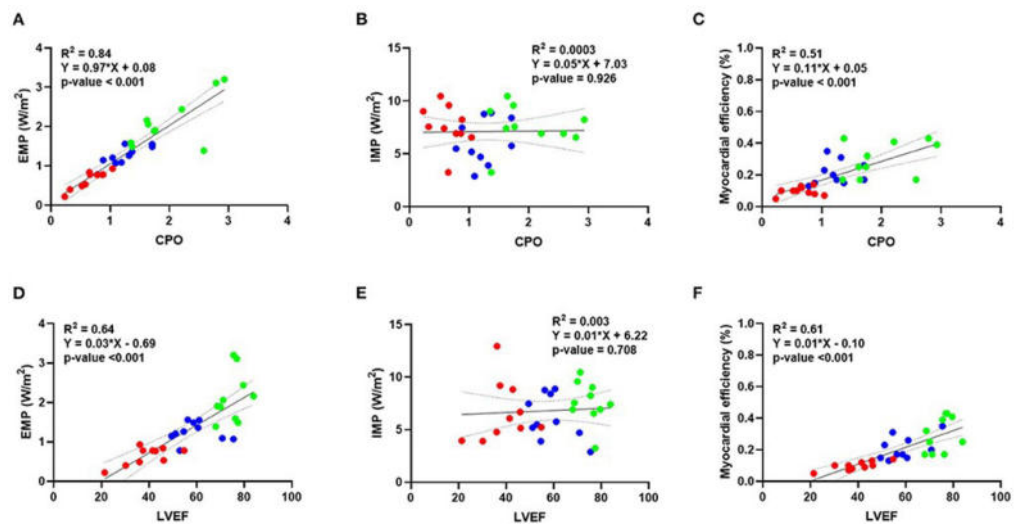


Figure 53. Correlations between heart powers and myocardial efficiency parameters vs. invasively measured hemodynamic parameters. **A:** linear regression analysis between external myocardial power (EMP) and cardiac power output (CPO). **B:** linear regression analysis between internal myocardial power (IMP) and CPO. **C:** linear regression analysis between the myocardial efficiency, calculated as the ratio between EMP and IMP, and CPO. **D, E** and **F** same as **A, B** and **C** but vs. left ventricular ejection fraction (LVEF). Dots represent the animals ($n=10$), the colors represent the different hemodynamic states (blue=baseline; green=dobutamine; red=verapamil). In each panel are showed the coefficient of correlation (R^2), the equation of the straight line, and p -value of the slope. From Faragli and Alogna et al[200].

The EMP showed a good correlation between both CPO and LVEF ($R^2=0.84$ and $R^2=0.64$, respectively), whereas there was no correlation between IMP and both CPO and LVEF. The calculated myocardial efficiency showed a moderate correlation between both CPO and LVEF ($R^2=0.51$ and $R^2=0.61$, respectively). In conclusion, our non-invasive CMR-based approach showed that external myocardial power reflects the hemodynamic changes under both stress (dobutamine) and ischemic conditions (verapamil). The external work of the heart is classically described as the sum of the area within the PV-loop and the potential energy stored in the myocardium[12]. This invasive measurement represents the most comprehensive way to describe ventricular performance[201]. Moreover, CPO can be considered a surrogate of external power as it was found to accurately reflect the left ventricular stroke work per minute over a wide range of inotropic states[202]. In our study we observed a good correlation for EMP vs. both CPO (a load-independent parameter) and LVEF (a load-dependent parameter) showing that this measure has the potential to be useful in patients with compromised LV function.

On the contrary, we did not observe significant changes in internal myocardial power during our protocol, possibly because the animals' healthy heart was able to mask the drug-induced hemodynamic alterations in afterload. In fact, a decrease in IMP corresponds to an improved heart work efficiency that is not expected in a healthy heart. Accordingly, an increase in IMP corresponds to a compromised heart work efficiency which is associated with pathological changes that, however, require time. Therefore, it was expected that transient changes in heart work conditions, as investigated in the current study, did not generate alterations in IMP and explains why the parameter did not correlate with the invasively measured CPO and LVEF.

Interestingly, myocardial efficiency was found at human control levels in resting conditions[159] and, as expected, was not altered during dobutamine stress[194]. Accordingly, an impaired myocardial efficiency was observed under ischemic conditions induced by verapamil administration.

This study highlights the potential of this non-invasive approach in human subjects, but in particular those with altered myocardial performance.

Vi.Ki.E.’s frequency relationship – Attachment 4

As the name suggests, the Video Kinematic Evaluation technique (Vi.Ki.E.) has its roots in kinematics, a subfield of physics that describes the motion of points, objects or groups of objects without considering the forces that cause them to move. Thus, the frequency at which the heart is beating can influence the path (trajectory) and displacement at the base of all Vi.Ki.E.’s parameters.

Therefore, we performed a study on both male and female rat hearts to assess how our parameters behaved at increasing frequency of stimulation.

In detail, after median thoracotomy, the heart was stimulated with a cathodal suprathreshold train of stimuli at different basic cycle length (BCL) ranging from 390 ms to 160 ms.

To evaluate the heart kinematic behavior at increasing frequency of stimulation, we recorded 2 s videos with a temporal resolution of 500 fps at each BCL and followed the analysis protocol already described in the Methods section “*Video Kinematic Evaluation*”.

In Figure 54 are displayed the kinematics parameters of both male and female hearts at increasing frequency of stimulation.

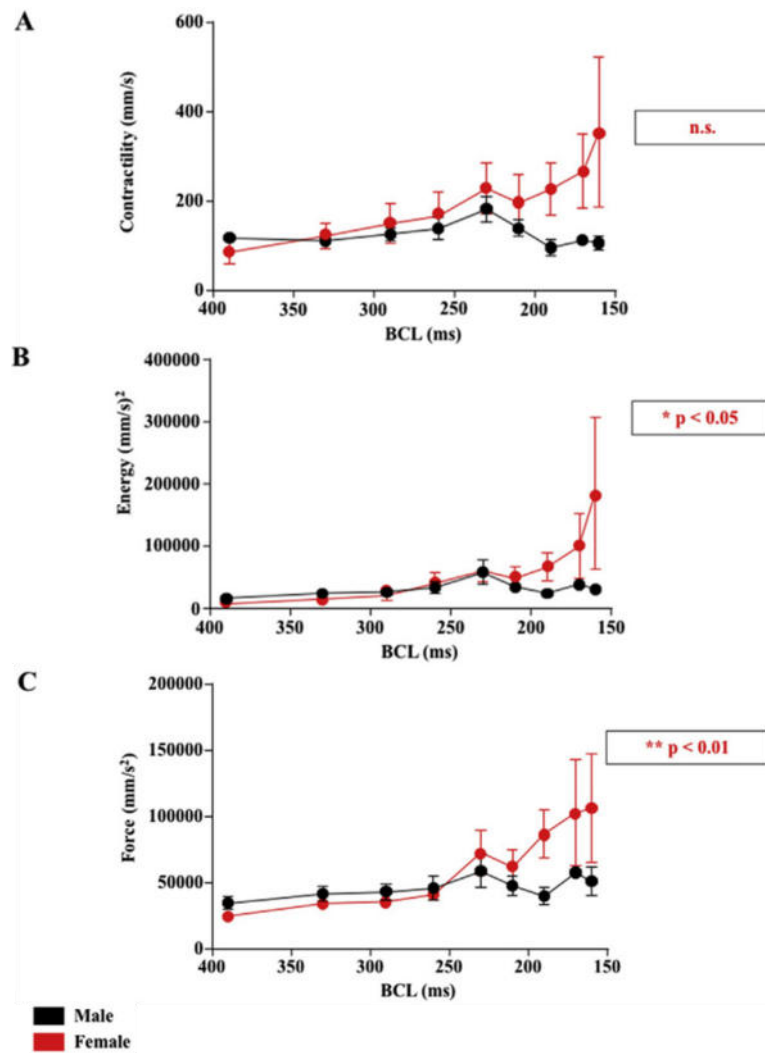


Figure 54. Graphs displaying the effect of increase in heart rate on the Vi.Ki.E. kinematic parameters for both male (black) and female (red) during our stimulation protocol. **A:** relationship between Contractility and basic cycle length (BCL). **B** and **C:** same as A but for Energy and Force, respectively. Data are showed as mean \pm SEM. * $p < 0.05$; ** $p < 0.01$; n.s.: not significant. From Lo Muzio and Rozzi et al[90].

We observed that male cardiac kinematics are inclined to maintain the same Contractility, Force and Energy, whereas the female's kinematics tend to increase at increasing frequency of stimulation. Moreover, we noted that an increase of the kinematics parameters occurred in all animals until BCL= 230 ms and that from this point onward different behaviors between male and female can be appreciated.

Therefore, we focused on the gender-related mechanical behavior in the following timepoints (BCL: 230 ms, 210 ms, 190 ms, 170 ms) which resemble the physiological range of the rat heart rate. In Figure 55 are displayed the

trajectories of representative experiments. As it can be appreciated, the male trajectories changed at increasing frequency of stimulation (Figure 55 A-A3), while the female's pattern of contraction were more preserved throughout the experiment (Figure 55 B-B3).

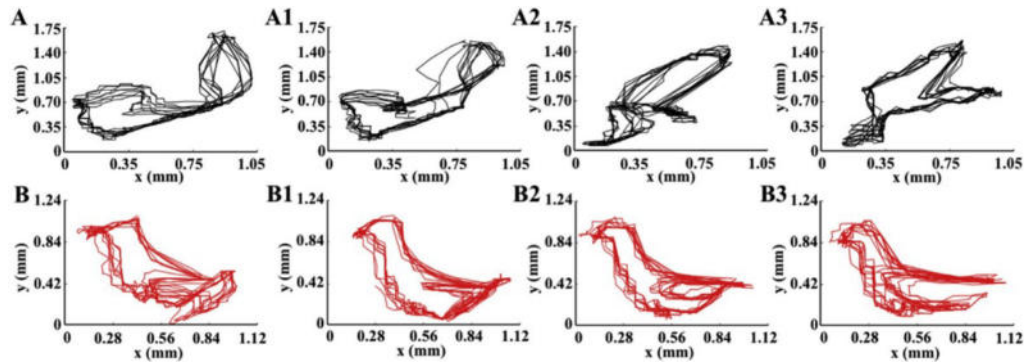


Figure 55. Trajectories of a male (black) and female (red) at four different frequencies of stimulation. **A-A3:** male trajectories at basic cycle lengths 230 ms, 210 ms, 190 ms and 170 ms, respectively. **B-B3:** same as A but for female rat heart. Modified from Lo Muzio and Rozzi et al[90].

The differences in the pattern of contraction between male and female suggested that the frequency-dependent epicardial deformation can be related to gender. Therefore, we sought to investigate the mechanical behavior at different BCL evaluating the changes in the Perimeter of the trajectories. In line with the qualitative observation of Figure 56, male rat hearts (black) displayed not-preserved perimeters (from 5.890 ± 0.5597 mm to 3.747 ± 0.3422 mm) at increasing frequency of stimulation compared to female hearts (from 4.220 ± 0.1566 mm to 4.566 ± 0.8934 mm).

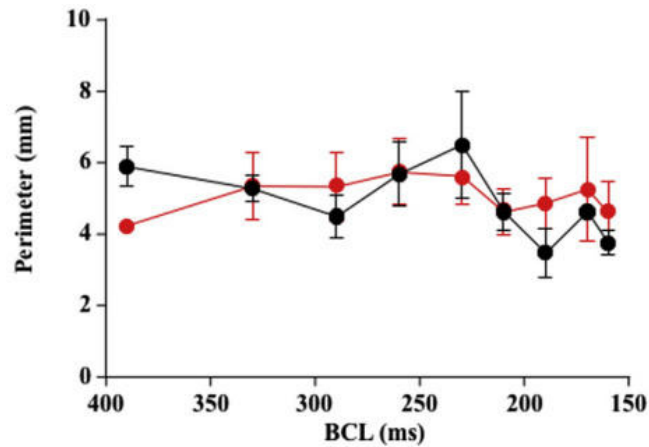


Figure 56. Relationship between the perimeter of the trajectories at different basic cycle length (BCL). Male (black) and female (red) perimeter corrected for the number of acquired cardiac cycles for each BCL. Data are shown as mean \pm SEM. Modified from Lo Muzio and Rozzi et al[90].

To conclude, this study showed that Vi.Ki.E. is able to capture the kinematic changes following an increase in heart rate to such degree that we can also speculate it was able to reveal mechanical heterogeneities related to gender. This difference in mechanical performance could be related to the positive role exerted by estrogens on the excitation-contraction machinery[203] including the SERCA activity[204]. Therefore, the different pattern of contraction observed in male hearts at increasing frequency of stimulation could be a needed acute adaptation to compensate for the absence of the same mechanism that is available for the female.

Vi.Ki.E. assessment of the right ventricle in Tetralogy of Fallot patients - Attachment 5

Pulmonary regurgitation is the most common condition late after repair of tetralogy of Fallot (ToF) leading to chronic right ventricle (RV) volume overload which results in varying degrees of ventricular dilatation and dysfunction that are associated with arrhythmias, cardiac failure and premature death[205].

Pulmonary valve replacement (PVR) has been shown to be effective in resolving pulmonary regurgitation[206], although some studies report a non-uniform clinical improvement after surgery[207]. These observations would suggest that the current indications for PVR could be excessively conservative leading to intervention when irreversible RV dysfunction has already occurred[208]. Thus, the timing for PVR is still controversial and remains a topic of debate.

The current international guidelines for PVR focus on RV functional deterioration even in asymptomatic patients[209]. However, both load-dependent and -independent indices of RV function assessed by cardiac magnetic resonance may play a key role in guiding indication for PVR[210]. In fact, both RV end-diastolic and end-systolic volumes (RVEDV and RVESV, respectively) are used to assess the correct timing of PVR[211]. However, an important limitation is that these indices can be measured only in the preoperative phase and in follow-up.

Intraoperative imaging could add insightful prognostic information, but transoesophageal echocardiography comes short of assessing the RV function[48]. Therefore, we employed Vi.Ki.E. to evaluate the RV mechanics in a selected cohort of ToF patients with the main objective to establish its safety and efficacy in assessing the acute functional changes occurring after PVR. A secondary goal was to evaluate possible correlation between the measured kinematics parameters and cardiac magnetic resonance.

Between November 2016 and February 2018, 6 consecutive patients were enrolled. All patients underwent preoperative CMR and transthoracic

echocardiographic evaluation. Both demographic and measured variables are reported in Table 6.

	N=6	Mean	Median	Range
Gender (male/female)	3/3			
BSA (m ²)		1.3 ± 0.2	1.4	0.7–1.7
Age at PVR (years)		13.0 ± 2.3	12.2	6.9–20.1
Age at ToF repair (months)		3.0 ± 0.6	2	1–5
Time to PVR (years)		13.8 ± 2.6	12.5	6.9–19.8
NYHA class II–III	4/6			
SR, complete RBBB (EKG)	4/6			
QRS duration (ms)		156.5 ± 8.7	162	128–174
Severe PR (ECHO)	5/6			
Preoperative CMR				
RVEDVi (ml/m ²)		115.6 ± 16.2	108.5	62.5–183.0
RVESVi (ml/m ²)		61.5 ± 14.6	53.7	12.5–104.0
RVEF (%)		55.1 ± 5.5	53.8	42.0–79.0
PR fraction (%)		49.0 ± 6.9	49.0	22.0–73.0
LVEF (%)		56.0 ± 1.7	54.5	51.0–62.0

Table 6. Table showing the demographic parameters and different measured variables in our ToF population. BSA: body surface area; CMR: cardiac magnetic resonance; LVEF: left ventricular ejection fraction; NYHA: New York Heart Association; PR: pulmonary regurgitation; PVR: pulmonary valve replacement; RBBB: right bundle; RVEDVi: right ventricular end-diastolic volume index; RVEF: right ventricular ejection fraction; RVESVi: right ventricular end-systolic volume index; SR: sinus rhythm; ToF: tetralogy of Fallot. Modified from Rozzi and Lo Muzio et al[89].

There were no perioperative complications, except for 1 patient experiencing reversible subclinical hepatic dysfunction. Patients were discharged after a mean of 7.0 ± 2.0 days (5–9 days) of hospitalization. Transthoracic echocardiogram prior to discharge documented the recovery of normal RV dimensions in 5 out of 6 patients (83%), preserved RV ejection fraction (RVEF) in 3 out of 6 patients (>50%) and mildly reduced RVEF in 3 out of 6 patients (>40%). On Doppler examination there was absence of PR in all patients and a mean peak trans-prosthetic pulmonary valve gradient of 16.5 ± 7.1 mmHg. During a mean follow-up of 8.5 ± 4.5 months (2–15 months), all patients were in New York Heart Association (NYHA) I, except for one patient in NYHA II. No patient experienced adverse cardiovascular events and all were in regular sinus rhythm. The follow-up echocardiogram was similar to that taken before discharge, with a mean peak trans-prosthetic pulmonary valve gradient of 14.5 ± 7.9 mmHg and preserved RVEF in 5 out of 6 patients.

The kinematic parameters of our patients and the individual patient mechanical performance following PVR are displayed in Figure 57.

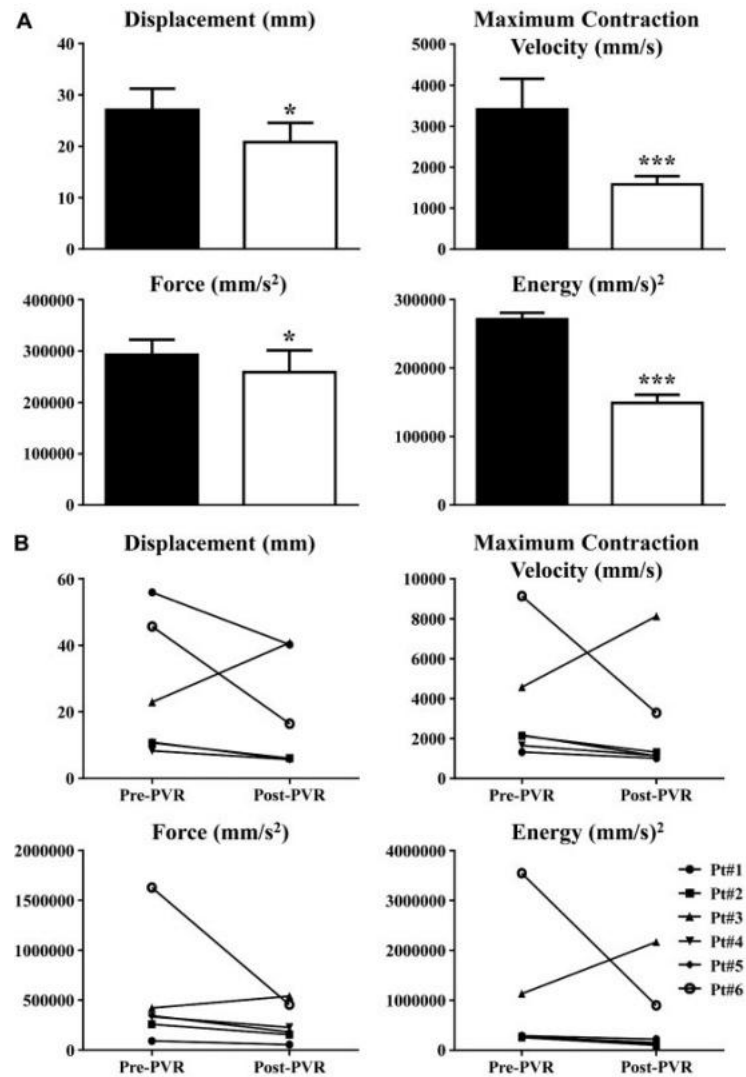


Figure 57. Kinematic parameters in Tetralogy of Fallot patients and individual mechanical performances following pulmonary valve replacement (PVR). **A:** Difference in the Vi.Ki.E. parameters of Displacement, Contractility, Force and Energy between Pre-PVR (black columns) and Post-PVR (white columns). **B:** Graphical representation of the mechanical performance of each patient after surgery. Data are shown as mean \pm SEM. * $p < 0.05$ versus pre-PVR, *** $p < 0.001$ versus Pre-PVR. From Rozzi and Lo Muzio et al[89].

As it can be appreciated, all kinematic parameters significantly decreased (Figure 57 A) after PVR. On an average, displacement decreased by 23%, maximum contraction velocity by 54%, force by 12% and energy by 45%. Regarding the individual mechanical performance (Figure 57 B), all patients showed a decreasing trend for the Vi.Ki.E. parameters with the exception of

patient #3 who exhibited an increasing trend. Intraoperatively, this patient showed atrial ectopic tachycardia Post-PVR, which was initially refractory to antiarrhythmic therapy and eventually subsided six hours after surgery.

Patient #6 showed the highest values for each parameter before surgery and the greatest percentage decrease Post-PVR. In particular, patient #6 values Post-PVR were greater than the rest of the study population and still remained twofold higher than Pre-PVR values of the rest of the study population.

Finally, to investigate possible clinical correlations between our parameters and cardiac magnetic resonance, the average Energy and Force parameters of each patient were plotted against their respective preoperative RVEDVi (Figure 58). Among our kinematics parameters, these two hold the strongest clinical implication given that the Energy estimates the total energy expended during the cardiac cycle (Figure 58 A) and the Force is a surrogate for the cardiac fatigue (Figure 58 B).

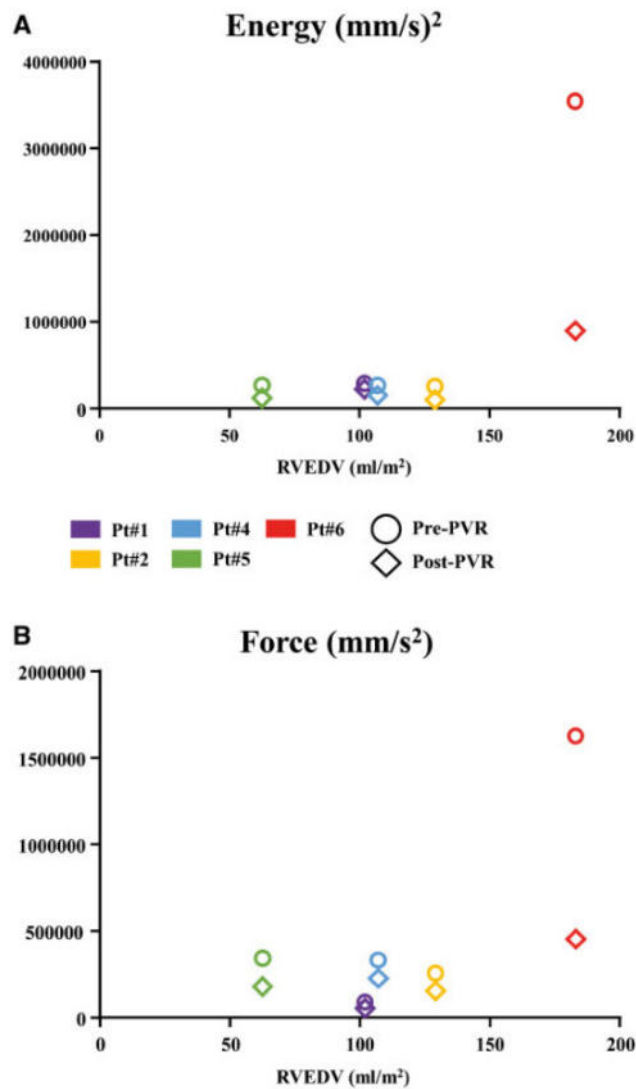


Figure 58. Graphical representation of a possible correlation between preoperative right ventricle end-diastolic volume (RVEDV) and right ventricle Vi.Ki.E. parameters of Energy and Force. **A:** Graph displaying the relationship between RVEDV and Energy. **B:** Same as A but for Force. PVR: pulmonary valve replacement. Colors represent different patients (see legend), circle is Pre-PVR and diamond is Post-PVR. From Rozzi and Lo Muzio et al[89].

In both graphs, patients undergoing surgery with a RVEDV_i below 129 ml/m² showed a consistent decrease after PVR, in line with recovery of minimal contraction energy and force. Patient #6, who underwent PVR with a RVEDV_i of 183 ml/m² displayed lower values of both parameters after PVR with the greatest decrease. However, both kinematics parameters in this patient remained higher than the remainder of the study population.

In conclusion, our technique did not interfere with the surgical procedure and, thus, is a safe technique to employ in the operating room.

This pilot study provides evidence that PVR may afford immediate recovery of RV mechanical function in children and young adults late after ToF repair. In fact, we observed a decrease of all our kinematics parameters due to the expected decrease in preload following PVR. A plausible explanation for the observed outcome lays in the Frank–Starling law which asserts that a decrease in RV preload generates less stretch of the myocardium and, consequently, a decrease in actin–myosin crossbridge activity resulting in less cardiac force and kinetic energy[212].

Finally, our preliminary results indicate a possible correlation with RVEDV measured with cardiac magnetic resonance recommending lowering the current preoperative RV threshold volumes. Therefore, our results are in line with prior experimental findings using cardiac catheterization and magnetic resonance, where a rapid decline in RV power and efficiency were seen at critical values of 139 ml/m² RVEDV and 75 ml/m² RVESV indexes[213].

Timing of pulmonary valve replacement is a key factor in determining recovery of the right ventricle in ToF – Attachment 6

Timing of PVR in repaired ToF patients is still a matter of debate due to limitations in estimating RV dysfunction and in predicting its recovery [206,210]. Among the parameters currently proposed to determine the timing of PVR, there are the RVEDVi and RVESVi measured by cardiac magnetic resonance. In accordance with the recent guidelines, RVEDV > 160 ml/m² and RVESV > 80 ml/m² are the values at which PVR is recommended in patients with a moderate pulmonary regurgitation[214]. However, some studies showed that these values may still preclude a portion of patients from recovering RV function[208,215,216], suggesting that both RVEDVi and RVESVi thresholds should be further lowered. Nonetheless, both indices are limited at only the preoperative and follow-up phases.

Intraoperative imaging could provide insightful information on the impact of the surgery, but transoesophageal echocardiography is not suited for the evaluation of the RV function. Therefore, in our previous pilot study we aimed to prove the safety and efficacy of Vi.Ki.E. to describe RV functional changes in ToF patients before and after PVR[89].

In this study, we expanded our results by enrolling more patients aiming to establish whether Vi.Ki.E. could offer prognostic insight into the timing of PVR.

The demographic and MRI variables of the patient population are reported in Table 7.

	N = 12	Mean ± SD	Median	Range
Gender (male/female)	7/5			
BSA (m ²)		1.6 ± 0.41	1.7	0.73-1.97
Age at PVR (years)		27.1 ± 19.1	20	6-64
ToF to PVR (years)		22.2 ± 13.3	19.5	6-48
RVEDVi (ml/m ²)		136.9 ± 35.7	147.5	62.5-183
RVESVi (ml/m ²)		74.0 ± 30.1	81	12.5-104
RVEF (%)		50.1 ± 12.0	51	37-79
LVEF (%)		54.3 ± 5.9	54	42-62

Table 7. Demographic and MRI variables in our ToF population. BSA: body surface area; LVEF: left ventricular ejection fraction; PVR: pulmonary valve replacement; RVEDVi: right

ventricular end-diastolic volume index; RVEF: right ventricular ejection fraction; RVESVi: right ventricular end-systolic volume index. Modified from Rozzi and Lo Muzio et al[91].

All patients underwent surgical PVR on the beating heart: 5 patients received 23-mm stented bioprostheses; 2 patients, 25 mm; 2 patients, 21 mm; and 3 patients received a pulmonary homograft (size 27 mm in 2, and 25 mm in 1). A temporary period of cardioplegic cardiac arrest was needed to complete a right-sided Maze procedure using cryoablation catheters in 3 patients with a history of paroxysmal atrial fibrillation. There were no perioperative complications, except for 1 patient who experienced reversible subclinical hepatic dysfunction and 1 patient who required 2 days of inotropic support in the intensive care unit. Patients were discharged in regular sinus rhythm after a mean of 7.2 ± 2.4 days (5–12 days) of hospitalization.

Transthoracic echocardiography upon discharge documented the recovery of normal RV dimensions in 8 patients (67%) and moderate dilation in 4 (33%). Preserved (>50%) RV ejection fraction was found in 7 (58%) patients, mildly reduced (>40%) in 4, and severely reduced in 1 patient who was the oldest in this series. Doppler examination showed the absence of pulmonary regurgitation in all patients and a mean peak trans-prosthetic pulmonary valve gradient of 16.5 ± 7.1 mmHg. During a mean follow-up of 24.6 ± 12.5 months (13–39 months), all patients were in NYHA functional class I, except for 1 patient who was in NYHA functional class II. No patient experienced adverse cardiovascular events except for one patient who developed complete atrioventricular block six months after both PVR and Maze procedure, thus requiring a permanent pacemaker implant.

As in our pilot study[89], to investigate possible correlation, the Pre-PVR Vi.Ki.E. parameters that held the strongest clinical implications were plotted against preoperative RVEDVi (Figure 59).

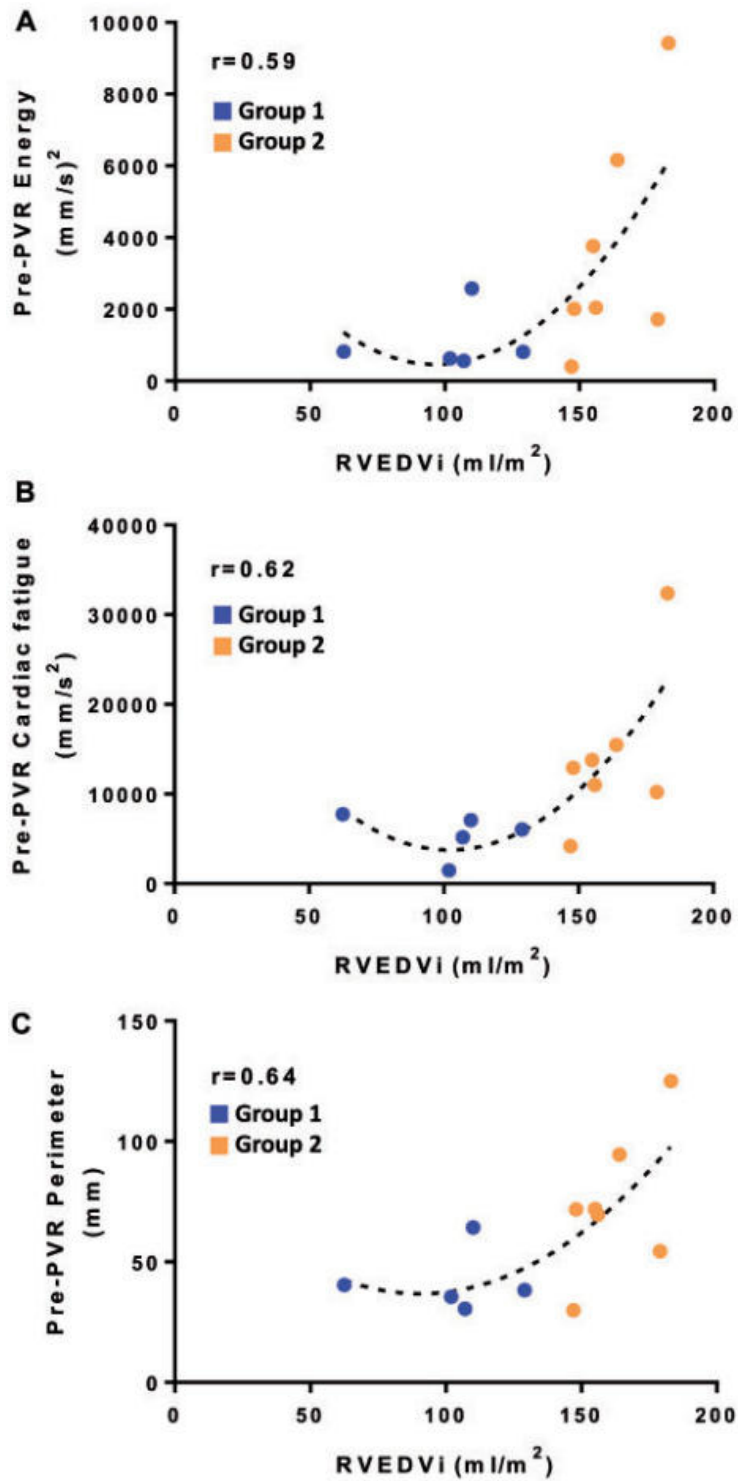


Figure 59. Correlation between the before surgery Vi.Ki.E. parameters and preoperative RVEDVi in ToF patients. **A:** Correlation between the average Energy parameter and RVEDVi. **B** and **C:** Same as A but for Cardiac Fatigue and the Perimeter, respectively. Blue: patients with RVEDVi ≤ 147 ml/m². Orange: patients with RVEDVi >147 ml/m². The dashed line represents the best fitting curve which is exponential. r : correlation coefficient. PVR: pulmonary valve replacement; RVEDVi: right ventricular end-diastolic volume index. From Rozzi and Lo Muzio et al[91].

As it can be noted, we obtain a moderate correlation for all the Vi.Ki.E. parameters. In detail, the correlation coefficient for the energy expended was $r = 0.59$, for the cardiac fatigue was $r = 0.62$, and for the perimeter of contraction was $r = 0.64$. Moreover, a cut-off value of 145 ml/m^2 emerged after which the curve becomes exponential.

The kinematic parameters of all patients are displayed in Figure 60.

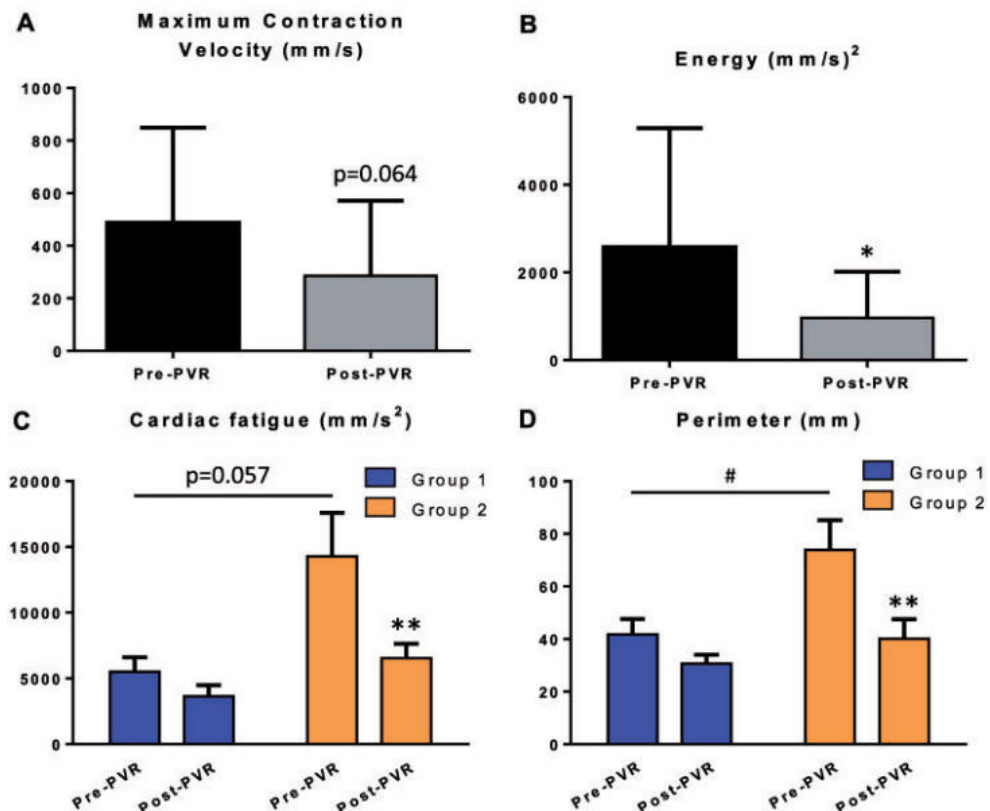


Figure 60. Vi.Ki.E. parameters in our Tetralogy of Fallot population (N = 12) before and after pulmonary valve replacement (PVR). **A:** Maximum contraction velocity in patients with tetralogy of Fallot at both Pre-PVR (black) and Post-PVR (grey). **B:** Same as **A** but for the Energy parameter. **C:** two-way ANOVA for repeated measures analysis for the Cardiac fatigue in both group 1 (blue, N = 5) and group 2 (orange, N = 7). **D:** Same as **C** but for the Perimeter. Data are shown as mean ± SEM. *P < 0.05; **p < 0.01 versus Pre-PVR. # p < 0.05 versus group 1. From Rozzi and Lo Muzio et al[91].

As it can be noted, our ToF population presented prompt recovery of RV mechanical function with a significant decrease in most of the kinematic parameters Post-PVR. In detail, the maximum contraction velocity (Figure 60 A) decreased from 486.8 ± 104.2 to 285.4 ± 82.4 mm/s, and the energy expenditure (Figure 60 B) from $2.55 \times 10^3 \pm 7.84 \times 10^2$ to $9.65 \times 10^2 \pm 3.03 \times 10^2$

mm²/s². The two-way ANOVA for repeated measures yielded a main effect of both ‘time’ (F[1,10] = 6.810; p = 0.026) and ‘group’ (F[1,10] = 5.635; p = 0.039) on cardiac fatigue, reflecting a significant difference between Pre-PVR and Post-PVR and between group 1 and group 2 (Figure 60 C). Similarly, the two-way ANOVA revealed a main effect of ‘time’ (F[1,10] = 13.13; p = 0.005) on the perimeter of contraction, reflecting a significant difference between Pre-PVR and Post-PVR (Figure 60 D). Post hoc analysis also revealed that group 2 showed almost significantly higher Pre- and Post-PVR values of cardiac fatigue compared to group 1 (p = 0.057 and p = 0.082, respectively). In addition, the average Pre-PVR value of perimeter was higher in group 2 than in group 1 (p = 0.05). Finally, we observed a significant decrease after surgery of both cardiac fatigue (p = 0.009) and perimeter (p = 0.002) within group 2.

Given that the correlation between preoperative RVEDVi and before surgery kinematic parameters clearly separated our ToF patients in two groups around the cut-off value of 145 ml/m², we stratified the population in two groups to investigate possible differences that could affect the impact of the surgery. As it can be noted in Table 8, significant differences emerged between the two groups showing that patients in group 1 were younger (p = 0.005), had a shorter time interval from ToF repair to PVR (p = 0.03), presented with greater RVESVi (p = 0.054) and had greater RVEF and left ventricular ejection fraction (although not significant.)

	RVEDVi < 145 ml/m ²			RVEDVi > 145 ml/m ²			P-value
	Mean ± SD	Median	Range	Mean ± SD	Median	Range	
BSA (m ²)	1.2 ± 0.4	1.3	0.73-1.61	1.8 ± 0.1	1.86	1.64-1.97	0.025
Age at PVR (years)	11.2 ± 5.0	10	6.0-19.0	38.4 ± 17.0	39	20.0-64.0	0.005
ToF to PVR (years)	11.0 ± 5.2	10	6.0-19.0	30.1 ± 11.3	25	18.0-48.0	0.03
RVESVi (ml/m ²)	53.0 ± 32.4	48	12.5-102.0	91.5 ± 12.7	94.5	72-104	0.054
RVEF (%)	57.5 ± 13.6	55	42-79	44.0 ± 6.3	43	37-52	0.1
LVEF (%)	56.4 ± 4.5	55	51-62	52.5 ± 6.8	54	42-62	0.18

Table 8. Stratification of our ToF population in accordance to the preoperative right ventricular end-diastolic volume. BSA: body surface area; LVEF: left ventricular ejection fraction; PVR: pulmonary valve replacement; RVEDVi: right ventricular end-diastolic volume index; RVEF: right ventricular ejection fraction; RVESVi: right ventricular end-systolic volume index. Modified from Rozzi and Lo Muzio et al[91].

Then, the kinematic parameters were also compared between the two groups for the Maximum contraction velocity and Energy because, contrary to the Cardiac

fatigue and Perimeter, they were not suitable for the two-way ANOVA comparison (Figure 61).

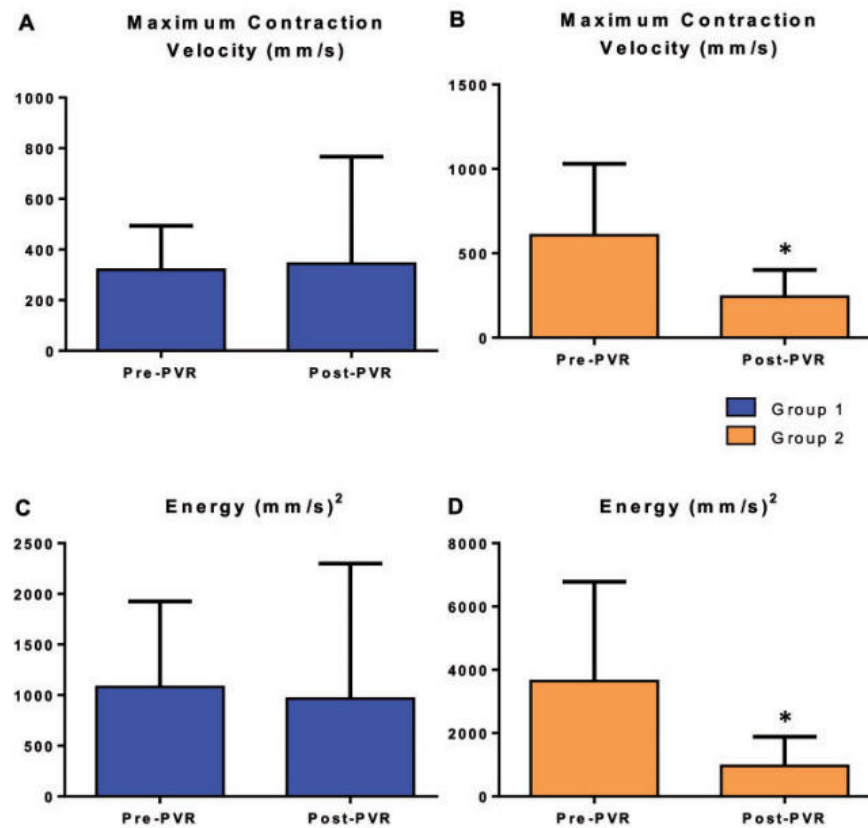


Figure 61. Maximum contraction velocity and Energy in both group 1 (blue) and group 2 (orange). **A:** Maximum contraction velocity in group 1 (N = 5) before and after PVR (Pre- and Post-PVR, respectively). **B:** Same as A but for group 2 (N = 7). **C** and **D:** Same as A and B but for the Energy parameter. PVR: pulmonary valve replacement. Data are shown as mean \pm SEM. * $p < 0.05$ versus Pre-PVR. From Rozzi and Lo Muzio et al[91].

In group 1, we observed an increasing trend of for the Maximum contraction velocity (Figure 61 A) and a decreasing one for the Energy (Figure 61 C). The trend observed for the Maximum contraction velocity was probably influenced by one patient experiencing reversible atrial tachycardia after PVR that was discussed in our previous work[89]. In group 2, we observed a significant decrease for both Maximum contraction velocity and Energy (Figure 61 B-D, respectively).

Finally, in order to provide prognostic insight about the timing for PVR, the difference of the recovery rate between Pre- and Post-PVR for the parameters

that held the strongest clinical implication was compared in the 2 groups (Figure 62).

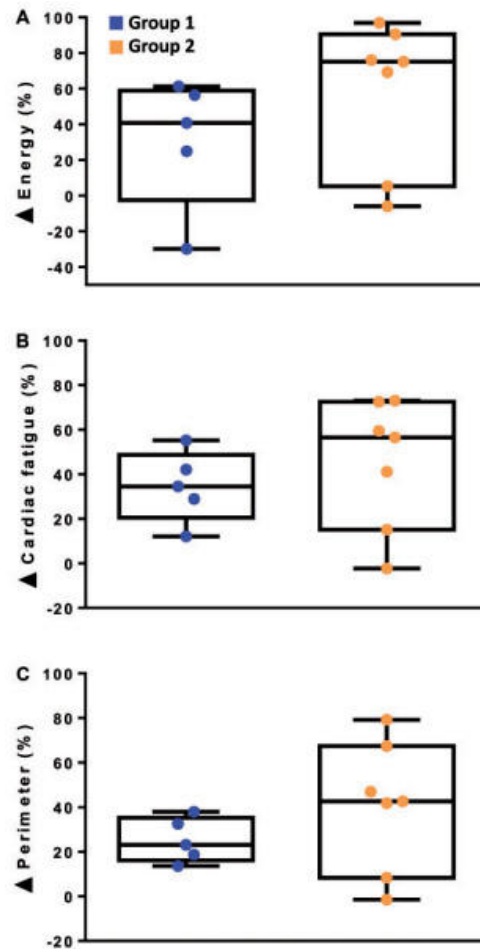


Figure 62. Relative recovery ($\Delta\%$) in Energy, Cardiac fatigue and Perimeter for both group 1 and group 2. **A:** Relative recovery ($\Delta\%$) was calculated as the difference between the values of Energy at Pre-PVR and Post-PVR for both groups. **B** and **C:** same as **A** but for Cardiac fatigue and Perimeter. From Rozzi and Lo Muzio et al[91].

Patients in group 2 showed higher variability in postoperative outcomes but a greater recovery rate compared to group 1. In detail, the energy expenditure decreased by 58% vs 31% (Figure 62 A), cardiac fatigue by 45% vs 35% (Figure 62 B) and perimeter of contraction by 41% vs 25% (Figure 62 C).

In conclusion, this study showed that Vi.Ki.E. assessment can capture early RV functional recovery after PVR and provides insight into factors influencing prompt ventricular recovery. All our patients showed prompt improvement in of the mechanical function displaying a significant decrease in all kinematic parameters following PVR. As stated in our pilot study on the first 6 patients of

this series, these results may be explained by the Frank-Starling law, which asserts that a decrease in ventricular preload is followed by a reduction of the force generated, a less-stretched myocardium and a lower velocity of shortening of the cardiac fibre[212].

The exponential correlation observed between preoperative RVEDVi and before surgery Vi.Ki.E. parameters was expected because long-standing RV volume overload due to PR is directly associated with preoperative RV dysfunction. Moreover, a threshold of 145 ml/m² emerged which clearly separated our population in two groups. Finally, a preoperative RVEDVi lower than 145 ml/m², which in the present work defines earlier timing of PVR, is associated with intraoperative RV functional recovery and a less variable outcome.

Previous clinical studies support the present experimental analysis. One prospective study has identified thresholds for complete RV remodeling at MRI which closely mirror our findings[208]. Furthermore, a previous observational study on a patient population, comparable to the one herein in terms of age at PVR, time of original repair and preoperative MRI profile, showed how more proactive indications (RVEDVi < 150 ml/m²) may afford negligible early and late mortality, recovery of RV volumes and improvement in biventricular function[215]. Finally, recent studies support the hypothesis that earlier timing of PVR could be beneficial in reducing the risk of malignant arrhythmias and mortality[217].

Vi.Ki.E. based supervised machine learning classifiers to support decision-making during surgery – Attachment 7

Artificial Intelligence (AI) implementation can discover and use information hidden in the massive amount of data usually available to clinicians[218]. Different AI systems have been tested in various field of research[219] and demonstrated to be promising tools to assist clinicians in making better clinical decisions[220,221].

As it concerns the cardiac imaging field, AI has been proposed for analyzing CT-scan[222], MRI[223] and transthoracic echocardiography data[224]. However, AI systems related to cardiac imaging are currently not employed during open-chest surgery. Moreover, apart from TEE which is able to evaluate the LV, there is still a lack of a safe intraoperative imaging technique to assess the RV. This is particularly important for complex congenital heart diseases in which the RV dysfunctions are common features[225].

Therefore, in this study we developed two supervised machine learning (SML) classifiers based on the Vi.Ki.E. technique (Figure 63) to predict the outcome of ToF patients undergoing PVR aiming to provide a decision-making tool to support the medical team during open-chest surgery.

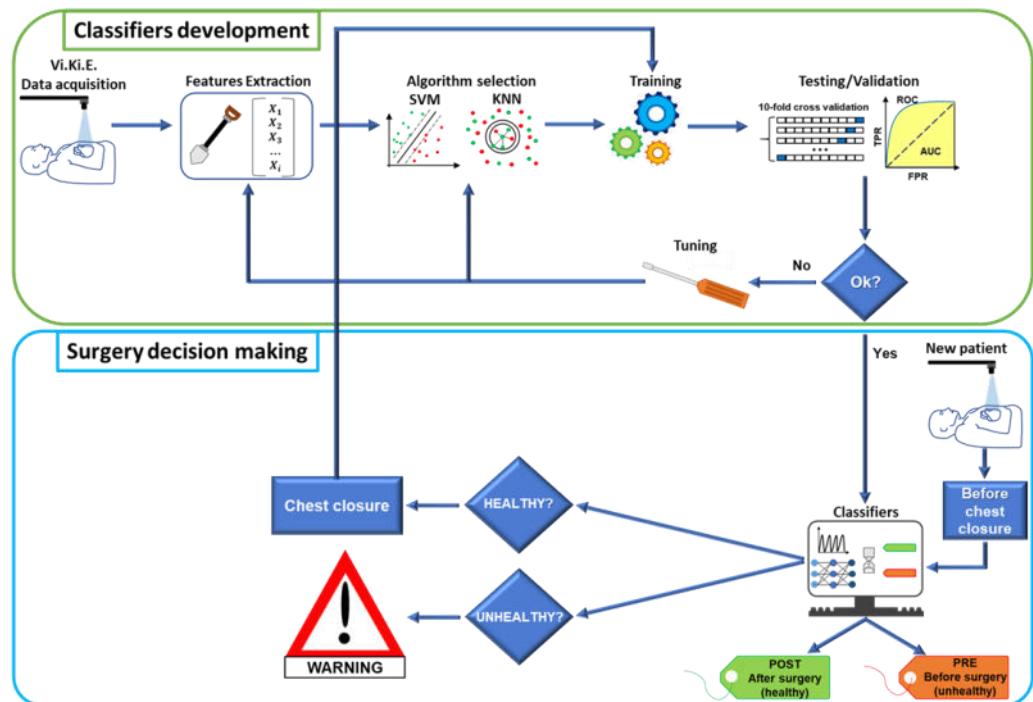


Figure 63. Schematic representation of the framework employed to develop the Vi.Ki.E. based classifiers and their clinical application. **Green box:** The classifiers’ development starts from videos acquired in the operating room via our intraoperative approach (Vi.Ki.E). Following the videos processing, features are extracted and used to select the classification model in terms of best classification accuracy. Then, the model is trained and validated through 10-fold-cross validation and optimization processes. **Blue box:** Before the chest closure of a new Tetralogy of Fallot (ToF) patient, the video recordings are classified by the optimized models. The classifiers predict the patient outcome as one of the two illustrated labels: before surgery (unhealthy) or after surgery (healthy). If the patient is classified as unhealthy the models will display a warning to the surgeons. In case the video recordings are classified as healthy, the surgeons can proceed to close the chest and the patient dataset will be added in the training process refining the model. Modified from Lo Muzio and Rozzi et al[226].

To develop suitable SML models, we extracted features from the frequency domain[227] of the RV epicardial movement recorded in the ToF population which was already studied through the Vi.Ki.E. assessment[91]. The features are an overall measure of the mechanical movement represented by the Vi.Ki.E.’s x and y coordinates. In Table 9 are listed the seven MATLAB® functions (Release R2020a, The MathWorks, Inc., Natick, MA, USA) used to calculate the features for each of the 86 video recordings.

Feature/Predictor	MATLAB[®] function
Band power [pixel]: it returns the ‘average power’ or average l_2 norm (average Euclidean norm) of the input signal [pixel]	bandpower https://it.mathworks.com/help/signal/ref/bandpower.html
Power bandwidth [Hz]: it returns the 3 dB (half-power) bandwidth of the input signal	powerbw https://it.mathworks.com/help/signal/ref/powerbw.html
Occupied bandwidth [Hz]: it returns the 99% occupied bandwidth of the input signal	obw https://it.mathworks.com/help/signal/ref/obw.html
Spurious free dynamic range [dB]: it returns the SFDR of the real sinusoidal-like input signal	sfdr https://it.mathworks.com/help/signal/ref/sfdr.html
Signal to noise and distortion ratio [dB]: it returns the SINAD of the real sinusoidal-like input signal	sinad https://it.mathworks.com/help/signal/ref/sinad.html
Signal to noise ratio [dB]: it returns the SNR of the input signal	SNR https://it.mathworks.com/help/signal/ref/snr.html
Spectral entropy (information content) of the input signal	pentropy https://it.mathworks.com/help/signal/ref/pentropy.html

Table 9. List of features extracted from the periodic movement of the RV calculated for both x and y coordinates. From Lo Muzio and Rozzi et al[226].

The frequency-domain-related features extracted from the epicardial movement of the RV were processed by the Classification Learner Application in MATLAB[®] to test different classification models. In Table 10 are reported the list of tested classifiers and their classification accuracy. Only the k-nearest neighbors (KNN) and support vector machine (SVM) models displayed an accuracy $\geq 75\%$ and, thus, were adopted[228].

Classifier	Accuracy (%)
Boosted trees[229] (ensemble of trees using the AdaBoost [Adaptive Boosting] algorithm)	46.5
RUSBoosted trees[230] (ensemble of trees using the RUSBoost [Random Undersampling Boosting] algorithm)	46.5
Linear discriminant[231]	66.3
Kernel naïve Bayes[232]	68.6
Gaussian naïve Bayes[233]	69.8
Fine Gaussian (Radial Basis) support vector machine (SVM)[234]	79.1
Fine k -nearest neighbor (KNN)[235]	86.0

Table 10. All the tested classifiers ranked in terms of accuracy (%). From Lo Muzio and Rozzi et al[226].

At the end of the optimized training of both models, we obtained the confusion matrix of the predicted class (Figure 64 A and C) from which we calculated the probabilities (Figure 64 B and D) to truly recognize the class (or True Positive Rate, TPR) and to misrecognize it (or False Negative Rate, FNR).

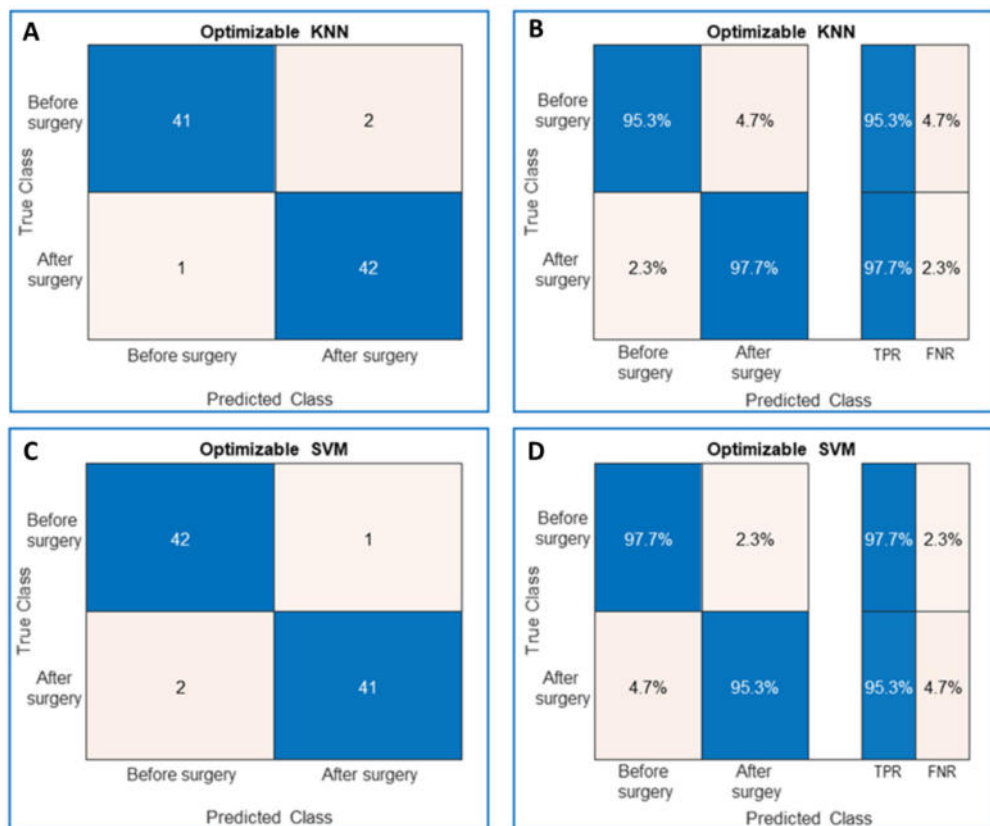


Figure 64. Performance of both k-nearest neighbors (KNN) and support vector machine (SVM) models after training. **A:** Confusion matrix showing the number of both truly (blue) and falsely (pink) recognized videos via KNN model. **B:** the corresponding True Positive Rate (TPR) in

blue and False Negative Rate (FNR) in pink of both classes. **C** and **D**: same as **A** and **B** but for the SVM model. Modified from Lo Muzio and Rozzi et al[226].

In detail, the KNN displayed a TPR of 95.3% and a FNR of 4.7% before surgery, whereas after surgery the TPR was 97.7% and the FNR was 2.3%. Similarly, the SVM showed a TPR of 97.7% and a FNR of 2.3% before surgery, while the TPR was 95.3% and the FNR was 4.7% after surgery.

We also obtained the optimized parameters of the 10-fold cross-validated models (Figure 65A and C) and the AUC (or Area Under Curve) of the Receiving Operating Characteristic Curve (ROC) (Figure 65 B and D).

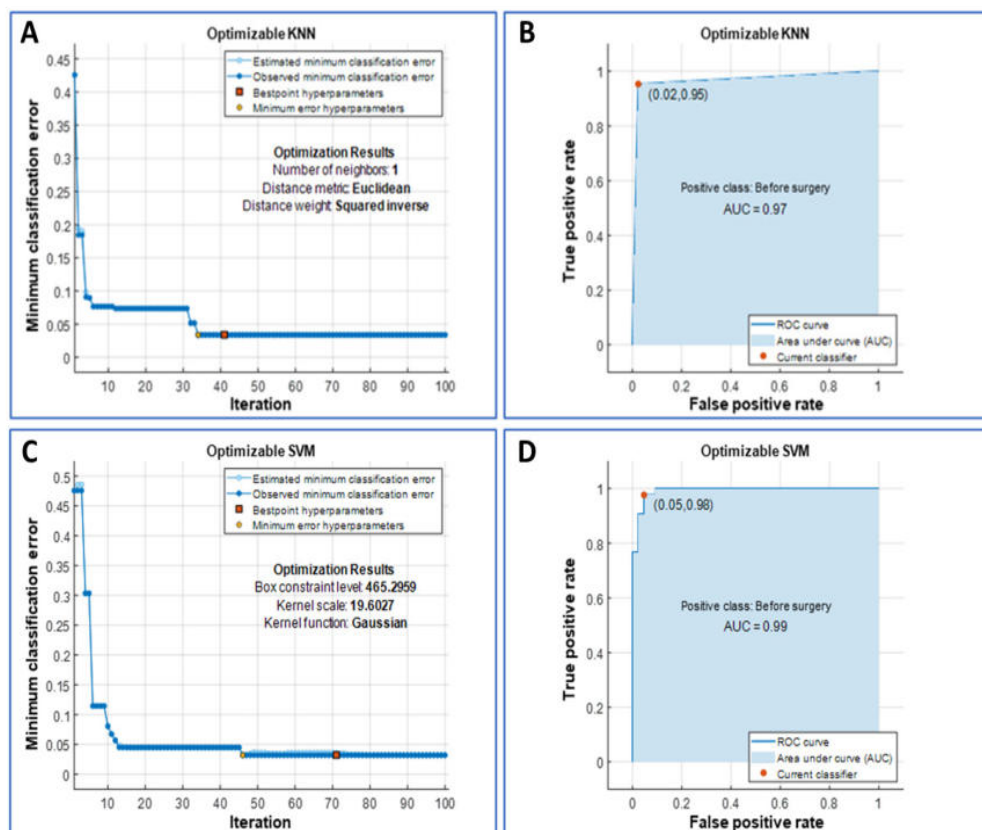


Figure 65. Optimization parameters of both k-nearest neighbors (KNN) and support vector machine (SVM). **A**: The KNN classifier was optimized during the 10-fold cross validation via the minimization of the classification error and its optimized hyperparameters are reported in the “Optimization Results” box. **B**: Receiver Operating Characteristic (ROC) curve with the area under the curve (AUC) portrayed in blue. **C** and **D**: same as **A** and **B** but for the SVM model. Modified from Lo Muzio and Rozzi et al[226].

In detail, after the 10-fold cross validation, each iteration was evaluated in terms of classification error and the iteration with the minimum error provided the

best point hyperparameters. The KNN was optimized for a number of neighbors equal to 1, for the Euclidean distance metric and the squared inverse distance weight. The SVM was optimized considering a Gaussian kernel function, a kernel scale of 19.6027 and a box constraint level of 465.2959. In addition, the AUC of both models was close to 1 (0.97 for KNN and 0.99 for SVM) which is the value of a perfect classification.

After training and optimization, we aimed to test the prediction ability of both classifiers in two additional patients having different clinical outcome: one patient that underwent PVR and was discharged after 7 days of hospitalization (Figure 66), the other underwent PVR for isolated congenital pulmonary valve regurgitation who died two weeks after surgery (Figure 67).

In the first patient, we performed a Vi.Ki.E. assessment and observed a decreasing trend for all kinematic parameters (Figure 66 A) which was significant for the Energy and Perimeter. This trend was in line with what we observed in our previous work on ToF patients[91]. Then, the Vi.Ki.E. coordinates were processed by both classification models to build the decision surfaces (Figure 66 B) selecting, as a representative feature, the signal-to-noise ratio (SNR). Both before- and after-surgery video recordings were correctly classified in the unhealthy and healthy class by both trained models, respectively.

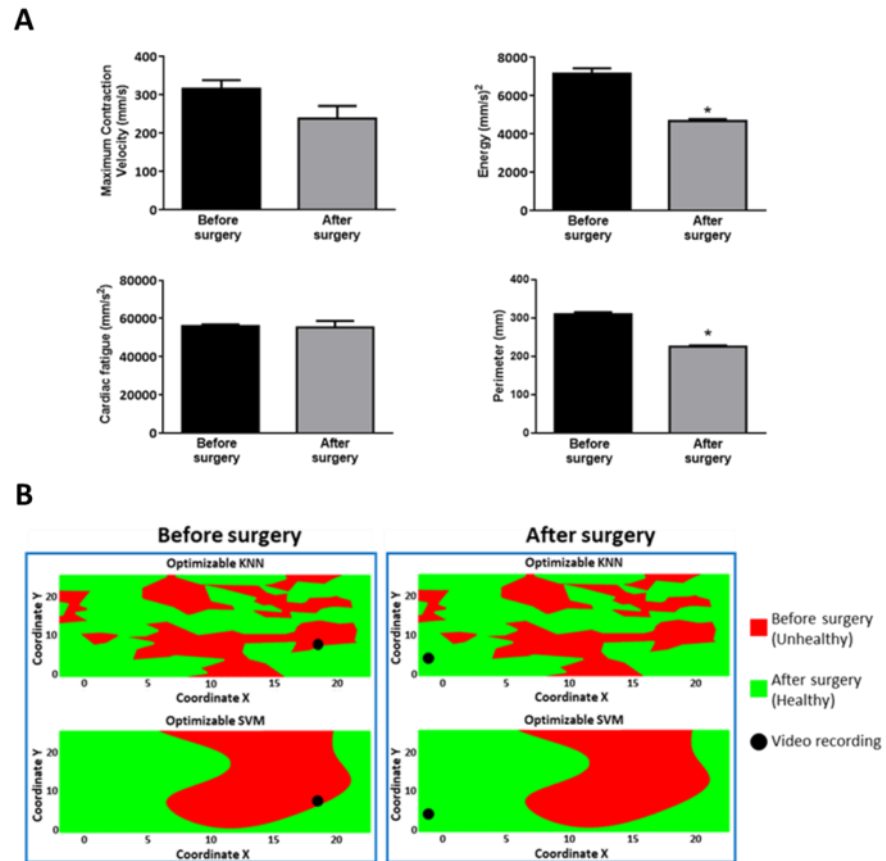


Figure 66. Vi.Ki.E. data and decision surfaces of a patient that underwent PVR with a known favorable clinical outcome. **A:** the average Maximum Contraction Velocity (top left), Energy (top right), Force (bottom left), and Perimeter (bottom right) calculated before- and after-surgery (black and grey, respectively). Data are shown as mean \pm SEM. * $p < 0.05$ versus before surgery. **B:** the decision surfaces of the signal-to-noise ratio (SNR) for both our classification models before and after surgery. The black circle represents the classification of the patient's video via the KNN (top) and SVM (bottom) models. The red area represents the prediction of unhealthy, whereas the green area a prediction of healthy. Modified from Lo Muzio and Rozzi et al[226].

Likewise, we assessed the cardiac kinematics in the other patient with an unfortunate clinical outcome (Figure 67 A). We observed an increasing trend which was opposite to our ToF population cardiac kinematics. As for the other patient, we inputted the Vi.Ki.E. coordinates in both SMLs to build the decision surfaces for the SNR feature (Figure 67 B). The before surgery video recordings were correctly classified in the unhealthy class by both trained models, but the after surgery ones were still classified in the unhealthy class instead of the healthy one.

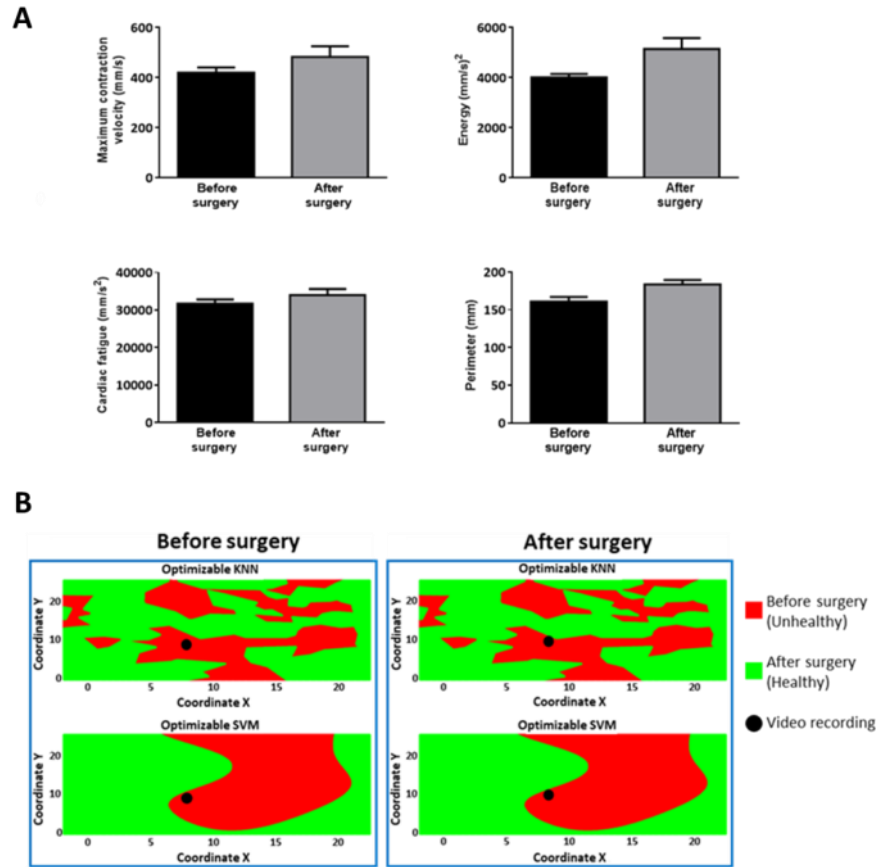


Figure 67. Vi.Ki.E. data and decision surfaces of a patient that underwent PVR who died two weeks after surgery. **A:** the average Maximum Contraction Velocity (top left), Energy (top right), Force (bottom left), and Perimeter (bottom right) calculated before- and after-surgery (black and grey, respectively). Data shown as mean \pm SEM. **B:** the decision surfaces of the signal-to-noise ratio (SNR) for both our classification models before and after surgery. The black circle represents the classification of the patient's video via the KNN (top) and SVM (bottom) models. The red area represents the prediction of unhealthy, whereas the green area a prediction of healthy. Modified from Lo Muzio and Rozzi et al[226].

In conclusion, we were able to develop two SMLs classifiers prompt to be used in the operating room in combination with our kinematic assessment to assist surgeons in decision making. The two classification models that showed the best performance for our data and medical aim were the KNN and SVM. Interestingly, both models are widely used in the clinical field. For instance, KNN has been employed for accurate delineation of the QRS complex[236] and to predict length of hospitalization stay after isolated coronary artery bypass grafting[237]. The SVM model has also been extensively used for the prediction of complications after cardiac surgery[238,239].

The prediction ability of our classifiers was tested in two additional patients not employed during the training process who had different clinical outcome. In one ToF patient who had a favorable clinical outcome (discharged after 7 days of hospitalization), both SML classifiers correctly predicted the before surgery video recordings in the unhealthy class, whereas the after surgery ones were recognized in the healthy one. Therefore, the patient was classified in line with his known prognosis.

The other patient, unfortunately, died two weeks after PVR for isolated congenital pulmonary valve regurgitation. Even in this case, both SML classifiers correctly predicted the patient outcome in line with his known prognosis. In fact, as the before surgery video recordings were recognized in the unhealthy class, the after surgery ones were still classified in the unhealthy one instead of the healthy and, thus, in line with his/her adverse prognosis. This clinical situation clearly showed that any additional tool which may aid in predicting postoperative recovery, including intraoperative imaging combined with AI elaboration, is potentially beneficial and deserved to be pursued.

Finally, an important strength of the AI-tools is that the models can be improved over time as new patients are followed up and included in the training dataset.

Work in progress: global excitation-contraction coupling with Vi.Ki.E.

This section presents the preliminary results obtained from one experiment performed to define the protocol for the measurement of the electromechanical delay with our imaging technique. Therefore, the results should be considered as a starting point for a future study.

Figure 68 shows the first result of the algorithm developed to calculate the electromechanical delay during ventricular pacing. The signal in blue is the ECG while the trace in red represents one Vi.Ki.E. coordinate. The different stars highlights the points of interest used to measure different parameters. In detail, the blue star is the electrical onset generated by the epicardial stimulation and is followed by a ventricular beat. The green star is the detected R-peak of the ECG. The two red stars represents the 5% and the 95%, respectively, of the upstroke of the Vi.Ki.E. signal which corresponds to the systole (in this experiment setup). The star at the beginning of the upstroke is the mechanical onset, while the one at the end of is the systolic peak.

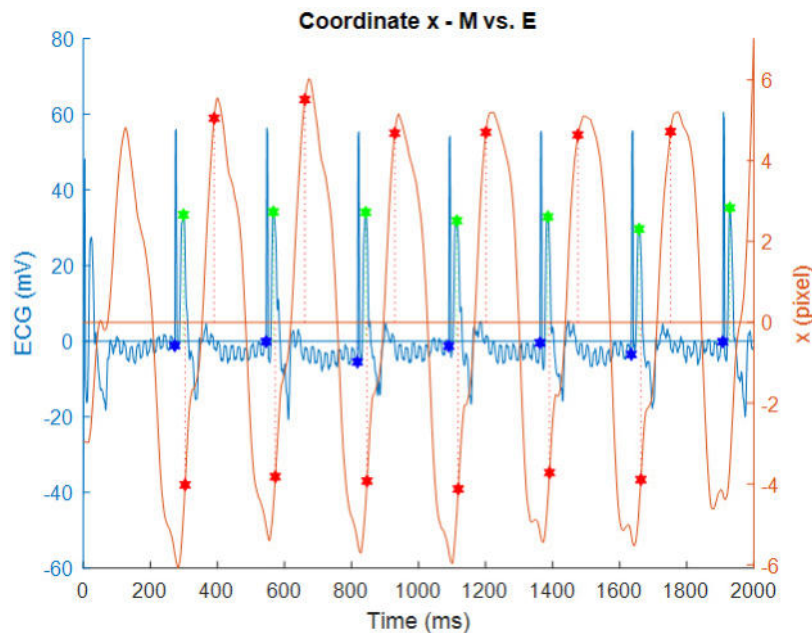


Figure 68. Representation of the points of interest (stars) extracted by the custom algorithm from the ECG signal (E) and one Vi.Ki.E. coordinate (M) during ventricular epicardial pacing. The blue star corresponds to the electrical onset (the epicardial ventricular stimulation). The two red stars represents the 5% and the 95%, respectively, of the upstroke of the mechanical signal

which corresponds to the systole. The star at the beginning of the upstroke is defined as the mechanical onset, while the one at the end is defined as the systolic peak.

Instead, in Figure 69 is portrayed the electromechanical delay measured with the same protocol but in sinus rhythm. In fact, it can be noted a train of seven subthreshold stimulations that are not followed by a ventricular beat. In this case, the electrical onset is defined as the beginning of the Q-wave on the ECG signal.

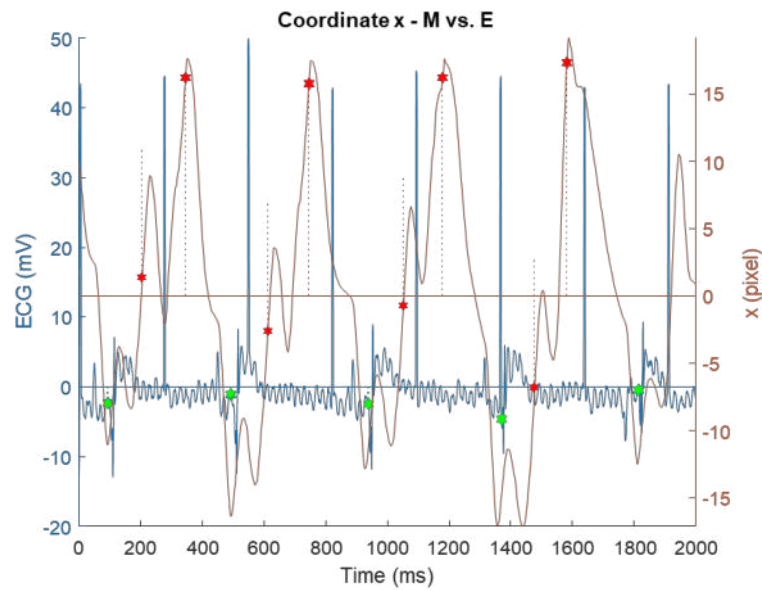


Figure 69. Superimposition of the ECG signal with the Vi.Ki.E. coordinate acquired in sinus rhythm. The green star corresponds to the beginning of the Q-wave on the ECG. The two red stars represents the mechanical onset, while the one at the end of the upstroke is defined as the systolic peak.

In Table 11 are reported the parameters that can be calculated with the points extracted from both ECG and Vi.Ki.E. signals (Figure 68 and 69) and their definition.

Parameter	Definition
QEMD	Q-Electromechanical delay: The time between the onset of the electrical activity and the respective onset of the mechanical function for one beat.
REMD	R-Electromechanical delay: The time elapsing the electrical onset and the systolic peak for one beat.
EQQ	Electrical Q-Q interval: Time difference between two consecutive electrical onsets.
MQQ	Mechanical Q-Q interval: Time difference between two consecutive mechanical onsets.
MRR	Mechanical R-R interval: Time difference between two consecutive systolic peaks.
MAT	Mechanical activation time: Time difference between the mechanical onset and its peak.

Table 11. The different time parameters that can be calculated with our custom algorithm from the simultaneous acquisition of both ECG and Vi.Ki.E. signals.

As already explained, these parameters are still object of discussion and might be implemented or modified in the future.

In conclusion, although the experiments and analyses are still ongoing, the preliminary results obtained in one Sprague-Dawley control rat showed that the ventricular electromechanical delay was 10ms. Compared to the results obtained by other groups with other approaches and animal model[150,154], a small value might be expected because the rat action potential is shorter than other species as they lack the L-type Ca^{2+} channel that will prolong the repolarization time. As it concerns the sinus rhythm protocol, the electromechanical delay was 25ms. Again, this value might be expected knowing that in non-resting condition the QRS duration is in the range of 12-22ms[240] and, thus, anesthesia can prolong this time.

Conclusions

The cardiac mechanical function plays a critical role in governing and regulating its performance under both normal and pathological conditions, respectively.

The left ventricle (LV) has been historically considered as the mainstay of normal hemodynamics for both congenital and acquired heart disease. Consequently, the right ventricle (RV) has been underappreciated and was often referred to as the “forgotten ventricle”. However, over the past few decades, there has been increasing recognition of its role in determining functional mechanical performance in multiple conditions and its importance is now unquestioned. Nonetheless, the ventricles are interdependent and share different anatomical features like the septum, the subepicardial layer, and are encircled with common myocardial fibers[241,242]. Therefore, changes in the filling of one ventricle may alter the mechanical function of its counterpart. This phenomenon, known as ventricular interdependence, remains even after the removal of the pericardium following constrictive pericarditis or during open chest surgery.

Interestingly, during open chest surgery, only the RV mechanical activity is qualitatively checked by the surgeon and cardiologist because of the absence of an intraoperative imaging technique able to evaluate its complex geometry. Moreover, most of the imaging techniques available in the clinical routine are well defined for the assessment of the LV, with its ejection fraction (LVEF) being the most used parameter. However, the latter is a measure of global systolic function which fails in identifying regional myocardial impairment and the mechanical contraction of the heart[180,181]. It is one of the main reasons why the clinicians are embracing strain imaging to better quantify myocardial LV deformation.

All the above observations lead to the conclusion that new approaches should be pursued to study the mechanics of both ventricles and correctly assess the cardiac mechanical performance.

In this thesis, I studied the LV mechanical function through different modalities of cardiac magnetic resonance (CMR) aiming to assess the feasibility of its use in a translational animal model (swine) and the degree of correlation with invasively measured hemodynamics. As it concerns the RV, its mechanical

function was investigated through an innovative imaging technique developed during my PhD, named Video Kinematic Evaluation (Vi.Ki.E.), in patients undergoing open chest surgery.

New perspectives on the left ventricle assessment

Among the different techniques available to clinicians for the assessment of the LV mechanics, a relatively novel method is the CMR feature tracking (CMR-FT). This technique focuses on endocardial and epicardial contouring and is able to detect the contrast between myocardium and blood pool[64,243]. CMR-FT has been widely tested and displayed an excellent inter- and intra-observer reproducibility of its parameters in humans[168-170]. Given the parameters the technique can offer, CMR is beginning to be more employed in animal research[179] where there is scarce literature on translational animal models, a lack of standardization and reproducibility studies. Therefore, we aimed to evaluate the inter- and intra-observer reproducibility of CMR-FT derived strain measurements in a highly translational porcine model of dobutamine-induced hyper-contractility (Dob) and verapamil-induced hypo-contractility (Ver).

Our results showed there was a good to excellent inter-observer reproducibility for global longitudinal strain (GLS) and global circumferential strain (GCS), whereas global radial strain (GRS) displayed to be highly variable between repeated measurements confirming its weak reproducibility reported in other studies[173-176]. Throughout this work, GLS also demonstrated to be the most reproducible parameter during the inter-observer analysis, while the intra-observer reproducibility was predictably higher for most of the strain values as it was found in other studies[165].

Having established the feasibility and degree of reproducibility of CMR-FT strain, we took a step forward by assessing to what extent these values reflect hemodynamic parameters such as cardiac power output (CPO), cardiac index (CI) and end-systolic elastance (Ees). Therefore, we performed an analysis on the degree of correlation between CMR-derived strain and invasively measured hemodynamics under different inotropic states in the same animal population of the previous work.

The linear regression analysis showed a moderate correlation of GLS and GCS with either CPO, CI or Ees while a poor one was observed for GRS. Indexing global strain parameters either for mean aortic pressure or for wall stress, as described by Rhea et al. and Reichek et al.[157,158], improved their correlations with either CPO, CI or Ees but GRS was still the worst performing.

Through this work, we could show a role of CMR LV strain as a surrogate of classic hemodynamic parameters such as CI, CPO, and a load-independent parameter of cardiac contractility such as Ees, which are established parameters to describe the hemodynamic and mechanical function of the heart[201]. Moreover, our results suggest that implementing strain measurements with pressure-derived variables may increase the accuracy in the evaluation of the heart mechanical function, making the case for the use of LV strain as a better representative of LV systolic function than LVEF.

Finally, among the recently explored parameters to quantify the LV function, there is the CMR derived myocardial efficiency which represents the ratio between the external mechanical power (EMP) required to maintain blood flow against systemic vascular resistance and the internal myocardial power (IMP) required by the LV to contract[192]. Changes in this mechanical proportion can be altered by several factors such as medical treatment[244] or surgical intervention[197]. The research interest in myocardial efficiency has recently increased as it was shown to be associated to myocardial performance and myocardial remodeling[194] in patients with cardiac diseases such as valvular heart disease[196,197], heart failure[198], and cardiomyopathy[245]. Furthermore, efficiency can be influenced by stress and ischemic hemodynamic conditions and, thus, its quantification holds the potential to provide insights into myocardial pathophysiology. Nonetheless, even in resting conditions, the quantification of myocardial efficiency has not been established as a clinical standard since it is traditionally based on invasive measurements. A novel CMR-based approach has been introduced to assess alterations in mechanical myocardial power and myocardial efficiency[159]. Therefore, we aimed to quantify myocardial power and efficiency in the same animal population of the previous works. Our results showed that EMP changed significantly after Dob and Ver, while we did not observe significant differences for IMP. The myocardial efficiency changed significantly from baseline to Ver, but only a

decreasing trend was observed between after Dob. We also assessed the degree of correlation between EMP, IMP or myocardial efficiency, and the invasively measured parameters of CPO and LVEF. We observed a good correlation between EMP and both CPO and LVEF. On the contrary, no correlation was observed between IMP and CPO or LVEF, while a moderate correlation was obtained between myocardial efficiency and both hemodynamic parameters.

To conclude, the above-described works on CMR emphasize the potential of these new approaches to quantify the LV mechanical function in both animal and clinical studies, particularly in those conditions where myocardial performance is altered because of compromised hemodynamic conditions.

Video Kinematic Evaluation of the right ventricle

Vi.Ki.E. is a video-based and contactless technique invented, customized, and tested through a collaboration between University of Pavia, University of Verona, and University of Parma. It consists in placing a camera above the exposed heart to acquire high temporal resolution videos from which extract cardiac kinematic parameters.

This technology is versatile as it may be applied for both basic and clinical researches and in conjunction with standard monitoring procedures without interfering with open-chest cardiac surgery. In fact, Vi.Ki.E. showed promising results in patients undergoing surgical myocardial revascularization, whose RV is poorly explored by conventional transoesophageal echocardiography, and in the rat ischaemic/reperfused heart model[88]. Given that the RV is the only visible structure at the open chest, our technique could be an important tool in those pathologies where the RV function is compromised. Therefore, we decided to study Tetralogy of Fallot (ToF) which is one of the most common congenital heart defects. The choice to study the ToF pathology was driven by the unique condition offered by patients with long-standing RV volume overload due to chronic pulmonary regurgitation. Following pulmonary valve replacement (PVR), they immediately have cessation of any RV volume overload. There are no similar clinical conditions, amenable to surgical management, where chronic RV pressure overload (pulmonary hypertension)

can effectively be abolished by a simple surgical procedure and, thus, it represents a good clinical model to be investigated through our imaging technique.

In our pilot study on ToF^[89] we aimed to assess the safety and efficacy of our kinematic technique to capture prompt improvement of the right ventricular mechanical function after surgery. The results of the study demonstrate that in patients with previously operated ToF, RV preload reduction by PVR allows: (i) decrease of the cardiac fatigue by 12%; (ii) decrease of energy expended by 45%; and (iii) decrease of maximum contraction velocity and displacement because of less RV epicardial movement. One plausible and expected mechanism that could explain this trend is related to the Frank–Starling law: a decrease in RV preload generates a decrease in myocardium stretch (less tension development) and, consequently, a decrease in actin–myosin crossbridge activity leading to less cardiac force and kinetic energy^[212].

The study has provided evidence that PVR may afford immediate recovery of RV mechanical function in teenagers and young adults late after ToF repair. Moreover, our results suggest a correlation between RV volumes at CMR and the Vi.Ki.E. parameters of contraction force (an index of cardiac fatigue) and energy in patients with preoperative RV end-diastolic volume (RVEDV) lower than current “proactive” (ca. 115 vs 152 ml/m²) recommendations for surgery.

We then extended this study by enrolling six more ToF patients aiming to assess if our technique could offer prognostic insight into the timing of PVR. Our entire patient population showed prompt improvement in all kinematic parameters after PVR with a significant decrease in maximum contraction velocity, cardiac fatigue, energy consumption and, indirectly, increase in ventricular compliance. Interestingly, we assessed the degree of correlation between before surgery Vi.Ki.E. parameters and preoperative RVEDV_i and observed a moderate-to-good correlation with an exponential trend, confirming the finding of the previous study. The latter was expected because long-standing RV volume overload due to pulmonary regurgitation is directly correlated with preoperative RV dysfunction and, thus, adult patients have higher values of both RVEDV_i and Vi.Ki.E. parameters.

This observation led us to investigate if there were any differences between the two groups in respect to the impact of the surgery. The adult patients, presenting with RVEDVi greater than 147 ml/m², had a distinct behavior compared with those with lower RV volume overload. In fact, recovery of baseline kinematic functional parameters was not always complete and was less predictable. Therefore, we inferred that recovery of the RV directly depends on the timing of PVR, possibly suggesting performing PVR at a lower RVEDVi value and at a younger age.

The results obtained in the clinical setting showed that Vi.Ki.E. could be an useful intraoperative technique able to provide useful observations regarding the acute recovery of the RV mechanical function of ToF patients after PVR. However, due to the lack of correlation with other imaging techniques, it does not provide an insight on the patients' outcome, leaving both researchers and clinicians to speculate on its results.

Therefore, we developed two supervised machine learning (SML) models based on the heart movement acquired with our imaging technique to predict the ToF patient's outcome after PVR. We opted for SML due to its capability to consider not only the data but also the patient's documented clinical outcome, reducing the classification error and providing more clinically relevant results.

We tested different machine learning algorithms in terms of classification accuracy and the two best models were the support vector machine (SVM) and the *k*-nearest neighbors (KNN). Thus, we trained and optimized these two algorithms via 10-fold cross validation and obtained a true positive rate above 95% and a false negative rate below 5% for both classifiers.

Then, we tested the prediction ability of our SMLs in two additional patients never considered before and having different clinical outcomes: one patient had a favorable hospital course (discharged after 7 days of hospitalizations) while the other died two weeks after surgery in the intensive care unit.

The Vi.Ki.E. assessment of the patient with a favorable outcome showed a decreasing trend for all kinematic parameters, which was in line with our previous studies on RV unloading, and both classification models correctly predicted the patient positive outcome. However, the same did not occurred for the patient who had an unfortunate hospital course. In fact, the Vi.Ki.E. assessment showed an opposite trend compared to our ToF population, denoting

a still fatigued heart, and both classifiers highlighted the still complex clinical condition predicting an adverse outcome.

This single-center pilot study further demonstrated that any additional tool which may aid in predicting postoperative recovery, including a novel intraoperative technology integrated with AI elaboration, is potentially applicable and beneficial.

Finally, in professor Michele Miragoli's lab, we are going to apply the Vi.Ki.E. technique to study in vivo the excitation contraction coupling by simultaneously acquiring both mechanical and electrical signals of the heart through the experimental setup I described in this thesis. The preliminary results obtained in one control rat were promising showing the feasibility of our approach to measure the electromechanical delay (EMD), defined as the time elapsing from the electrical onset to the mechanical one, during both ventricular pacing and sinus rhythm. Although different groups have proposed their own methods for the evaluation of the EMD, there is still uncertainty as to its range of values in both physiological and pathological conditions. Therefore, our research will improve the knowledge on the in vivo cardiac electromechanical behavior. This study might be clinically relevant as our approach could be adopted in the detection of dyssynchronous ventricles supporting the cardiac electrophysiologist before the implantation of the pacemakers for resynchronization therapy.

References

1. Kutzt-Buschbeck, J.P.; Drake-Holland, A.; Noble, M.I.M.; Lohff, B.; Schaefer, J. Rediscovery of Otto Frank's contribution to science. *Journal of molecular and cellular cardiology* **2018**, *119*, 96-103, doi:10.1016/j.yjmcc.2018.04.017.
2. Suga, H. Ventricular energetics. *Physiological reviews* **1990**, *70*, 247-277, doi:10.1152/physrev.1990.70.2.247.
3. Baan, J.; van der Velde, E.T.; Steendijk, P. Ventricular pressure-volume relations in vivo. *European heart journal* **1992**, *13 Suppl E*, 2-6, doi:10.1093/eurheartj/13.suppl_e.2.
4. Burkhoff, D.; Mirsky, I.; Suga, H. Assessment of systolic and diastolic ventricular properties via pressure-volume analysis: a guide for clinical, translational, and basic researchers. *American journal of physiology. Heart and circulatory physiology* **2005**, *289*, H501-512, doi:10.1152/ajpheart.00138.2005.
5. Schreuder, J.J.; Castiglioni, A.; Maisano, F.; Steendijk, P.; Donelli, A.; Baan, J.; Alfieri, O. Acute decrease of left ventricular mechanical dyssynchrony and improvement of contractile state and energy efficiency after left ventricular restoration. *The Journal of thoracic and cardiovascular surgery* **2005**, *129*, 138-145, doi:10.1016/j.jtcvs.2004.03.057.
6. Burkhoff, D.; Sayer, G.; Doshi, D.; Uriel, N. Hemodynamics of Mechanical Circulatory Support. *Journal of the American College of Cardiology* **2015**, *66*, 2663-2674, doi:10.1016/j.jacc.2015.10.017.
7. Little, W.C. Diastolic dysfunction beyond distensibility: adverse effects of ventricular dilatation. *Circulation* **2005**, *112*, 2888-2890, doi:10.1161/CIRCULATIONAHA.105.578161.
8. Westermann, D.; Kasner, M.; Steendijk, P.; Spillmann, F.; Riad, A.; Weitmann, K.; Hoffmann, W.; Poller, W.; Pauschinger, M.; Schultheiss, H.P.; et al. Role of left ventricular stiffness in heart failure with normal ejection fraction. *Circulation* **2008**, *117*, 2051-2060, doi:10.1161/CIRCULATIONAHA.107.716886.
9. Bastos, M.B.; Burkhoff, D.; Maly, J.; Daemen, J.; den Uil, C.A.; Ameloot, K.; Lenzen, M.; Mahfoud, F.; Zijlstra, F.; Schreuder, J.J.; et al. Invasive left ventricle pressure-volume analysis: overview and practical clinical implications. *European heart journal* **2020**, *41*, 1286-1297, doi:10.1093/eurheartj/ehz552.
10. Burkhoff, D.; van der Velde, E.; Kass, D.; Baan, J.; Maughan, W.L.; Sagawa, K. Accuracy of volume measurement by conductance catheter in isolated, ejecting canine hearts. *Circulation* **1985**, *72*, 440-447, doi:10.1161/01.cir.72.2.440.
11. Klotz, S.; Dickstein, M.L.; Burkhoff, D. A computational method of prediction of the end-diastolic pressure-volume relationship by single beat. *Nature protocols* **2007**, *2*, 2152-2158, doi:10.1038/nprot.2007.270.
12. Chambers, D.; Huang, C.; Matthews, G. Basic Physiology for Anaesthetists. *Basic Physiology for Anaesthetists* **2015**, 1-447, doi:10.1017/Cbo9781139226394.
13. Haddad, F.; Doyle, R.; Murphy, D.J.; Hunt, S.A. Right ventricular function in cardiovascular disease, part II: pathophysiology, clinical importance, and management of right ventricular failure. *Circulation* **2008**, *117*, 1717-1731, doi:10.1161/CIRCULATIONAHA.107.653584.

14. van Wolferen, S.A.; van de Veerdonk, M.C.; Mauritz, G.J.; Jacobs, W.; Marcus, J.T.; Marques, K.M.J.; Bronzwaer, J.G.F.; Heymans, M.W.; Boonstra, A.; Postmus, P.E.; et al. Clinically significant change in stroke volume in pulmonary hypertension. *Chest* **2011**, *139*, 1003-1009, doi:10.1378/chest.10-1066.
15. van de Veerdonk, M.C.; Kind, T.; Marcus, J.T.; Mauritz, G.J.; Heymans, M.W.; Bogaard, H.J.; Boonstra, A.; Marques, K.M.; Westerhof, N.; Vonk-Noordegraaf, A. Progressive right ventricular dysfunction in patients with pulmonary arterial hypertension responding to therapy. *Journal of the American College of Cardiology* **2011**, *58*, 2511-2519, doi:10.1016/j.jacc.2011.06.068.
16. Kind, T.; Marcus, J.T.; Westerhof, N.; Vonk-Noordegraaf, A. Longitudinal and transverse movements of the right ventricle: both are important in pulmonary arterial hypertension. *Chest* **2011**, *140*, 556-557, doi:10.1378/chest.10-3195.
17. Mauritz, G.J.; Kind, T.; Marcus, J.T.; Bogaard, H.J.; van de Veerdonk, M.; Postmus, P.E.; Boonstra, A.; Westerhof, N.; Vonk-Noordegraaf, A. Progressive changes in right ventricular geometric shortening and long-term survival in pulmonary arterial hypertension. *Chest* **2012**, *141*, 935-943, doi:10.1378/chest.10-3277.
18. Marcus, J.T.; Mauritz, G.J.; Kind, T.; Vonk-Noordegraaf, A. Interventricular mechanical dyssynchrony in pulmonary arterial hypertension: early or delayed strain in the right ventricular free wall? *The American journal of cardiology* **2009**, *103*, 894-895, doi:10.1016/j.amjcard.2009.01.002.
19. Westerhof, N.; Stergiopoulos, N.; Noble, M.I.M. *Snapshots of hemodynamics : an aid for clinical research and graduate education*, 2nd ed.; Springer Verlag: New York, 2010; pp. xi, 271 p.
20. Vonk-Noordegraaf, A.; Westerhof, N. Describing right ventricular function. *The European respiratory journal* **2013**, *41*, 1419-1423, doi:10.1183/09031936.00160712.
21. Brimiouille, S.; Wauthy, P.; Ewalenko, P.; Rondelet, B.; Vermeulen, F.; Kerbaul, F.; Naeije, R. Single-beat estimation of right ventricular end-systolic pressure-volume relationship. *American journal of physiology. Heart and circulatory physiology* **2003**, *284*, H1625-1630, doi:10.1152/ajpheart.01023.2002.
22. Trip, P.; Kind, T.; van de Veerdonk, M.C.; Marcus, J.T.; de Man, F.S.; Westerhof, N.; Vonk-Noordegraaf, A. Accurate assessment of load-independent right ventricular systolic function in patients with pulmonary hypertension. *The Journal of heart and lung transplantation : the official publication of the International Society for Heart Transplantation* **2013**, *32*, 50-55, doi:10.1016/j.healun.2012.09.022.
23. Schulz-Menger, J.; Bluemke, D.A.; Bremerich, J.; Flamm, S.D.; Fogel, M.A.; Friedrich, M.G.; Kim, R.J.; von Knobelsdorff-Brenkenhoff, F.; Kramer, C.M.; Pennell, D.J.; et al. Standardized image interpretation and post-processing in cardiovascular magnetic resonance - 2020 update : Society for Cardiovascular Magnetic Resonance (SCMR): Board of Trustees Task Force on Standardized Post-Processing. *Journal of cardiovascular magnetic resonance : official journal of the Society for Cardiovascular Magnetic Resonance* **2020**, *22*, 19, doi:10.1186/s12968-020-00610-6.
24. Lang, R.M.; Badano, L.P.; Mor-Avi, V.; Afilalo, J.; Armstrong, A.; Ernande, L.; Flachskampf, F.A.; Foster, E.; Goldstein, S.A.; Kuznetsova, T.; et al. Recommendations for cardiac chamber quantification by echocardiography in adults: an update from the American Society of Echocardiography and the

- European Association of Cardiovascular Imaging. *European heart journal. Cardiovascular Imaging* **2015**, *16*, 233-270, doi:10.1093/ehjci/jev014.
25. Mohamed, A.A.; Arifi, A.A.; Omran, A. The basics of echocardiography. *Journal of the Saudi Heart Association* **2010**, *22*, 71-76, doi:10.1016/j.jsha.2010.02.011.
 26. Daly, C.A.; Abbasi, S.; Kwong, R.Y. Cardiac Imaging. *Pathobiology of Human Disease: A Dynamic Encyclopedia of Disease Mechanisms* **2014**, 4019-4045, doi:10.1016/B978-0-12-386456-7.07611-5.
 27. Ashley, E.A.; Niebauer, J. In *Cardiology Explained*; London, 2004.
 28. Oqlat, A.A.; Matjafri, M.Z.; Suardi, N.; Oqlat, M.A.; Abdelrahman, M.A.; Oqlat, A.A. A Review of Medical Doppler Ultrasonography of Blood Flow in General and Especially in Common Carotid Artery. *Journal of medical ultrasound* **2018**, *26*, 3-13, doi:10.4103/JMU.JMU_11_17.
 29. Ho, C.Y.; Solomon, S.D. A clinician's guide to tissue Doppler imaging. *Circulation* **2006**, *113*, e396-398, doi:10.1161/CIRCULATIONAHA.105.579268.
 30. Isaz, K.; Thompson, A.; Ethevenot, G.; Cloez, J.L.; Brembilla, B.; Pernot, C. Doppler echocardiographic measurement of low velocity motion of the left ventricular posterior wall. *The American journal of cardiology* **1989**, *64*, 66-75, doi:10.1016/0002-9149(89)90655-3.
 31. Abraham, T.P.; Dimaano, V.L.; Liang, H.Y. Role of tissue Doppler and strain echocardiography in current clinical practice. *Circulation* **2007**, *116*, 2597-2609, doi:10.1161/CIRCULATIONAHA.106.647172.
 32. Kadappu, K.K.; Thomas, L. Tissue Doppler Imaging in Echocardiography: Value and Limitations. *Heart Lung Circ* **2015**, *24*, 224-233, doi:10.1016/j.hlc.2014.10.003.
 33. Nikitin, N.P.; Loh, P.H.; Silva, R.; Ghosh, J.; Khaleva, O.Y.; Goode, K.; Rigby, A.S.; Alamgir, F.; Clark, A.L.; Cleland, J.G. Prognostic value of systolic mitral annular velocity measured with Doppler tissue imaging in patients with chronic heart failure caused by left ventricular systolic dysfunction. *Heart* **2006**, *92*, 775-779, doi:10.1136/hrt.2005.067140.
 34. Wang, M.; Yip, G.; Yu, C.M.; Zhang, Q.; Zhang, Y.; Tse, D.; Kong, S.L.; Sanderson, J.E. Independent and incremental prognostic value of early mitral annulus velocity in patients with impaired left ventricular systolic function. *Journal of the American College of Cardiology* **2005**, *45*, 272-277, doi:10.1016/j.jacc.2004.09.059.
 35. Nagueh, S.F.; Appleton, C.P.; Gillebert, T.C.; Marino, P.N.; Oh, J.K.; Smiseth, O.A.; Waggoner, A.D.; Flachskampf, F.A.; Pellikka, P.A.; Evangelisa, A. Recommendations for the evaluation of left ventricular diastolic function by echocardiography. *European journal of echocardiography : the journal of the Working Group on Echocardiography of the European Society of Cardiology* **2009**, *10*, 165-193, doi:10.1093/ejechocard/jep007.
 36. Garcia, M.J.; Thomas, J.D.; Klein, A.L. New Doppler echocardiographic applications for the study of diastolic function. *Journal of the American College of Cardiology* **1998**, *32*, 865-875, doi:10.1016/s0735-1097(98)00345-3.
 37. Bax, J.J.; Abraham, T.; Barold, S.S.; Breithardt, O.A.; Fung, J.W.; Garrigue, S.; Gorcsan, J., 3rd; Hayes, D.L.; Kass, D.A.; Knuuti, J.; et al. Cardiac resynchronization therapy: Part 1--issues before device implantation. *Journal of the American College of Cardiology* **2005**, *46*, 2153-2167, doi:10.1016/j.jacc.2005.09.019.

38. Meluzin, J.; Spinarova, L.; Bakala, J.; Toman, J.; Krejci, J.; Hude, P.; Kara, T.; Soucek, M. Pulsed Doppler tissue imaging of the velocity of tricuspid annular systolic motion; a new, rapid, and non-invasive method of evaluating right ventricular systolic function. *European heart journal* **2001**, *22*, 340-348, doi:10.1053/euhj.2000.2296.
39. Yamamoto, T.; Oki, T.; Yamada, H.; Tanaka, H.; Ishimoto, T.; Wakatsuki, T.; Tabata, T.; Ito, S. Prognostic value of the atrial systolic mitral annular motion velocity in patients with left ventricular systolic dysfunction. *Journal of the American Society of Echocardiography : official publication of the American Society of Echocardiography* **2003**, *16*, 333-339, doi:10.1016/s0894-7317(02)74537-9.
40. Voigt, J.U.; Nixdorff, U.; Bogdan, R.; Exner, B.; Schmiedehausen, K.; Platsch, G.; Kuwert, T.; Daniel, W.G.; Flachskampf, F.A. Comparison of deformation imaging and velocity imaging for detecting regional inducible ischaemia during dobutamine stress echocardiography. *European heart journal* **2004**, *25*, 1517-1525, doi:10.1016/j.ehj.2004.05.014.
41. Heimdal, A.; Stoylen, A.; Torp, H.; Skjaerpe, T. Real-time strain rate imaging of the left ventricle by ultrasound. *Journal of the American Society of Echocardiography : official publication of the American Society of Echocardiography* **1998**, *11*, 1013-1019, doi:10.1016/s0894-7317(98)70151-8.
42. Lindqvist, P.; Waldenstrom, A.; Henein, M.; Morner, S.; Kazzam, E. Regional and global right ventricular function in healthy individuals aged 20-90 years: a pulsed Doppler tissue imaging study: Umea General Population Heart Study. *Echocardiography* **2005**, *22*, 305-314, doi:10.1111/j.1540-8175.2005.04023.x.
43. Vegas, A. *Perioperative two-dimensional transesophageal echocardiography : a practical handbook*; pp. xv, 235 pages.
44. Shanewise, J.S.; Cheung, A.T.; Aronson, S.; Stewart, W.J.; Weiss, R.L.; Mark, J.B.; Savage, R.M.; Sears-Rogan, P.; Mathew, J.P.; Quinones, M.A.; et al. ASE/SCA guidelines for performing a comprehensive intraoperative multiplane transesophageal echocardiography examination: recommendations of the American Society of Echocardiography Council for Intraoperative Echocardiography and the Society of Cardiovascular Anesthesiologists Task Force for Certification in Perioperative Transesophageal Echocardiography. *Journal of the American Society of Echocardiography : official publication of the American Society of Echocardiography* **1999**, *12*, 884-900, doi:10.1016/s0894-7317(99)70199-9.
45. Hahn, R.T.; Abraham, T.; Adams, M.S.; Bruce, C.J.; Glas, K.E.; Lang, R.M.; Reeves, S.T.; Shanewise, J.S.; Siu, S.C.; Stewart, W.; et al. Guidelines for performing a comprehensive transesophageal echocardiographic examination: recommendations from the American Society of Echocardiography and the Society of Cardiovascular Anesthesiologists. *Anesthesia and analgesia* **2014**, *118*, 21-68, doi:10.1213/ANE.0000000000000016.
46. Mahmood, F.; Shernan, S.K. Perioperative transoesophageal echocardiography: current status and future directions. *Heart* **2016**, *102*, 1159-1167, doi:10.1136/heartjnl-2015-307962.
47. Levine, R.A.; Gibson, T.C.; Aretz, T.; Gillam, L.D.; Guyer, D.E.; King, M.E.; Weyman, A.E. Echocardiographic measurement of right ventricular volume. *Circulation* **1984**, *69*, 497-505, doi:10.1161/01.cir.69.3.497.

48. Silverton, N.A.; Patel, R.; Zimmerman, J.; Ma, J.; Stoddard, G.; Selzman, C.H.; Morrissey, C.K. Intraoperative Transesophageal Echocardiography and Right Ventricular Failure After Left Ventricular Assist Device Implantation. *Journal of cardiothoracic and vascular anesthesia* **2018**, *32*, 2096-2103, doi:10.1053/j.jvca.2018.02.023.
49. Mayo, P.H.; Narasimhan, M.; Koenig, S. Critical Care Transesophageal Echocardiography. *Chest* **2015**, *148*, 1323-1332, doi:10.1378/chest.15-0260.
50. Lee, W.W. Recent Advances in Nuclear Cardiology. *Nuclear medicine and molecular imaging* **2016**, *50*, 196-206, doi:10.1007/s13139-016-0433-x.
51. Sabharwal, N.K. State of the art in nuclear cardiology. *Heart* **2017**, *103*, 790-799, doi:10.1136/heartjnl-2015-308670.
52. Henzlova, M.J.; Duvall, W.L.; Einstein, A.J.; Travin, M.I.; Verberne, H.J. ASNC imaging guidelines for SPECT nuclear cardiology procedures: Stress, protocols, and tracers. *Journal of nuclear cardiology : official publication of the American Society of Nuclear Cardiology* **2016**, *23*, 606-639, doi:10.1007/s12350-015-0387-x.
53. Schroeder, S.; Achenbach, S.; Bengel, F.; Burgstahler, C.; Cademartiri, F.; de Feyter, P.; George, R.; Kaufmann, P.; Kopp, A.F.; Knuuti, J.; et al. Cardiac computed tomography: indications, applications, limitations, and training requirements: report of a Writing Group deployed by the Working Group Nuclear Cardiology and Cardiac CT of the European Society of Cardiology and the European Council of Nuclear Cardiology. *European heart journal* **2008**, *29*, 531-556, doi:10.1093/eurheartj/ehm544.
54. McKavanagh, P.; Walls, G.; McCune, C.; Malloy, J.; Harbinson, M.T.; Ball, P.A.; Donnelly, P.M. The Essentials of Cardiac Computerized Tomography. *Cardiology and therapy* **2015**, *4*, 117-129, doi:10.1007/s40119-015-0052-0.
55. Tseng, W.Y.; Su, M.Y.; Tseng, Y.H. Introduction to Cardiovascular Magnetic Resonance: Technical Principles and Clinical Applications. *Acta Cardiologica Sinica* **2016**, *32*, 129-144, doi:10.6515/acs20150616a.
56. Saeed, M.; Van, T.A.; Krug, R.; Hetts, S.W.; Wilson, M.W. Cardiac MR imaging: current status and future direction. *Cardiovascular diagnosis and therapy* **2015**, *5*, 290-310, doi:10.3978/j.issn.2223-3652.2015.06.07.
57. Messroghli, D.R.; Radjenovic, A.; Kozerke, S.; Higgins, D.M.; Sivanathan, M.U.; Ridgway, J.P. Modified Look-Locker inversion recovery (MOLLI) for high-resolution T-1 mapping of the heart. *Magn Reson Med* **2004**, *52*, 141-146, doi:10.1002/mrm.20110.
58. Wacker, C.M.; Bock, M.; Hartlep, A.W.; Beck, G.; van Kaick, G.; Ertl, G.; Bauer, W.R.; Schad, L.R. Changes in myocardial oxygenation and perfusion under pharmacological stress with dipyridamole: assessment using T*2 and T1 measurements. *Magn Reson Med* **1999**, *41*, 686-695, doi:10.1002/(sici)1522-2594(199904)41:4<686::aid-mrm6>3.0.co;2-9.
59. Wacker, C.M.; Fidler, F.; Dueren, C.; Hirn, S.; Jakob, P.M.; Ertl, G.; Haase, A.; Bauer, W.R. Quantitative assessment of myocardial perfusion with a spin-labeling technique: preliminary results in patients with coronary artery disease. *Journal of magnetic resonance imaging : JMRI* **2003**, *18*, 555-560, doi:10.1002/jmri.10386.
60. Waldman, L.K.; Fung, Y.C.; Covell, J.W. Transmural myocardial deformation in the canine left ventricle. Normal in vivo three-dimensional finite strains. *Circulation research* **1985**, *57*, 152-163, doi:10.1161/01.res.57.1.152.
61. Mada, R.O.; Lysyansky, P.; Daraban, A.M.; Duchenne, J.; Voigt, J.U. How to define end-diastole and end-systole?: Impact of timing on strain

- measurements. *JACC. Cardiovascular imaging* **2015**, *8*, 148-157, doi:10.1016/j.jcmg.2014.10.010.
62. Jasaityte, R.; Heyde, B.; D'Hooge, J. Current state of three-dimensional myocardial strain estimation using echocardiography. *Journal of the American Society of Echocardiography : official publication of the American Society of Echocardiography* **2013**, *26*, 15-28, doi:10.1016/j.echo.2012.10.005.
 63. Amzulescu, M.S.; De Craene, M.; Langet, H.; Pasquet, A.; Vancraeynest, D.; Pouleur, A.C.; Vanoverschelde, J.L.; Gerber, B.L. Myocardial strain imaging: review of general principles, validation, and sources of discrepancies. *European heart journal. Cardiovascular Imaging* **2019**, *20*, 605-619, doi:10.1093/ehjci/jez041.
 64. Pedrizzetti, G.; Claus, P.; Kilner, P.J.; Nagel, E. Principles of cardiovascular magnetic resonance feature tracking and echocardiographic speckle tracking for informed clinical use. *Journal of cardiovascular magnetic resonance : official journal of the Society for Cardiovascular Magnetic Resonance* **2016**, *18*, 51, doi:10.1186/s12968-016-0269-7.
 65. Bijmens, B.H.; Cikes, M.; Claus, P.; Sutherland, G.R. Velocity and deformation imaging for the assessment of myocardial dysfunction. *European journal of echocardiography : the journal of the Working Group on Echocardiography of the European Society of Cardiology* **2009**, *10*, 216-226, doi:10.1093/ejehocardi/jen323.
 66. Langeland, S.; Wouters, P.F.; Claus, P.; Leather, H.A.; Bijmens, B.; Sutherland, G.R.; Rademakers, F.E.; D'Hooge, J. Experimental assessment of a new research tool for the estimation of two-dimensional myocardial strain. *Ultrasound in medicine & biology* **2006**, *32*, 1509-1513, doi:10.1016/j.ultrasmedbio.2006.06.021.
 67. Geyer, H.; Caracciolo, G.; Abe, H.; Wilansky, S.; Carerj, S.; Gentile, F.; Nesser, H.J.; Khandheria, B.; Narula, J.; Sengupta, P.P. Assessment of Myocardial Mechanics Using Speckle Tracking Echocardiography: Fundamentals and Clinical Applications. *J Am Soc Echocardiogr* **2010**, *23*, 351-369, doi:10.1016/j.echo.2010.02.015.
 68. Amundsen, B.H.; Helle-Valle, T.; Edvardsen, T.; Torp, H.; Crosby, J.; Lyseggen, E.; Stoylen, A.; Ihlen, H.; Lima, J.A.; Smiseth, O.A.; et al. Noninvasive myocardial strain measurement by speckle tracking echocardiography: validation against sonomicrometry and tagged magnetic resonance imaging. *Journal of the American College of Cardiology* **2006**, *47*, 789-793, doi:10.1016/j.jacc.2005.10.040.
 69. Urheim, S.; Edvardsen, T.; Torp, H.; Angelsen, B.; Smiseth, O.A. Myocardial strain by Doppler echocardiography. Validation of a new method to quantify regional myocardial function. *Circulation* **2000**, *102*, 1158-1164, doi:10.1161/01.cir.102.10.1158.
 70. Kumada, T.; Karliner, J.S.; Pouleur, H.; Gallagher, K.P.; Shirato, K.; Ross, J., Jr. Effects of coronary occlusion on early ventricular diastolic events in conscious dogs. *The American journal of physiology* **1979**, *237*, H542-549, doi:10.1152/ajpheart.1979.237.5.H542.
 71. Becker, M.; Hoffmann, R.; Kuhl, H.P.; Grawe, H.; Katoh, M.; Kramann, R.; Bucker, A.; Hanrath, P.; Heussen, N. Analysis of myocardial deformation based on ultrasonic pixel tracking to determine transmural strain in chronic myocardial infarction. *European heart journal* **2006**, *27*, 2560-2566, doi:10.1093/eurheartj/ehl288.

72. Kalam, K.; Otahal, P.; Marwick, T.H. Prognostic implications of global LV dysfunction: a systematic review and meta-analysis of global longitudinal strain and ejection fraction. *Heart* **2014**, *100*, 1673-1680, doi:10.1136/heartjnl-2014-305538.
73. Roes, S.D.; Mollema, S.A.; Lamb, H.J.; van der Wall, E.E.; de Roos, A.; Bax, J.J. Validation of echocardiographic two-dimensional speckle tracking longitudinal strain imaging for viability assessment in patients with chronic ischemic left ventricular dysfunction and comparison with contrast-enhanced magnetic resonance imaging. *The American journal of cardiology* **2009**, *104*, 312-317, doi:10.1016/j.amjcard.2009.03.040.
74. Afonso, L.; Kondur, A.; Simegn, M.; Niraj, A.; Hari, P.; Kaur, R.; Ramappa, P.; Pradhan, J.; Bhandare, D.; Williams, K.A.; et al. Two-dimensional strain profiles in patients with physiological and pathological hypertrophy and preserved left ventricular systolic function: a comparative analyses. *BMJ open* **2012**, *2*, doi:10.1136/bmjopen-2012-001390.
75. Authors/Task Force, m.; Elliott, P.M.; Anastasakis, A.; Borger, M.A.; Borggrefe, M.; Cecchi, F.; Charron, P.; Hagege, A.A.; Lafont, A.; Limongelli, G.; et al. 2014 ESC Guidelines on diagnosis and management of hypertrophic cardiomyopathy: the Task Force for the Diagnosis and Management of Hypertrophic Cardiomyopathy of the European Society of Cardiology (ESC). *European heart journal* **2014**, *35*, 2733-2779, doi:10.1093/eurheartj/ehu284.
76. Arfken, G.B. *University physics*; Academic Press: Orlando, 1984; pp. xii, 905 p.
77. Meier, G.D.; Ziskin, M.C.; Santamore, W.P.; Bove, A.A. Kinematics of the beating heart. *IEEE transactions on bio-medical engineering* **1980**, *27*, 319-329, doi:10.1109/TBME.1980.326740.
78. McCulloch, A.D.; Smaill, B.H.; Hunter, P.J. Regional left ventricular epicardial deformation in the passive dog heart. *Circulation research* **1989**, *64*, 721-733, doi:10.1161/01.res.64.4.721.
79. La Gerche, A.; Robberecht, C.; Kuiperi, C.; Nuyens, D.; Willems, R.; de Ravel, T.; Matthijs, G.; Heidbuchel, H. Lower than expected desmosomal gene mutation prevalence in endurance athletes with complex ventricular arrhythmias of right ventricular origin. *Heart* **2010**, *96*, 1268-1274, doi:10.1136/hrt.2009.189621.
80. Teske, A.J.; Cox, M.G.; De Boeck, B.W.; Doevendans, P.A.; Hauer, R.N.; Cramer, M.J. Echocardiographic tissue deformation imaging to quantify regional right ventricular function in arrhythmogenic right ventricular dysplasia/cardiomyopathy. *European heart journal* **2008**, *29*, 796-796.
81. Soltani, A.; Lahti, J.; Jarvela, K.; Curtze, S.; Laurikka, J.; Hokka, M.; Kuokkala, V.T. An Optical Method for the In-Vivo Characterization of the Biomechanical Response of the Right Ventricle. *Scientific reports* **2018**, *8*, doi:Artn 6831
10.1038/S41598-018-25223-Z.
82. Palanca, M.; Brugo, T.M.; Cristofolini, L. Use of Digital Image Correlation to Investigate the Biomechanics of the Vertebra. *J Mech Med Biol* **2015**, *15*, doi:Unsp 1540004
10.1142/S0219519415400047.
83. Hokka, M.; Mirow, N.; Nagel, H.; Vogt, S.; Kuokkala, V.T. DIC Measurements of the Human Heart During Cardiopulmonary Bypass Surgery. *C Proc Soc Exp Mech* **2016**, 51-59, doi:10.1007/978-3-319-21455-9_6.

84. Lionello, G.; Cristofolini, L. A practical approach to optimizing the preparation of speckle patterns for digital-image correlation. *Meas Sci Technol* **2014**, *25*, doi:Artn 107001
10.1088/0957-0233/25/10/107001.
85. Barrangera, Y.; Doumalin, P.; Dupre, J.C.; Germaneau, A. Digital Image Correlation accuracy: influence of kind of speckle and recording setup. *Epj Web Conf* **2010**, *6*, doi:Artn 31002
10.1051/Epjconf/20100631002.
86. Hijazi, A.; Kahler, C.J. Contribution of the Imaging System Components in the Overall Error of the Two-Dimensional Digital Image Correlation Technique. *J Test Eval* **2017**, *45*, 369-384, doi:10.1520/Jte20150437.
87. Haddadi, H.; Belhabib, S. Use of rigid-body motion for the investigation and estimation of the measurement errors related to digital image correlation technique. *Opt Laser Eng* **2008**, *46*, 185-196, doi:10.1016/j.optlaseng.2007.05.008.
88. Fassina, L.; Rozzi, G.; Rossi, S.; Scacchi, S.; Galetti, M.; Lo Muzio, F.P.; Del Bianco, F.; Colli Franzone, P.; Petrilli, G.; Faggian, G.; et al. Cardiac kinematic parameters computed from video of in situ beating heart. *Scientific reports* **2017**, *7*, 46143, doi:10.1038/srep46143.
89. Rozzi, G.; Lo Muzio, F.P.; Sandrini, C.; Rossi, S.; Fassina, L.; Faggian, G.; Miragoli, M.; Luciani, G.B. Real-time video kinematic evaluation of the in situ beating right ventricle after pulmonary valve replacement in patients with tetralogy of Fallot: a pilot study. *Interactive cardiovascular and thoracic surgery* **2019**, *29*, 625-631, doi:10.1093/icvts/ivz120.
90. Lo Muzio, F.P.; Rozzi, G.; Rossi, S.; Gerboles, A.G.; Fassina, L.; Pela, G.; Luciani, G.B.; Miragoli, M. In-situ optical assessment of rat epicardial kinematic parameters reveals frequency-dependent mechanic heterogeneity related to gender. *Progress in biophysics and molecular biology* **2020**, *154*, 94-101, doi:10.1016/j.pbiomolbio.2019.05.003.
91. Rozzi, G.; Lo Muzio, F.P.; Fassina, L.; Rossi, S.; Statello, R.; Sandrini, C.; Laricchiuta, M.; Faggian, G.; Miragoli, M.; Luciani, G.B. Right ventricular functional recovery depends on timing of pulmonary valve replacement in tetralogy of Fallot: a video kinematic study. *European journal of cardiothoracic surgery : official journal of the European Association for Cardiothoracic Surgery* **2021**, *59*, 1329-1336, doi:10.1093/ejcts/ezab026.
92. Fassina, L.; Di Grazia, A.; Naro, F.; Monaco, L.; De Angelis, M.G.; Magenes, G. Video evaluation of the kinematics and dynamics of the beating cardiac syncytium: an alternative to the Langendorff method. *The International journal of artificial organs* **2011**, *34*, 546-558, doi:10.5301/IJAO.2011.8510.
93. Stummann, T.C.; Wronski, M.; Sobanski, T.; Kumpfmüller, B.; Hareng, L.; Bremer, S.; Whelan, M.P. Digital movie analysis for quantification of beating frequencies, chronotropic effects, and beating areas in cardiomyocyte cultures. *Assay and drug development technologies* **2008**, *6*, 375-385, doi:10.1089/adt.2008.129.
94. Hossain, M.M.; Shimizu, E.; Saito, M.; Rao, S.R.; Yamaguchi, Y.; Tamiya, E. Non-invasive characterization of mouse embryonic stem cell derived cardiomyocytes based on the intensity variation in digital beating video. *The Analyst* **2010**, *135*, 1624-1630, doi:10.1039/c0an00208a.
95. Bazan, C.; Torres Barba, D.; Blomgren, P.; Paolini, P. Image processing techniques for assessing contractility in isolated neonatal cardiac myocytes.

- International journal of biomedical imaging* **2011**, 2011, 729732, doi:10.1155/2011/729732.
96. Bers, D.M. *Excitation-contraction coupling and cardiac contractile force*, 2nd ed.; Kluwer Academic Publishers: Dordrecht ; Boston, 2001; pp. xxiv, 427 p.
 97. Miragoli, M.; Sanchez-Alonso, J.L.; Bhargava, A.; Wright, P.T.; Sikkil, M.; Schobesberger, S.; Diakonov, I.; Novak, P.; Castaldi, A.; Cattaneo, P.; et al. Microtubule-Dependent Mitochondria Alignment Regulates Calcium Release in Response to Nanomechanical Stimulus in Heart Myocytes. *Cell reports* **2016**, *14*, 140-151, doi:10.1016/j.celrep.2015.12.014.
 98. Franzone, P.C.; Pavarino, L.F.; Scacchi, S. Bioelectrical effects of mechanical feedbacks in a strongly coupled cardiac electro-mechanical model. *Math Mod Meth Appl S* **2016**, *26*, doi:10.1142/S0218202516500020.
 99. Oei, G.T.; Aslami, H.; Kerindongo, R.P.; Steenstra, R.J.; Beurskens, C.J.; Tuip-de Boer, A.M.; Juffermans, N.P.; Hollmann, M.W.; Preckel, B.; Weber, N.C. Prolonged helium postconditioning protocols during early reperfusion do not induce cardioprotection in the rat heart in vivo: role of inflammatory cytokines. *Journal of immunology research* **2015**, 2015, 216798, doi:10.1155/2015/216798.
 100. Kloner, R.A.; Przyklenk, K.; Kay, G.L. Clinical evidence for stunned myocardium after coronary artery bypass surgery. *Journal of cardiac surgery* **1994**, *9*, 397-402, doi:10.1111/jocs.1994.9.3s.397.
 101. Pavlov, D.A.; Landesberg, A. The cross-bridge dynamics is determined by two length-independent kinetics: Implications on muscle economy and Frank-Starling Law. *Journal of molecular and cellular cardiology* **2016**, *90*, 94-101, doi:10.1016/j.yjmcc.2015.11.007.
 102. Heinzl, F.R.; Bito, V.; Volders, P.G.A.; Antoons, G.; Mubagwa, K.; Sipido, K.R. Spatial and temporal inhomogeneities during Ca²⁺ release from the sarcoplasmic reticulum in pig ventricular myocytes. *Circulation research* **2002**, *91*, 1023-1030, doi:10.1161/01.Res.0000045940.67060.Dd.
 103. Cordeiro, J.M.; Greene, L.; Heilmann, C.; Antzelevitch, D.; Antzelevitch, C. Transmural heterogeneity of calcium activity and mechanical function in the canine left ventricle. *Am J Physiol-Heart C* **2004**, *286*, H1471-H1479, doi:10.1152/ajpheart.00748.2003.
 104. Hohendanner, F.; Ljubojevic, S.; MacQuaide, N.; Sacherer, M.; Sedej, S.; Biesmans, L.; Wakula, P.; Platzer, D.; Sokolow, S.; Herchuelz, A.; et al. Intracellular dyssynchrony of diastolic cytosolic [Ca(2)(+)] decay in ventricular cardiomyocytes in cardiac remodeling and human heart failure. *Circulation research* **2013**, *113*, 527-538, doi:10.1161/CIRCRESAHA.113.300895.
 105. Esposito, F.; Limonta, E.; Ce, E. Passive stretching effects on electromechanical delay and time course of recovery in human skeletal muscle: new insights from an electromyographic and mechanomyographic combined approach. *European journal of applied physiology* **2011**, *111*, 485-495, doi:10.1007/s00421-010-1659-4.
 106. Cavanagh, P.R.; Komi, P.V. Electromechanical delay in human skeletal muscle under concentric and eccentric contractions. *European journal of applied physiology and occupational physiology* **1979**, *42*, 159-163, doi:10.1007/BF00431022.
 107. Esposito, F.; Ce, E.; Rampichini, S.; Veicsteinas, A. Acute passive stretching in a previously fatigued muscle: Electrical and mechanical response during tetanic stimulation. *J Sport Sci* **2009**, *27*, 1347-1357, doi:10.1080/02640410903165093.

108. Esposito, F.; Limonta, E.; Ce, E. Time course of stretching-induced changes in mechanomyogram and force characteristics. *J Electromyogr Kines* **2011**, *21*, 795-802, doi:10.1016/j.jelekin.2011.07.012.
109. Hug, F.; Lacourpaille, L.; Nordez, A. Electromechanical delay measured during a voluntary contraction should be interpreted with caution. *Muscle & nerve* **2011**, *44*, 838-839, doi:10.1002/mus.22139.
110. Russell, K.; Smiseth, O.A.; Gjesdal, O.; Qvigstad, E.; Norseng, P.A.; Sjaastad, I.; Opdahl, A.; Skulstad, H.; Edvardsen, T.; Remme, E.W. Mechanism of prolonged electromechanical delay in late activated myocardium during left bundle branch block. *Am J Physiol-Heart C* **2011**, *301*, H2334-H2343, doi:10.1152/ajpheart.00644.2011.
111. Prinzen, F.W.; Augustijn, C.H.; Allesie, M.A.; Arts, T.; Delhaas, T.; Reneman, R.S. The time sequence of electrical and mechanical activation during spontaneous beating and ectopic stimulation. *European heart journal* **1992**, *13*, 535-543, doi:10.1093/oxfordjournals.eurheartj.a060210.
112. Ashikaga, H.; Omens, J.H.; Ingels, N.B.; Covell, J.W. Transmural mechanics at left ventricular epicardial pacing site. *Am J Physiol-Heart C* **2004**, *286*, H2401-H2407, doi:10.1152/ajpheart.01013.2003.
113. Sengupta, P.P.; Khandheria, B.K.; Korinek, J.; Wang, J.W.; Jahangir, A.; Seward, J.B.; Belohlavek, M. Apex-to-base dispersion in regional timing of left ventricular shortening and lengthening. *Journal of the American College of Cardiology* **2006**, *47*, 163-172, doi:10.1016/j.jacc.2005.08.073.
114. Usyk, T.P.; McCulloch, A.D. Relationship between regional shortening and asynchronous electrical activation in a three-dimensional model of ventricular electromechanics. *J Cardiovasc Electr* **2003**, *14*, S196-S202, doi:10.1046/j.1540.8167.90311.x.
115. Gurev, V.; Constantino, J.; Rice, J.J.; Trayanova, N.A. Distribution of Electromechanical Delay in the Heart: Insights from a Three-Dimensional Electromechanical Model. *Biophys J* **2010**, *99*, 745-754, doi:10.1016/j.bpj.2010.05.028.
116. Cleland, J.G.; Freemantle, N.; Erdmann, E.; Gras, D.; Kappenberger, L.; Tavazzi, L.; Daubert, J.C. Long-term mortality with cardiac resynchronization therapy in the Cardiac Resynchronization-Heart Failure (CARE-HF) trial. *European journal of heart failure* **2012**, *14*, 628-634, doi:10.1093/eurjhf/hfs055.
117. Bristow, M.R.; Feldman, A.M.; Saxon, L.A.; Comm, C.S.; Investigators, C.C. Heart failure management using implantable devices for ventricular resynchronization: Comparison of medical therapy, pacing, and defibrillation in chronic heart failure (COMPANION) trial. *J Card Fail* **2000**, *6*, 276-285, doi:DOI 10.1054/jcaf.2000.9501.
118. Ghio, S.; Constantin, C.; Klersy, C.; Serio, A.; Fontana, A.; Campana, C.; Tavazzi, L. Interventricular and intraventricular dyssynchrony are common in heart failure patients, regardless of QRS duration. *European heart journal* **2004**, *25*, 571-578, doi:10.1016/j.ehj.2003.09.030.
119. Schuster, I.; Habib, G.; Jegu, C.; Thuny, F.; Avierinos, J.F.; Derumeaux, G.; Beck, L.; Medail, C.; Franceschi, F.; Renard, S.; et al. Diastolic asynchrony is more frequent than systolic asynchrony in dilated cardiomyopathy and is less improved by cardiac resynchronization therapy. *Journal of the American College of Cardiology* **2005**, *46*, 2250-2257, doi:10.1016/j.jacc.2005.02.096.
120. Vernooy, K.; Verbeek, X.A.; Peschar, M.; Crijns, H.J.; Arts, T.; Cornelussen, R.N.; Prinzen, F.W. Left bundle branch block induces ventricular remodelling

- and functional septal hypoperfusion. *European heart journal* **2005**, *26*, 91-98, doi:10.1093/eurheartj/ehi008.
121. Prinzen, F.W.; Hunter, W.C.; Wyman, B.T.; McVeigh, E.R. Mapping of regional myocardial strain and work during ventricular pacing: experimental study using magnetic resonance imaging tagging. *Journal of the American College of Cardiology* **1999**, *33*, 1735-1742, doi:10.1016/s0735-1097(99)00068-6.
 122. Constantino, J.; Hu, Y.; Trayanova, N.A. A computational approach to understanding the cardiac electromechanical activation sequence in the normal and failing heart, with translation to the clinical practice of CRT. *Progress in biophysics and molecular biology* **2012**, *110*, 372-379, doi:10.1016/j.pbiomolbio.2012.07.009.
 123. Chakir, K.; Daya, S.K.; Aiba, T.; Tunin, R.S.; Dimaano, V.L.; Abraham, T.P.; Jacques, K.; Lai, E.W.; Pacak, K.; Zhu, W.Z.; et al. Mechanisms of Enhanced beta-Adrenergic Reserve From Cardiac Resynchronization Therapy. *Circulation* **2009**, *119*, 1231-U1222, doi:10.1161/Circulationaha.108.774752.
 124. Spragg, D.D.; Kass, D.A. Pathobiology of left ventricular dyssynchrony and resynchronization. *Prog Cardiovasc Dis* **2006**, *49*, 26-41, doi:10.1016/j.pcad.2006.05.001.
 125. Kass, D.A.; Chen, C.H.; Curry, C.; Talbot, M.; Berger, R.; Fetcs, B.; Nevo, E. Improved left ventricular mechanics from acute VDD pacing in patients with dilated cardiomyopathy and ventricular conduction delay. *Circulation* **1999**, *99*, 1567-1573, doi:10.1161/01.cir.99.12.1567.
 126. Kirk, J.A.; Kass, D.A. Electromechanical Dyssynchrony and Resynchronization of the Failing Heart. *Circulation research* **2013**, *113*, 765-776, doi:10.1161/Circresaha.113.300270.
 127. Cazeau, S.; Ritter, P.; Bakdach, S.; Lazarus, A.; Limousin, M.; Henao, L.; Mundler, O.; Daubert, J.C.; Mugica, J. Four chamber pacing in dilated cardiomyopathy. *Pacing and clinical electrophysiology : PACE* **1994**, *17*, 1974-1979, doi:10.1111/j.1540-8159.1994.tb03783.x.
 128. Auricchio, A.; Stellbrink, C.; Block, M.; Sack, S.; Vogt, J.; Bakker, P.; Klein, H.; Kramer, A.; Ding, J.; Salo, R.; et al. Effect of pacing chamber and atrioventricular delay on acute systolic function of paced patients with congestive heart failure. The Pacing Therapies for Congestive Heart Failure Study Group. The Guidant Congestive Heart Failure Research Group. *Circulation* **1999**, *99*, 2993-3001, doi:10.1161/01.cir.99.23.2993.
 129. Ukkonen, H.; Beanlands, R.S.; Burwash, I.G.; de Kemp, R.A.; Nahmias, C.; Fallen, E.; Hill, M.R.; Tang, A.S. Effect of cardiac resynchronization on myocardial efficiency and regional oxidative metabolism. *Circulation* **2003**, *107*, 28-31, doi:10.1161/01.cir.0000047068.02226.95.
 130. Nelson, G.S.; Berger, R.D.; Fetcs, B.J.; Talbot, M.; Spinelli, J.C.; Hare, J.M.; Kass, D.A. Left ventricular or biventricular pacing improves cardiac function at diminished energy cost in patients with dilated cardiomyopathy and left bundle-branch block. *Circulation* **2000**, *102*, 3053-3059, doi:10.1161/01.cir.102.25.3053.
 131. Kerckhoffs, R.C.; Omens, J.H.; McCulloch, A.D. Mechanical discoordination increases continuously after the onset of left bundle branch block despite constant electrical dyssynchrony in a computational model of cardiac electromechanics and growth. *Europace : European pacing, arrhythmias, and cardiac electrophysiology : journal of the working groups on cardiac pacing, arrhythmias, and cardiac cellular electrophysiology of the European Society of Cardiology* **2012**, *14 Suppl 5*, v65-v72, doi:10.1093/europace/eus274.

132. Kass, D.A. An epidemic of dyssynchrony: but what does it mean? *Journal of the American College of Cardiology* **2008**, *51*, 12-17, doi:10.1016/j.jacc.2007.09.027.
133. Kalogeropoulos, A.P.; Georgiopoulou, V.V.; Howell, S.; Pernetz, M.A.; Fisher, M.R.; Lerakis, S.; Martin, R.P. Evaluation of right intraventricular dyssynchrony by two-dimensional strain echocardiography in patients with pulmonary arterial hypertension. *Journal of the American Society of Echocardiography : official publication of the American Society of Echocardiography* **2008**, *21*, 1028-1034, doi:10.1016/j.echo.2008.05.005.
134. Brili, S.; Stamatopoulos, I.; Misailidou, M.; Chrysohoou, C.; Tousoulis, D.; Tatsis, I.; Stefanadis, C. Longitudinal strain curves in the RV free wall differ in morphology in patients with pulmonary hypertension compared to controls. *International journal of cardiology* **2013**, *167*, 2753-2756, doi:10.1016/j.ijcard.2012.06.089.
135. Marcus, J.T.; Gan, C.T.; Zwanenburg, J.J.; Boonstra, A.; Allaart, C.P.; Gotte, M.J.; Vonk-Noordegraaf, A. Interventricular mechanical asynchrony in pulmonary arterial hypertension: left-to-right delay in peak shortening is related to right ventricular overload and left ventricular underfilling. *Journal of the American College of Cardiology* **2008**, *51*, 750-757, doi:10.1016/j.jacc.2007.10.041.
136. Roche, S.L.; Grosse-Wortmann, L.; Redington, A.N.; Slorach, C.; Smith, G.; Kantor, P.F.; Friedberg, M.K. Exercise induces biventricular mechanical dyssynchrony in children with repaired tetralogy of Fallot. *Heart* **2010**, *96*, 2010-2015, doi:10.1136/hrt.2010.206169.
137. Hui, W.; Slorach, C.; Bradley, T.J.; Jaeggi, E.T.; Mertens, L.; Friedberg, M.K. Measurement of right ventricular mechanical synchrony in children using tissue Doppler velocity and two-dimensional strain imaging. *Journal of the American Society of Echocardiography : official publication of the American Society of Echocardiography* **2010**, *23*, 1289-1296, doi:10.1016/j.echo.2010.09.009.
138. Friedberg, M.K.; Fernandes, F.P.; Roche, S.L.; Slorach, C.; Grosse-Wortmann, L.; Manlhiot, C.; Fackoury, C.; McCrindle, B.W.; Mertens, L.; Kantor, P.F. Relation of right ventricular mechanics to exercise tolerance in children after tetralogy of Fallot repair. *American heart journal* **2013**, *165*, 551-557, doi:10.1016/j.ahj.2012.06.029.
139. Murphy, J.G.; Gersh, B.J.; Mair, D.D.; Fuster, V.; McGoon, M.D.; Ilstrup, D.M.; McGoon, D.C.; Kirklin, J.W.; Danielson, G.K. Long-term outcome in patients undergoing surgical repair of tetralogy of Fallot. *The New England journal of medicine* **1993**, *329*, 593-599, doi:10.1056/NEJM199308263290901.
140. Knauth, A.L.; Gauvreau, K.; Powell, A.J.; Landzberg, M.J.; Walsh, E.P.; Lock, J.E.; del Nido, P.J.; Geva, T. Ventricular size and function assessed by cardiac MRI predict major adverse clinical outcomes late after tetralogy of Fallot repair. *Heart* **2008**, *94*, 211-216, doi:10.1136/hrt.2006.104745.
141. Janousek, J.; Kovanda, J.; Lozek, M.; Tomek, V.; Vojtovic, P.; Gebauer, R.; Kubus, P.; Krejcir, M.; Lumens, J.; Delhaas, T.; et al. Pulmonary Right Ventricular Resynchronization in Congenital Heart Disease: Acute Improvement in Right Ventricular Mechanics and Contraction Efficiency. *Circulation. Cardiovascular imaging* **2017**, *10*, doi:10.1161/CIRCIMAGING.117.006424.
142. Taylor, J. The 2010 version of the ESC guidelines for the management of grown-up adult congenital heart disease are discussed by guidelines task

- force chairman H. Baumgartner. *European heart journal* **2010**, *31*, 2825-2826, doi:10.1093/eurheartj/ehq309.
143. Gorcsan, J., 3rd; Abraham, T.; Agler, D.A.; Bax, J.J.; Derumeaux, G.; Grimm, R.A.; Martin, R.; Steinberg, J.S.; Sutton, M.S.; Yu, C.M.; et al. Echocardiography for cardiac resynchronization therapy: recommendations for performance and reporting--a report from the American Society of Echocardiography Dyssynchrony Writing Group endorsed by the Heart Rhythm Society. *Journal of the American Society of Echocardiography : official publication of the American Society of Echocardiography* **2008**, *21*, 191-213, doi:10.1016/j.echo.2008.01.003.
 144. Oyenuga, O.; Hara, H.; Tanaka, H.; Kim, H.N.; Adelstein, E.C.; Saba, S.; Gorcsan, J., 3rd. Usefulness of echocardiographic dyssynchrony in patients with borderline QRS duration to assist with selection for cardiac resynchronization therapy. *JACC. Cardiovascular imaging* **2010**, *3*, 132-140, doi:10.1016/j.jcmg.2009.09.020.
 145. Hui, W.; Slorach, C.; Dragulescu, A.; Mertens, L.; Bijmens, B.; Friedberg, M.K. Mechanisms of right ventricular electromechanical dyssynchrony and mechanical inefficiency in children after repair of tetralogy of fallot. *Circulation. Cardiovascular imaging* **2014**, *7*, 610-618, doi:10.1161/CIRCIMAGING.113.001483.
 146. Yim, D.; Hui, W.; Larios, G.; Dragulescu, A.; Grosse-Wortmann, L.; Bijmens, B.; Mertens, L.; Friedberg, M.K. Quantification of Right Ventricular Electromechanical Dyssynchrony in Relation to Right Ventricular Function and Clinical Outcomes in Children with Repaired Tetralogy of Fallot. *Journal of the American Society of Echocardiography : official publication of the American Society of Echocardiography* **2018**, *31*, 822-830, doi:10.1016/j.echo.2018.03.012.
 147. Kroon, W.; Lumens, J.; Potse, M.; Suerder, D.; Klersy, C.; Regoli, F.; Murzilli, R.; Moccetti, T.; Delhaas, T.; Krause, R.; et al. In vivo electromechanical assessment of heart failure patients with prolonged QRS duration. *Heart rhythm* **2015**, *12*, 1259-1267, doi:10.1016/j.hrthm.2015.03.006.
 148. Gyongyosi, M.; Dib, N. Diagnostic and prognostic value of 3D NOGA mapping in ischemic heart disease. *Nature reviews. Cardiology* **2011**, *8*, 393-404, doi:10.1038/nrcardio.2011.64.
 149. Hara, H.; Oyenuga, O.A.; Tanaka, H.; Adelstein, E.C.; Onishi, T.; McNamara, D.M.; Schwartzman, D.; Saba, S.; Gorcsan, J., 3rd. The relationship of QRS morphology and mechanical dyssynchrony to long-term outcome following cardiac resynchronization therapy. *European heart journal* **2012**, *33*, 2680-2691, doi:10.1093/eurheartj/ehs013.
 150. Provost, J.; Lee, W.N.; Fujikura, K.; Konofagou, E.E. Imaging the electromechanical activity of the heart in vivo. *Proceedings of the National Academy of Sciences of the United States of America* **2011**, *108*, 8565-8570, doi:10.1073/pnas.1011688108.
 151. Wang, S.; Lee, W.N.; Provost, J.; Luo, J.; Konofagou, E.E. A composite high-frame-rate system for clinical cardiovascular imaging. *IEEE transactions on ultrasonics, ferroelectrics, and frequency control* **2008**, *55*, 2221-2233, doi:10.1109/TUFFC.921.
 152. Walker, W.F.; Trahey, G.E. A Fundamental Limit on the Performance of Correlation-Based Phase Correction and Flow Estimation Techniques. *Ieee T Ultrason Ferr* **1994**, *41*, 644-654, doi:10.1109/58.308499.

153. Badke, F.R.; Boinay, P.; Covell, J.W. Effects of ventricular pacing on regional left ventricular performance in the dog. *The American journal of physiology* **1980**, *238*, H858-867, doi:10.1152/ajpheart.1980.238.6.H858.
154. Wyman, B.T.; Hunter, W.C.; Prinzen, F.W.; McVeigh, E.R. Mapping propagation of mechanical activation in the paced heart with MRI tagging. *The American journal of physiology* **1999**, *276*, H881-891, doi:10.1152/ajpheart.1999.276.3.H881.
155. Faris, O.P.; Evans, F.J.; Ennis, D.B.; Helm, P.A.; Taylor, J.L.; Chesnick, A.S.; Guttman, M.A.; Ozturk, C.; McVeigh, E.R. Novel technique for cardiac electromechanical mapping with magnetic resonance imaging tagging and an epicardial electrode sock. *Annals of biomedical engineering* **2003**, *31*, 430-440, doi:10.1114/1.1560618.
156. Kelly, R.P.; Ting, C.T.; Yang, T.M.; Liu, C.P.; Maughan, W.L.; Chang, M.S.; Kass, D.A. Effective Arterial Elastance as Index of Arterial Vascular Load in Humans. *Circulation* **1992**, *86*, 513-521, doi:10.1161/01.Cir.86.2.513.
157. Rhea, I.B.; Rehman, S.; Jarori, U.; Choudhry, M.W.; Feigenbaum, H.; Sawada, S.G. Prognostic utility of blood pressure-adjusted global and basal systolic longitudinal strain. *Echo research and practice* **2016**, *3*, 17-24, doi:10.1530/ERP-15-0037.
158. Reichel, N.; Wilson, J.; St John Sutton, M.; Plappert, T.A.; Goldberg, S.; Hirshfeld, J.W. Noninvasive determination of left ventricular end-systolic stress: validation of the method and initial application. *Circulation* **1982**, *65*, 99-108, doi:10.1161/01.cir.65.1.99.
159. Lee, C.B.; Goubergrits, L.; Fernandes, J.F.; Nordmeyer, S.; Knosalla, C.; Berger, F.; Falk, V.; Kuehne, T.; Kelm, M. Surrogates for myocardial power and power efficiency in patients with aortic valve disease. *Scientific reports* **2019**, *9*, 16407, doi:10.1038/s41598-019-52909-9.
160. Warnes, C.A.; Williams, R.G.; Bashore, T.M.; Child, J.S.; Connolly, H.M.; Dearani, J.A.; Del Nido, P.; Fasules, J.W.; Graham, T.P., Jr.; Hijazi, Z.M.; et al. ACC/AHA 2008 guidelines for the management of adults with congenital heart disease: a report of the American College of Cardiology/American Heart Association Task Force on Practice Guidelines (Writing Committee to Develop Guidelines on the Management of Adults With Congenital Heart Disease). Developed in Collaboration With the American Society of Echocardiography, Heart Rhythm Society, International Society for Adult Congenital Heart Disease, Society for Cardiovascular Angiography and Interventions, and Society of Thoracic Surgeons. *Journal of the American College of Cardiology* **2008**, *52*, e143-e263, doi:10.1016/j.jacc.2008.10.001.
161. Bodhey, N.K.; Beerbaum, P.; Sarikouch, S.; Kropf, S.; Lange, P.; Berger, F.; Anderson, R.H.; Kuehne, T. Functional analysis of the components of the right ventricle in the setting of tetralogy of Fallot. *Circulation. Cardiovascular imaging* **2008**, *1*, 141-147, doi:10.1161/CIRCIMAGING.108.783795.
162. Weaver, B.; Wuensch, K.L. SPSS and SAS programs for comparing Pearson correlations and OLS regression coefficients. *Behav Res Methods* **2013**, *45*, 880-895, doi:10.3758/s13428-012-0289-7.
163. Armitage, P. A Resource for Medical and Biostatistics - a Citation Classic Commentary on Statistical-Methods in Medical-Research by Armitage, P. *Cc/Life Sci* **1990**, 16-16.
164. Liu, Y.; Chen, S.; Zuhlke, L.; Black, G.C.; Choy, M.K.; Li, N.; Keavney, B.D. Global birth prevalence of congenital heart defects 1970-2017: updated systematic

- review and meta-analysis of 260 studies. *International journal of epidemiology* **2019**, *48*, 455-463, doi:10.1093/ije/dyz009.
165. Schuster, A.; Hor, K.N.; Kowallick, J.T.; Beerbaum, P.; Kutty, S. Cardiovascular Magnetic Resonance Myocardial Feature Tracking: Concepts and Clinical Applications. *Circulation. Cardiovascular imaging* **2016**, *9*, e004077, doi:10.1161/CIRCIMAGING.115.004077.
 166. Schneeweis, C.; Lapinskas, T.; Schnackenburg, B.; Berger, A.; Hucko, T.; Kelle, S.; Fleck, E.; Gebker, R. Comparison of myocardial tagging and feature tracking in patients with severe aortic stenosis. *The Journal of heart valve disease* **2014**, *23*, 432-440.
 167. Moody, W.E.; Taylor, R.J.; Edwards, N.C.; Chue, C.D.; Umar, F.; Taylor, T.J.; Ferro, C.J.; Young, A.A.; Townend, J.N.; Leyva, F.; et al. Comparison of magnetic resonance feature tracking for systolic and diastolic strain and strain rate calculation with spatial modulation of magnetization imaging analysis. *Journal of magnetic resonance imaging : JMRI* **2015**, *41*, 1000-1012, doi:10.1002/jmri.24623.
 168. Morton, G.; Schuster, A.; Jogiya, R.; Kutty, S.; Beerbaum, P.; Nagel, E. Inter-study reproducibility of cardiovascular magnetic resonance myocardial feature tracking. *Journal of cardiovascular magnetic resonance : official journal of the Society for Cardiovascular Magnetic Resonance* **2012**, *14*, 43, doi:10.1186/1532-429X-14-43.
 169. Schuster, A.; Morton, G.; Hussain, S.T.; Jogiya, R.; Kutty, S.; Asrress, K.N.; Makowski, M.R.; Bigalke, B.; Perera, D.; Beerbaum, P.; et al. The intra-observer reproducibility of cardiovascular magnetic resonance myocardial feature tracking strain assessment is independent of field strength. *European journal of radiology* **2013**, *82*, 296-301, doi:10.1016/j.ejrad.2012.11.012.
 170. Schuster, A.; Paul, M.; Bettencourt, N.; Hussain, S.T.; Morton, G.; Kutty, S.; Bigalke, B.; Chiribiri, A.; Perera, D.; Nagel, E.; et al. Myocardial feature tracking reduces observer-dependence in low-dose dobutamine stress cardiovascular magnetic resonance. *PloS one* **2015**, *10*, e0122858, doi:10.1371/journal.pone.0122858.
 171. Faragli, A.; Tanacli, R.; Kolp, C.; Lapinskas, T.; Stehning, C.; Schnackenburg, B.; Lo Muzio, F.P.; Perna, S.; Pieske, B.; Nagel, E.; et al. Cardiovascular magnetic resonance feature tracking in pigs: a reproducibility and sample size calculation study. *The international journal of cardiovascular imaging* **2020**, *36*, 703-712, doi:10.1007/s10554-020-01767-y.
 172. Bland, J.M.; Altman, D.G. Measuring agreement in method comparison studies. *Statistical methods in medical research* **1999**, *8*, 135-160, doi:10.1177/096228029900800204.
 173. Barreiro-Perez, M.; Curione, D.; Symons, R.; Claus, P.; Voigt, J.U.; Bogaert, J. Left ventricular global myocardial strain assessment comparing the reproducibility of four commercially available CMR-feature tracking algorithms. *European radiology* **2018**, *28*, 5137-5147, doi:10.1007/s00330-018-5538-4.
 174. Schmidt, B.; Dick, A.; Treutlein, M.; Schiller, P.; Bunck, A.C.; Maintz, D.; Baessler, B. Intra- and inter-observer reproducibility of global and regional magnetic resonance feature tracking derived strain parameters of the left and right ventricle. *European journal of radiology* **2017**, *89*, 97-105, doi:10.1016/j.ejrad.2017.01.025.
 175. Swoboda, P.P.; Larghat, A.; Zaman, A.; Fairbairn, T.A.; Motwani, M.; Greenwood, J.P.; Plein, S. Reproducibility of Myocardial Strain and Left

- Ventricular Twist Measured Using Complementary Spatial Modulation of Magnetization. *Journal of Magnetic Resonance Imaging* **2014**, *39*, 887-894, doi:10.1002/jmri.24223.
176. Zhong, J.; Liu, W.; Yu, X. Characterization of three-dimensional myocardial deformation in the mouse heart: An MR tagging study. *Journal of Magnetic Resonance Imaging* **2008**, *27*, 1263-1270, doi:10.1002/jmri.21367.
 177. Schuster, A.; Stahnke, V.C.; Unterberg-Buchwald, C.; Kowallick, J.T.; Lamata, P.; Steinmetz, M.; Kutty, S.; Fasshauer, M.; Staab, W.; Sohns, J.M.; et al. Cardiovascular magnetic resonance feature-tracking assessment of myocardial mechanics: Intervendor agreement and considerations regarding reproducibility. *Clin Radiol* **2015**, *70*, 989-998, doi:10.1016/j.crad.2015.05.006.
 178. Helle-Valle, T.M.; Yu, W.C.; Fernandes, V.R.S.; Rosen, B.D.; Lima, J.A.C. Usefulness of Radial Strain Mapping by Multidetector Computer Tomography to Quantify Regional Myocardial Function in Patients With Healed Myocardial Infarction. *American Journal of Cardiology* **2010**, *106*, 483-491, doi:10.1016/j.amjcard.2010.03.063.
 179. Sampath, S.; Parimal, A.S.; Feng, D.; Chang, M.M.L.; Baumgartner, R.; Klimas, M.; Jacobsen, K.; Manigbas, E.; Gsell, W.; Evelhoch, J.L.; et al. Quantitative MRI Biomarkers to Characterize Regional Left Ventricular Perfusion and Function in Nonhuman Primates During Dobutamine-Induced Stress: A Reproducibility and Reliability Study. *Journal of Magnetic Resonance Imaging* **2017**, *45*, 556-569, doi:10.1002/jmri.25379.
 180. Stanton, T.; Leano, R.; Marwick, T.H. Prediction of All-Cause Mortality From Global Longitudinal Speckle Strain Comparison With Ejection Fraction and Wall Motion Scoring. *Circ-Cardiovasc Imag* **2009**, *2*, 356-364, doi:10.1161/Circimaging.109.862334.
 181. Stokke, T.M.; Hasselberg, N.E.; Smedsrud, M.K.; Sarvari, S.I.; Haugaa, K.H.; Smiseth, O.A.; Edvardsen, T.; Remme, E.W. Geometry as a Confounder When Assessing Ventricular Systolic Function Comparison Between Ejection Fraction and Strain. *Journal of the American College of Cardiology* **2017**, *70*, 942-954, doi:10.1016/j.jacc.2017.06.046.
 182. Hasselberg, N.E.; Haugaa, K.H.; Sarvari, S.I.; Gullestad, L.; Andreassen, A.K.; Smiseth, O.A.; Edvardsen, T. Left ventricular global longitudinal strain is associated with exercise capacity in failing hearts with preserved and reduced ejection fraction. *Eur Heart J-Card Img* **2015**, *16*, 217-224, doi:10.1093/ehjci/jeu277.
 183. Kraigher-Krainer, E.; Shah, A.M.; Gupta, D.K.; Santos, A.; Claggett, B.; Pieske, B.; Zile, M.R.; Voors, A.A.; Lefkowitz, M.P.; Packer, M.; et al. Impaired Systolic Function by Strain Imaging in Heart Failure With Preserved Ejection Fraction. *Journal of the American College of Cardiology* **2014**, *63*, 447-456, doi:10.1016/j.jacc.2013.09.052.
 184. Yotti, R.; Bermejo, J.; Benito, Y.; Sanz-Ruiz, R.; Ripoll, C.; Martinez-Legazpi, P.; del Villar, C.P.; Elizaga, J.; Gonzalez-Mansilla, A.; Barrio, A.; et al. Validation of Noninvasive Indices of Global Systolic Function in Patients With Normal and Abnormal Loading Conditions A Simultaneous Echocardiography Pressure-Volume Catheterization Study. *Circ-Cardiovasc Imag* **2014**, *7*, 164-172, doi:10.1161/Circimaging.113.000722.
 185. Nagata, Y.; Takeuchi, M.; Wu, V.C.C.; Izumo, M.; Suzuki, K.; Sato, K.; Seo, Y.; Akashi, Y.J.; Aonuma, K.; Otsuji, Y. Prognostic Value of LV Deformation Parameters Using 2D and 3D Speckle-Tracking Echocardiography in

- Asymptomatic Patients With Severe Aortic Stenosis and Preserved LV Ejection Fraction. *Jacc-Cardiovasc Imag* **2015**, *8*, 235-245, doi:10.1016/j.jcmg.2014.12.009.
186. Eitel, I.; Stiermaier, T.; Lange, T.; Rommel, K.P.; Koschalka, A.; Kowallick, J.T.; Lotz, J.; Kutty, S.; Gutberlet, M.; Hasenfuss, G.; et al. Cardiac Magnetic Resonance Myocardial Feature Tracking for Optimized Prediction of Cardiovascular Events Following Myocardial Infarction. *Jacc-Cardiovasc Imag* **2018**, *11*, 1433-1444, doi:10.1016/j.jcmg.2017.11.034.
187. Onishi, T.; Saha, S.K.; Delgado-Montero, A.; Ludwig, D.R.; Onishi, T.; Schelbert, E.B.; Schwartzman, D.; Gorcsan, J. Global Longitudinal Strain and Global Circumferential Strain by Speckle-Tracking Echocardiography and Feature-Tracking Cardiac Magnetic Resonance Imaging: Comparison with Left Ventricular Ejection Fraction. *J Am Soc Echocardiog* **2015**, *28*, 587-596, doi:10.1016/j.echo.2014.11.018.
188. Romano, S.; Judd, R.M.; Kim, R.J.; Kim, H.W.; Klem, I.; Heitner, J.F.; Shah, D.J.; Jue, J.; White, B.E.; Indorkar, R.; et al. Feature-Tracking Global Longitudinal Strain Predicts Death in a Multicenter Population of Patients With Ischemic and Nonischemic Dilated Cardiomyopathy Incremental to Ejection Fraction and Late Gadolinium Enhancement. *Jacc-Cardiovasc Imag* **2018**, *11*, 1419-1429, doi:10.1016/j.jcmg.2017.10.024.
189. Faragli, A.; Tanacli, R.; Kolp, C.; Abawi, D.; Lapinskas, T.; Stehning, C.; Schnackenburg, B.; Lo Muzio, F.P.; Fassina, L.; Pieske, B.; et al. Cardiovascular magnetic resonance-derived left ventricular mechanics-strain, cardiac power and end-systolic elastance under various inotropic states in swine. *Journal of cardiovascular magnetic resonance : official journal of the Society for Cardiovascular Magnetic Resonance* **2020**, *22*, 79, doi:10.1186/s12968-020-00679-z.
190. Bouchez, S.; Heyde, B.; Barbosa, D.; Vandenheuvel, M.; Houle, H.; Wang, Y.; D'Hooge, J.; Wouters, P.F. In-vivo validation of a new clinical tool to quantify three-dimensional myocardial strain using ultrasound. *The international journal of cardiovascular imaging* **2016**, *32*, 1707-1714, doi:10.1007/s10554-016-0962-5.
191. Bing, R.J.; Hammond, M.M.; et al. The measurement of coronary blood flow, oxygen consumption, and efficiency of the left ventricle in man. *American heart journal* **1949**, *38*, 1-24, doi:10.1016/0002-8703(49)90788-7.
192. Burkhoff, D.; Sagawa, K. Ventricular Efficiency Predicted by an Analytical Model. *American Journal of Physiology* **1986**, *250*, 1021-1027, doi:DOI 10.1152/ajpregu.1986.250.6.R1021.
193. Schipke, J.D. Cardiac efficiency. *Basic research in cardiology* **1994**, *89*, 207-240, doi:10.1007/BF00795615.
194. Knaapen, P.; Germans, T.; Knuuti, J.; Paulus, W.J.; Dijkmans, P.A.; Allaart, C.P.; Lammertsma, A.A.; Visser, F.C. Myocardial energetics and efficiency: current status of the noninvasive approach. *Circulation* **2007**, *115*, 918-927, doi:10.1161/CIRCULATIONAHA.106.660639.
195. Akins, C.W.; Travis, B.; Yoganathan, A.P. Energy loss for evaluating heart valve performance. *The Journal of thoracic and cardiovascular surgery* **2008**, *136*, 820-833, doi:10.1016/j.jtcvs.2007.12.059.
196. Hansson, N.H.S.; Sorensen, J.; Harms, H.J.; Kim, W.Y.; Nielsen, R.; Tolbod, L.P.; Frokiaer, J.; Bouchelouche, K.; Dodt, K.K.; Sihm, I.; et al. Myocardial Oxygen Consumption and Efficiency in Aortic Valve Stenosis Patients With and Without Heart Failure. *J Am Heart Assoc* **2017**, *6*, doi:ARTN e004810

10.1161/JAHA.116.004810.

197. Guclu, A.; Knaapen, P.; Harms, H.J.; Vonk, A.B.A.; Stooker, W.; Groepenhoff, H.; Lammertsma, A.A.; van Rossum, A.C.; Germans, T.; van der Velden, J. Myocardial efficiency is an important determinant of functional improvement after aortic valve replacement in aortic valve stenosis patients: a combined PET and CMR study. *Eur Heart J-Card Imag* **2015**, *16*, 882-889, doi:10.1093/ehjci/jev009.
198. Cetin, M.S.; Cetin, E.H.O.; Canpolat, U.; Sasmaz, H.; Temizhan, A.; Aydogdu, S. Prognostic significance of myocardial energy expenditure and myocardial efficiency in patients with heart failure with reduced ejection fraction. *Int J Cardiovas Imag* **2018**, *34*, 211-222, doi:10.1007/s10554-017-1226-8.
199. Sorensen, J.; Harms, H.J.; Aalen, J.M.; Baron, T.; Smiseth, O.A.; Flachskampf, F.A. Myocardial Efficiency A Fundamental Physiological Concept on the Verge of Clinical Impact. *Jacc-Cardiovasc Imag* **2020**, *13*, 1564-1576, doi:10.1016/j.jcmg.2019.08.030.
200. Faragli, A.; Alogna, A.; Lee, C.B.; Zhu, M.; Ghorbani, N.; Lo Muzio, F.P.; Schnackenburg, B.; Stehning, C.; Kuehne, T.; Post, H.; et al. Non-invasive CMR-Based Quantification of Myocardial Power and Efficiency Under Stress and Ischemic Conditions in Landrace Pigs. *Front Cardiovasc Med* **2021**, *8*, doi:Artn 689255
- 10.3389/Fcvm.2021.689255.
201. Kass, D.A.; Maughan, W.L. From 'Emax' to pressure-volume relations: a broader view. *Circulation* **1988**, *77*, 1203-1212, doi:10.1161/01.cir.77.6.1203.
202. Abawi, D.; Faragli, A.; Schwarzl, M.; Manninger, M.; Zweiker, D.; Kresoja, K.P.; Verderber, J.; Zirngast, B.; Maechler, H.; Steendijk, P.; et al. Cardiac power output accurately reflects external cardiac work over a wide range of inotropic states in pigs. *BMC cardiovascular disorders* **2019**, *19*, 217, doi:10.1186/s12872-019-1212-2.
203. Ravens, U. Sex differences in cardiac electrophysiology. *Canadian journal of physiology and pharmacology* **2018**, *96*, 985-990, doi:10.1139/cjpp-2018-0179.
204. Farrell, S.R.; Ross, J.L.; Howlett, S.E. Sex differences in mechanisms of cardiac excitation-contraction coupling in rat ventricular myocytes. *American journal of physiology. Heart and circulatory physiology* **2010**, *299*, H36-45, doi:10.1152/ajpheart.00299.2010.
205. Gatzoulis, M.A.; Balaji, S.; Webber, S.A.; Siu, S.C.; Hokanson, J.S.; Poile, C.; Rosenthal, M.; Nakazawa, M.; Moller, J.H.; Gillette, P.C.; et al. Risk factors for arrhythmia and sudden cardiac death late after repair of tetralogy of Fallot: a multicentre study. *Lancet* **2000**, *356*, 975-981, doi:10.1016/S0140-6736(00)02714-8.
206. Ferraz Cavalcanti, P.E.; Sa, M.P.; Santos, C.A.; Esmeraldo, I.M.; de Escobar, R.R.; de Menezes, A.M.; de Azevedo, O.M., Jr.; de Vasconcelos Silva, F.P.; Lins, R.F.; Lima Rde, C. Pulmonary valve replacement after operative repair of tetralogy of Fallot: meta-analysis and meta-regression of 3,118 patients from 48 studies. *Journal of the American College of Cardiology* **2013**, *62*, 2227-2243, doi:10.1016/j.jacc.2013.04.107.
207. Harrild, D.M.; Berul, C.I.; Cecchin, F.; Geva, T.; Gauvreau, K.; Pigula, F.; Walsh, E.P. Pulmonary valve replacement in tetralogy of Fallot: impact on survival and ventricular tachycardia. *Circulation* **2009**, *119*, 445-451, doi:10.1161/CIRCULATIONAHA.108.775221.

208. Heng, E.L.; Gatzoulis, M.A.; Uebing, A.; Sethia, B.; Uemura, H.; Smith, G.C.; Diller, G.P.; McCarthy, K.P.; Ho, S.Y.; Li, W.; et al. Immediate and Midterm Cardiac Remodeling After Surgical Pulmonary Valve Replacement in Adults With Repaired Tetralogy of Fallot: A Prospective Cardiovascular Magnetic Resonance and Clinical Study. *Circulation* **2017**, *136*, 1703-1713, doi:10.1161/CIRCULATIONAHA.117.027402.
209. Warnes, C.A.; Williams, R.G.; Bashore, T.M.; Child, J.S.; Connolly, H.M.; Dearani, J.A.; del Nido, P.; Fasules, J.W.; Graham, T.P., Jr.; Hijazi, Z.M.; et al. ACC/AHA 2008 Guidelines for the Management of Adults with Congenital Heart Disease: a report of the American College of Cardiology/American Heart Association Task Force on Practice Guidelines (writing committee to develop guidelines on the management of adults with congenital heart disease). *Circulation* **2008**, *118*, e714-833, doi:10.1161/CIRCULATIONAHA.108.190690.
210. Bokma, J.P.; Winter, M.M.; Oosterhof, T.; Vliegen, H.W.; van Dijk, A.P.; Hazekamp, M.G.; Koolbergen, D.R.; Groenink, M.; Mulder, B.J.; Bouma, B.J. Preoperative thresholds for mid-to-late haemodynamic and clinical outcomes after pulmonary valve replacement in tetralogy of Fallot. *European heart journal* **2016**, *37*, 829-835, doi:10.1093/eurheartj/ehv550.
211. Geva, T.; Mulder, B.; Gauvreau, K.; Babu-Narayan, S.V.; Wald, R.M.; Hickey, K.; Powell, A.J.; Gatzoulis, M.A.; Valente, A.M. Preoperative Predictors of Death and Sustained Ventricular Tachycardia After Pulmonary Valve Replacement in Patients With Repaired Tetralogy of Fallot Enrolled in the INDICATOR Cohort. *Circulation* **2018**, *138*, 2106-2115, doi:10.1161/CIRCULATIONAHA.118.034740.
212. Amiad Pavlov, D.; Landesberg, A. The cross-bridge dynamics is determined by two length-independent kinetics: Implications on muscle economy and Frank-Starling Law. *Journal of molecular and cellular cardiology* **2016**, *90*, 94-101, doi:10.1016/j.yjmcc.2015.11.007.
213. Fogel, M.A.; Sundareswaran, K.S.; de Zelicourt, D.; Dasi, L.P.; Pawlowski, T.; Rome, J.; Yoganathan, A.P. Power loss and right ventricular efficiency in patients after tetralogy of Fallot repair with pulmonary insufficiency: clinical implications. *The Journal of thoracic and cardiovascular surgery* **2012**, *143*, 1279-1285, doi:10.1016/j.jtcvs.2011.10.066.
214. Stout, K.K.; Daniels, C.J.; Aboulhosn, J.A.; Bozkurt, B.; Broberg, C.S.; Colman, J.M.; Crumb, S.R.; Dearani, J.A.; Fuller, S.; Gurvitz, M.; et al. 2018 AHA/ACC Guideline for the Management of Adults With Congenital Heart Disease: Executive Summary: A Report of the American College of Cardiology/American Heart Association Task Force on Clinical Practice Guidelines. *Circulation* **2019**, *139*, e637-e697, doi:10.1161/CIR.0000000000000602.
215. Frigiola, A.; Tsang, V.; Bull, C.; Coats, L.; Khambadkone, S.; Derrick, G.; Mist, B.; Walker, F.; van Doorn, C.; Bonhoeffer, P.; et al. Biventricular response after pulmonary valve replacement for right ventricular outflow tract dysfunction: is age a predictor of outcome? *Circulation* **2008**, *118*, S182-190, doi:10.1161/CIRCULATIONAHA.107.756825.
216. Lee, C.; Choi, E.S.; Lee, C.H. Long-term outcomes of pulmonary valve replacement in patients with repaired tetralogy of Fallot. *European journal of cardio-thoracic surgery : official journal of the European Association for Cardio-thoracic Surgery* **2020**, *58*, 246-252, doi:10.1093/ejcts/ezaa030.
217. Romeo, J.L.R.; Takkenberg, J.J.M.; Cuyppers, J.; de Groot, N.M.S.; van de Woestijne, P.; Bruining, N.; Bogers, A.; Mokhles, M.M. Timing of pulmonary

- valve replacement in patients with corrected Fallot to prevent QRS prolongation. *European journal of cardio-thoracic surgery : official journal of the European Association for Cardio-thoracic Surgery* **2020**, *58*, 559-566, doi:10.1093/ejcts/ezaa049.
218. Jayaraman, P.P.; Forkan, A.R.M.; Morshed, A.; Haghghi, P.D.; Kang, Y.B. Healthcare 4.0: A review of frontiers in digital health. *Wires Data Min Knowl* **2020**, *10*, doi:Artn E1350
- 10.1002/Widm.1350.
219. Chen, Y.; McElvain, L.E.; Tolpygo, A.S.; Ferrante, D.; Friedman, B.; Mitra, P.P.; Karten, H.J.; Freund, Y.; Kleinfeld, D. An active texture-based digital atlas enables automated mapping of structures and markers across brains. *Nature methods* **2019**, *16*, 341-350, doi:10.1038/s41592-019-0328-8.
220. Jiang, F.; Jiang, Y.; Zhi, H.; Dong, Y.; Li, H.; Ma, S.F.; Wang, Y.L.; Dong, Q.; Shen, H.P.; Wang, Y.J. Artificial intelligence in healthcare: past, present and future. *Stroke Vasc Neurol* **2017**, *2*, 230-243, doi:10.1136/svn-2017-000101.
221. Bal, M.; Amasyali, M.F.; Sever, H.; Kose, G.; Demirhan, A. Performance Evaluation of the Machine Learning Algorithms Used in Inference Mechanism of a Medical Decision Support System. *Sci World J* **2014**, doi:Artn 137896
- 10.1155/2014/137896.
222. Oikonomou, E.K.; Siddique, M.; Antoniadou, C. Artificial intelligence in medical imaging: A radiomic guide to precision phenotyping of cardiovascular disease. *Cardiovasc Res* **2020**, *116*, 2040-2054, doi:10.1093/cvr/cvaa021.
223. Knott, K.D.; Seraphim, A.; Augusto, J.B.; Xue, H.; Chacko, L.; Aung, N.; Petersen, S.E.; Cooper, J.A.; Manisty, C.; Bhuva, A.N.; et al. The Prognostic Significance of Quantitative Myocardial Perfusion An Artificial Intelligence-Based Approach Using Perfusion Mapping. *Circulation* **2020**, *141*, 1282-1291, doi:10.1161/Circulationaha.119.044666.
224. Genovese, D.; Rashedi, N.; Weinert, L.; Narang, A.; Addetia, K.; Patel, A.R.; Prater, D.; Goncalves, A.; Mor-Avi, V.; Lang, R.M. Machine Learning-Based Three-Dimensional Echocardiographic Quantification of Right Ventricular Size and Function: Validation Against Cardiac Magnetic Resonance. *Journal of the American Society of Echocardiography : official publication of the American Society of Echocardiography* **2019**, *32*, 969-977, doi:10.1016/j.echo.2019.04.001.
225. Hinton, R.B.; Ware, S.M. Heart Failure in Pediatric Patients With Congenital Heart Disease. *Circulation research* **2017**, *120*, 978-994, doi:10.1161/Circresaha.116.308996.
226. Lo Muzio, F.P.; Rozzi, G.; Rossi, S.; Luciani, G.B.; Foresti, R.; Cabassi, A.; Fassina, L.; Miragoli, M. Artificial Intelligence Supports Decision Making during Open-Chest Surgery of Rare Congenital Heart Defects. *J Clin Med* **2021**, *10*, doi:Artn 5330
- 10.3390/Jcm10225330.
227. Sevakula, R.K.; Au-Yeung, W.T.M.; Singh, J.P.; Heist, E.K.; Isselbacher, E.M.; Armoundas, A.A. State-of-the-Art Machine Learning Techniques Aiming to Improve Patient Outcomes Pertaining to the Cardiovascular System. *J Am Heart Assoc* **2020**, *9*, doi:10.1161/Jaha.119.013924.
228. Lu, Z.Q.J. The Elements of Statistical Learning: Data Mining, Inference, and Prediction, 2nd edition. *J R Stat Soc a Stat* **2010**, *173*, 693-694.

229. Freund, Y.; Schapire, R.E. A decision-theoretic generalization of on-line learning and an application to boosting. *J Comput Syst Sci* **1997**, *55*, 119-139, doi:DOI 10.1006/jcss.1997.1504.
230. Seiffert, C.; Khoshgoftaar, T.M.; Van Hulse, J.; Napolitano, A. RUSBoost: Improving Classification Performance when Training Data is Skewed. *Int C Patt Recog* **2008**, 3650-3653.
231. Melillo, P.; Fusco, R.; Sansone, M.; Bracale, M.; Pecchia, L. Discrimination power of long-term heart rate variability measures for chronic heart failure detection. *Med Biol Eng Comput* **2011**, *49*, 67-74, doi:10.1007/s11517-010-0728-5.
232. Melillo, P.; Izzo, R.; Orrico, A.; Scala, P.; Attanasio, M.; Mirra, M.; De Luca, N.; Pecchia, L. Automatic Prediction of Cardiovascular and Cerebrovascular Events Using Heart Rate Variability Analysis. *PloS one* **2015**, *10*, doi:ARTN e0118504
10.1371/journal.pone.0118504.
233. Ali, L.; Khan, S.U.; Golilarz, N.A.; Yakubu, I.; Qasim, I.; Noor, A.; Nour, R. A Feature-Driven Decision Support System for Heart Failure Prediction Based on chi 2 Statistical Model and Gaussian Naive Bayes. *Comput Math Method M* **2019**, *2019*, doi:Artn 6314328
10.1155/2019/6314328.
234. Dutta, S.; Chatterjee, A.; Munshi, S. Correlation technique and least square support vector machine combine for frequency domain based ECG beat classification. *Med Eng Phys* **2010**, *32*, 1161-1169, doi:10.1016/j.medengphy.2010.08.007.
235. Liu, G.; Wang, L.; Wang, Q.; Zhou, G.; Wang, Y.; Jiang, Q. A new approach to detect congestive heart failure using short-term heart rate variability measures. *PloS one* **2014**, *9*, e93399, doi:10.1371/journal.pone.0093399.
236. Saini, I.; Singh, D.; Khosla, A. QRS detection using K-Nearest Neighbor algorithm (KNN) and evaluation on standard ECG databases. *Journal of advanced research* **2013**, *4*, 331-344, doi:10.1016/j.jare.2012.05.007.
237. Alshakhs, F.; Alharthi, H.; Aslam, N.; Khan, I.U.; Elasheri, M. Predicting Postoperative Length of Stay for Isolated Coronary Artery Bypass Graft Patients Using Machine Learning. *International journal of general medicine* **2020**, *13*, 751-762, doi:10.2147/IJGM.S250334.
238. Tseng, P.Y.; Chen, Y.T.; Wang, C.H.; Chiu, K.M.; Peng, Y.S.; Hsu, S.P.; Chen, K.L.; Yang, C.Y.; Lee, O.K.S. Prediction of the development of acute kidney injury following cardiac surgery by machine learning. *Crit Care* **2020**, *24*, doi:ARTN 478
10.1186/s13054-020-03179-9.
239. Fernandes, M.P.B.; Armengol de la Hoz, M.; Rangasamy, V.; Subramaniam, B. Machine Learning Models with Preoperative Risk Factors and Intraoperative Hypotension Parameters Predict Mortality After Cardiac Surgery. *Journal of cardiothoracic and vascular anesthesia* **2021**, *35*, 857-865, doi:10.1053/j.jvca.2020.07.029.
240. Konopelski, P.; Ufnal, M. Electrocardiography in rats: a comparison to human. *Physiological research* **2016**, *65*, 717-725, doi:10.33549/physiolres.933270.
241. Tretter, J.T.; Redington, A.N. The Forgotten Ventricle? The Left Ventricle in Right-Sided Congenital Heart Disease. *Circulation. Cardiovascular imaging* **2018**, *11*, e007410, doi:10.1161/CIRCIMAGING.117.007410.

242. Friedberg, M.K. Imaging Right-Left Ventricular Interactions. *JACC. Cardiovascular imaging* **2018**, *11*, 755-771, doi:10.1016/j.jcmg.2018.01.028.
243. Claus, P.; Omar, A.M.S.; Pedrizzetti, G.; Sengupta, P.P.; Nagel, E. Tissue Tracking Technology for Assessing Cardiac Mechanics: Principles, Normal Values, and Clinical Applications. *JACC. Cardiovascular imaging* **2015**, *8*, 1444-1460, doi:10.1016/j.jcmg.2015.11.001.
244. Eichhorn, E.J.; Bristow, M.R. Medical therapy can improve the biological properties of the chronically failing heart - A new era in the treatment of heart failure. *Circulation* **1996**, *94*, 2285-2296, doi:Doi 10.1161/01.Cir.94.9.2285.
245. Katz, A.M. Cardiomyopathy of overload. A major determinant of prognosis in congestive heart failure. *The New England journal of medicine* **1990**, *322*, 100-110, doi:10.1056/NEJM199001113220206.

Acknowledgments

I would like to thank the people I worked with during my PhD and that have played an important role in my scientific education throughout these years.

First, I want to thank Professor Michele Miragoli for the opportunity he provided me when I was just a Master of Science student: working in his team paved the way for my career and contributed to my decision to become a research scientist. I would especially like to thank you for showing me how the research world works and for your precious supervision during these years.

Then, I want to thank Professor Giovanni Battista Luciani and the University of Verona for the opportunity to pursue my education in the cardiovascular research field and perform high quality research in both the Universities of Verona and Parma. In particular, I want to thank Professor Luciani for providing the clinical perspective behind my work and for giving me one of the greatest experiences in my life: entering the operating room and assist an open chest cardiac surgery.

I want to thank doctors Alessio Alogna and Alessandro Faragli for the opportunity to boost my career by working on their projects and for believing in me and my skills. I never told anybody, and maybe it was just a phase that any PhD student goes through, but before collaborating with you I was wondering if I should consider quitting research. Working with you lighted a fire inside me and provided the confidence I needed to complete my PhD education.

I want to thank Giacomo Rozzi because he started the Vi.Ki.E. project and for being the main reason behind the solid collaboration with all the medical teams we worked with during both our PhDs. As a collaborator and a friend, you also provided some of the best memories during these years and I am grateful to have met you.

I want to thank Amparo Guerrero Gerbolès and Cristina Caffarra for putting up with me during these years. Your kindness was a relief when I was feeling down because of work or personal stuff.

Finally, I want to thank Stefano Rossi for his mentoring during my PhD. As professor Miragoli, he showed me how the research world works and taught me some very important life lessons.


To conclude, I would like to thank the most important people in my life. My parents, sister and grandparents that never stopped believing in me and always supported my dream to pursue a career in research. I would not be the man I am today without your support.

Finally, I want to thank Alice because she put up with me during these years especially when I was at my lowest and for the support she always showed.

Francesco P. Lo Murro



Cardiovascular magnetic resonance feature tracking in pigs: a reproducibility and sample size calculation study

A. Faragli^{1,2,3} · R. Tanacli⁴ · C. Kolp¹ · T. Lapinskas^{4,5} · C. Stehning⁶ · B. Schnackenburg⁶ · F. P. Lo Muzio^{7,8} · S. Perna⁹ · B. Pieske^{1,2,3,4} · E. Nagel¹⁰ · H. Post^{1,2,3,11} · S. Kelle^{1,2,3} · A. Alogna^{1,2,3} 

Received: 1 November 2019 / Accepted: 2 January 2020 / Published online: 16 January 2020
© The Author(s) 2020

Abstract

Cardiovascular magnetic resonance feature tracking (CMR-FT) is a novel technique for non-invasive assessment of myocardial motion and deformation. Although CMR-FT is standardized in humans, literature on comparative analysis from animal models is scarce. In this study, we measured the reproducibility of global strain under various inotropic states and the sample size needed to test its relative changes in pigs. Ten anesthetized healthy Landrace pigs were investigated. After baseline (BL), two further steps were performed: (I) dobutamine-induced hyper-contractility (Dob) and (II) verapamil-induced hypocontractility (Ver). Global longitudinal (GLS), circumferential (GCS) and radial strain (GRS) were assessed. This study shows a good to excellent inter- and intra-observer reproducibility of CMR-FT in pigs under various inotropic states. The highest inter-observer reproducibility was observed for GLS at both BL (ICC 0.88) and Ver (ICC 0.79). According to the sample size calculation for GLS, a small number of animals could be used for future trials.

Keywords Cardiovascular magnetic resonance · Feature tracking · Left ventricular strain · Reproducibility · Sample size · Porcine model

Introduction

Myocardial strain has been demonstrated as an effective method for the assessment of the regional myocardial function and deformation, and in particular, the cardiovascular magnetic resonance (CMR) tissue tracking approach has

S. Kelle and A. Alogna have equally contributed to this work.

✉ A. Alogna
alessio.alogna@charite.de

¹ Department of Internal Medicine and Cardiology, Charité – Universitätsmedizin Berlin, Campus Virchow-Klinikum, Augustenburgerplatz 1, 13353 Berlin, Germany

² Berlin Institute of Health (BIH), Berlin, Germany

³ DZHK (German Centre for Cardiovascular Research), partner site, Berlin, Germany

⁴ Department of Internal Medicine / Cardiology, Deutsches Herzzentrum Berlin, Augustenburger Platz 1, 13353 Berlin, Germany

⁵ Department of Cardiology, Medical Academy, Lithuanian University of Health Sciences, Eiveniu Street 2, 50161 Kaunas, Lithuania

⁶ Clinical Science, Philips Healthcare, Röntgenstr. 24, 22335 Hamburg, Germany

⁷ Department of Surgery, Dentistry, Paediatrics and Gynaecology, University of Verona, Via S. Francesco 22, 37129 Verona, Italy

⁸ Department of Medicine and Surgery, University of Parma, Via Gramsci 14, 43126 Parma, Italy

⁹ Department of Biology, College of Science, University of Bahrain, Sakhir Campus, P.O. Box 32038, Zallaq, Bahrain

¹⁰ Institute of Experimental and Translational Cardiac Imaging, DZHK Centre for Cardiovascular Imaging, Goethe University Hospital Frankfurt, Theodor-Stern-Kai 7, 60590 Frankfurt, Germany

¹¹ Department of Cardiology, Contilia Heart and Vessel Centre, St. Marien-Hospital Mülheim, Kaiserstraße 50, 45468 Mülheim, Germany

been established as a technique comparable to the highly validated speckle tracking echocardiography [19]. CMR feature tracking (CMR-FT) is a relatively novel technique that focuses on endocardial and epicardial contouring and is able to detect the contrast between myocardium and blood pool [4, 14]. CMR-FT has been validated against myocardial tagging technique for the assessment of regional myocardial motion in humans [8, 12, 17]. As every new technique CMR-FT has been widely tested for reproducibility, and what has been already shown in human is the excellent inter- and intra-observer reproducibility, for different parameters and at different field strength MRI scanners [13, 20, 21]. However, since CMR is becoming widely utilized in animal research, there is a lack of standardization, a lack of reference databases and a lack of reproducibility studies. For this reason, a previous study from our group demonstrated the high reproducibility of strain measurements through feature tracking in a model of small animals (mice) which has already been acknowledged in the recent guidelines for animal research [9, 10]. Nonetheless, the main limitation of this previous study was indeed the model, recognized to be not translational enough for a comparison with the humans, in particular regarding the assessment of myocardial function. Large animals, such as Landrace pigs, are instead more suited to investigate myocardial function under various pharmacological interventions given a cardiac anatomy and physiology closer to humans. There is only one study in the literature that has assessed the reproducibility of myocardial deformation parameters in large animals (macaque) [15] and no studies have performed such an analysis in pigs. Accordingly, we performed this preliminary study to evaluate inter- and intra-observer reproducibility of CMR-FT derived strain measurements in a porcine model of pharmacologically induced hyper- and hypo-contraction. Furthermore, we performed a sample size calculation based on global strain values useful to define the number of animals required for future studies.

Methods

Data from ten Landrace pigs were selected from an ongoing experiment at our center. The experimental protocols were approved by the local bioethics committee of Berlin, Germany (G0138/17), and conform to the “European Convention for the Protection of Vertebrate Animals used for Experimental and other Scientific Purposes” (Council of Europe No 123, Strasbourg 1985).

Experimental setup

Briefly, female Landrace pigs ($n = 10$, 51 ± 10 kg) were fasted overnight with free access to water, sedated and intubated on the day of the experiment. Anesthesia was

continued with isoflurane, fentanyl, midazolam, ketamine and pancuronium. Pigs were ventilated (Cato, Dräger Medical, Germany) with a FiO_2 of 0.5, an I: E-ratio of 1:1.5, the positive end-expiratory pressure was set at 5 mmHg and a tidal volume (VT) of 10 ml kg^{-1} . The respiratory rate was adjusted constantly to maintain an end-expiratory carbon dioxide partial pressure between 35 and 45 mmHg. Under fluoroscopic guidance all animals were instrumented with a floating balloon catheter in the right atrium as well as in the coronary sinus (Arrow Balloon Wedge-Pressure Catheters, Teleflex Inc USA). In order to avoid MRI artefacts, the balloon-tip was cut before introducing the catheters in the vessel. Respiratory gases (PM 8050 MRI, Dräger Medical, Germany), heart rate and arterial blood pressure continuously monitored. Body temperature was monitored by a sublingual thermometer and was maintained at 38°C during CMR imaging via air ventilation and/or infusion of cold saline solution. The experimental setup can be visualized in Fig. 1a, b.

Experimental protocols

After acute instrumentation the animals were transported to the MRI facility for measurements, pigs were ventilated with an MRI compatible machine (Titus, Dräger Medical, Germany) (see Fig. 1c, d). After baseline measurements (BL), two steps were performed: (I) dobutamine-induced hypercontractility (Dob) and (II) verapamil-induced hypocontractility (Ver). At each protocol, MRI images were acquired at short axis (SAX), two chambers (2Ch), three chambers (3Ch) and four chambers (4Ch) views. After the MRI measurements were concluded the animals were transported back to the operating room for sacrifice.

Cardiac magnetic resonance

All CMR images were acquired in a supine position using a 3 Tesla (3 T) (Achieva, Philips Healthcare, Best, The Netherlands) MRI scanner with an anterior- and the built-in posterior coil element, where up to 30 coil elements were employed, depending on the respective anatomy. All animals were scanned using identical comprehensive imaging protocol. The study protocol included initial scouts to determine cardiac imaging planes. Cine images were acquired using ECG-gated balanced steady state free precession (bSSFP) sequence in three left ventricular (LV) long-axis (two-chamber, three-chamber and four-chamber) planes. The ventricular two-chamber and four-chamber planes were used to plan stack of short-axis slices covering entire LV. The following imaging parameters were used: repetition time (TR) = 2.9 ms, echo time (TE) = 1.45 ms, flip angle = 45° , voxel size = $1.9 \times 1.9 \times 8.0 \text{ mm}^3$ and 40 phases per cardiac cycle.

Fig. 1 The experimental setting. The animals were acutely instrumented closed chest in the operating room (a, b) and then transported to the MRI facility where anesthesia and monitoring was maintained during the whole experimental protocol (c, d)

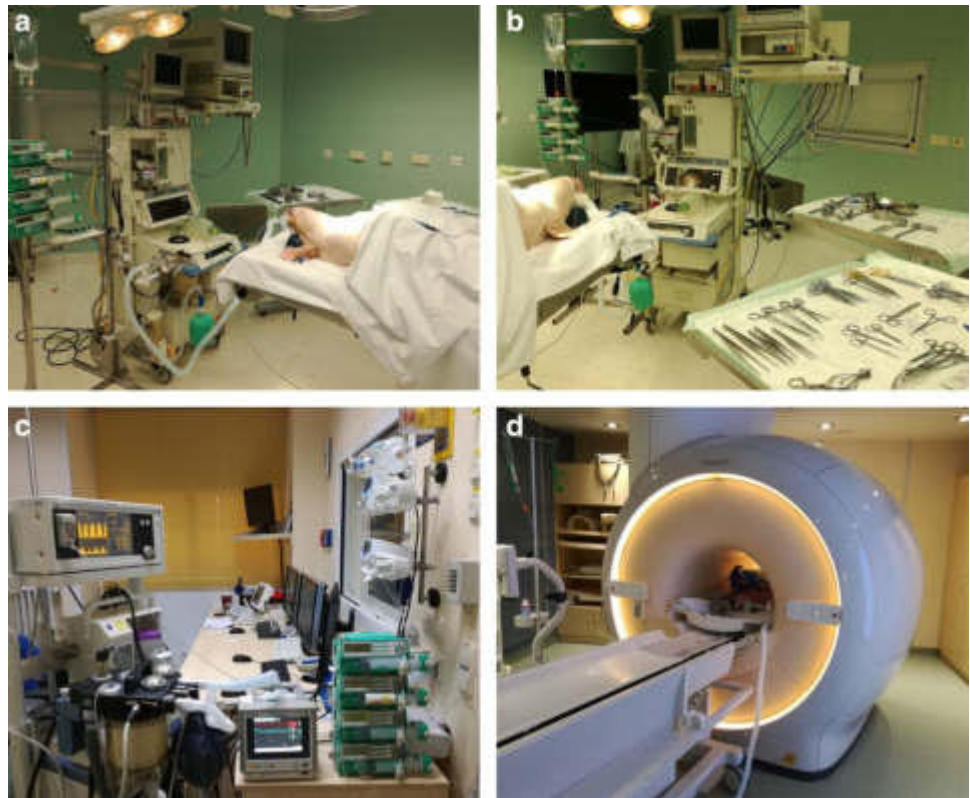


Image analysis

All images were analyzed offline using commercially available software (Medis Suite, version 3.1, Leiden, The Netherlands) in accordance to recent consensus document for quantification of LV function using CMR. In the strain analysis were included 2Ch, 3Ch and 4Ch cine images, and respectively, three preselected mid-ventricle slices from the LV short-axis stack. The endocardial and epicardial contours drawn on cine images with QMass version 8.1 were transferred to QStrain RE version 2.0, where after the application of tissue tracking algorithm endocardial and epicardial borders were detected throughout all the cardiac cycle. These long-axis cine images were further used to compute global myocardial longitudinal (GLS) strain and short-axis images were used to compute circumferential (GCS) and radial (GRS) strain and strain-rate. The global values were obtained through averaging the values according to an AHA 17 segments model, apex being excluded, as follows: GCS and GRS from averaging CS and RS for 6 basal, 6 mid and 4 apical segmental individual values; GLS from 2Ch, 3Ch and 4Ch averaging 6 basal, 6 mid and 4 apical segments using a bull-eye view.

Statistical analysis

Data were analyzed using Microsoft Excel and IBM SPSS Statistics version 23.0 software (SPSS Inc., Chicago, IL, USA) for Windows. Figures 1, 2, 3, 4 were made with Microsoft PowerPoint version 17, while Figs. 2, 3 were made with GraphPad Prism version 8. All data are presented as mean \pm SD. Data between groups at different inotropic states were analyzed by one-way ANOVA for repeated measurements. Post-hoc testing was performed by Tukey's test. A p-value < 0.05 was considered significant.

Reproducibility testing

Data are expressed as mean \pm standard deviation (SD). The Shapiro–Wilk test was used to determine whether the data were normally distributed. Nonparametric variables were compared using the Wilcoxon test. A p-value of < 0.05 was considered statistically significant. Inter- and intra-observer reproducibility was quantified using intra-class correlation coefficient (ICC) and Bland–Altman analysis (13). Agreement was considered excellent for ICC > 0.74 , good for ICC 0.60–0.74, fair for ICC 0.40–0.59, and poor for ICC < 0.40 .

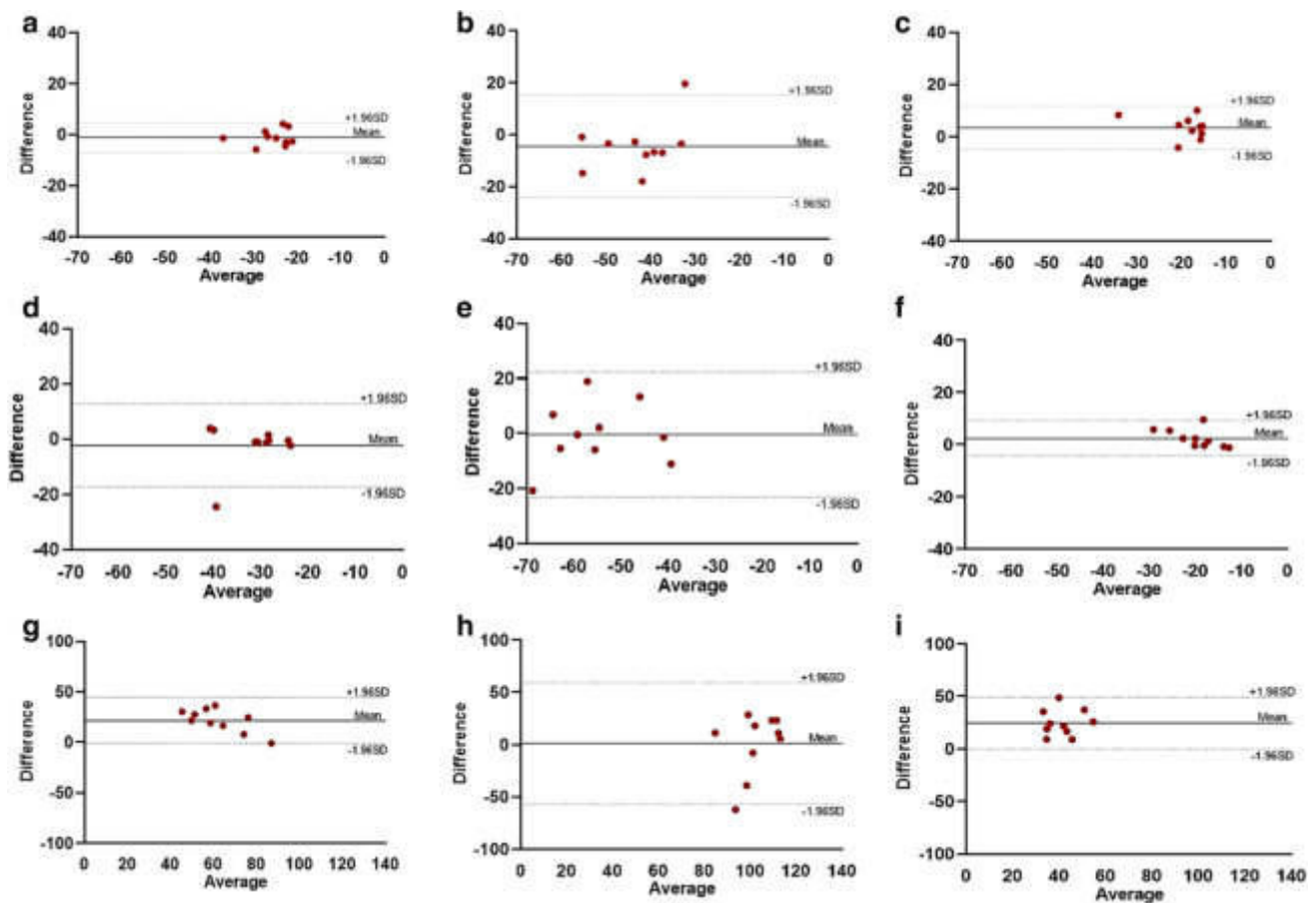


Fig. 2 Bland–Altman plots for inter-observer reproducibility of global strain values. Bland–Altman plots showing inter-observer reproducibility for GLS (top row, panels a–c), GCS (middle row, panels d–f) and GRS analysis (bottom row, panels g–i) during BL, Dob

and Ver steps respectively. *BL* baseline, *Dob* Dobutamine, *Ver* Verapamil, *GLS* global longitudinal strain, *GCS* global circumferential strain, *GRS* global radial strain

(14). To assess intra-observer agreement data analysis was repeated after 4 weeks. All the operators took the measurements twice and the average values were taken.

Sample size calculation

Study sample size required to detect a relative 5, 8 and 10% change in strain with power of 80% and significance of 5% was calculated as follows (15):

$$n = f(\alpha, P)\sigma^2/\delta$$

where n is the sample size, α the significance level, P the study power required and f the value of the factor for different values of α and P ($f = 10.5$ for $\alpha = 0.05$ and $p = 0.080$), with σ the standard deviation of differences in measurements between two studies and δ the desired difference to be detected. Sample size calculation was performed for baseline values only.

Results

The volumetric and functional parameters of study population are summarized in Table 1. All studies were completed, and image quality was sufficient to perform CMR-FT analysis. Table 2 demonstrates CMR-FT derived strain parameters obtained by two independent investigators.

Inter-observer and intra-observer reproducibility

Mean differences \pm SD, limits of agreement and ICC for strain parameters are given in Table 3. There was an excellent inter-observer reproducibility for GLS during BL and Ver steps, while during Dob the observed reproducibility was good. Regarding the GCS analysis, there was a good reproducibility during BL and Ver steps; while during Dob, the reproducibility was only fair. The GRS analysis showed, instead, an excellent reproducibility for BL, while during Dob and Ver steps the reproducibility was poor. Concerning the intra-observer analysis, the level of reproducibility was

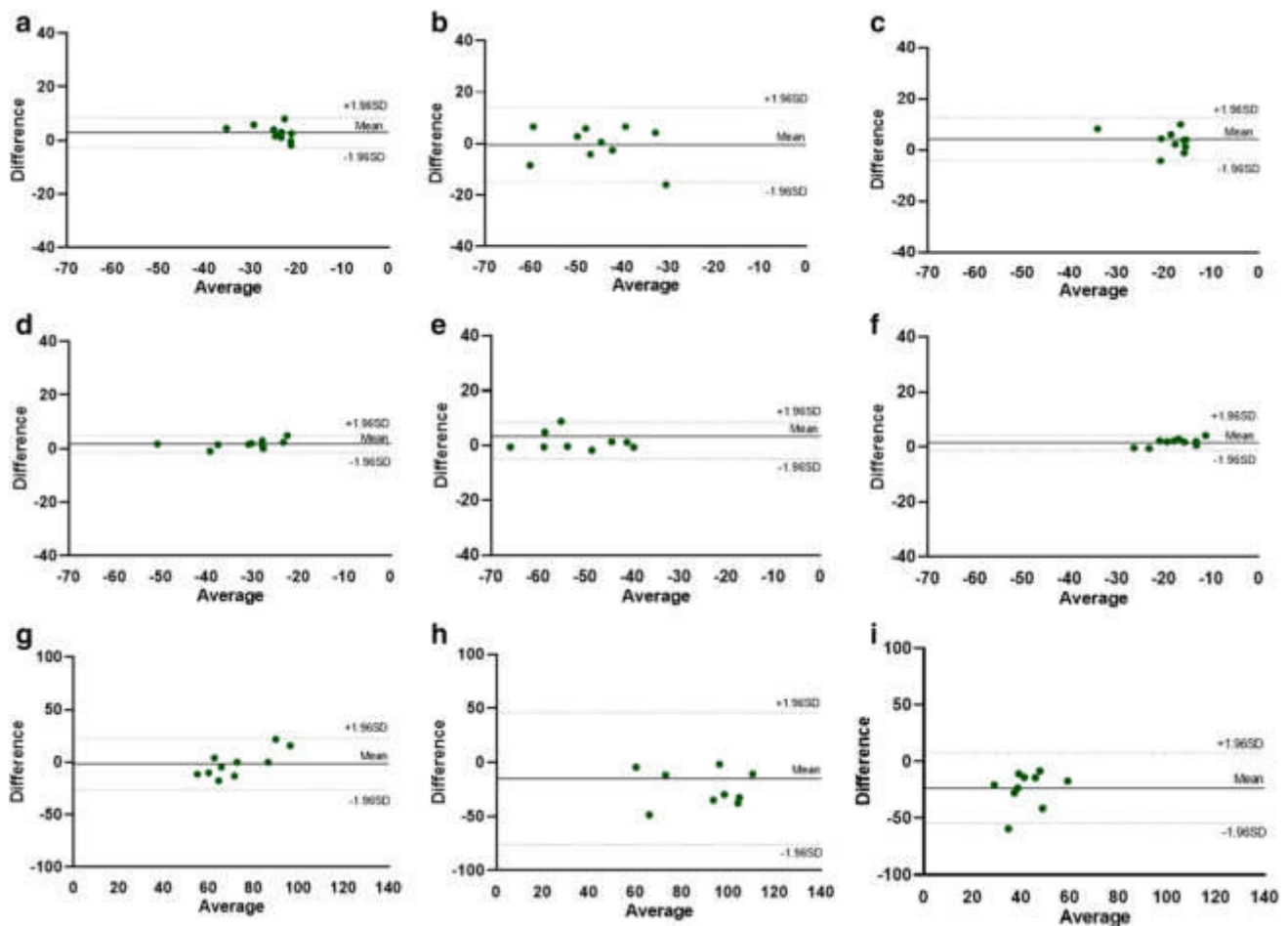


Fig. 3 Bland–Altman plots for intra-observer reproducibility of global strain values. Bland–Altman plots showing intra-observer reproducibility for GLS (top row, panels a–c), GCS (middle row, panels d–f) and GRS analysis (bottom row, panels g–i) during BL, Dob

and Ver steps respectively. *BL* baseline, *Dob* Dobutamine, *Ver* Verapamil, *GLS* global longitudinal strain, *GCS* global circumferential strain, *GRS* global radial strain

generally excellent for most of the measurements. GLS and GCS showed an excellent reproducibility for all steps, while GRS showed an excellent reproducibility during BL, a good one during Dob and a poor one during Ver. Bland–Altman plots demonstrate inter-observer and intra-observer reproducibility for GLS, GCS and GRS analysis during BL, Dob and Ver steps (see Figs. 2, 3).

Sample size calculation for baseline values

The change in reproducibility has an impact on the sample size required to detect significant differences in strain parameters. Table 4 lists the required sample sizes for each strain-derived parameter. For example, to show a relative 10% change in GLS in pigs would require five animals (not measures—Fig. 4). In contrast, 20 pigs are required to detect a 5% change in GLS with CMR-FT (power of 80% and α error of 0.05).

Discussion

While studies analyzing reproducibility of CMR-FT in humans are already present in the literature [3, 16], works on the reproducibility of myocardial deformation parameters of large animal models are, instead, lacking. The current study was designed, therefore, to assess the inter-observer and intra-observer reproducibility of CMR-FT for the analysis of global LV strain in a porcine model of hyper- and hypo-contractility. Here we show a good to excellent inter- and intra-observer reproducibility of CMR-FT technique in pigs under different inotropic states. Furthermore, sample size calculation demonstrates that for GLS analysis a small number of animals could be enough for future trials. A previous study from our group has demonstrated a high reproducibility in the LV strain measurements in a murine model [9]. This current study provides a more extensive analysis in pigs and confirms the previous one regarding the most reproducible parameters derived from

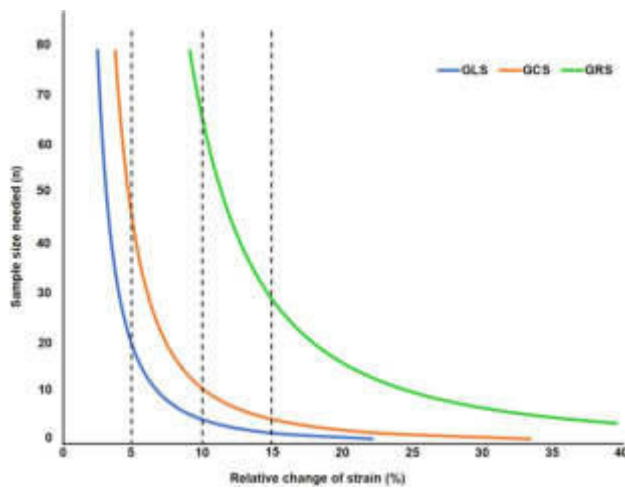


Fig. 4 Graphical representation of the sample size calculation for global strain values. Representation of the sample size calculation for GLS (blue), GCS (red) and GRS (green) baseline measurements to detect the desired % relative change of strain with 80% power and α error of 0.05. Dashed lines represent the relative change of strain at 5%, 10% and 15% respectively. *GLS* global longitudinal strain, *GCS* global circumferential strain, *GRS* global radial strain

Table 1 Volumetric and functional characteristics of study subjects

Parameter	Value	
Study population	10	
LV EDV (ml)	BL	101 ± 24
	Dob	83 ± 21*
	Ver	108 ± 25 [†]
LV ESV (ml)	BL	41 ± 10
	Dob	19 ± 7*
	Ver	66 ± 18* [†]
LV SV (ml)	BL	60 ± 19
	Dob	64 ± 18
	Ver	42 ± 12* [†]
LV EF (%)	BL	59 ± 8
	Dob	77 ± 7*
	Ver	39 ± 9* [†]
Cardiac output (l/min)	BL	6 ± 1
	Dob	9 ± 2*
	Ver	4 ± 1* [†]
Heart rate (bpm)	BL	106 ± 15
	Dob	146 ± 12*
	Ver	98 ± 19 [†]
LV Mass (g)	81 ± 20	

Results are reported as mean ± standard deviation

BL baseline, Dob Dobutamine, EDV end-diastolic volume, EF ejection fraction, ESV end-systolic volume, LV left ventricle/ventricular SV stroke volume, Ver Verapamil

*p-value < 0.05 versus BL

[†]p-value < 0.05 versus Dob

CMR-FT. Good to excellent inter-observer reproducibility was found for global longitudinal and global circumferential strain, whereas radial strain confirms, instead, to be highly variable between repeated measurements, in particular when considering the inter-observers measurements. The weak reproducibility of radial strain has also been reported in previous studies [2, 16, 23, 28]. While global longitudinal strain was the most reproducible parameter during the inter-observer analysis, the intra-observer reproducibility was predictably higher for most of the strain values and excellent for global circumferential strain, as already described in previous studies [13, 22]. In a previous study from our group, we were able to show the positive additional role of LV strain analysis during dobutamine stress in a group of patients with coronary artery disease [18]. A good reproducibility and a low inter-observer variability of dobutamine stress Echo and CMR has been previously observed in human [21, 26] and animal studies [15]. However, only few studies concentrated on the reproducibility of LV strain in hyper- and hypo-contraction model. With this study, we were able to assess the reproducibility of the LV strain measurements under various inotropic states. During the infusion of dobutamine, aiming at an increase of at least 25% of the baseline HR, we were able to observe a clinically significant increase in LV EF and LV cardiac output. In our study, the high HR obtained during dobutamine infusion (mean 146 ± 12 bpm) was, however, detrimental to the reproducibility of the measurements when measured by another observer. This can be explained by a worse resolution of the MRI processed images and by an increase in frame rates under such fast heart beats, as already described in other studies [7, 15]. In one of the studies by Schuster et al. a high reproducibility of CMR-FT in a group of ischemic cardiomyopathy patients after dobutamine infusion for stress test was observed [21]. Nevertheless, it is worth to mention that in that study no reference to the heart rate at which the sequences were recorded was mentioned, making the comparison with our model not consistent. In our study, we were able to show that at lower heart rates, such as during baseline state and verapamil infusion, the reproducibility was generally higher for all the strain values. With the advent, development and availability of computers, large datasets can be used in statistical analysis to calculate the sample sizes necessary for clinical studies. Sample size calculation is an important aspect of study design and enables determination of how large the study sample should be. Estimates of required sample size depend on the variability of the population—the greater the variability, the larger the required sample size. This is particularly relevant for CMR studies, where the role of sample size is extremely useful to test the reliability of new imaging techniques [11, 16]. The same should be applicable to animal studies, where the reduction of the numbers of animals used is of extreme value [25]. In some cases, by using previously published studies, the use of animals can be totally avoided by eliminating unnecessary replications [1]. Modern

Table 2 Comparison of CMR-FT derived average of global strain parameters obtained by observers in ten pigs during BL, Dob and Ver steps

Measurements obtained by two observers (inter-observer level)		
	First observer	Second observer
BL (%)		
GLS	-26.1 ± 5	-25.1 ± 4
GCS	-32.7 ± 8	-30.4 ± 6
GRS	73.3 ± 9	51.5 ± 17
Dob (%)		
GLS	$-45.1 \pm 11^*$	$-40.6 \pm 7^*$
GCS	-55.1 ± 12	$-54.7 \pm 10^*$
GRS	103.0 ± 20	$101.8 \pm 14^*$
Ver (%)		
GLS	$-20.8 \pm 6^\dagger$	$-17.3 \pm 5^{*\dagger}$
GCS	$-18.6 \pm 4^\dagger$	$-21.0 \pm 6^{*\dagger}$
GRS	$53.9 \pm 10^\dagger$	$29.1 \pm 9^{*\dagger}$
Measurements obtained by one observer (intra-observer level)		
	First measurement	Second measurement
BL (%)		
GLS	-26.1 ± 5	-23.3 ± 4
GCS	-32.7 ± 8	-31.0 ± 8
GRS	73.3 ± 9	71.7 ± 19
Dob (%)		
GLS	$-45.1 \pm 11^*$	$-45.6 \pm 9^*$
GCS	-55.1 ± 12	$-53.3 \pm 11^*$
GRS	103.0 ± 20	87.9 ± 36
Ver (%)		
GLS	$-20.8 \pm 6^\dagger$	$-16.5 \pm 3^{*\dagger}$
GCS	$-18.6 \pm 4^\dagger$	$-16.9 \pm 5^{*\dagger}$
GRS	$53.9 \pm 10^\dagger$	$30.3 \pm 13^{*\dagger}$

All the operators took the measurements twice and the average values were taken

BL baseline, Dob Dobutamine, GCS global circumferential strain, GLS global longitudinal strain, GRS global radial strain, Ver Verapamil

*p-value < 0.05 versus BL

†p value < 0.05 versus Dob

imaging techniques in conjunction with new statistical analysis methods also allow reductions in the numbers of animals used, for example, by providing greater information per animal [27]. Too small sample size can miss the real effect, whereas too large sample size leads to unnecessary waste of time and resources (animals) [1, 25, 27]. In the already published pilot study on sample size calculation and variability in small animals by our study group, we demonstrated that the number of animals needed to test a hypothesis could be reduced if the effect of animal-to-animal variation on the measurement is eliminated or highly reduced [9]. With the present study, we were able to show that in this cohort a relatively small sample size of animals (not measures) is required to detect a 5, 10 and 15% change in strain parameters for global longitudinal strain. We also observed that a higher sample size is necessary for circumferential strain, and particularly high for radial strain.

The ability to apply human-like settings to model animals increases the chances of translation of new effective diagnostic and therapeutic interventions [24]. The importance of large animal research in the field of human diseases is evident in most medical settings, however, this holds particularly true for cardiology where in terms of anatomy, physiology and size, large animals such as pigs represent the closest comparison to humans [24]. In the European Union, the Directive 2010/63/EU voted in 2010 has been implemented in 2013 in the European Medicines Agency (EMA) guidelines, resulting in restrictions in the use of nonhuman primates in biomedical research (EMA 2014) and promoting instead the utilization of non-rodents species such as pigs and sheep that should be chosen based on their similarity to humans with regard to in vitro metabolic profile [6]. In order to appropriately assure translational success and safety, at least two animal species that are

Table 3 Inter-observer and intra-observer reproducibility for GLS, GCS and GRS

	Parameter	Steps	Mean difference \pm SD	Limits of agreement	ICC (95% CI)
Inter-observer variability	GLS	BL	-1.0 ± 3.0	-6.9 to 4.8	0.88 (0.57–0.97)
		Dob	-4.5 ± 10.0	-24.1 to 15.1	0.60 (-0.35 to 0.89)
		Ver	3.5 ± 4.2	-4.7 to 11.7	0.79 (0.10–0.95)
	GCS	BL	-2.2 ± 7.6	-17.2 to 12.6	0.66 (-0.21 to 0.92)
		Dob	-0.4 ± 11.5	-23.0 to 22.2	0.51 (-0.23 to 0.87)
		Ver	2.4 ± 3.4	-4.3 to 9.2	0.61 (-0.40 to 0.90)
	GRS	BL	21.7 ± 11.6	-0.9 to 44.5	0.80 (0.21–0.95)
		Dob	1.2 ± 29.6	-56.9 to 59.3	-1.60 (-9.47 to 0.35)
		Ver	24.7 ± 12.6	0.1 to 49.4	0.24 (-2.03 to 0.81)
Intra-observer variability	GLS	BL	2.8 ± 2.9	-2.8 to 8.5	0.81 (0.41–0.95)
		Dob	-0.4 ± 7.3	-14.8 to 14.0	0.87 (0.45–0.96)
		Ver	4.3 ± 4.3	-4.1 to 12.7	0.75 (0.01–0.94)
	GCS	BL	1.7 ± 1.5	-1.3 to 4.7	0.98 (0.77–0.99)
		Dob	1.8 ± 3.4	-4.8 to 8.4	0.97 (0.89–0.99)
		Ver	1.6 ± 1.4	-1.1 to 4.4	0.95 (0.36–0.99)
	GRS	BL	-1.5 ± 12.7	-26.4 to 23.3	0.79 (0.15–0.94)
		Dob	-15.1 ± 31.1	-76.0 to 45.8	0.62 (-0.50 to 0.90)
		Ver	-23.6 ± 15.7	-54.4 to 7.2	0.14 (-2.43 to 0.78)

Results are reported as mean \pm standard deviation

BL baseline, CI confidence interval, Dob Dobutamine, GCS global circumferential strain, GLS global longitudinal strain, GRS global radial strain, ICC intra-class correlation coefficient, Ver Verapamil

Table 4 Sample size calculation for GLS, GCS and GRS (baseline measurements) to detect the desired % relative change with 80% power and α error of 0.05

	Mean difference \pm SD pooled	Sample size (n)		
		5%	10%	15%
GLS	-1.1 ± 4.9	20	5	2
GCS	-2.3 ± 7.4	45	11	5
GRS	21.7 ± 17.9	NA	68	30

The mean difference is calculated from the inter-observer mean difference analysis. The pooled SD has been obtained by applying Cohen formula: $SD_{\text{pooled}} = \sqrt{(SD_1^2 + SD_2^2)^{-1}}$

GCS global circumferential strain, GLS global longitudinal strain, GRS global radial strain, SD standard deviation

phylogenetically somewhat apart like a rodent and a non-rodent species are necessary. Without necessarily requiring closeness to man, this is the general rule supported by the current international guidelines like the International Council for Harmonization of Technical Requirements for Pharmaceuticals for Human Use, Guidance M3 (Revision 2; 2009) [6]. Nonetheless, the employment of large animal models carries ethical problems and higher costs, mainly because of the size of the animals and husbandry needed when compared to smaller models [24]. It is evident that all the necessary methods should be introduced to reduce, refine and replace the unnecessary animal experiments [5]. In accordance with the

3Rs principles on animal use (Directive 2010/63/EU), a scientifically satisfactory method or testing strategy, not entailing the use of live animals, should be used wherever possible [6]. For this reason, our preliminary study could be paving the road to the realization of an open access database of cardiovascular magnetic resonance data that could be of great need for future laboratory experiments, to reduce the number of animal experiments performed and to be utilized as a platform for simulation and testing of novel compounds. The experiments were performed during anesthesia, being a possible confounder for reproducibility of the measurements. The animals were not awake limiting the translation to clinical settings. The study is limited due to the small number of animals and larger sample size may be required to detect more subtle differences. The addition of a 25% dropout rate (proportion of eligible subjects who will not complete the study or provide only partial information) before planning a study will further increase the final sample size.

Conclusion

Global LV strain parameters analyzed by CMR-FT analyzed in a large animal model (pig) of hyper- and hypocontractility are highly reproducible. The most reproducible measures are global circumferential and global longitudinal strain, whereas reproducibility of radial strain is weak.

Sample size calculation are an essential tool that could help to reduce the number of animal experiments and databases on large animals can be used as a platform to test the effect of novel compounds.

Acknowledgements Open Access funding provided by Projekt DEAL. Burkert Pieske reports having received consultancy and lecture honoraria from Bayer Daiichi Sankyo, MSD, Novartis, Sanofi-Aventis, Stealth Peptides and Vifor Pharma; and editor honoraria from the Journal of the American College of Cardiology.

Author contributions AA, SK, HP conceived the experiment, AF, AA, SK, CK, CS conducted the experiments, AF, RT, AA, SP, CS, analyzed the results. All authors revised the manuscript.

Funding Alessandro Faragli, Heiner Post, Alessio Alogna and Sebastian Kelle received funding from DZHK (German Centre for Cardiovascular Research—Grant Number: 81X2100305).

Compliance with ethical standards

Conflict of interest All authors declare that they have no conflict of interest.

Ethical approval All institutional and national guidelines for the care and use of laboratory animals were followed and approved by the appropriate institutional committees. The experimental protocols were approved by the local bioethics committee of Berlin, Germany (G0138/17), and conform to the “European Convention for the Protection of Vertebrate Animals used for Experimental and other Scientific Purposes” (Council of Europe No 123, Strasbourg 1985).

Open Access This article is licensed under a Creative Commons Attribution 4.0 International License, which permits use, sharing, adaptation, distribution and reproduction in any medium or format, as long as you give appropriate credit to the original author(s) and the source, provide a link to the Creative Commons licence, and indicate if changes were made. The images or other third party material in this article are included in the article’s Creative Commons licence, unless indicated otherwise in a credit line to the material. If material is not included in the article’s Creative Commons licence and your intended use is not permitted by statutory regulation or exceeds the permitted use, you will need to obtain permission directly from the copyright holder. To view a copy of this licence, visit <http://creativecommons.org/licenses/by/4.0/>.

References

- Allgoewer A, Mayer B (2017) Sample size estimation for pilot animal experiments by using a Markov Chain Monte Carlo approach. *Alter Lab Anim* 45:83–90
- Barreiro-Pérez M, Curione D, Symons R et al (2018) Left ventricular global myocardial strain assessment comparing the reproducibility of four commercially available CMR-feature tracking algorithms. *Eur Radiol* 28:5137–5147
- Barreiro-Pérez M, Curione D, Symons R et al (2018) Left ventricular global myocardial strain assessment comparing the reproducibility of four commercially available CMR-feature tracking algorithms. *Eur Radiol* 28:5137–5147
- Claus P, Omar AMS, Pedrizzetti G et al (2015) Tissue tracking technology for assessing cardiac mechanics: principles, normal values, and clinical applications. *JACC Cardiovasc Imaging* 8:1444–1460
- Flecknell P (2002) Replacement, reduction and refinement. *Altex* 19:73–78
- Heining P, Ruyschaert T (2016) The use of minipig in drug discovery and development: pros and cons of minipig selection and strategies to use as a preferred nonrodent species. *Toxicol Pathol* 44:467–473
- Helle-Valle TM, Yu W-C, Fernandes VRS et al (2010) Usefulness of radial strain mapping by multidetector computer tomography to quantify regional myocardial function in patients with healed myocardial infarction. *Am J Cardiol* 106:483–491
- Kraitchman DL, Sampath S, Castillo E et al (2003) Quantitative ischemia detection during cardiac magnetic resonance stress testing by use of FastHARP. *Circulation* 107:2025–2030
- Lapinskas T, Grune J, Zamani SM et al (2017) Cardiovascular magnetic resonance feature tracking in small animals—a preliminary study on reproducibility and sample size calculation. *BMC Med Imaging* 17:51
- Lindsey ML, Kassiri Z, JaI V et al (2018) Guidelines for measuring cardiac physiology in mice. *Am J Physiol Heart Circ Physiol* 314:H733–H752
- Liu S, Han J, Nacif MS et al (2012) Diffuse myocardial fibrosis evaluation using cardiac magnetic resonance T1 mapping: sample size considerations for clinical trials. *J Cardiovasc Magn Res* 14:90
- Moody WE, Taylor RJ, Edwards NC et al (2015) Comparison of magnetic resonance feature tracking for systolic and diastolic strain and strain rate calculation with spatial modulation of magnetization imaging analysis. *J Magn Res Imaging* 41:1000–1012
- Morton G, Schuster A, Jogiya R et al (2012) Inter-study reproducibility of cardiovascular magnetic resonance myocardial feature tracking. *J Cardiovasc Magn Res* 14:43
- Pedrizzetti G, Claus P, Kilner PJ et al (2016) Principles of cardiovascular magnetic resonance feature tracking and echocardiographic speckle tracking for informed clinical use. *J Cardiovasc Magn Res* 18:51
- Sampath S, Parimal AS, Feng D et al (2017) Quantitative MRI biomarkers to characterize regional left ventricular perfusion and function in nonhuman primates during dobutamine-induced stress: a reproducibility and reliability study. *J Magn Res Imaging* 45:556–569
- Schmidt B, Dick A, Treutlein M et al (2017) Intra- and inter-observer reproducibility of global and regional magnetic resonance feature tracking derived strain parameters of the left and right ventricle. *Eur J Radiol* 89:97–105
- Schneeweis C, Lapinskas T, Schnackenburg B et al (2014) Comparison of myocardial tagging and feature tracking in patients with severe aortic stenosis. *J Heart Valve Dis* 23:432–440
- Schneeweis C, Qiu J, Schnackenburg B et al (2014) Value of additional strain analysis with feature tracking in dobutamine stress cardiovascular magnetic resonance for detecting coronary artery disease. *J Cardiovasc Magn* 16:72
- Schuster A, Hor Kan N, Kowallick Johannes T et al (2016) Cardiovascular magnetic resonance myocardial feature tracking. *circulation*. *Cardiovasc Imaging* 9:e004077
- Schuster A, Morton G, Hussain ST et al (2013) The intra-observer reproducibility of cardiovascular magnetic resonance myocardial feature tracking strain assessment is independent of field strength. *Eur J Radiol* 82:296–301
- Schuster A, Paul M, Bettencourt N et al (2015) Myocardial feature tracking reduces observer-dependence in low-dose dobutamine stress cardiovascular magnetic resonance. *PLoS ONE* 10:e0122858
- Schuster A, Stahnke VC, Unterberg-Buchwald C et al (2015) Cardiovascular magnetic resonance feature-tracking assessment of

- myocardial mechanics: Intervendor agreement and considerations regarding reproducibility. *Clin Radiol* 70:989–998
23. Swoboda PP, Larghat A, Zaman A et al (2014) Reproducibility of myocardial strain and left ventricular twist measured using complementary spatial modulation of magnetization. *J Magn Res Imaging* 39:887–894
 24. Tsang HG, Rashdan NA, Whitelaw CBA et al (2016) Large animal models of cardiovascular disease. *Cell Biochem Funct* 34:113–132
 25. Voelkl B, Vogt L, Sena ES et al (2018) Reproducibility of preclinical animal research improves with heterogeneity of study samples. *PLoS Biol* 16:e2003693
 26. Yamada A, Luis SA, Sathianathan D et al (2014) Reproducibility of regional and global longitudinal strains derived from two-dimensional speckle-tracking and doppler tissue imaging between expert and novice readers during quantitative dobutamine stress echocardiography. *J Am Soc Echocardiogr* 27:880–887
 27. Yoon SJ, Yoon DY, Cho YK et al (2017) Characteristics and quality of published animal research in the field of radiology. *Acta Radiol* 58:685–691
 28. Zhong J, Liu W, Yu X (2008) Characterization of three-dimensional myocardial deformation in the mouse heart: an MR tagging study. *J Magn Res Imaging* 27:1263–1270

Publisher's Note Springer Nature remains neutral with regard to jurisdictional claims in published maps and institutional affiliations.

RESEARCH

Open Access



Cardiovascular magnetic resonance-derived left ventricular mechanics—strain, cardiac power and end-systolic elastance under various inotropic states in swine

A. Faragli^{1,2,3,4}, R. Tanacli^{1,4}, C. Kolp¹, D. Abawi¹, T. Lapinskas^{4,5}, C. Stehning⁶, B. Schnackenburg⁶, F. P. Lo Muzio^{7,8}, L. Fassina⁹, B. Pieske^{1,2,3,4}, E. Nagel¹⁰, H. Post^{1,2,3,11}, S. Kelle^{1,2,3,4†} and A. Alogna^{1,2,3*†}

Abstract

Background: Cardiovascular magnetic resonance (CMR) strain imaging is an established technique to quantify myocardial deformation. However, to what extent left ventricular (LV) systolic strain, and therefore LV mechanics, reflects classical hemodynamic parameters under various inotropic states is still not completely clear. Therefore, the aim of this study was to investigate the correlation of LV global strain parameters measured via CMR feature tracking (CMR-FT, based on conventional cine balanced steady state free precession (bSSFP) images) with hemodynamic parameters such as cardiac index (CI), cardiac power output (CPO) and end-systolic elastance (Ees) under various inotropic states.

Methods: Ten anaesthetized, healthy Landrace swine were acutely instrumented closed-chest and transported to the CMR facility for measurements. After baseline measurements, two steps were performed: (1) dobutamine-stress (Dobutamine) and (2) verapamil-induced cardiovascular depression (Verapamil). During each protocol, CMR images were acquired in the short axis and apical 2Ch, 3Ch and 4Ch views. MEDIS software was utilized to analyze global longitudinal (GLS), global circumferential (GCS), and global radial strain (GRS).

Results: Dobutamine significantly increased heart rate, CI, CPO and Ees, while Verapamil decreased them. Absolute values of GLS, GCS and GRS accordingly increased during Dobutamine infusion, while GLS and GCS decreased during Verapamil. Linear regression analysis showed a moderate correlation between GLS, GCS and LV hemodynamic parameters, while GRS correlated poorly. Indexing global strain parameters for indirect measures of afterload, such as mean aortic pressure or wall stress, significantly improved these correlations, with GLS indexed for wall stress reflecting LV contractility as the clinically widespread LV ejection fraction.

Conclusion: GLS and GCS correlate accordingly with LV hemodynamics under various inotropic states in swine. Indexing strain parameters for indirect measures of afterload substantially improves this correlation, with GLS being as good as LV ejection fraction in reflecting LV contractility. CMR-FT-strain imaging may be a quick and promising tool to characterize LV hemodynamics in patients with varying degrees of LV dysfunction.

*Correspondence: alessio.alogna@charite.de

†S. Kelle and A. Alogna contributed equally to this work

¹ Department of Internal Medicine and Cardiology, Charité-Universitätsmedizin Berlin, Campus Virchow-Klinikum, Augustenburger Platz 1, 13353 Berlin, Germany

Full list of author information is available at the end of the article



© The Author(s) 2020. **Open Access** This article is licensed under a Creative Commons Attribution 4.0 International License, which permits use, sharing, adaptation, distribution and reproduction in any medium or format, as long as you give appropriate credit to the original author(s) and the source, provide a link to the Creative Commons licence, and indicate if changes were made. The images or other third party material in this article are included in the article's Creative Commons licence, unless indicated otherwise in a credit line to the material. If material is not included in the article's Creative Commons licence and your intended use is not permitted by statutory regulation or exceeds the permitted use, you will need to obtain permission directly from the copyright holder. To view a copy of this licence, visit <http://creativecommons.org/licenses/by/4.0/>. The Creative Commons Public Domain Dedication waiver (<http://creativecommons.org/publicdomain/zero/1.0/>) applies to the data made available in this article, unless otherwise stated in a credit line to the data.

Keywords: Cardiovascular magnetic resonance, Feature tracking, Left ventricular strain, Contractile function, Porcine model, Translational studies, Hemodynamics

Background

The routine assessment of left ventricular (LV) ejection fraction (LVEF), being a measure of global systolic function, falls short in identifying regional myocardial impairment and the mechanical contraction of the heart [1, 2]. Therefore, strain imaging has emerged in the past years to better quantify myocardial LV deformation in various patient populations [3–7]. Numerous studies have validated and shown the utility of myocardial strain in the diagnosis of several pathologies, identifying subclinical myocardial changes, and even by showing an impact on the prognosis of cardiovascular pathologies [8–15]. Recently, cardiovascular magnetic resonance (CMR) feature tracking (FT) strain analysis was shown to be accurate in the detection of myocardial dysfunction as well as useful as a predictor of major adverse cardiac events, with the advantage of utilizing conventional balanced steady-state free precession (bSSFP) cine sequences [15–19]. Impaired LV systolic function and cardiac reserve can be clinically assessed by hemodynamic parameters such as cardiac index (CI), as well as by cardiac power output (CPO) at rest and during pharmacological stress. In particular, the latest has been shown to strongly correlate with the clinical outcome of chronic heart failure patients [20, 21]. Moreover, LV CPO is able to provide an assessment of the intraventricular flow as well as of its mechanics much more than other hemodynamic parameters, since it couples not only with the cardiac work, but also with the response of the vasculature [22, 23]. The invasively measured end-systolic elastance (Ees) is instead, a relatively load-independent parameter describing the LV inotropic state [24]. Recently, Seeman and colleagues successfully investigated a novel CMR method to noninvasively quantify Ees [25]. Whether or not, and to what extent CMR-FT LV strain reflects the above-mentioned hemodynamic parameters under various inotropic states has not been investigated thus far. Therefore, the aim of this study was to validate the correlation of CMR LV strain parameters against hemodynamic parameters such as CI, CPO and the Ees mentioned above, under various inotropic states in swine.

Methods

The experimental protocols were approved by the local bioethics committee of Berlin, Germany (G0138/17), and conform to the “European Convention for the Protection of Vertebrate Animals used for Experimental and other

Scientific Purposes” (Council of Europe No 123, Strasbourg 1985).

Experimental setup

Female Landrace swine ($n = 10$, 51 ± 10 kg) were fasted overnight with free access to water, and then sedated and intubated on the day of the experiment. Anaesthesia was continued with fentanyl, midazolam, ketamine and pancuronium as needed. The anesthesia regimen included low-dose isoflurane to obtain a deeper sedation and stabilize hemodynamics without impacting much on systemic vascular resistance. Animals were ventilated (Cato, Dräger Medical, Lubeck, Germany) with a FiO₂ of 0.5, an I: E-ratio of 1:1.5, the positive end-expiratory pressure was set at 5 mmHg and a tidal volume of 10 ml kg⁻¹. The respiratory rate was continuously adjusted to maintain an end-expiratory carbon dioxide partial pressure between 35 and 45 mmHg. Under fluoroscopic guidance, all animals were instrumented with a floating balloon catheter in the right atrium, as well as in the coronary sinus (Arrow Balloon Wedge-Pressure Catheters, Teleflex Inc, Wayne, Pennsylvania USA). In order to avoid CMR-artefacts, the balloon-tip was cut before introducing the catheters in the vessel. Respiratory gases (PM 8050 MRI, Dräger Medical), heart rate (HR), and invasively derived arterial blood pressure were continuously monitored (Precess 3160, InVivo, Gainesville, Florida, USA) via a sheath access surgically prepared in the internal carotid artery. Body temperature was monitored by a sublingual thermometer and was maintained at 38 °C during CMR imaging via air ventilation or infusion of cold saline solution.

Experimental protocols

After acute instrumentation, the animals were transported to the CMR facility for measurements. After baseline measurements, two steps were performed: (1) Dobutamine-stress (Dobutamine) and (2) verapamil-induced cardiovascular depression (Verapamil). Dobutamine infusion was titrated aiming at a 25% HR increase compared to baseline values, while verapamil was given as single 2.5 mg bolus, aiming at a 25% decrease of CI. This protocol was established beforehand with a small pilot study (data not shown), in which the titration of dobutamine and verapamil was assessed by LV invasive conductance measurements according to previous publications by our group [26]. The cumulative dose for each experiment was achieved via careful titration of

verapamil, administered as a 2.5 mg bolus in order to avoid a pronounced hypotension leading to hemodynamic instability. In the pilot experiments CI was continuously assessed online via a Swan-Ganz catheter in the pulmonary artery (Edwards Lifesciences CCO connected to Vigilance I, Edwards Lifesciences, Irvine, California, USA). In the CMR study, after the first bolus, we estimated stroke volume via short-axis cine imaging after reaching a hemodynamic steady state (around 5 min after bolus injection). In case CI was not decreased as much as 25%, we proceeded with a further bolus of verapamil. Between the different protocol steps there was a wash-out period of 30 min. The anaesthesia regimen included low dose isoflurane to obtain a deeper sedation and stabilize hemodynamics without impacting much on systemic vascular resistance. This protocol was established beforehand with a small pilot study (data not shown), in which the titration of dobutamine and verapamil was assessed by LV invasive conductance measurements according to previous publications by our group [26]. At each protocol step, CMR images were acquired in the short axis (SAx), two-chamber (2Ch), three-chamber (3Ch) and four-chamber (4Ch) views. At the end of the measurements, animals were transported back to the operating room for sacrifice. Sacrifice was performed with an intracoronary 80 mmol potassium bolus.

Cardiovascular magnetic resonance

All CMR images were acquired in a supine position using a 3 T CMR scanner (Ingenia, Philips Healthcare, Best, The Netherlands) CMR scanner with an anterior- and a built-in posterior coil element, where up to 30 coil elements were employed, depending on the individual anatomy. All animals were scanned using identical comprehensive imaging protocol. The study protocol included initial scouts to determine cardiac imaging planes. Cine images were acquired using electrocardiogram (ECG)-gated bSSFP cine sequence in three LV long-axis (2Ch, 3Ch, 4Ch) planes. The ventricular 2Ch and 4Ch planes were used to plan stack of SAx slices covering entire LV. The following imaging parameters were used: repetition time (TR) = 2.9 ms, echo time (TE) = 1.45 ms, flip angle = 45°, measured voxel size = $1.9 \times 1.9 \times 8.0 \text{ mm}^3$, reconstructed voxel size $1.0 \times 1.0 \times 8 \text{ mm}^3$, and 40 cardiac phases.

Image analysis

All images were analyzed offline using a commercially available software (Medis Suite, version 3.1, Leiden, The Netherlands) in accordance with a recent consensus document for quantification of LV function using CMR [27]. A numeric code was assigned to the sequences of different measurements steps and the observers were

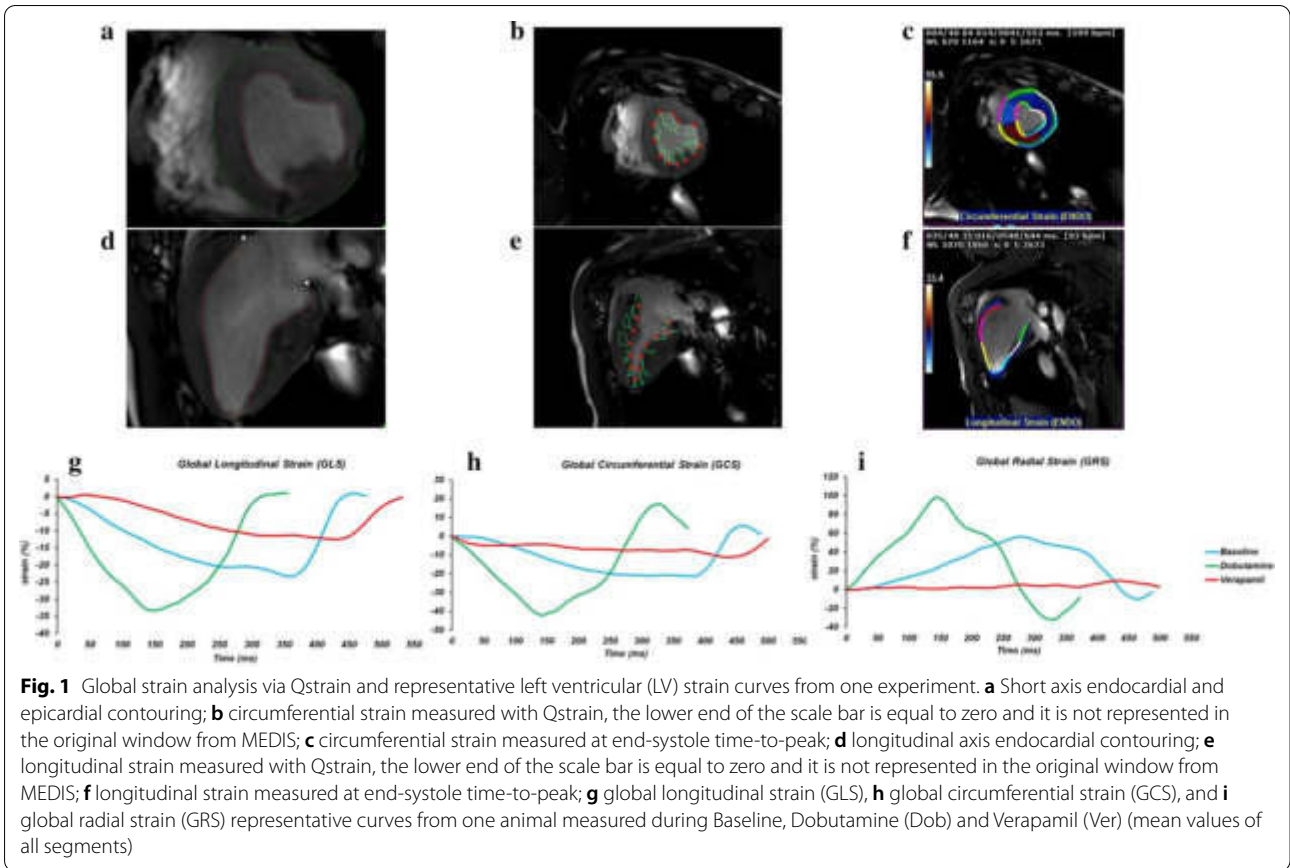
therefore blinded to the pharmacological interventions. Given the excellent inter-observer reproducibility, we averaged values obtained by several measurements from one observer.

On SAx view, the outline of the endocardial border of the LV was manually traced on all slices of each phase. Volumes were computed by Simpson method of disks summation, whereby the sum of cross-sectional areas was multiplied by slice thickness (8 mm). The LVEF was calculated using the Simpson method. The LV outflow tract was included as LV blood volume. Papillary muscles and trabeculation were included as LV volume. The ascending aorta was outlined in all the images and flow calculation was performed in the corresponding velocity-encoded phase images. The average flow velocity (cm/s) was multiplied by the area of the vessel (cm^2) to obtain the flow (ml/s) and integrated over one cardiac cycle to obtain the stroke volume (SV). Then, the cardiac output (CO) is indirectly calculated as the product of SV and HR. Finally, the CI is calculated as the CO divided by the body surface area (BSA) [28]. For the strain analysis 2Ch, 3Ch and 4Ch cine images, and respectively, 3 pre-selected mid-ventricle slices from the LV SAx stack were included. The endocardial and epicardial contours drawn on cine images with QMass (version 8.1, Medis Medical) were transferred to QStrain RE (version 2.0, Medis Medical) where after the application of tissue tracking algorithm, endocardial and epicardial borders were detected throughout all the cardiac cycle (Fig. 1a, d). These long-axis cine images were further used to compute myocardial global longitudinal strain (GLS), and SAx images were used to compute global circumferential strain (GCS) and global radial strain (GRS) and strain-rate (Fig. 1b, e). The global values were obtained by averaging the values of systolic peak strain according to an AHA 17 segments model, apex being excluded, as follows: GCS from averaging circumferential strain for 6 basal, 6 mid and 4 apical segmental individual values; GLS from 2Ch, 3Ch and 4Ch averaging 6 basal, 6 mid and 4 apical segments using a bull-eye view (Fig. 1c, f, g, h, i). Data on strain rate are presented in Table 3. In line with the global strain parameters, dobutamine increased peak systolic SR. Verapamil significantly decreased peak systolic SR compared to dobutamine but not to baseline values.

Hemodynamic parameters

Systolic blood pressure (SBP), diastolic blood pressure (DBP) and mean aortic pressure (mAoP) were invasively measured throughout the entire protocol study via a sheath access surgically prepared in an internal carotid artery.

The systemic vascular resistance was calculated as follows:



$$SVR_{mmHg/L} = \frac{\text{Mean Arterial Pressure (MAP)} - \text{Right Atrial Pressure}}{\text{Cardiac Output (CO)}}$$

CPO, CI and Ees were calculated as follows:

$$CPO = \frac{CO \times mAoP}{451}$$

$$CI = \frac{CO}{BSA}$$

$$Ees = \frac{LVP_{sys}}{V_{LVP_{max}} - V_0}$$

where:

$$LVP_{sys} = \frac{2}{3} \text{Systolic Blood Pressure} + \frac{1}{3} \text{Diastolic Blood Pressure}$$

$$V_0 = 0$$

as described in the work by Kelly et al [29].
GLS, GCS and GRS were indexed to the measured mAoP adapting the formula from the previous study by Rhea et al. [30] as follows:

$$\frac{\text{Global Strain} \times mAoP}{\text{avg}(mAoP)}$$

where Global Strain was the global value of either longitudinal (GLSi), circumferential (GCSi) or radial (GRSi) strain and avg(mAoP) was the average of the mAoP

$$V_{LVP_{max}} = \text{End} - \text{Systolic Volume}$$

measured for each protocol step, namely at baseline, dobutamine and verapamil (Table 1).

Table 1 Systemic hemodynamics and cardiac mechanics parameters during BL, Dob and Ver steps

	Baseline	Dobutamine	Verapamil
HR (bpm)	106 ± 15	146 ± 12*	98 ± 19 ^{*.5}
LVEF (%)	59 ± 8	77 ± 7*	39 ± 9 ^{*.5}
CO (L/min)	6 ± 1	9 ± 2*	4 ± 1 ^{*.5}
CI (L/min/m ²)	2.5 ± 0.2	3.8 ± 0.5*	1.7 ± 0.7 ^{*.5}
CPO (W)	1.2 ± 0.3	2.0 ± 0.6*	0.7 ± 0.2 ^{*.5}
SVR (dyn s cm ⁻⁵)	15 ± 5	11 ± 4*	19 ± 9 ^{*.5}
mAoP (mmHg)	90 ± 12	98 ± 19	70 ± 10 ^{*.5}
Wall stress (mmHg)	0.12 ± 0.02	0.16 ± 0.04*	0.10 ± 0.02 ⁵

HR heart rate, LVEF left ventricular ejection fraction, CO cardiac output, CI cardiac index, CPO cardiac power output, SVR systemic vascular resistance, mAoP mean aortic pressure

*p < 0.05 vs. Baseline; ⁵p < 0.05 vs. Dobutamine

Meridional wall stress was calculated via the following formula [31]:

$$LV \text{ wall stress} = \frac{(0.334 \times LVP_{sys} \times LVEDD)}{PWT \times [1 + PWT/LVID]}$$

where LVEDD = left ventricular end-systolic diameter and PWT = posterior wall thickness as described in the paper by Reichek et al. [31]. PLT was measured by averaging three separate measurements in the basal short axis sequence.

GLS, GCS and GRS were indexed to the measured wall stress adapting the formula from the study by Reichek et al. [31] as follows:

$$\frac{\text{Global Strain} \times LV \text{ wall stress}}{\text{avg}(LV \text{ wall stress})}$$

where Global Strain was the global value of either global longitudinal (GLSw), global circumferential (GCSw) or global radial (GRSw) strain. The average for both LV wall stress were calculated for each step, namely at baseline, dobutamine and verapamil (Table 1).

Statistical analysis

All data are presented as mean ± SD. The association between strain data and hemodynamic data was assessed by linear regression analysis. The condition (baseline, dobutamine, verapamil) was included as a regressor into the linear regression model. To verify whether the linear regressions were significantly different (p-value < 0.05), using custom-made scripts in MATLAB (release R2020a; The MathWorks, Inc., Natick, Massachusetts, USA), we compared slopes, intercepts as well as correlation coefficients: (i) via t-test (for slopes and intercepts) and (ii) via the Fisher's r-to-z transformation followed by z-test

(for correlation coefficients), as previously described by Weaver and Wuensch [32]. Data between groups at different inotropic states were analysed by one-way ANOVA for repeated measurements. Post-hoc testing was performed by Tukey's test. A p-value < 0.05 was considered significant. For statistical calculations, we used the software Sigmasat (Version 4.0, Systat Software, Inc., Cranes Software, Karnataka, India) and SPSS (Version 23.0, Statistical Package for the Social Sciences, International Business Machines, Inc., Armonk, New York, USA).

Results

The dose of dobutamine needed to induce a 25% HR increase was 6.4 ± 2.5 µg/kg/min, while the dose of verapamil needed to decrease CI significantly was 5 ± 2 mg.

Systemic hemodynamics

Systemic hemodynamic data are summarized in Table 1. mAoP was not affected by Dobutamine, but significantly decreased during Verapamil. Dobutamine increased baseline HR, CO and LVEF, while Verapamil decreased them. Systemic vascular resistance (SVR) substantially decreased during Dobutamine, while increased during Verapamil. CPO and CI both increased during Dobutamine and decreased during Verapamil. Ees, the slope of the end-systolic pressure–volume relationship, increased during Dobutamine and decreased during Verapamil infusion (Fig. 2).

Global strain parameters

Strain parameters are summarized in Table 2a, b and c. GLS as well as GCS increased during Dobutamine, while decreased during Verapamil. GRS was not significantly affected by Dobutamine, while decreased significantly during Verapamil.

Systolic strain rate

Data on strain rate (SR) are presented in Table 3. In line with the global strain parameters, Dobutamine increased peak systolic SR. Verapamil significantly decreased peak systolic SR compared to Dobutamine but not to baseline values.

Indexing strain parameters for indirect measures of afterload

Indexing global strain parameters for either mAoP (Table 2b) or for meridional wall stress (Table 2c) did not significantly impact the above-described changes induced by Dobutamine and Verapamil.

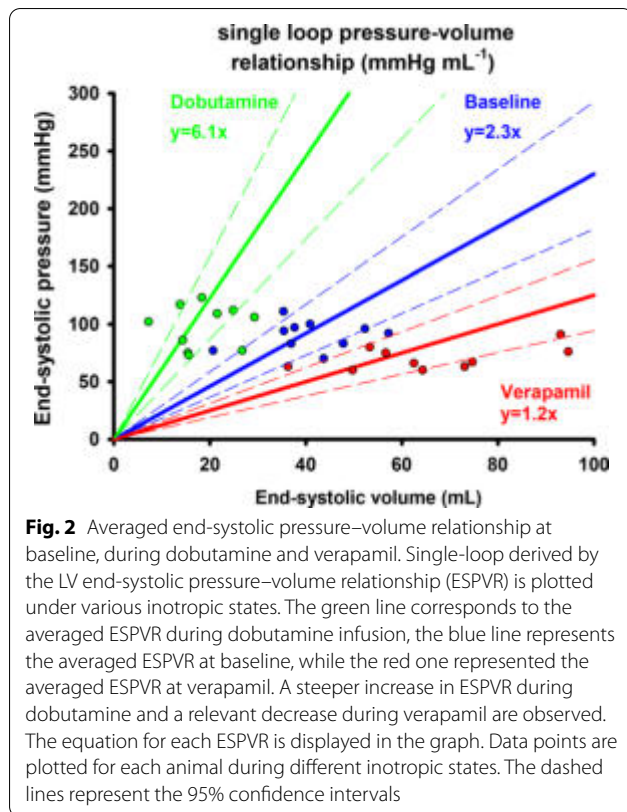


Table 2 Global strain and indexed global strain values measured at different inotropic states

	Baseline	Dobutamine	Verapamil
(A)			
GLS (%)	-23 ± 4	-45 ± 9*	-16 ± 3* [§]
GCS (%)	-31 ± 8	-53 ± 10*	-17 ± 5* [§]
GRS (%)	72 ± 19	88 ± 36	30 ± 12* [§]
(B)			
GLSi (%)	-23 ± 4	-45 ± 10*	-16 ± 4* [§]
GCSi (%)	-30 ± 8	-52 ± 8*	-16 ± 5* [§]
GRSi (%)	71 ± 19	84 ± 23	30 ± 13* [§]
(C)			
GLSw (%)	-23 ± 5	-44 ± 10*	-16 ± 3* [§]
GCSw (%)	-31 ± 9	-52 ± 13*	-17 ± 17* [§]
GRSw (%)	71 ± 20	90 ± 54	35 ± 27* [§]

(A) Global strain: GLS global longitudinal strain, GCS global circumferential strain, GRS global radial strain; (B) Global strain indexed for mean aortic pressure (mAoP): GLSi global longitudinal strain indexed for mAoP, GCSi global circumferential strain indexed for mAoP, GRSi global radial strain indexed for mAoP; (C) Global strain indexed for meridional wall stress: GLSw global longitudinal strain indexed for wall stress, GCSw global circumferential strain indexed for wall stress, GRSw global radial strain indexed for wall stress. *p < 0.05 vs. baseline; [§]p < 0.05 vs. Dobutamine

Table 3 Global peak systolic strain rates values measured at different inotropic states

	Baseline	Dobutamine	Verapamil
GLS peak systolic SR (s-1)	-2.5 ± 0.6	-6.4 ± 1.5*	-2.1 ± 1.1 [§]
GCS peak systolic SR (s-1)	-3.2 ± 2.2	-8.7 ± 2.5*	-2.0 ± 1.3 [§]
GRS peak systolic SR (s-1)	2.7 ± 1.0	5.5 ± 0.9	2.2 ± 1.5 [§]

Strain Rate (SR). *p < 0.05 vs. Baseline; [§]p < 0.05 vs. Dobutamine

Correlation between global strain, LVEF and LV hemodynamic parameters

Linear regression analysis showed a moderate correlation between GLS, GCS and CPO, while a poor one was observed between GRS and CPO (Fig. 3a). A similar correlation was observed between GLS, GCS and CI (Fig. 3b), with GRS worst performing. A moderate correlation was observed between GLS, GCS and Ees, while a poor one was observed between GRS and Ees (Fig. 3c). Indexing global strain parameters either for mAoP or for wall stress improved their correlations with CPO (Figs. 4a and 5a), with CI (Figs. 4b and 5b) as well as with Ees (Figs. 4c and 5c). LVEF moderately correlated with CI and CPO (r² = 0.81 and r² = 0.69, respectively) as GLSw with CI and CPO (r² = 0.74 and r² = 0.72, respectively). GLSw moderately correlated with Ees as well as LVEF with Ees (r² = 0.74 versus r² = 0.74). The above-mentioned correlations were both statistically significant with a p < 0.0001.

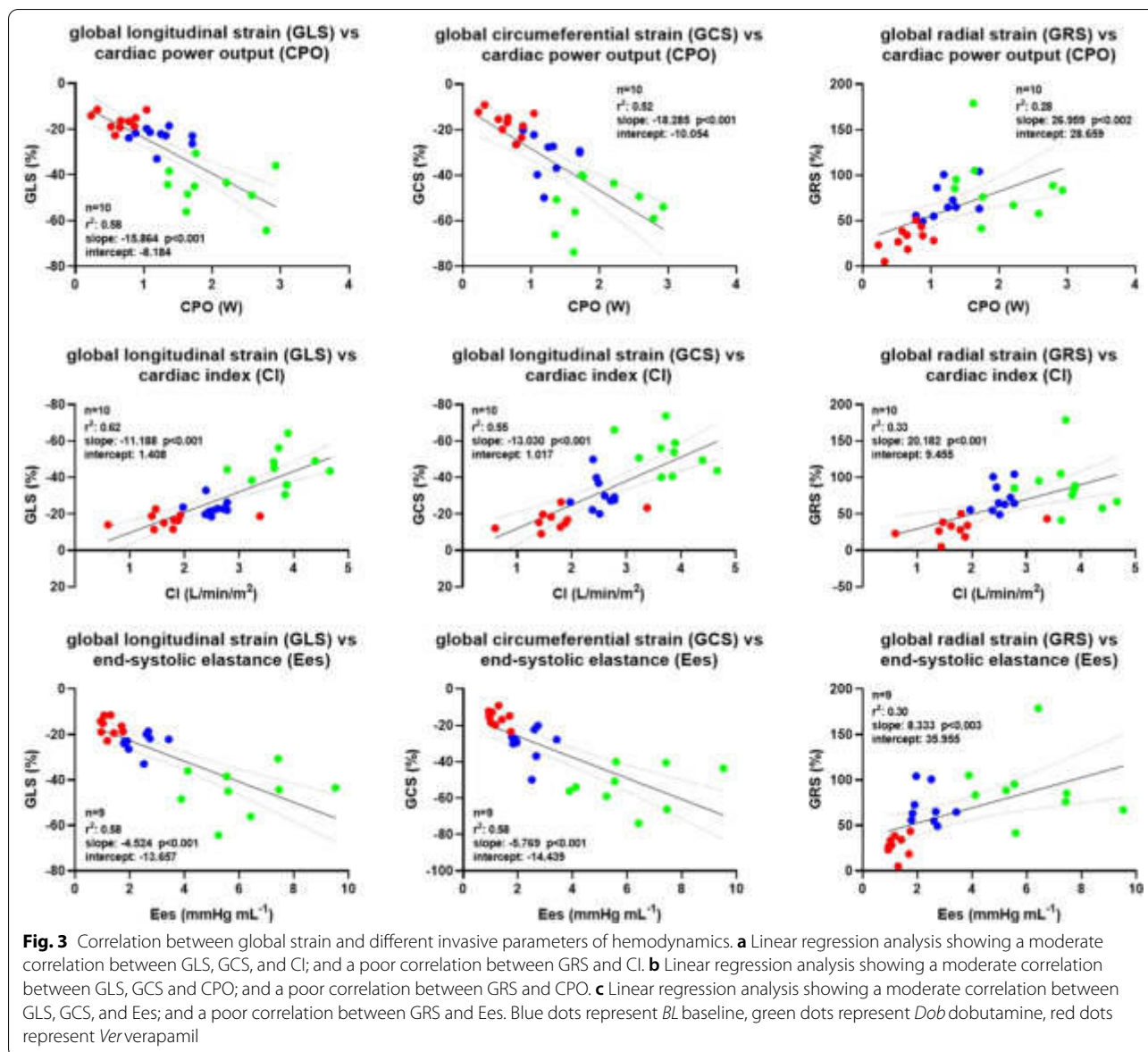
Relative change of mechanics under various inotropic states

In Fig. 6, we plotted the relative change of mechanics (global LV strain parameters) as well as hemodynamic parameters during Dobutamine and Verapamil in comparison to baseline.

Among global strain parameters, GLS showed a higher relative change than GRS during both Dobutamine and Verapamil, while the same was valid for GCS during dobutamine only. Moreover, the impact of Dobutamine was more prominently expressed by GLS than by CI, while the impact of Verapamil on GRS was negligible when in comparison to CI. The impact of Dobutamine and Verapamil on the rest of the mechanic and hemodynamic parameters was comparable.

Discussion

CMR strain imaging is an established technique to quantify myocardial deformation. However, to what extent LV systolic strain, and therefore LV mechanics, reflects classical hemodynamic parameters under various inotropic states is still not completely clear. In the current study, we set out to investigate the correlation of LV global strain parameters measured via CMR-FT with hemodynamic

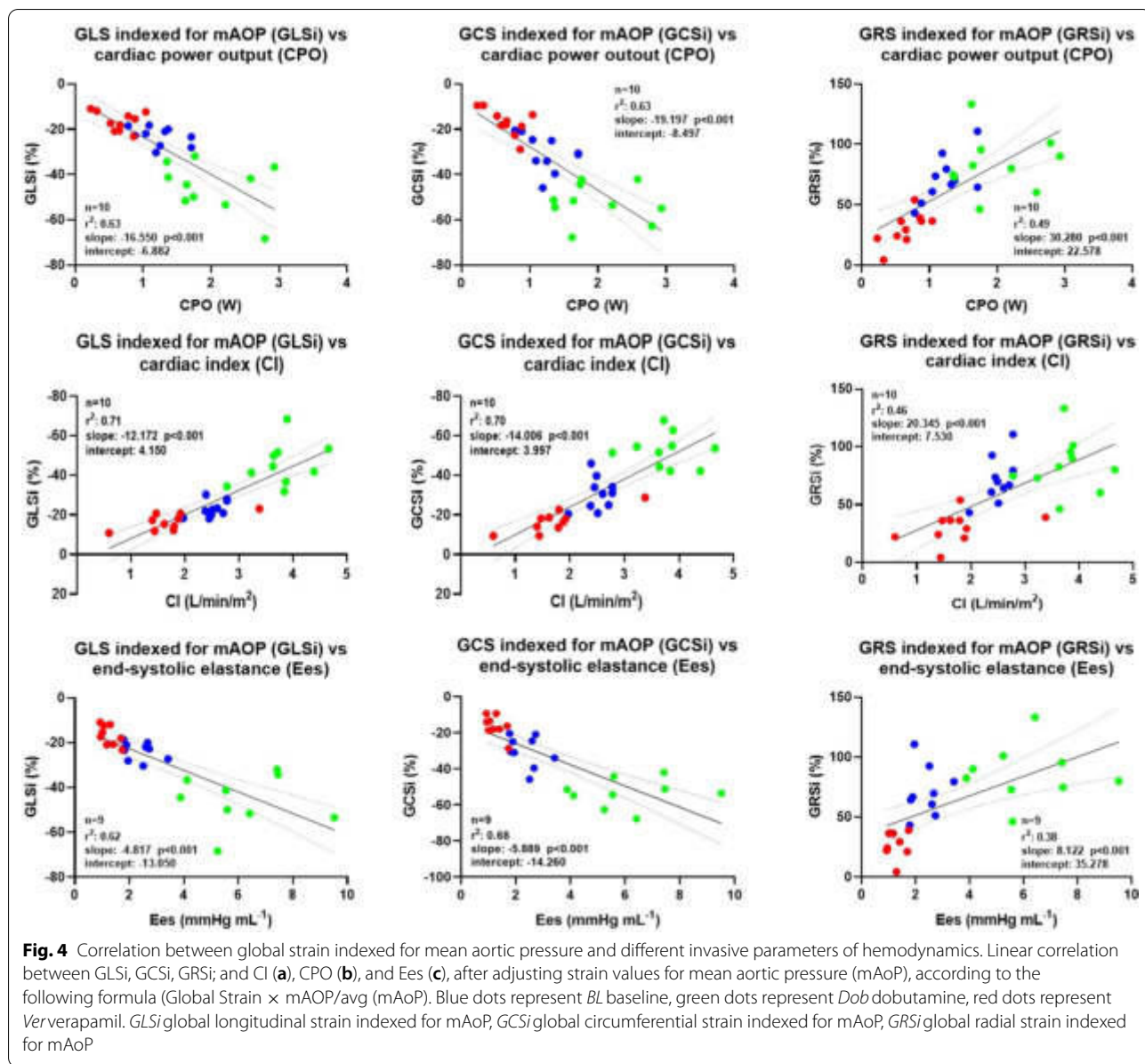


parameters under various inotropic states in swine. We observed a moderate correlation of global strain parameters with LV hemodynamics. Interestingly, indexing strain parameters for indirect measures of afterload substantially improved this correlation, with GLS indexed for wall stress reflecting LV contractility as the clinically widespread LVEF.

Correlation between global strain, LVEF and LV hemodynamic parameters

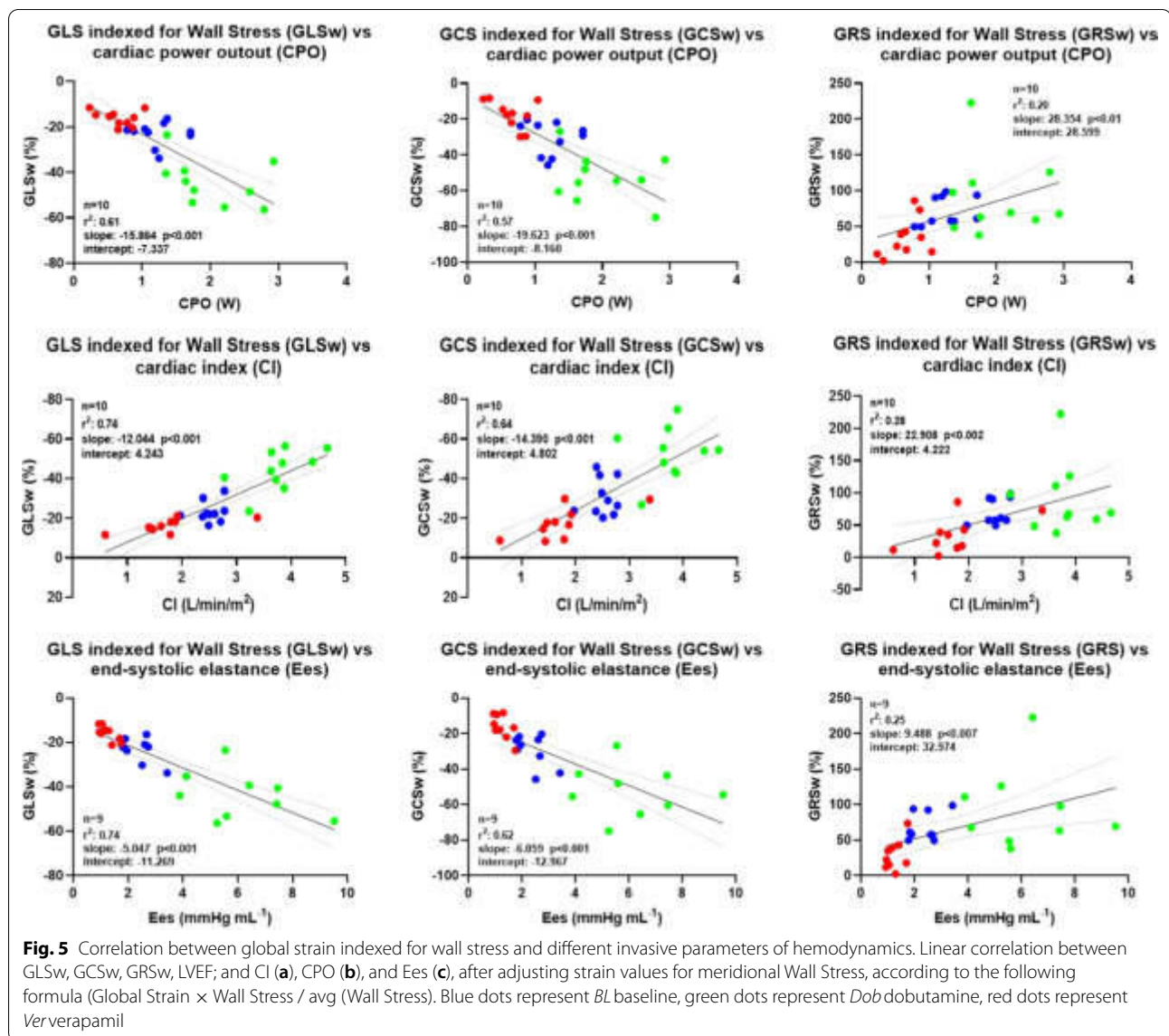
Numerous studies have reported a significant diagnostic as well as a prognostic role of LV strain in the assessment of LV mechanics in various study populations [10, 11], including patients with heart failure with preserved

ejection fraction, coronary artery disease, diabetes mellitus, hypertensive heart disease, hypertrophic cardiomyopathy, and arrhythmia [1–7]. Recently, CMR-FT strain analysis was shown to be accurate in the detection of myocardial dysfunction and as well useful as a predictor of major adverse cardiac events in ischemic or non-ischemic cardiomyopathy [18], with the advantage of utilizing simple bSSFP cine sequences [15–19, 33, 34]. However, notwithstanding the multitude of published papers assessing the clinical usefulness of strain, there is a notable lack of in-vivo validation studies [35]. Whether CMR-FT LV strain represents a valid tool to assess the cardiac mechanics of the myocardium, and how this varies under different inotropic states, is still unclear. In this



work, we could show a role of CMR LV strain as a surrogate of classic hemodynamic parameters such as CI, CPO, and a load-independent parameter of cardiac contractility such as Ees, which are established parameters to describe the hydraulic and mechanical role of the heart as a pump [22, 24]. Previous in vivo studies concentrated on the role of 2D and 3D speckle tracking echocardiography (STE) [35]. The main validation studies analysed the correlation of STE with the sonomicrometry technique in open-chest large animal models, showing an overall good agreement of the two techniques [35]. Similarly to our study, Weidemann et al. showed the ability of strain as well as strain rate to reflect swine LV-contractility under

different inotropic states and independently of heart rate [36]. The invasively measured Ees, the slope of the end-systolic pressure–volume relationship, is a relatively load-independent parameter describing the LV inotropic state [24]. A recent study by Seeman et al. established a reliable method to assess Ees via CMR imaging [25]. In the current work, we showed a moderate to good correlation between both GLS, GCS, and Ees. The accuracy of GLS in reflecting Ees improved when indexing for wall stress. In line with our data, Yotti et al [8] showed a moderate correlation between echocardiographic assessed GCS and invasive pressure–volume catheterization data, while on the opposite, GLS correlated poorly. The authors

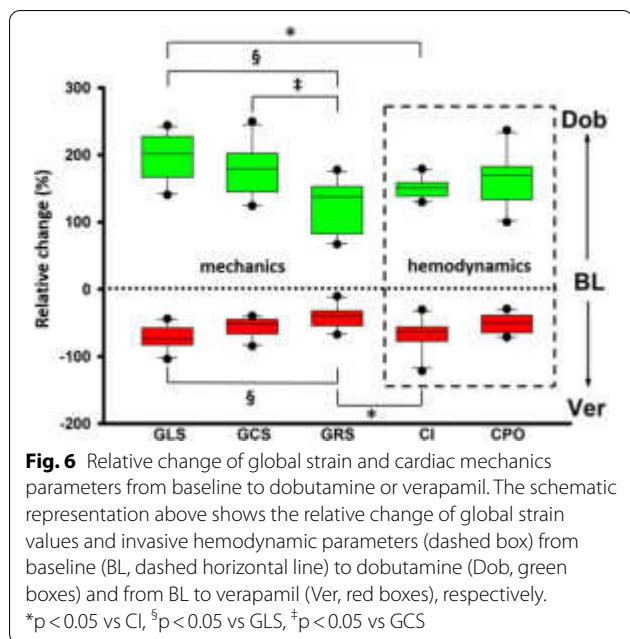


highlighted how the GCS measurements, as opposed to the GLS, did not change in patients with aortic stenosis or hypertension. They hypothesized this could be related to a lower load-dependency [8] of the first in comparison to the latter ones, but the different methodology of strain assessment in comparison to our study is probably playing a role as well.

Indexing strain parameters for indirect measures of afterload

In the current study, in order to minimize the load-dependency of the strain measurements, we indexed all the global strain values for indirect measures of afterload, such as the invasively measured mAoP as well

as the meridional wall stress, as already described by Rhea et al. and Reichel et al [30, 31]. Correcting the strain measurements, as mentioned above, improved the ability of strain parameters to reflect LV hemodynamics. Yingchoncharoen et al. already demonstrated that blood pressure adjustment of strain is advisable in patients with large deviations of SBP from the normal-reference value [37]. Furthermore, in a study by Weiner et al. on the impact of isometric handgrip testing on LV twist mechanics, it was shown that longitudinal strain is influenced by blood pressure [38]. Finally, in line with our study, Rhea et al. showed an improved accuracy of pressure-adjusted GLS in predicting cardiac events and mortality [30].



Relative change of mechanics under various inotropic states

In order to investigate to what extent global LV strain parameters reflect hemodynamic changes we plotted the relative change of these parameters during Dobutamine and Verapamil compared to baseline. The relative change of GLS during Dobutamine was higher than the one of CI, while the impact of Verapamil on GRS was negligible when compared to CI, overall in line with the poor reproducibility of GRS measurements. The impact of Dobutamine and Verapamil on the rest of the mechanic and hemodynamic parameters was comparable. In line with previous reproducibility studies [39–42], we showed that radial strain is a poorly reproducible and inaccurate measurement. In this study we did not show the inter- and intra-observer reproducibility because it was already assessed in a previous work from our group based on the same cohort [43]. Our analysis showed that measurements at baseline were good to excellent (good ICC 0.60–0.74; excellent ICC > 0.74) for GLS, GCS and GRS, but that only GLS and GCS displayed good reproducibility during both dobutamine and verapamil steps, whereas radial strain was highly variable [43].

Clinical and translational perspective

In this *in vivo* study, we could show that CMR-FT strain parameters, such as GLS and GCS, reflect classic hemodynamic parameters such as CI, CPO, as well as a load-independent parameter of cardiac contractility such as Ees. LV strain has indeed emerged in the past year as

a valid technique to assess LV deformation with high reproducibility. However, the spread of this technique in the clinical routine is limited by the often lengthy post-processing of the sequences, confining this important resource to the mere research field [44]. FT-strain, in particular, possesses the advantage of a quick assessment, being based on conventional bSSFP cine sequences [15–19], and seems to be therefore a promising technique to allow a more extensive clinical use of LV strain. Furthermore, indexing the global strain values for indirect measures of afterload, such as the invasively measured mAoP as well as the meridional wall stress, improves the ability of strain parameters to reflect LV hemodynamics. After accounting for meridional wall stress, GLS performed as good as LVEF in reflecting LV contractility, expressed as Ees, confirming the potential role of this novel parameter in the clinical arena. These results suggest that implementing strain measurements with pressure-derived variables may add accuracy to the evaluation of the mechanical and contractile function of the heart, improving the impact of LV strain in the clinical routine and helping to overcome the limitations of LVEF as a surrogate parameter of LV systolic function. In daily clinical routine, this could be potentially achieved even with a standard sphygmomanometer, as shown in the paper by Seeman et al [25].

Finally, we envision a promising role for CMR-FT LV strain investigation of chronic heart failure patients. In particular heart failure with preserved ejection fraction patients seem that they would benefit the most from this assessment, since previous studies have already shown a diagnostic and prognostic impact of strain measurements [2].

Limitations

Specific limitation of the study are related to the fact that animals were investigated under general anaesthesia, in order to minimize the animals’ distress and to obtain stable hemodynamic conditions. Due to easier housing and milder behaviour, all the animals were females. We therefore cannot draw any relevant conclusions on the role of gender on strain variability. A limitation regarding the strain analysis is that only endocardial values of strain were analysed. Moreover, an inter-vendor software variability should be considered if looking at the absolute strain values. Another limitation is that the animals were healthy, and even if conditions of hyper-contractility and hypo-contractility were induced, these were only transient and acutely assessed. We believe the data to be representative enough for the clinical translation, however further studies are needed in a clinical setting.

In conclusion, CMR-FT derived LV strain parameters, such as GLS and GCS, correlate accordingly with

LV hemodynamics in swine under various inotropic states. Indexing strain parameters for indirect measures of afterload substantially improves this correlation, with GLS being as good as LVEF in reflecting LV contractility. CMR-FT strain imaging may be a quick and promising tool to characterize LV hemodynamics in patients with a various degree of LV dysfunction.

Abbreviations

2Ch: Two chambers; 3Ch: Three chambers; 4Ch: Four chambers; BSA: Body surface area; bSSFP: Balanced steady-state free precession; CI: Cardiac index; CMR: Cardiovascular magnetic resonance; CMR-FT: Cardiovascular magnetic resonance feature tracking; CO: Cardiac output; CPO: Cardiac power output; DBP: Diastolic blood pressure; ECG: Electrocardiogram; Ees: End-systolic elastance; ESPVR: End-systolic pressure–volume relationship; FT: Feature tracking; GCS: Global circumferential strain; GCSi: Global circumferential strain indexed for mAoP; GCSw: Global circumferential strain indexed for meridional wall stress; GLS: Global longitudinal strain; GLSi: Global longitudinal strain indexed for mAoP; GLSw: Global longitudinal strain indexed for meridional wall stress; GRS: Global radial strain; GRSi: Global radial strain indexed for mAoP; GRSw: Global radial strain indexed for meridional wall stress; HR: Heart rate; LV: Left ventricle/ left ventricular; LVEF: Left ventricular ejection fraction; LVESD: Left ventricular end-systolic diameter; LVP: Left ventricular pressure; mAoP: Mean aortic pressure; PWT: Posterior wall thickness; SAx: Short axis; SBP: Systolic blood pressure; SR: Strain rate; STE: Speckle tracking echocardiography; SVR: Systemic vascular resistance; TE: Echo time; TR: Repetition time.

Acknowledgements

Not applicable.

Authors' contributions

AA, SK, HP conceived the experiment, AF, AA, SK, CK, CS conducted the experiments, AF, RT, DA, AA, SP, CS, FPLM, LF analyzed the results. All authors revised the manuscript. All authors read and approved the final manuscript.

Funding

Open access funding enabled and organized by Projekt DEAL. Alessandro Faragli, Heiner Post, Sebastian Kelle and Alessio Alogna received funding from DZHK (c) and by the BMBF (German Ministry of Education and Research). Sebastian Kelle is supported by a grant from Philips Healthcare.

Availability of data

Not applicable

Ethics approval and consent to participate

Not applicable.

Consent for publication

Not applicable.

Competing interests

Apart from Alessandro Faragli, Heiner Post, Sebastian Kelle and Alessio Alogna, who declare to have received funding in the Funding section, none of the other authors reports a relationship with industry and other relevant entities—financial or otherwise—that might pose a conflict of interest in connection with the submitted article. The following authors report financial activities outside the submitted work: Burkert Pieske reports having received consultancy and lecture honoraria from Bayer Daiichi Sankyo, MSD, Novartis, Sanofi-Aventis, Stealth Peptides and Vifor Pharma; and editor honoraria from the Journal of the American College of Cardiology.

Author details

¹ Department of Internal Medicine and Cardiology, Charité-Universitätsmedizin Berlin, Campus Virchow-Klinikum, Augustenburger Platz 1, 13353 Berlin, Germany. ² Berlin Institute of Health (BIH), Berlin, Germany. ³ DZHK (German Centre for Cardiovascular Research), partner site, Berlin, Germany.

⁴ Department of Internal Medicine/Cardiology, Deutsches Herzzentrum Berlin, Augustenburger Platz 1, 13353 Berlin, Germany. ⁵ Department of Cardiology, Medical Academy, Lithuanian University of Health Sciences, Eiveniu Street 2, 50161 Kaunas, Lithuania. ⁶ Clinical Science, Philips Healthcare, Röntgenstr. 24, 22335 Hamburg, Germany. ⁷ Department of Surgery, Dentistry, Paediatrics and Gynaecology, University of Verona, Via S. Francesco 22, 37129 Verona, Italy. ⁸ Department of Medicine and Surgery, University of Parma, Via Gramsci 14, 43126 Parma, Italy. ⁹ Department of Electrical, Computer and Biomedical Engineering (DIII), Centre for Health Technologies (CHT), University of Pavia, Via Ferrata 5, 27100 Pavia, Italy. ¹⁰ Institute of Experimental and Translational Cardiac Imaging, DZHK Centre for Cardiovascular Imaging, Goethe University Hospital Frankfurt, Frankfurt am Main, Germany. ¹¹ Department of Cardiology, Contilia Heart and Vessel Centre, St. Marien-Hospital Mülheim, 45468 Mülheim, Germany.

Received: 17 November 2019 Accepted: 6 October 2020

Published online: 30 November 2020

References

1. Stanton T, Leano R, Marwick TH. Prediction of all-cause mortality from global longitudinal speckle strain: comparison with ejection fraction and wall motion scoring. *Circ Cardiovasc Imaging*. 2009;2:356–64.
2. Stokke TM, Hasselberg NE, Smedsrud MK, Sarvari SI, Haugaa KH, Smiseth OA, Edvardsen T, Remme EW. Geometry as a confounder when assessing ventricular systolic function: comparison between ejection fraction and strain. *J Am Coll Cardiol*. 2017;70:942–54.
3. Kraigher-Krainer E, Shah AM, Gupta DK, Santos A, Claggett B, Pieske B, Zile MR, Voors AA, Lefkowitz MP, Packer M, McMurray JJ, Solomon SD, Investigators P. Impaired systolic function by strain imaging in heart failure with preserved ejection fraction. *J Am Coll Cardiol*. 2014;63:447–56.
4. Hasselberg NE, Haugaa KH, Sarvari SI, Gullestad L, Andreassen AK, Smiseth OA, Edvardsen T. Left ventricular global longitudinal strain is associated with exercise capacity in failing hearts with preserved and reduced ejection fraction. *Eur Heart J Cardiovasc Imaging*. 2015;16:217–24.
5. Smedsrud MK, Sarvari S, Haugaa KH, Gjesdal O, Orn S, Aaberge L, Smiseth OA, Edvardsen T. Duration of myocardial early systolic lengthening predicts the presence of significant coronary artery disease. *J Am Coll Cardiol*. 2012;60:1086–93.
6. Yang H, Sun JP, Lever HM, Popovic ZB, Drinko JK, Greenberg NL, Shiota T, Thomas JD, Garcia MJ. Use of strain imaging in detecting segmental dysfunction in patients with hypertrophic cardiomyopathy. *J Am Soc Echocardiogr*. 2003;16:233–9.
7. Fang ZY, Yuda S, Anderson V, Short L, Case C, Marwick TH. Echocardiographic detection of early diabetic myocardial disease. *J Am Coll Cardiol*. 2003;41:611–7.
8. Yotti R, Bermejo J, Benito Y, Sanz-Ruiz R, Ripoll C, Martinez-Legazpi P, del Villar CP, Elizaga J, Gonzalez-Mansilla A, Barrio A, Banares R, Fernandez-Aviles F. Validation of noninvasive indices of global systolic function in patients with normal and abnormal loading conditions: a simultaneous echocardiography pressure-volume catheterization study. *Circ Cardiovasc Imaging*. 2014;7:164–72.
9. Gorcsan J 3rd, Tanaka H. Echocardiographic assessment of myocardial strain. *J Am Coll Cardiol*. 2011;58:1401–13.
10. Dahlslett T, Karlsen S, Grenne B, Eek C, Sjøli B, Skulstad H, Smiseth OA, Edvardsen T, Brunvand H. Early assessment of strain echocardiography can accurately exclude significant coronary artery stenosis in suspected non-ST-segment elevation acute coronary syndrome. *J Am Soc Echocardiogr*. 2014;27:512–9.
11. Ng AC, Sitges M, Pham PN, da Tran T, Delgado V, Bertini M, Nucifora G, Vidaic J, Allman C, Holman ER, Bax JJ, Leung DY. Incremental value of 2-dimensional speckle tracking strain imaging to wall motion analysis for detection of coronary artery disease in patients undergoing dobutamine stress echocardiography. *Am Heart J*. 2009;158:836–44.
12. Nagata Y, Takeuchi M, Wu VC, Izumo M, Suzuki K, Sato K, Seo Y, Akashi YJ, Aonuma K, Otsuji Y. Prognostic value of LV deformation parameters using 2D and 3D speckle-tracking echocardiography in asymptomatic patients with severe aortic stenosis and preserved LV ejection fraction. *JACC Cardiovasc Imaging*. 2015;8:235–45.

13. Rhea IB, Uppuluri S, Sawada S, Schneider BP, Feigenbaum H. Incremental prognostic value of echocardiographic strain and its association with mortality in cancer patients. *J Am Soc Echocardiogr*. 2015;28:667–73.
14. Buss SJ, Emami M, Mereles D, Korosoglou G, Kristen AV, Voss A, Schellberg D, Zugck C, Galuschky C, Giannitsis E, Hegenbart U, Ho AD, Katus HA, Schonland SO, Hardt SE. Longitudinal left ventricular function for prediction of survival in systemic light-chain amyloidosis: incremental value compared with clinical and biochemical markers. *J Am Coll Cardiol*. 2012;60:1067–76.
15. Eitel I, Stiermaier T, Lange T, Rommel KP, Koschalka A, Kowallick JT, Lotz J, Kutty S, Gutberlet M, Hasenfuss G, Thiele H, Schuster A. Cardiac magnetic resonance myocardial feature tracking for optimized prediction of cardiovascular events following myocardial infarction. *JACC Cardiovasc Imaging*. 2018;11:1433–44.
16. Onishi T, Saha SK, Delgado-Montero A, Ludwig DR, Onishi T, Schelbert EB, Schwartzman D, Gorcsan J 3rd. Global longitudinal strain and global circumferential strain by speckle-tracking echocardiography and feature-tracking cardiac magnetic resonance imaging: comparison with left ventricular ejection fraction. *J Am Soc Echocardiogr*. 2015;28:587–96.
17. Mangion K, Carrick D, Carberry J, Mahrous A, McComb C, Oldroyd KG, Eteiba H, Lindsay M, McEntegart M, Hood S, Petrie MC, Watkins S, Davie A, Zhong X, Epstein FH, Haig CE, Berry C. Circumferential strain predicts major adverse cardiovascular events following an acute ST-segment-elevation myocardial infarction. *Radiology*. 2018. <https://doi.org/10.1148/radiol.2018181253>.
18. Romano S, Judd RM, Kim RJ, Kim HW, Klem I, Heitner JF, Shah DJ, Jue J, White BE, Indorkar R, Shenoy C, Farzaneh-Far A. Feature-tracking global longitudinal strain predicts death in a multicenter population of patients with ischemic and nonischemic dilated cardiomyopathy incremental to ejection fraction and late gadolinium enhancement. *JACC Cardiovasc Imaging*. 2018;11:1419–29.
19. Schneeweis C, Qiu J, Schnackenburg B, Berger A, Kelle S, Fleck E, Gebker R. Value of additional strain analysis with feature tracking in dobutamine stress cardiovascular magnetic resonance for detecting coronary artery disease. *J Cardiovasc Magn Reson*. 2014;16:72.
20. Williams SG, Cooke GA, Wright DJ, Parsons WJ, Riley RL, Marshall P, Tan LB. Peak exercise cardiac power output; a direct indicator of cardiac function strongly predictive of prognosis in chronic heart failure. *Eur Heart J*. 2001;22:1496–503.
21. Fincke R, Hochman JS, Lowe AM, Menon V, Slater JN, Webb JG, LeJemtel TH, Cotter G, Investigators S. Cardiac power is the strongest hemodynamic correlate of mortality in cardiogenic shock: a report from the SHOCK trial registry. *J Am Coll Cardiol*. 2004;44:340–8.
22. Cotter G, Williams SG, Vered Z, Tan LB. Role of cardiac power in heart failure. *Curr Opin Cardiol*. 2003;18:215–22.
23. Abawi D, Faragli A, Schwarzl M, Manninger M, Zweiker D, Kresoja K-P, Verderber J, Zirngast B, Maechler H, Steendijk P, Pieske B, Post H, Alogna A. Cardiac power output accurately reflects external cardiac work over a wide range of inotropic states in pigs. *BMC Cardiovasc Disord*. 2019;19:217.
24. Kass DA, Maughan WL. From 'Emax' to pressure-volume relations: a broader view. *Circulation*. 1988;77:1203–12.
25. Seemann F, Arvidsson P, Nordlund D, Kopic S, Carlsson M, Arheden H, Heiberg E. Noninvasive quantification of pressure-volume loops from brachial pressure and cardiovascular magnetic resonance. *Circ Cardiovasc Imaging*. 2019;12:e008493.
26. Alogna A, Manninger M, Schwarzl M, Zirngast B, Steendijk P, Verderber J, Zweiker D, Maechler H, Pieske BM, Post H. Inotropic effects of experimental hyperthermia and hypothermia on left ventricular function in pigs-comparison with dobutamine. *Crit Care Med*. 2016;44:e158–67.
27. Schulz-Menger J, Bluemke DA, Bremerich J, Flamm SD, Fogel MA, Friedrich MG, Kim RJ, von Knobelsdorff-Brenkenhoff F, Kramer CM, Pennell DJ, Plein S, Nagel E. Standardized image interpretation and post processing in cardiovascular magnetic resonance: Society for Cardiovascular Magnetic Resonance (SCMR) board of trustees task force on standardized post processing. *J Cardiovasc Magn Reson*. 2013;15:35.
28. Carlsson M, Andersson R, Bloch KM, Steding-Ehrenborg K, Mosén H, Stahlberg F, Ekmehag B, Arheden H. Cardiac output and cardiac index measured with cardiovascular magnetic resonance in healthy subjects, elite athletes and patients with congestive heart failure. *J Cardiovasc Magn Reson*. 2012;14:51.
29. Kelly RP, Ting CT, Yang TM, Liu CP, Maughan WL, Chang MS, Kass DA. Effective arterial elastance as index of arterial vascular load in humans. *Circulation*. 1992;86:513–21.
30. Rhea IB, Rehman S, Jarori U, Choudhry MW, Feigenbaum H, Sawada SG. Prognostic utility of blood pressure-adjusted global and basal systolic longitudinal strain. *Echo Res Pract*. 2016;3:17–24.
31. Reichek N, Wilson J, John Sutton M, Plappert TA, Goldberg S, Hirshfeld JW. Noninvasive determination of left ventricular end-systolic stress: validation of the method and initial application. *Circulation*. 1982;65:99–108.
32. Weaver B, Wuensch KL. SPSS and SAS programs for comparing Pearson correlations and OLS regression coefficients. *Behav Res Methods*. 2013;45:880–95.
33. Scateteia A, Baritussio A, Bucciarelli-Ducci C. Strain imaging using cardiac magnetic resonance. *Heart Fail Rev*. 2017;22:465–76.
34. Schuster A, Hor KN, Kowallick J, Beerbaum P, Kutty S. Cardiovascular magnetic resonance myocardial feature tracking: concepts and clinical applications. *Circ Cardiovasc Imaging*. 2016;9:e004077.
35. Amzulescu MS, De Craene M, Langet H, Pasquet A, Vancraeynest D, Pouleur AC, Vanoverschelde JL, Gerber BL. Myocardial strain imaging: review of general principles, validation, and sources of discrepancies. *Eur Heart J Cardiovasc Imaging*. 2019;20:605–19.
36. Weidemann F, Jamal F, Kowalski M, Kukulski T, D'Hooge J, Bijmens B, Hatle L, De Scheerder I, Sutherland GR. Can strain rate and strain quantify changes in regional systolic function during dobutamine infusion, B-blockade, and atrial pacing—implications for quantitative stress echocardiography. *J Am Soc Echocardiogr*. 2002;15:416–24.
37. Yingchoncharoen T, Agarwal S, Popovic ZB, Marwick TH. Normal ranges of left ventricular strain: a meta-analysis. *J Am Soc Echocardiogr*. 2013;26:185–91.
38. Weiner RB, Weyman AE, Kim JH, Wang TJ, Picard MH, Baggish AL. The impact of isometric handgrip testing on left ventricular twist mechanics. *J Physiol*. 2012;590:5141–50.
39. Bouchez S, Heyde B, Barbosa D, Vandenheuvel M, Houle H, Wang Y, D'Hooge J, Wouters PF. In-vivo validation of a new clinical tool to quantify three-dimensional myocardial strain using ultrasound. *Int J Cardiovasc Imaging*. 2016;32:1707–14.
40. Barreiro-Pérez M, Curione D, Symons R, Claus P, Voigt J-U, Bogaert J. Left ventricular global myocardial strain assessment comparing the reproducibility of four commercially available CMR-feature tracking algorithms. *Eur Radiol*. 2018;28:5137–47.
41. Swoboda PP, Larget A, Zaman A, Fairbairn TA, Motwani M, Greenwood JP, Plein S. Reproducibility of myocardial strain and left ventricular twist measured using complementary spatial modulation of magnetization. *J Magn Reson Imaging*. 2014;39:887–94.
42. Schmidt B, Dick A, Treutlein M, Schiller P, Bunck AC, Maintz D, Baeßler B. Intra- and inter-observer reproducibility of global and regional magnetic resonance feature tracking derived strain parameters of the left and right ventricle. *Eur J Radiol*. 2017;89:97–105.
43. Faragli A, Tanacli R, Kolp C, Lapinskas T, Stehning C, Schnackenburg B, Lo Muzio FP, Perna S, Pieske B, Nagel E, Post H, Kelle S, Alogna A. Cardiovascular magnetic resonance feature tracking in pigs: a reproducibility and sample size calculation study. *Int J Cardiovasc Imaging*. 2020;36:703–12.
44. Reichek N. Myocardial strain: still a long way to go. *Circ Cardiovasc Imaging*. 2017. <https://doi.org/10.1161/CIRCIMAGING.117.007145>.

Publisher's Note

Springer Nature remains neutral with regard to jurisdictional claims in published maps and institutional affiliations.



Non-invasive CMR-Based Quantification of Myocardial Power and Efficiency Under Stress and Ischemic Conditions in Landrace Pigs

Alessandro Faragli^{1,2,3,4†}, Alessio Alogna^{2,3,4†}, Chong Bin Lee^{1,4,5}, Miry Zhu⁵, Niky Ghorbani^{4,5}, Francesco Paolo Lo Muzio^{6,7}, Bernhard Schnackenburg⁸, Christian Stehning⁸, Titus Kuehne^{4,5,9}, Heiner Post^{2,3,4,10}, Leonid Goubergrits^{5,11}, Eike Nagel¹², Burkert Pieske^{1,2,3,4}, Sebastian Kelle^{1,2,4‡} and Marcus Kelm^{3,5,9*‡}

OPEN ACCESS

Edited by:

Giulia Elena Mandoli,
University of Siena, Italy

Reviewed by:

Giuseppe Ciliberti,
Azienda Ospedaliero Universitaria
Ospedali Riuniti, Italy
Andrea Baggiano,
Monzino Cardiology Center
(IRCCS), Italy

*Correspondence:

Marcus Kelm
mkelm@dhzb.de

[†]These authors share first authorship

[‡]These authors have contributed
equally to this work and share last
authorship

Specialty section:

This article was submitted to
Cardiovascular Imaging,
a section of the journal
Frontiers in Cardiovascular Medicine

Received: 31 March 2021

Accepted: 18 June 2021

Published: 26 July 2021

Citation:

Faragli A, Alogna A, Lee CB, Zhu M, Ghorbani N, Lo Muzio FP, Schnackenburg B, Stehning C, Kuehne T, Post H, Goubergrits L, Nagel E, Pieske B, Kelle S and Kelm M (2021) Non-invasive CMR-Based Quantification of Myocardial Power and Efficiency Under Stress and Ischemic Conditions in Landrace Pigs. *Front. Cardiovasc. Med.* 8:689255. doi: 10.3389/fcvm.2021.689255

¹ Department of Internal Medicine and Cardiology, Deutsches Herzzentrum Berlin, Berlin, Germany, ² Charité – Universitätsmedizin Berlin, Department of Internal Medicine and Cardiology, Campus Virchow-Klinikum, Berlin, Germany, ³ Berlin Institute of Health, Berlin, Germany, ⁴ DZHK (German Centre for Cardiovascular Research), Partner Site Berlin, Berlin, Germany, ⁵ Institute for Computational and Imaging Science in Cardiovascular Medicine, Charité – Universitätsmedizin Berlin, Berlin, Germany, ⁶ Department of Surgery, Dentistry, Paediatrics and Gynaecology, University of Verona, Verona, Italy, ⁷ Department of Medicine and Surgery, University of Parma, Parma, Italy, ⁸ Clinical Science, Philips Healthcare, Hamburg, Germany, ⁹ Department of Congenital Heart Disease, Deutsches Herzzentrum Berlin, Berlin, Germany, ¹⁰ Department of Cardiology, Contilia Heart and Vessel Centre, St. Marien-Hospital Mülheim, Mülheim, Germany, ¹¹ Einstein Center Digital Future, Berlin, Germany, ¹² Institute of Experimental and Translational Cardiac Imaging, DZHK Centre for Cardiovascular Imaging, Goethe University Hospital Frankfurt, Frankfurt, Germany

Background: Myocardial efficiency should be maintained stable under light-to-moderate stress conditions, but ischemia puts the myocardium at risk for impaired functionality. Additionally, the measurement of such efficiency typically requires invasive heart catheterization and exposure to ionizing radiation. In this work, we aimed to non-invasively assess myocardial power and the resulting efficiency during pharmacological stress testing and ischemia induction.

Methods: In a cohort of $n = 10$ healthy Landrace pigs, dobutamine stress testing was performed, followed by verapamil-induced ischemia alongside cardiac magnetic resonance (CMR) imaging. External myocardial power, internal myocardial power, and myocardial efficiency were assessed non-invasively using geometrical and functional parameters from CMR volumetric as well as blood flow and pressure measurements.

Results: External myocardial power significantly increased under dobutamine stress [2.3 (1.6–3.1) W/m² vs. 1.3 (1.1–1.6) W/m², $p = 0.005$] and significantly decreased under verapamil-induced ischemia [0.8 (0.5–0.9) W/m², $p = 0.005$]. Internal myocardial power [baseline: 5.9 (4.6–8.5) W/m²] was not affected by dobutamine [7.5 (6.9–9.0) W/m², $p = 0.241$] nor verapamil [5.8 (4.7–8.8) W/m², $p = 0.878$]. Myocardial efficiency did not change from baseline to dobutamine [21% (15–27) vs. 31% (20–44), $p = 0.059$] but decreased significantly during verapamil-induced ischemia [10% (8–13), $p = 0.005$].

Conclusion: In healthy Landrace pigs, dobutamine stress increased external myocardial power, whereas myocardial efficiency was maintained stable. On the contrary,

verapamil-induced ischemia substantially decreased external myocardial power and myocardial efficiency. Non-invasive CMR was able to quantify these efficiency losses and might be useful for future clinical studies evaluating the effects of therapeutic interventions on myocardial energetics.

Keywords: myocardial efficiency, myocardial power, landrace pigs, dobutamine stress, myocardial ischaemia

INTRODUCTION

Myocardial efficiency represents the ratio between the external mechanical power required to maintain blood flow against systemic vascular resistance and the contraction power required by the left ventricular (LV) myocardium (1, 2). This mechanical efficiency proportion has increasingly become the focus of research, as it is associated to myocardial performance and myocardial remodeling (3, 4) in patients with cardiac diseases such as valvular heart disease (5, 6), heart failure (7), and cardiomyopathy (8).

Changes in myocardial efficiency can be triggered and altered by several factors, such as medical treatment (9) or surgical intervention (6), inducing hemodynamic changes in the cardiovascular system. Furthermore, efficiency can be influenced by stress and ischemic hemodynamic conditions, which can be pharmacologically induced by dobutamine (10–12) and verapamil (13, 14), respectively. The quantification of myocardial efficiency in such conditions holds the potential for providing insights into myocardial physiology as well as tolerance for stress and ischemia.

Nevertheless, even in resting conditions, the quantification of myocardial efficiency has not been established as a clinical standard since it is traditionally based on invasive measurements (3, 4). More recent concepts for its quantification have suggested the use of positron emission tomography (PET) in combination with concepts of mechanical external power (5, 6). However, PET is limited to specific clinical indications and includes exposure to ionizing radiation. A novel cardiac magnetic resonance (CMR)-based approach has been introduced to assess alterations in mechanical myocardial power and myocardial efficiency (15). The aim of this animal study was to quantify myocardial power and efficiency under stress and ischemic conditions using this non-invasive CMR approach.

METHODS

Data from $n = 10$ (51 ± 10 kg) Landrace pigs were selected from an already published study cohort from our group (16, 17), where dobutamine stress testing and verapamil ischemia induction were performed. Female Landrace swine were fasted overnight with free access to water and then sedated and intubated on the day of the experiment. Anesthesia was continued with fentanyl, midazolam, ketamine, and pancuronium as needed. The anesthesia regimen included a low-dose isoflurane to obtain deeper sedation and stabilize the hemodynamics without impacting much on systemic vascular resistance. Dobutamine infusion was titrated, aiming at a 25% heart rate (HR) increase

compared to baseline values, while verapamil was given as a single 2.5-mg bolus, aiming at a 25% decrease of cardiac index (CI). The experimental protocols were approved by the local bioethics committee of Berlin, Germany (G0138/17), and conform to the “European Convention for the Protection of Vertebrate Animals Used for Experimental and Other Scientific Purposes” (Council of Europe No. 123, Strasbourg 1985). The corresponding author had full access to all the data in the study and takes responsibility for its integrity and the data analysis.

Experimental Protocol

The experimental protocol has been already described in two published papers from our group (16, 17). Briefly, female Landrace pigs ($n = 10$, weight = 51 ± 10 kg) were acutely instrumented, and the animals were transported to the MRI facility for measurements. The pigs were ventilated with an MRI-compatible machine (Titus, Dräger Medical, Germany). After the baseline measurements, two steps were performed as follows: (I) dobutamine-induced stress (Dob) and (II) verapamil-induced ischemia (Ver). Dobutamine infusion was titrated, aiming at a 25% heart rate increase compared to the baseline values, while verapamil was given at boli of 2.5 mg each, aiming at a 25% decrease of CI. At each protocol, MRI images were acquired at short axis (SAX), 2Ch, 3Ch, and 4Ch views. After the MRI measurements, the animals were transported back to the operating room for sacrifice.

Cardiac Magnetic Resonance

All CMR images were acquired in a supine position using a 3T (Achieva, Philips Healthcare, Best, The Netherlands) MRI scanner with a flexible anterior and a built-in posterior receive coil, where up to 30 coil elements were employed depending on the respective anatomy. All animals were scanned using identical comprehensive imaging protocols. The study protocol included initial scouts to determine the cardiac imaging planes. Cine images were acquired using an ECG-gated balanced steady-state free precession sequence in three LV long-axis (2Ch, 3Ch, and 4Ch) planes. The ventricular two- and four-chamber planes were used to plan stack of SAX slices covering the entire LV. The following imaging parameters were used: repetition time (TR) = 2.9 ms, echo time (TE) = 1.45 ms, flip angle = 45° , acquired in-plane voxel size = 1.9×1.9 mm², reconstructed voxel size = 1.0×1.0 mm², slice thickness 8 mm, 40 reconstructed cardiac phases, and number of averages (NSA) 2. Flow was quantified using two-dimensional phase-contrast MRI: TR 3.9, ms; TE, 2.4 ms; flip angle, 15° ; 30 reconstructed cardiac phases; acquired in-plane voxel size, 2.1×2.1 mm²; reconstructed voxel size, 1.5×1.5 mm²; slice thickness, 10 mm; velocity encoding, 200 cm/s; and NSA, 2. The sequences were obtained (a) perpendicular to the

aorta to assess peak flow and aortic valve regurgitation as well as (b) between the mitral valve inflow and the left ventricular outflow tract to quantify the auxobaric contraction time, the isovolumetric contraction time, and the aortic pressure gradient, respectively. All images were acquired during normal respiration with no respiratory motion correction, as respiration-induced bulk cardiac motion was absent or very small in these animals. All images were analyzed offline using Medis Suite (version 3.1, Leiden, The Netherlands) and View Forum (R6.3V1L7 SP1, Philips Medical Systems Nederland B.V) in accordance to the consensus for quantification function and flow using CMR.

Myocardial Power and Power Efficiency

The clinical imaging and post-processing workflow to obtain CMR-derived myocardial power and efficiency is described in Figure 1.

Power is the rate of transferring or converting energy per unit time. Cardiac power output (CPO) defines the power needed to pump blood against a given afterload of the systemic circulation.

$$CPO (W) = \frac{MAP * CO_{total}}{451}$$

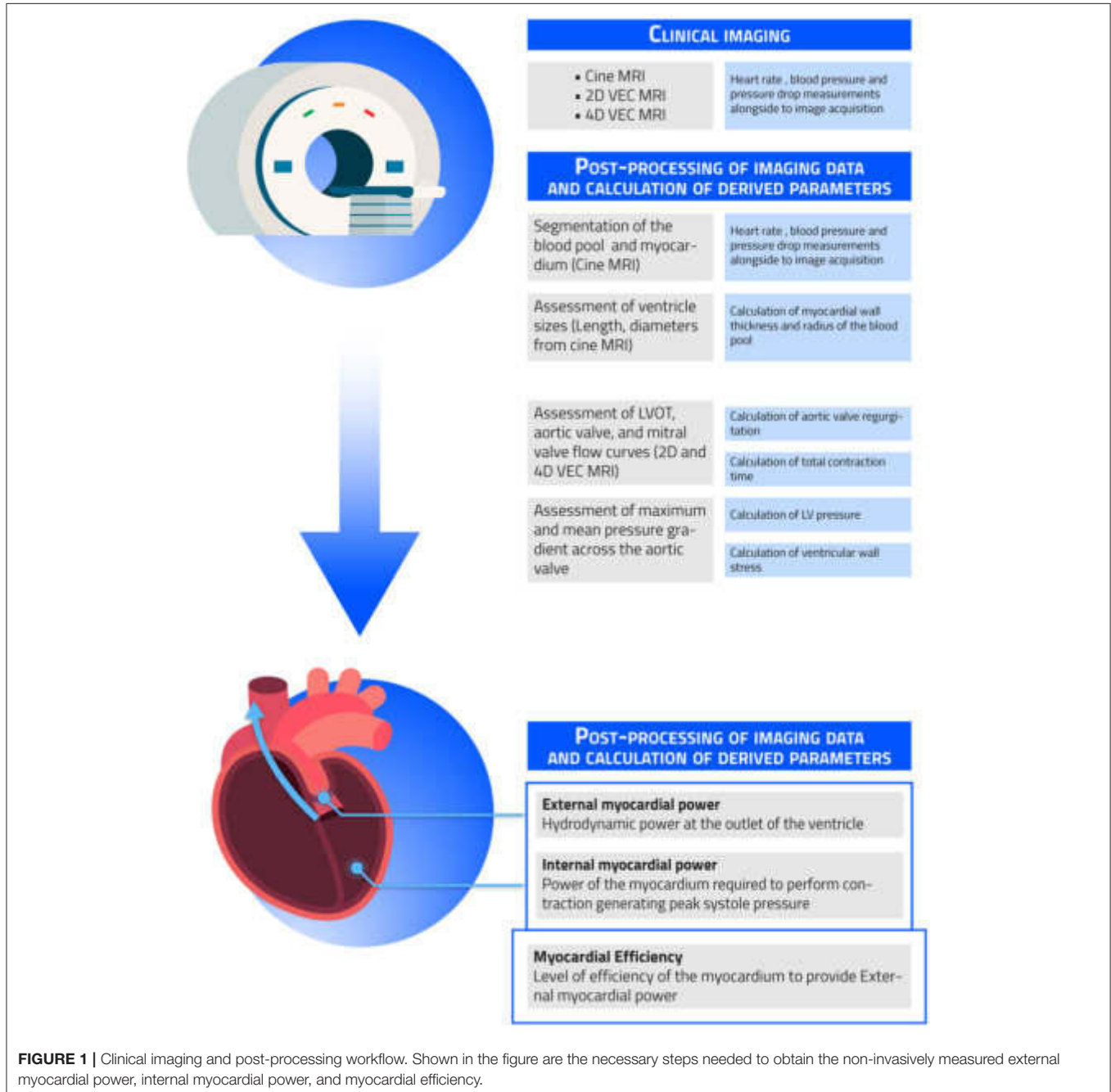


FIGURE 1 | Clinical imaging and post-processing workflow. Shown in the figure are the necessary steps needed to obtain the non-invasively measured external myocardial power, internal myocardial power, and myocardial efficiency.

with MAP = mean arterial pressure (converted from mmHg to Pa) measured invasively, 451 = the unit conversion in watt, and CO_{total} = total cardiac output (converted from L/min to qm/s). Cardiac output (CO) was calculated by the Simpson method to measure LV volumes using SAX MRI images. Simpson's technique is based on Simpson's rules, which for our purposes were essentially the sum of the cross-sectional areas of each slice accounting for slice thickness and the interval between slices in a stack of contiguous slices covering the entire LV. LV contours in all slices required to measure the cross-sectional areas in each slice were assessed manually. External myocardial power (EMP) defines the power needed to pump blood against a given afterload at the LVOT.

$$EMP (W) = (MAP + mean\Delta P_{AV}) * CO_{total}$$

The $mean\Delta P_{AV}$ is the mean pressure gradient across the aortic valve. In our cohort, EMP is nearly equivalent to the concept of cardiac power output and circulatory power (15), given the absence of aortic valve stenosis and aortic valve regurgitation.

The power required by the LV myocardium to perform contraction during systole is defined as internal myocardial power (IMP) (15, 18):

$$IMP (W) = \frac{V_{wall} * \sigma_{wall}}{t_{CS}}$$

where V_{wall} = myocardial wall volume, σ_{wall} = peak systolic wall stress, and t_{CS} = left ventricular systolic contraction time. EMP and IMP have been indexed to body surface area (BSA) to allow a better comparison between individuals. Wall stress was calculated using a simplified approach of the law of Laplace:

$$\sigma_{wall} = P_{sys} * \frac{R_{BP}}{2 * S_{wall}}$$

Where P_{SYS} = LV peak systolic pressure, R_{BP} = mean radius of the blood pool, and S_{wall} = mean myocardial wall thickness. S_{wall} and R_{BP} during systole were averaged from LV segmentations, considering LV as a cylindrical geometry for the correction of potential regional differences. P_{sys} = sum of the systolic blood pressure measured at the right arm and the maximum pressure gradient across the aortic valve. The ratio between IMP to the resulting EMP (IMP/EMP) is defined as myocardial efficiency.

Statistical Analysis

Continuous data are expressed as median and interquartile range (Q1–Q3) unless stated otherwise. Data distribution was tested using Shapiro–Wilk and Shapiro–Francia tests. The correlations between the CMR parameters of indexed IMP, indexed EMP, myocardial efficiency, and the hemodynamic parameters of CPO, CI, and left ventricular ejection fraction (LVEF) were assessed by linear regression analysis.

Wilcoxon signed rank test was used to assess differences between baseline and the intervention. The significance level was set at 0.05. Data were analyzed using Stata 15.1 (StataCorp, College Station, TX, USA) and GraphPad 8.0.2 (GraphPad Software, Inc., La Jolla, CA, USA).

TABLE 1 | Clinical characteristics, cardiac magnetic resonance geometric and functional parameters, and invasively measured hemodynamic parameters of pigs at rest, under stress (dobutamine), and under ischemia (verapamil).

Subjects (n = 10)	BL	Dob	Ver	p-value (BL vs. Dob)	p-value (BL vs. Ver)
sBP (mmHg)	108 (101–117)	136 (127–147)	87 (78–106)	0.007	0.005
dBP (mmHg)	79 (60–87)	84 (57–97)	58 (50–66)	0.646	0.012
Myocardial mass/BSA (g/m^2)	41 (34–52)	41 (34–52)	41 (34–52)	–	–
Myocardial volume (ml)	38 (32–50)	38 (32–50)	38 (32–50)	–	–
SV _{flow} (ml)	57 (44–80)	52 (45–78)	42 (47–53)	0.386	0.005
CO _{flow} (L/min)	5.6 (4.8–6.5)	6.0 (4.6–8.0)	3.9 (3.1–4.9)	0.220	0.013
Distensibility aorta ascendens ($10^{-3} mmHg^{-1}$)	11.2 (7.7–14.8)	9.7 (6.1–14.6)	5.5 (4.2–7.7)	0.721	0.017
Distensibility aorta descendens ($10^{-3} mmHg^{-1}$)	7.0 (4.4–9.6)	6.7 (4.5–8.6)	4.9 (1.5–7.0)	0.721	0.139
External myocardial power (W/m^2)	1.3 (1.1–1.6)	2.3 (1.6–3.1)	0.8 (0.5–0.9)	0.005	0.005
Internal myocardial power (W/m^2)	5.9 (4.6–8.5)	7.5 (6.9–9.0)	5.8 (4.7–8.8)	0.241	0.878
Myocardial efficiency (%)	21 (15–27)	31 (20–44)	10 (8–13)	0.059	0.005

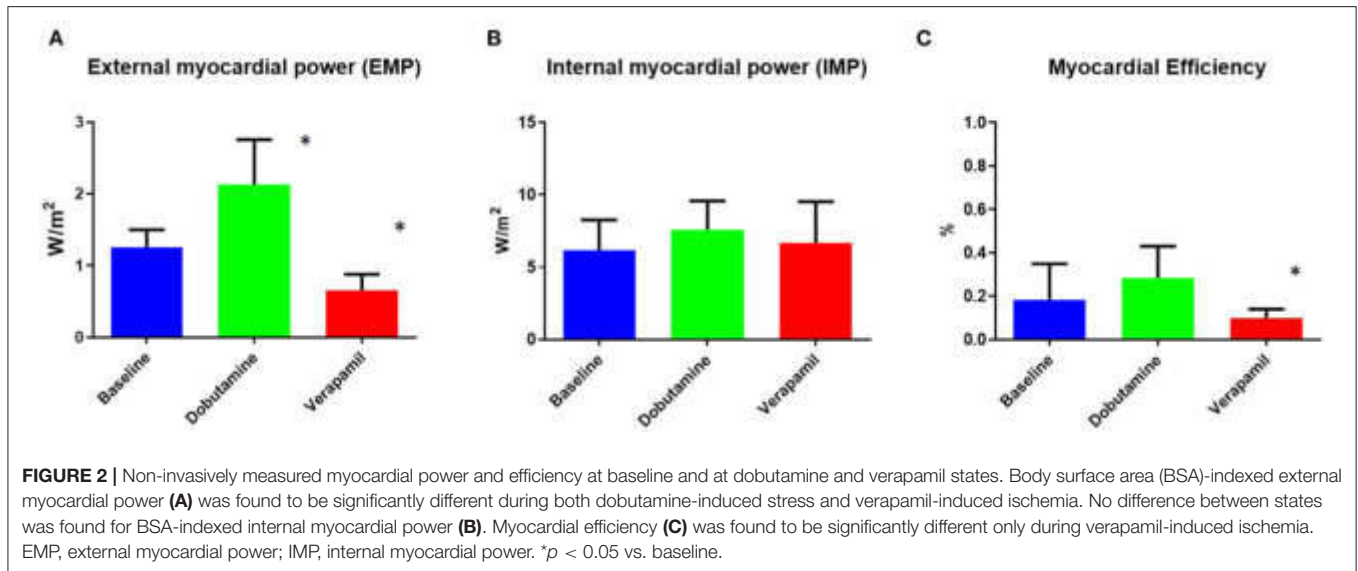
BSA, body surface area; BL, baseline; Dob, dobutamine infusion; Ver, verapamil infusion; sBP, systolic blood pressure; dBP, diastolic blood pressure; mAOP, mean arterial pressure; EDV, end-diastolic volume; ESV, end-systolic volume; LVEF, left ventricular ejection fraction; HR, heart rate; SV, stroke volume; CO, cardiac output. Data are presented as median and interquartile range.

RESULTS

Power and efficiency analyses were performed in $n = 10$ pigs. The hemodynamic and the CMR-based geometrical and functional parameters of the pigs at rest, under dobutamine and under verapamil, are reported in **Table 1**. The following hemodynamic data have been previously published (17), where a significant increase of HR, mean aortic pressure, and CPO under Dob and a respective significant decrease during Ver were observed; stroke volume and LVEF did not decrease significantly under Dob but decreased significantly instead during Ver.

Hemodynamic Parameters

Relevant differences for systolic blood pressure were seen between pigs under stress, whereas no differences were seen for diastolic blood pressure and mean arterial pressure between interventions (stress and ischemia) and rest. After stress induction with dobutamine, the heart rate increased



significantly, while HR did not change after ischemia induction with verapamil.

CO, calculated by the Simpson method, significantly increased during stress with dobutamine and also significantly decreased vs. baseline during ischemia. Invasively measured CPO significantly increased during dobutamine stress, and a significant decrease was observed during ischemia with verapamil. LVEF increased non-significantly during dobutamine but significantly decreased during verapamil.

Heart Power Analysis

EMP, IMP, and myocardial efficiency were assessed in all groups using CMR. EMP changed significantly during both dobutamine-induced stress and also after ischemia induction (Figure 2A). There were instead no significant differences in IMP after stress with dobutamine or ischemia with verapamil (Figure 2B). Myocardial efficiency changed significantly from baseline to verapamil, but only a decreasing trend was observed between baseline and dobutamine (Figure 2C).

Comparison With Hemodynamic Parameters (Left Ventricular Ejection Fraction, Cardiac Index, and Cardiac Power Output)

The linear regression analysis showed a good correlation between EMP and CPO (Figure 3A) and between external myocardial power and LVEF (Figure 3D). No correlation was observed between IMP and CPO (Figure 3B) and vs. LVEF (Figure 3E). A moderate correlation was observed instead between myocardial efficiency and CPO (Figure 3C) and LVEF (Figure 3F).

DISCUSSION

Summary of Main Findings

The results of our non-invasive MRI approach show that myocardial efficiency was not altered during dobutamine stress

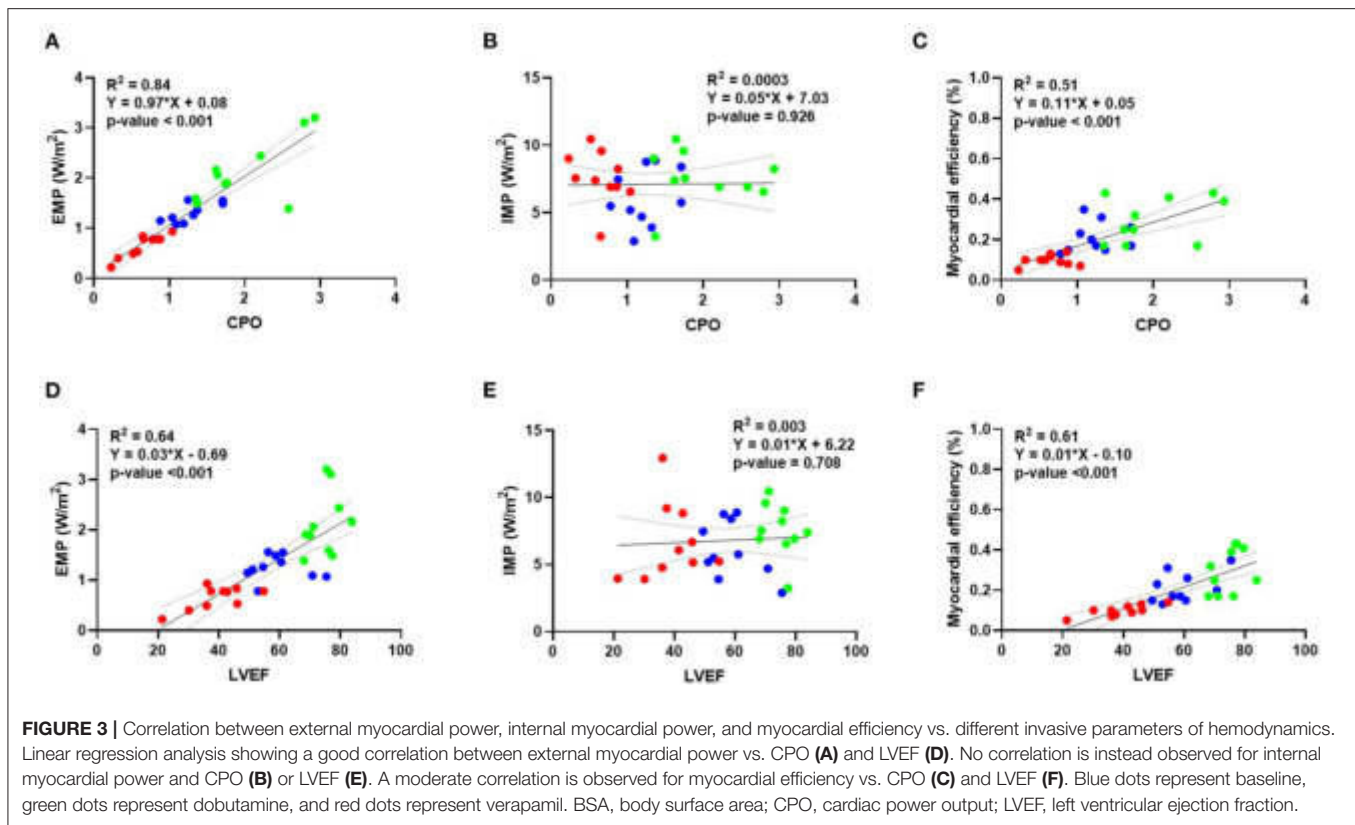
testing, whereas efficiency was decreased during verapamil-induced ischemia. While external myocardial power directly reflects the resulting hemodynamic responses under both stress and ischemic conditions, myocardial efficiency reveals the coupling between the left ventricle and the circulatory system.

External Myocardial Power

External power has been shown to predict mortality in patients with cardiogenic shock or outcome in chronic heart failure patients better than LVEF (19, 20). In a study from our group, we were able to show that CPO, as an external power measure, accurately reflects left ventricular stroke work per minute over a wide range of inotropic states (21). The area of the pressure-volume loop reflecting the external work of the heart is also called left ventricular stroke work (LV SW). Through an invasive pressure-volume analysis, this represents the most comprehensive way to describe ventricular performance (22). While LVEF provides a load-dependent measurement of heart function, LV SW and, in turn, CPO offer load-independent information extremely relevant in patients with altered inotropy due to heart failure (21).

Internal Myocardial Power and Myocardial Efficiency

The energy that the myocardium needs to generate external power and the resulting efficiency have been of particular interest from a clinical and a research standpoint, respectively. In the diseased myocardium, this efficiency is known to be reduced (3), and it has long been discussed whether this energy loss can help to describe the pathophysiology in the diseased state (8). In line with these concepts, Güçlü et al. (6) have demonstrated that myocardial efficiency plays a crucial role in myocardial remodeling processes in aortic valve stenosis and improvements can be measured after surgical valve replacement. These changes in external myocardial efficiency were shown to correlate to the changes in myocardial oxygen consumption (VO_2). A surrogate



for the mechanical internal power that does not require exposure to ionizing radiation and that can be related to the resulting external power (external myocardial efficiency) has been recently introduced (15). Similar to the findings by Güçlü et al. (6), internal myocardial power was found to be increased with a resulting reduced efficiency in patients with aortic valve stenosis compared to controls as what would be expected under conditions of increased afterload. While external myocardial power was not different between aortic stenosis patients and controls as long as the EF was preserved, circulatory efficiency was found below control levels, even in patients with normal EF (15).

Within this animal cohort, when the myocardium was not impaired, its efficiency was found to be at human control levels under resting conditions (15). During a dobutamine-induced stress response, the efficiency did not change. Based on previous concepts of myocardial energy (3), losses would not be expected under healthy conditions. In line with these concepts, an impaired myocardial efficiency was found under ischemic conditions when the LV contraction power resulted in less external myocardial power. The internal myocardial power already includes aspects of cardiac morphology, and future research is required to assess whether myocardial fibrosis and histological changes will be reflected in power measurements (23). Note that IMP did not change significantly between the three conditions. We suppose that this is due to a healthy heart, which is able to cover drug-simulated changes in afterload (stress and ischemia). A decrease in IMP means better heart work efficiency that we cannot expect in a healthy heart. An increase

in IMP means lower efficiency in heart work, which should be associated with pathological changes of the heart which, however, require time. Short-time changes in heart work conditions, as investigated in the current study, cannot be associated with such a pathological change. In a recently published work which investigated myocardial power and efficiency before and after treatment of the aortic valve, a significant decrease in IMP and a respective increase in efficiency due to treatment of the aortic valve were shown (24). Hence, IMP is not a constant value.

Invasively Measured CPO Against External Myocardial Power

In our study, we were able to show that external myocardial power measured with CMR is a feasible technique able to correlate CPO, measured invasively. This represents an advancement in CMR-based assessment of heart function, adding a potential new parameter that can be utilized in patients with compromised LV function.

Limitations

The calculation of myocardial power and efficiency focuses on systole as it accounts for most of the energy expenditure of the heart. Myocardial energetics were not considered in diastole even though diastolic relaxation is an active energy-requiring process involving ATP and oxygen consumption. Diastolic dysfunction plays a major role in the pathophysiology of several cardiac diseases such as heart failure, but the role of myocardial efficiency regarding its pathophysiology is still unknown. Hence, novel

concepts are required to quantify myocardial efficiency in the diastolic phase of the heart to get a deeper understanding of the pathophysiology of diastolic heart failure. Our approach did not include metabolic measures of myocardial energy consumption which traditionally had to be assessed with the use of an invasive conductance catheter. Modern concepts use PET, which allows measuring of myocardial energy consumption by indirectly quantifying metabolic oxygen consumption from the coronaries with the disadvantage of using ionizing radiation. This study was a pure mechanical MRI-only approach calculating the internal myocardial power with the assumption that internal power is the mechanical potential power generated by myocardial contraction. Furthermore, LV wall stress was calculated using a simplified approach of the law of Laplace. The geometrical shape of the LV as well as regional strain both determine LV wall stress and, subsequently, impact internal myocardial power. Hence, more precise models should be applied to calculate internal myocardial power more accurately in future projects. The current study was limited to testing of dobutamine and verapamil drugs. The effect of other drugs such as dipyridamole, adenosine, or levosimendan should be investigated in frames of future studies. This study was an animal study with a small cohort of $n = 10$. As animal studies can be an imprecise predictor of the reactions and physiology of humans, future clinical trials need to be carried out to prove our results in patients under various disease states.

CONCLUSIONS

This study underlines the concept of assessing internal and external myocardial power and their resulting efficiency in a completely non-invasive CMR-based approach. Efficiency measures were shown to maintain stability during stress testing as long as the myocardium is not impaired. Under ischemic conditions, however, quantifiable efficiency losses occurred. This study underlines the promising potential of the non-invasive approach in human subjects, in particular in those with altered myocardial performance.

DATA AVAILABILITY STATEMENT

The raw data supporting the conclusions of this article will be made available by the authors, without undue reservation.

REFERENCES

- Burkhoff D, Sagawa K. Ventricular efficiency predicted by an analytical model. *Am J Physiol*. (1986) 250:R1021–7. doi: 10.1152/ajpregu.1986.250.6.R1021
- Bing RJ, Hammond MM, Handelsman JC, Powers SR, Spencer FC, et al. The measurement of coronary blood flow, oxygen consumption, and efficiency of the left ventricle in man. *Am Heart J*. (1949) 38:1–24. doi: 10.1016/0002-8703(49)90788-7
- Knaapen P, Germans T, Knuuti J, Paulus WJ, Dijkmans PA, Allaart CP, et al. Myocardial energetics and efficiency: current status of the noninvasive approach. *Circulation*. (2007) 115:918–27. doi: 10.1161/CIRCULATIONAHA.106.660639

ETHICS STATEMENT

The experimental protocols were approved by the local bioethics committee of Berlin, Germany (G0138/17), and conform to the European Convention for the Protection of Vertebrate Animals used for Experimental and other Scientific Purposes (Council of Europe No 123, Strasbourg 1985).

AUTHOR'S NOTE

Professor Dragun passed away on December 28, 2020. This publication is dedicated to her memory as a mentor, role model, and stellar scientist.

AUTHOR CONTRIBUTIONS

SK, HP, AA, and MK: conceptualization and methodology. LG: software. MK, AF, and LG: formal analysis. CL, MZ, NG, MK, and AF: writing—original draft preparation. AF, AA, CL, MZ, NG, FL, BS, CS, TK, HP, LG, EN, BP, SK, and MK: writing—review and editing. All authors contributed to the article and approved the submitted version.

FUNDING

AF, HP, EN, AA, and SK received funding from DZHK (German Centre for Cardiovascular Research—Grant Number: 81X2100305). MK is a participant in the Charité Digital Clinician Scientist Program funded by DFG, and AA is a participant in the BIH-Charité Clinician Scientist Program funded by the Charité—Universitätsmedizin Berlin and the Berlin Institute of Health. Both programs were initiated and led by Professor Duska Dragun to enable resident physicians to pursue a career in academic medicine. Furthermore, AA was supported by the EU Horizon 2020 FETOPEN-2018-2020 Programme LIONHEARTED, grant agreement no. 828984, as well as by the EU Horizon 2020 NMBP-2016 Programme CUPIDO, grant agreement no. 720834.

ACKNOWLEDGMENTS

We thank Simone Proietti Timperi for performing the graphical illustration.

7. Cetin MS, Ozcan Cetin EH, Canpolat U, Sasmaz H, Temizhan A, Aydogdu S. Prognostic significance of myocardial energy expenditure and myocardial efficiency in patients with heart failure with reduced ejection fraction. *Int J Cardiovasc Imaging*. (2018) 34:211–22. doi: 10.1007/s10554-017-1226-8
8. Katz AM. Cardiomyopathy of overload. A major determinant of prognosis in congestive heart failure. *N Engl J Med*. (1990) 322:100–10. doi: 10.1056/NEJM19901113220206
9. Eichhorn EJ, Bristow MR. Medical therapy can improve the biological properties of the chronically failing heart. A new era in the treatment of heart failure. *Circulation*. (1996) 94:2285–96. doi: 10.1161/01.CIR.94.9.2285
10. Porenta G, Cherry S, Czernin J, Brunken R, Kuhle W, Hashimoto T, Schelbert HR. Noninvasive determination of myocardial blood flow, oxygen consumption and efficiency in normal humans by carbon-11 acetate positron emission tomography imaging. *Eur J Nucl Med*. (1999) 26:1465–74. doi: 10.1007/s002590050480
11. Vanoverschelde JL, Wijns W, Essamri B, Bol A, Robert A, Labar D, et al. Hemodynamic and mechanical determinants of myocardial O₂ consumption in normal human heart: effects of dobutamine. *Am J Physiol*. (1993) 265:H1884–92. doi: 10.1152/ajpheart.1993.265.6.H1884
12. Beanlands RS, Bach DS, Raylman R, Armstrong WF, Wilson V, Montieth M, et al. Acute effects of dobutamine on myocardial oxygen consumption and cardiac efficiency measured using carbon-11 acetate kinetics in patients with dilated cardiomyopathy. *J Am Coll Cardiol*. (1993) 22:1389–98. doi: 10.1016/0735-1097(93)90548-F
13. Ferlinz J, Easthope JL, Aronow WS. Effects of verapamil on myocardial performance in coronary disease. *Circulation*. (1979) 59:313–9. doi: 10.1161/01.CIR.59.2.313
14. Bania TC, Chu J, Perez E, Su M, Hahn IH. Hemodynamic effects of intravenous fat emulsion in an animal model of severe verapamil toxicity resuscitated with atropine, calcium, and saline. *Acad Emerg Med*. (2007) 14:105–11. doi: 10.1197/j.aem.2006.10.094
15. Lee CB, Goubergrits L, Fernandes JF, Nordmeyer S, Knosalla C, Berger F, et al. Surrogates for myocardial power and power efficiency in patients with aortic valve disease. *Sci Rep*. (2019) 9:16407. doi: 10.1038/s41598-019-52909-9
16. Faragli A, Tanacli R, Kolp C, Lapinskas T, Stehning C, Schnackenburg B, et al. Cardiovascular magnetic resonance feature tracking in pigs: a reproducibility and sample size calculation study. *Int J Cardiovasc Imaging*. (2020) 36:703–12. doi: 10.1007/s10554-020-01767-y
17. Faragli A, Tanacli R, Kolp C, Abawi D, Lapinskas T, Stehning C, et al. Cardiovascular magnetic resonance-derived left ventricular mechanics-strain, cardiac power and end-systolic elastance under various inotropic states in swine. *J Cardiovasc Magn Res*. (2020) 22:79. doi: 10.1186/s12968-020-00679-z
18. Preston RR, Wilson TE. *Lippincott's Illustrated Review: Physiology*. Philadelphia, PA; Alphen aan den Rijn: Lippincott Williams & Wilkins; SUA/Wolters Kluwer Health (2012). p. 203–13.
19. Fincke R, Hochman JS, Lowe AM, Menon V, Slater JN, Webb JG, et al. Cardiac power is the strongest hemodynamic correlate of mortality in cardiogenic shock: a report from the SHOCK trial registry. *J Am Coll Cardiol*. (2004) 44:340–8. doi: 10.1016/j.jacc.2004.03.060
20. Schlosshan D, Elliott M. Prognostic indicators in patients presenting with acute cardiogenic pulmonary edema treated with CPAP: it's not the acid that matters, it's back to basics. *Crit Care*. (2010) 14:1009–9. doi: 10.1186/cc9325
21. Abawi D, Faragli A, Schwarzl M, Manninger M, Zweiker D, Kresoja KP, et al. Cardiac power output accurately reflects external cardiac work over a wide range of inotropic states in pigs. *BMC Cardiovasc Disord*. (2019) 19:217. doi: 10.1186/s12872-019-1212-2
22. Kass DA, Maughan WL. From 'Emax' to pressure-volume relations: a broader view. *Circulation*. (1988) 77:1203–12. doi: 10.1161/01.CIR.77.6.1203
23. Faragli A, Merz S, Muzio FPL, Doeblin P, Tanacli R, Kolp C, et al. Estimation of total collagen volume: a T1 mapping versus histological comparison study in healthy landrace pigs. *Int J Cardiovasc Imaging*. (2020) 36:1761–1769. doi: 10.1007/s10554-020-01881-x
24. Nordmeyer S, Lee CB, Goubergrits L, Knosalla C, Berger F, Falk V, et al. Circulatory efficiency in patients with severe aortic valve stenosis before and after aortic valve replacement. *J Cardiovasc Magn Reson*. (2021) 23:15. doi: 10.1186/s12968-020-00686-0

Conflict of Interest: BP reports having received consultancy and lecture honoraria from Bayer Daiichi Sankyo, MSD, Novartis, Sanofi-Aventis, Stealth Peptides, and Vifor Pharma and editor honoraria from the *Journal of the American College of Cardiology*. SK reports receiving grants from Philips Healthcare and speaker honoraria from Medis. CS and BS are employees of Philips Healthcare.

The remaining authors declare that the research was conducted in the absence of any commercial or financial relationships that could be construed as a potential conflict of interest.

Publisher's Note: All claims expressed in this article are solely those of the authors and do not necessarily represent those of their affiliated organizations, or those of the publisher, the editors and the reviewers. Any product that may be evaluated in this article, or claim that may be made by its manufacturer, is not guaranteed or endorsed by the publisher.

Copyright © 2021 Faragli, Alogna, Lee, Zhu, Ghorbani, Lo Muzio, Schnackenburg, Stehning, Kuehne, Post, Goubergrits, Nagel, Pieske, Kelle and Kelm. This is an open-access article distributed under the terms of the Creative Commons Attribution License (CC BY). The use, distribution or reproduction in other forums is permitted, provided the original author(s) and the copyright owner(s) are credited and that the original publication in this journal is cited, in accordance with accepted academic practice. No use, distribution or reproduction is permitted which does not comply with these terms.



Contents lists available at ScienceDirect

Progress in Biophysics and Molecular Biology

journal homepage: www.elsevier.com/locate/pbiomolbio

Original Research

In-situ optical assessment of rat epicardial kinematic parameters reveals frequency-dependent mechanic heterogeneity related to gender

Francesco Paolo Lo Muzio ^{a, b, 1}, Giacomo Rozzi ^{a, b, 1}, Stefano Rossi ^b,
 Amparo Guerrero Gerbolés ^b, Lorenzo Fassina ^c, Giovanna Pelà ^b,
 Giovanni Battista Luciani ^a, Michele Miragoli ^{b, d, *}

^a Department of Surgery, Dentistry, Paediatrics and Gynaecology, University of Verona Via S. Francesco 22, 37129, Verona, Italy

^b Department of Medicine and Surgery, University di Parma, via Gramsci 14, 43126, Parma, Italy

^c Department of Industrial Engineering and Informatics, University of Pavia, Via Ferrata 1, 27100, Pavia, Italy

^d Humanitas Clinical and Research Center, Via Manzoni 56, 20089, Rozzano, Italy

ARTICLE INFO

Article history:

Received 11 March 2019

Received in revised form

6 May 2019

Accepted 8 May 2019

Available online xxx

Keywords:

Gender difference

Cardiac physiology

Cardiac mechanics

Artificial vision

Optical kinematic assessment

ABSTRACT

Background: Gender-related cardiac mechanics following the electrical activity has been investigated from basic to clinical research, but results are still controversial. The aim of this work is to study the gender related cardiac mechanics and to focus on its heart rate dependency.

Methods: We employed 12 Sprague Dawley rats (5 males and 7 females) of the same age and, through a novel high resolution artificial vision contactless approach, we evaluated *in-situ* cardiac kinematic. The hearts were paced on the right atria appendage via cathodal stimuli at rising frequency.

Results: Kinematic data obtained at rising pacing rates are different between male and female rat hearts: male tended to maintain the same level of cardiac force, energy and contractility, while female responded with an increment of such parameters at increasing heart rate. Female hearts preserved their pattern of contraction and epicardial torsion (vorticity) at rising pacing rates compared to male. Furthermore, we observed a difference in the mechanical restitution: systolic time vs. diastolic time, as an index of cardiac performance, reached higher value in male compared to female hearts.

Conclusion: Our innovative technology was capable to evaluate *in-situ* rat epicardial kinematic at high stimulation frequency, revealing that male preserved kinematic parameters but varying the pattern of contraction/relaxation. On the contrary, female preserved the pattern of contraction/relaxation increasing kinematic parameters.

© 2019 Elsevier Ltd. All rights reserved.

1. Introduction

The relationship between protection from cardiovascular diseases (CVDs) and gender has fascinated researchers and cardiologists for decades. The reason is strictly related to the presence of female and male hormones, targeting their effects almost in all part of the cardiomyocyte: ion channel repertoire (Ravens, 2018; Tadros et al., 2014), receptors (Dworatzek et al., 2019), calcium handling

machinery (Ayaz et al., 2019), mitochondria (Milerova et al., 2016), intracellular pathways, genome (Kerr et al., 2017) and epigenome (Cong et al., 2013). It emerges that cardiac electrophysiology is, undeniably, affected by estrogen and testosterone (Weerateerangkul et al., 2017), having effects on all phases of the action potential. This would suggest a possible “protection” against the progression towards CVDs for female in premenopausal age compared to male hearts. Nonetheless, all that glitters is not gold. Bazett in 1920 suggested how both sex difference and heart rate (HR) have an impact on the ECG (and he further developed the famous correction QT_c formula that report his name). Women have a long QT in respect to men and this exposes the female at risk of some life-threatening arrhythmias, such as *torsade de pointes* especially when is drug-induced (Makkar et al., 1993). Park et al.

* Corresponding author. Department of Medicine and Surgery University of Parma Via Gramsci 14, 43126, Parma, Italy.

E-mail address: michele.miragoli@unipr.it (M. Miragoli).

¹ Contributed equally.

List of abbreviations

CVD	Cardiovascular diseases
HR	Heart Rate
MHC	Myosin Heavy Chain
Vi.Ki.E	Video Kinematic Evaluation
BCL	Basic Cycle Length
S/D time	Systolic time/Diastolic time
S.E.M	Standard Error of the Mean
PIV	Particle Image Velocimetry
S/D area	systolic area/Diastolic area

(Parks and Howlett, 2013) elegantly summarized the physiological divergences between male and female heart. Moreover, at the single cell level, numerous studies did not observe gender difference in the peak of Ca^{2+} current except Farrell et al. (2010) that demonstrated significant modifications *via* voltage clamp. Cellular contraction has also been taken into account by numerous investigations. Rosenkranz-Weiss et al. reported that female rat ventricular myocytes display high-level of myosin heavy chain (MHC) as well as upregulation of actin mRNA compared to males (Rosenkranz-Weiss et al., 1994). Notably, they found no difference in the α -to β -ratio of MHC proteins, suggesting that those sex differences are abolished after post-translational modifications. Petre et al. (2007) and Schwertz et al. (2004) did not find any gender-related difference in terms of force of contraction in ventricular trabeculae. In detail, Schwertz et al. (2004) found that ATPase activity was higher in female rats at any given extracellular Ca^{2+} concentration compared to male, suggesting that the female contractile machinery had a greater Ca^{2+} sensitivity. Experimentally, the single cell contraction is smaller in female ventricular myocytes compared to male especially when those cells are paced at rapid rates (Grandy and Howlett, 2006). This would indicate that high stimulation frequency may highlight the gender difference in cardiac performance. Some authors showed an increment in isolated ventricular myocyte contraction (Curl et al., 2003), while others reported a reduction (Ren et al., 2003). A robust evidence regarding the role of female hormone on cardiac activity has been observed in female rats undergoing ovariectomy. To note such differences were completely reversed when 17- β -estradiol was replaced. Androgen receptors are usually present in cardiac tissue and study efforts were mostly focused on their action on intracellular Ca^{2+} handling machinery (Er et al., 2007) rather than contractile performance. Few studies have been performed at multicellular cardiac level after gonadectomy and reported a decrement in the maximum contraction and the peak of Ca^{2+} . Studies on papillary muscle (Schwertz et al., 2004) recapitulated the evidence observed at single cell level, i.e. the greater affinity of female myofibrils to Ca^{2+} , demanding less extracellular Ca^{2+} for evoking the same force of contraction in comparison to male. On the contrary, the same authors reported that in the Langerdorff perfused heart, male generated a greater ventricular pressure compared to female. Such disparate findings indicate that methodological preparations influenced gender dissimilarity.

Based on the observations above, it is evident that rodents are an appropriate animal model for studying the relationship between cardiac performance and gender (Raddino et al., 1989). In particular, rodent models may be well suited for dissecting the biophysical mechanisms underlying the propensity to develop CVDs. In spite of the great efforts and the results obtained at single cell and tissue levels, *in-vivo* investigations on gender-related ventricular kinematic are lacking. We are aware that canonical *in-vivo* gender-

related data are merely analyzed from echocardiography (Gori et al., 2014), cardiac MRI and SPECT (Shaw, 2016) exquisitely describing the heart global mechanical function. Unfortunately, these imaging techniques provide only minimal information on kinematic.

In this paper, we adopted the optical-image based technology called Video Kinematic Evaluation (Vi.Ki.E.) (Fassina et al., 2011, 2017; Meraviglia et al., 2016), completely developed in our laboratory, to evaluate *in-situ* high resolution ventricular tissue kinematic in male and female beating hearts, paced at different frequencies.

We observed a frequency-dependent increment of epicardial ventricular contractility, force and kinetic energy in female rat hearts compared to male. Female rats tended to preserve their pattern of contraction and the total perimeter of trajectories at different basic cycle lengths (BCL) resulting in less heart torsion compared to male. Sex difference does not influence the systolic area/diastolic area (S/D area) but it denotes a consistent variation in systolic time/diastolic time (S/D time) between the two groups. Data from our innovative optical-based and contactless technique indicate a profound gender difference in the heart mechanics, opening avenues for further evaluation in the clinical setting.

2. Materials and methods

2.1. Experimental animals

The study population consisted of 12 Sprague Dawley rats (5 males and 7 females) bred in our animal facility (approved protocols: 281/2017, 989/2017). The study was conformed to Italian (D.L.4/3/2014) and European guidelines (2010/63/UE). Rats, 6 months old weighting 250–275 g, were anesthetized with 0.20 mg/kg ip of a mixture of tiletamine hydrochloride and zolazepam hydrochloride (Zoletil; Virbac S.r.l., Carros, France) + 0.15 mg/kg ip medetomidine hydrochloride (Domitor; Orion Corporation, Espoo, Finland). The heart was exposed through a median thoracotomy and suspended in a pericardial cradle under artificial ventilation (RoVent® Small Animal Ventilator, Kent Scientific, CT, USA). Body temperature was maintained constantly at 37 °C with heat lamp radiation and further doses of anesthetic was administered as needed during the experiment. This type of anesthesia invariably suppressed the sympathetic tone in rodents and so our results are not biased by the autonomous nervous system (Tan et al., 2003). Animals were sacrificed with a lethal injection of sodium pentothal as indicated in the protocols.

2.2. In-vivo atrial stimulation

The heart was stimulated with a cathodal suprathreshold train of stimuli (10 Vpp) at different basic cycle length (BCL: 390 ms, 330 ms, 290 ms, 260 ms, 230 ms, 210 ms, 190 ms, 170 ms, 160 ms) by driving the right atrium with a silver electrode (0.05 mm) with one end connected to a stimulus generator (SIU-102, Warner Instruments CT, USA) and the other hooked to the atrial auricle appendage (Fig. 1A). The current return silver electrode has been placed in the right forearm. The stimulus generator was triggered by a function generator (Aim-TTi TG310, RS Components, Milano, IT).

2.3. In-situ optical assessment of kinematic parameters

To evaluate cardiac kinematic parameters, 2 s videos with the temporal resolution of 500 fps (Fig. 1B) were acquired for each BCL, with a spatial resolution of 1280 × 1024 pixel. The camera (Baumer HXC13, Baumer Italia S.r.l., Milano, Italy) was connected with full

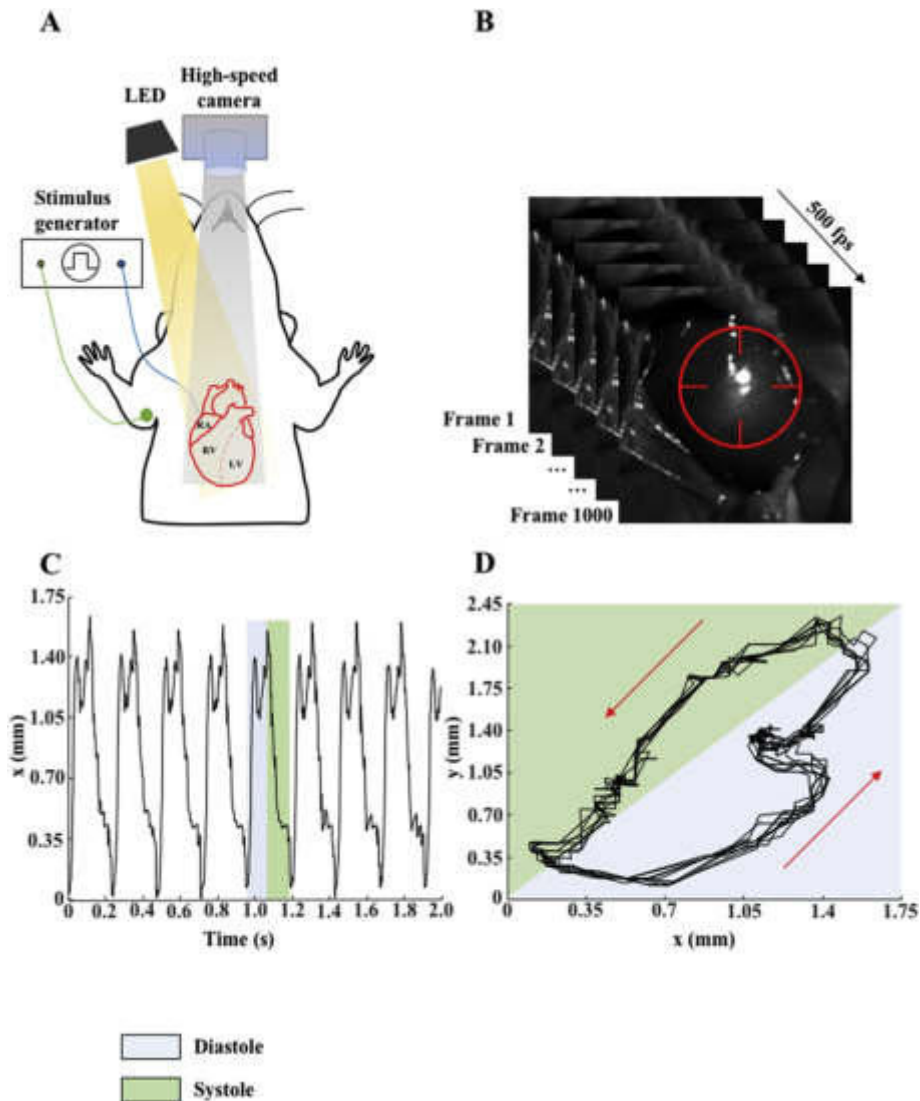


Fig. 1. Schematic representation of the experimental setup. **A.** The heart (red cartoon) is exposed after median thoracotomy. One end of the stimulating electrode (blue line) is hooked on the Right Atrial (RA) auricle appendage to perform atrial stimulation, while the other end is connected to a stimulus generator (black rectangular box). The current return electrode (green line) is placed on the right forearm. The high-speed camera is placed perpendicular to the heart to record anterior epicardial kinematic. The grey shaded region represents the video camera field of view. The LED is placed beside the camera. The yellow shaded region represents the light beam. RV, Right Ventricle; LV, Left Ventricle; dashed red line, interventricular septum. **B.** Stack of images of rat hearts recorded at 1280×1024 pixel at 500 fps. Red target represents the virtual marker positioned in that frame. **C.** Example of the marker movement in x coordinate during 2 s recording. The light blue rectangular indicates the diastolic phase, while the light green rectangle indicates the systolic phase. **D.** Example of trajectories in x-y plane drawn by the marker in 2 s recording. Each loop represents a single cardiac cycle. The light blue and the light green triangles represent the diastolic and systolic phases, respectively. Red arrows indicate the direction of the cardiac cycle.

CameraLink[®] interface to a frame grabber acquisition board PCIe 1433 (National Instruments, Assago, Italy) and placed at 20 cm above the heart. The camera was equipped with a macro-objective Kowa Industrial Lenses LM35XC, $F = 1:2.0$, $f = 35$ mm, picture size 13.8–18.4 mm (RMA Electronics, Hingham, MA, USA). The acquisition board was integrated into a Workstation HP Z220 (Crisel Instruments, Roma, Italy) with 24 GB RAM and the acquisition software was custom made in LabVIEW 2013 Visual Programming Language (National Instruments, Assago, Italy). Only videos with observed 1:1 capture were included in the final analysis.

The videos were elaborated by Video Spot Tracker, an open source software (VST, CISMM, Computer Integrated Systems for Microscopy and Manipulation, UNC Chapel Hill, NC, USA), that enables to place a virtual marker (Fig. 1B, red target) with a chosen kernel on the first video frame. The marker follows the light spots

onto the epicardial surface and tracks its coordinates in x and y for each frame. The movement of the light spot is a function of the surface curvature and because it moves back and forth from apex to base during cardiac cycle, it can be assumed as the direct deformation of the epicardial tissue (Supp. Video 1). Afterwards, a custom-made algorithm (Fassina et al., 2017) implemented with Matlab Programming Language (The MathWorks, Inc., Natick, MA, USA) analyzes these coordinates (Fig. 1C), draws the trajectories (Fig. 1D) and returns the following kinematic parameters (Fassina et al., 2017): i) Contractility, expressed in [mm/s], as the average of the maximum module of epicardial velocity for each systolic phase; ii) Force, expressed as [mm/s²], as the average of cardiac force expended over the entire cardiac cycle during the acquisition period; iii) Energy, expressed as [mm/s]², as the average of the cardiac kinetic energy expended over the entire cardiac cycle

during the acquisition period. Here we included the novel parameter of trajectory (perimeter, corrected for the number of beats) that measures the marker path length during cardiac cycles. We took advantage of a MathWorks tool named Particle Image Velocimetry (PIV; <https://it.mathworks.com/matlabcentral/fileexchange/27659-pivlab-particle-image-velocimetry-piv-tool>) as previously used from us (Fassina et al., 2017) and others (Goliash et al., 2013) for the evaluation of the epicardial torsion. Kinematic data are expressed in the standard SI unit following a conversion: we reconstruct a transformation pixel-to-mm curve by placing the camera at different heights above a graph paper (data not shown).

2.4. Systolic and diastolic area and time

We have extracted from the last complete cardiac cycle of the recorded video the maximal relaxation area (during the diastole) and the minimal contraction area (during systole) for each BCL. Areas were evaluated using a dedicate plug-in from Fiji (ImageJ 9.0, National Institutes of Health, USA) by selecting the frames displaying the maximum relaxation and maximum contraction. Moreover, the systolic and diastolic times were evaluated from the videos as the time interval between the maximum relaxation and maximum contraction and *vice-versa*, respectively.

2.5. Statistical analysis

All data are presented as mean \pm standard error of the mean (S.E.M.). The normality of the data was assessed with the Kolmogorov-Smirnov test. Kruskal Wallis test and 2-way ANOVA were performed. A value of $p < 0.05$ was considered significant. The program GraphPad v.6.0 (GraphPad Software, Inc., La Jolla, CA, USA) was used for the statistical analysis and results display.

3. Results

3.1. Frequency-dependent effects on rats epicardial kinematic parameters

We evaluate *via* Vi.Ki.E. technology the global epicardial kinematics at different BCL ranging from 390 ms to 160 ms. We observed that male hearts tend to maintain the same contractility, force and energy (Fig. 2A), while female rat hearts tend to increase the same parameters at the rising stimulation frequency (Fig. 2B). In detail female epicardial force and energy displayed a significant increasing trend ($p = 0.0019$ and $p = 0.017$ respectively). During our experimental protocol, we noticed that, from BCL = 230 ms onward, an increase of the kinematics parameters occurred in all animals. After this time-point we noticed different trends between male and female. Therefore, we studied in deep the gender-related mechanical behaviour in the following timepoints (BCL: 230 ms, 210 ms, 190 ms, 170 ms) that resemble the range of rat physiological HR. We highlighted this difference in Fig. 3 with representative experiments that display trajectories and coordinates for both male (black) and female (red). As it can be noticed male trajectories (Fig. 3 A-A3 top panels) varied at each BCL indicating different patterns of contraction. On the contrary, female trajectories (Fig. 3 B-B3 top panels) are preserved at each BCL for every cycle. The bottom panels in Fig. 3 A-B display the keeping of 1:1 capture for each cardiac cycle at increasing HR.

3.2. Frequency of epicardial torsion obtained via Particle Image Velocimetry

In order to provide a global information of epicardial torsion

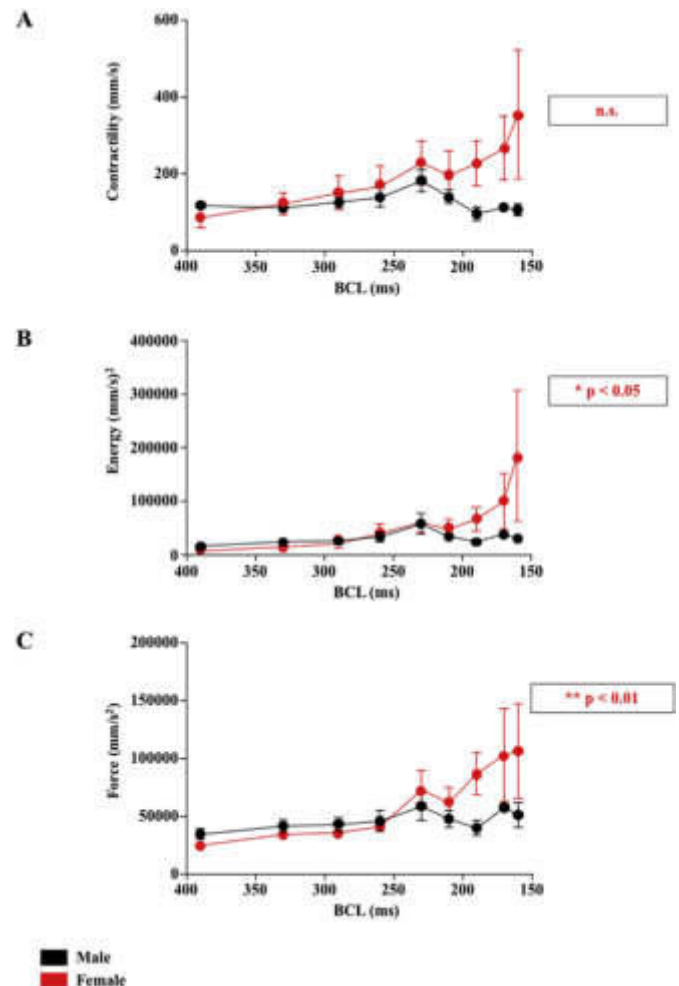


Fig. 2. Effect of the rising frequency of stimulation on epicardial kinematic parameters. Graphs displaying relationship between epicardial kinematic parameters and basic cycle length (BCL) for male (black) and female (red). Trend comparison between male and female for: Contractility (A), Energy (B) and Force (C). Data are shown as Mean \pm S.E.M. * $p < 0.05$, ** $p < 0.01$.

following the gender-related pattern of contraction observed in Fig. 3, we sought to evaluate, for each BCL, the cardiac vorticity by analyzing the videos with PIV (Fig. 4A). Fig. 4B shows that cardiac vorticity parameters display an increasing trend statistically significant for both gender during the stimulation protocol ($p = 0.0006$). Moreover, the male trend was statistically significant compared to female trend ($p < 0.0001$).

3.3. Geometrical spatiotemporal variation at different BCL

The dissimilarity of contraction patterns in male rats at rising frequency suggested that the frequency-dependent epicardial deformation can be related to gender. We sought to investigate the mechanical behaviour at different BCL for both trajectory's perimeter and the maximal contraction (systolic) and maximal relaxation (diastolic) areas. As expected, the data displayed a not-preserved perimeters (Fig. 5A) (ranging from 5.890 ± 0.5597 mm to 3.747 ± 0.3422 mm) over different BCL in male rat hearts (black) compared to female (red) (ranging from 4.220 ± 0.1566 mm to 4.566 ± 0.8934 mm). The male epicardial areas (Fig. 5B) during maximal systolic and diastolic phases were higher compared to

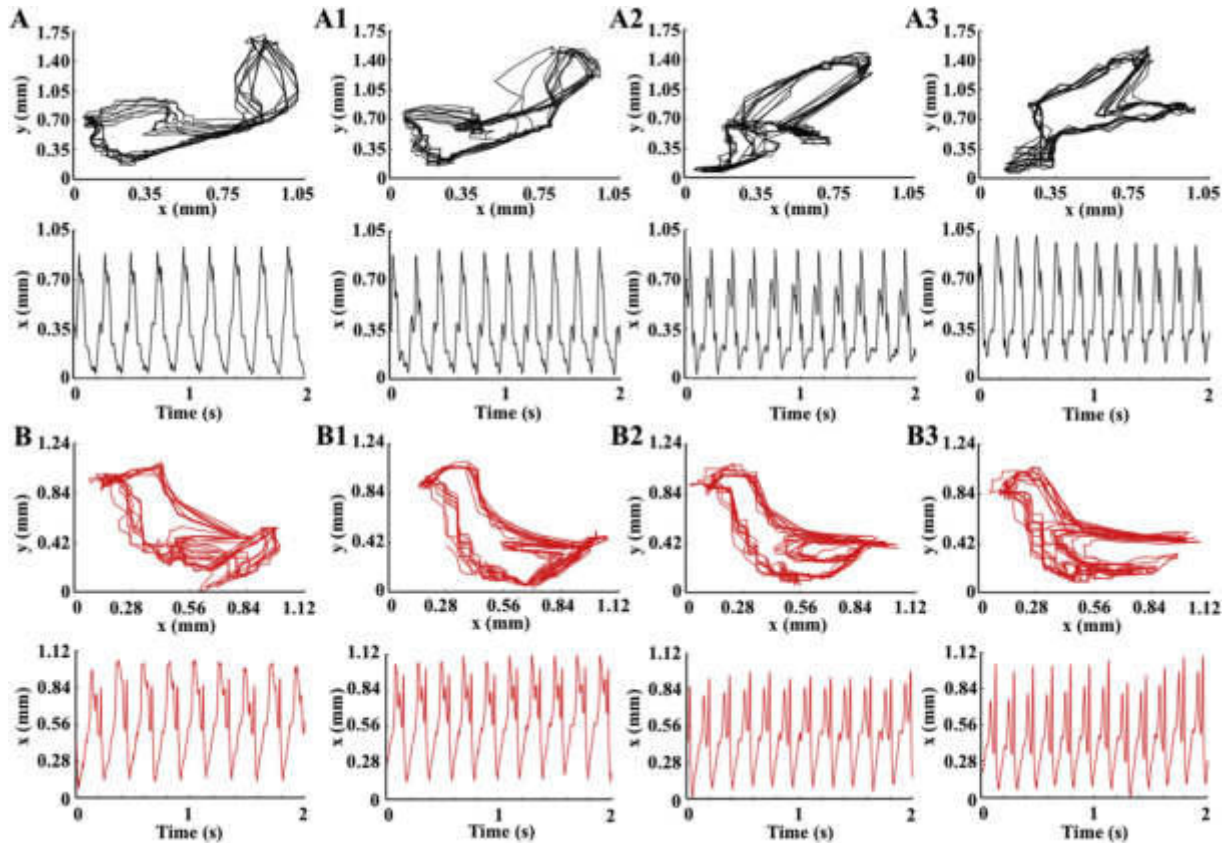


Fig. 3. Contraction patterns at different stimulation frequencies. Examples of male rat heart (black) and female rat heart (red) trajectories and coordinates at four different basic cycle length (BCL). **A, A1, A2, A3:** male trajectories (top panels) and respective coordinates vs. time (bottom panels) at 230 ms, 210 ms, 190 ms and 170 ms respectively. **B, B1, B2, B3:** same as A, but for female rat heart.

female rat hearts (by ca. 11%); however male areas were more statistically spread at higher frequency in contrast to female, suggesting once more a preservation of the mechanical phenotype of cardiac beating over different BCL in female rats.

3.4. Rising stimulation frequency unmasks gender difference at the single cardiac cycle

We thus recognized that sex differences can be also investigated during the single cardiac cycle extracted from different BCL. Therefore, we plotted the S/D time for both male and female rats beating hearts at rising frequencies of stimulation (Fig. 6). We demonstrated that while S/D area was preserved for both male and female hearts (average male 0.737 ± 0.026 , average female 0.753 ± 0.029), paradoxically the S/D time differed (Fig. 6). In the male rats we observed a significant increasing trend (from 0.359 ± 0.029 at 390 ms to 0.913 ± 0.049 at 160 ms, $p < 0.0001$). A significant increasing trend has also been observed for the female rat S/D time (from 0.357 ± 0.031 at 390 ms to 0.815 ± 0.067 at 160 ms, $p < 0.0003$). The S/D time data suggest a different gender-related mechanical restitution at high pacing rates.

4. Discussion

In this study, we applied our high spatial and temporal resolution video kinematic technology to understand the gender-related response of epicardial mechanics during atrial pacing. An additional goal was to examine whether female propensity to cardiac protection against CVDs can be unraveled thanks to our optical-

based experimental protocol. From a physiological standpoint it is well known that female has low BMI, low LVED pressure (Wingate, 1997) but higher velocity of contraction suggesting that women are in constant hyperdynamic state (Buonanno et al., 1982). In clinical research, sex difference in cardiac performance is unmasked during physiological exercise (Bombardini et al., 2008) and with RA pacing during cardiac catheterization (Wainstein et al., 2012). At the pathological level, gender has an influence on the manifestation of myocardial infarction (Mehta et al., 2016), with the incidence of ischemic heart disease being much lower in premenopausal women than age-matched men (Mehta et al., 2015). However, the incidence of CVDs after menopause exceed that of men (Blenck et al., 2016). Only recently, sex differences have been considered in clinical and preclinical studies for CVDs (Consideration of Sex as a Biological Variable in NIH-funded Research, 2015). It is also known that sex differences in ventricular mechanics occur during acute physiological challenges, exacerbated by adrenergic stimulation (Williams et al., 2017). In this work, we showed that *in-situ* female beating hearts tended to show a “kinetic reservoir” due to a possible female hyperdynamic state (Buonanno et al., 1982) in terms of contractility, energy and force that can be expended at lower BCL in accordance with the positive role exerted by estrogens on the excitation-contraction machinery (Ravens, 2018). However, we cannot exclude the gender-related difference in the excitation-contraction (EC) coupling machinery including the SERCa activity (Bupha-Intr et al., 2009; Farrell et al., 2010). In agreement to Williams et al. we would expect, for female hearts, an acute ventricular mechanical adaptation to the rising pacing rate. We also notice that female rats data dispersion occurred at high frequency of

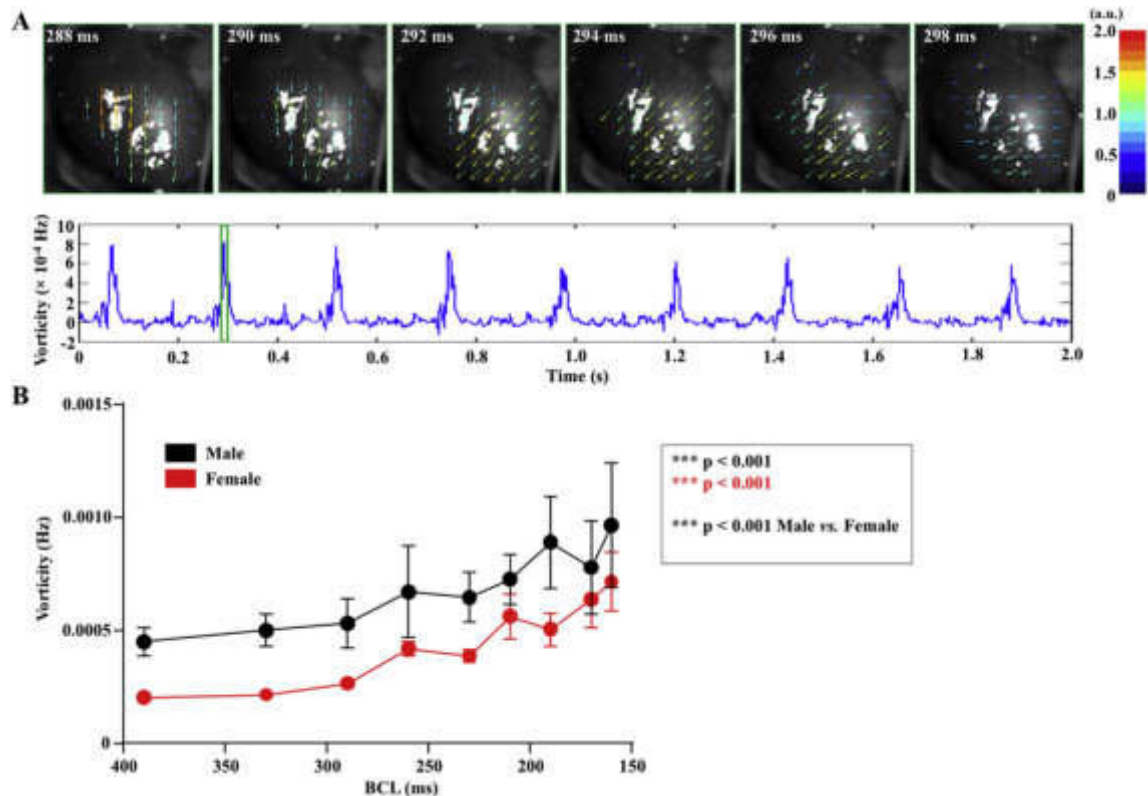


Fig. 4. Epicardial torsion observed by Particle Image Velocimetry. **A:** Upper panel. Six consecutive frames (step: 2 ms) of Particle Image Velocimetry (PIV) evaluation. The colored arrows represent the velocity vectors; the vector module and colors represent the different epicardial velocities. Bottom panel. Epicardial vorticity parameter (Hz) in 2 s recording. The green rectangle highlights the six frames displayed in top panel. **B:** Relationship between the mean Vorticity parameters and basic cycle length (BCL) in male (black) and female (red) rat hearts. Data are shown as Mean \pm S.E.M. *** $p < 0.001$.

stimulation according to what has been measured in human females during exercise by Bombardini et al. Moreover, our video kinematic technology captured a change in the mechanical pattern of epicardial mechanics (trajectories) for male hearts starting from BCL = 230 ms, whereas female hearts trajectories seem to be unaltered at rising frequency of stimulation. This is further confirmed by PIV and trajectory perimeter analysis where the epicardial vorticity and perimeter variation were higher in male compared to female. Because our technique can be applied during open chest surgery (Fassina et al., 2017) we investigated whether such changes may impact on the area of contraction of maximal ejection (systolic phase) and on the area of relaxation of maximal ventricular filling (diastolic phase). Epicardial area changes during heart stimulation and it is an index of ventricular ejection and filling (McCulloch et al., 1989), reflecting the Frank-Starling mechanism which leads to inotropic effect. Accordingly, the systolic and diastolic areas (bigger for male in respect to female, as expected) tended to decrease in male at increasing frequency of stimulation, whereas they seem to be preserved in female. This would suggest that the acute cardiac mechanical adaptation observed in male is necessary to compensate the nonappearance of the “kinetic reservoir” hypothesized in female rat hearts.

One of the echocardiographic index used in clinics is the ratio between systolic and diastolic time intervals (Sarnari et al., 2009). This parameter, together with the rising frequency of stimulation, can provide the mechanical restitution of the heart (Franz et al., 1983). Vi.Ki.E. can be adopted to measure S/D time at high temporal resolution extracted from our coordinates in x and in y. We observed a rising S/D time ratio in both male and female hearts displaying the difference in mechanical restitution. Moreover, the

tendency to reach important *quasi*-pathological values for S/D time ratio, i.e. > 1.0 has been observed only in male rats, which is in accordance to the major masculine CVDs-susceptibility observed in humans.

5. Conclusions and limitations

Our video technology unmasked gender-related kinematic cardiac differences *in-situ*, displaying two different mechanisms of adaptation for male and female heart at increasing frequency. Male hearts tended to change their intrinsic spatiotemporal pattern of contraction/relaxation at the rising frequency of stimulation and to preserve their kinematics for all BCL. Female hearts denoted an opposite trend tending to preserve the spatiotemporal pattern and modify their kinematic response at different BCL. Our results are limited by the absence of the z-dimension and we recapitulate a 3D phenomenon in a 2D analysis. However, this precise and repeatable approach is useful to simplify the analysis without losing the main goal of the study and allow us to make comparison between several experimental sets. Future technological implementation will aim to introduce a second high-speed camera together with a PV-loop, a pressure catheter for peripheral resistance measurement and echocardiographic investigation for simultaneous acquisition of 3D epicardial kinematics and cardiac function.

Source of funding

FFABR_MIUR_2017 to M.M.
PRIN_2015_INSIDE_20152T74ZL_005 to M.M.

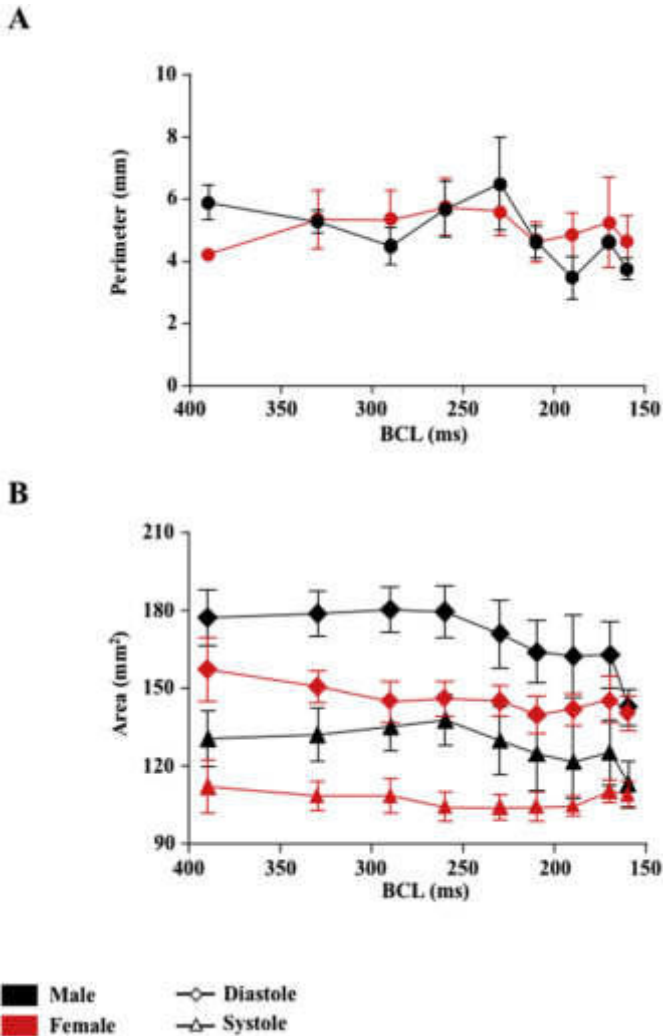


Fig. 5. Relationship between perimeter and area vs basic cycle length. **A:** Male (black) and female (red) perimeter corrected for the number of acquired cardiac cycles for each basic cycle length (BCL). **B:** Average systolic and diastolic area for each BCL in both male (black) and female (red). Diamond: diastole; Triangle: systole. Data are shown as Mean \pm S.E.M.

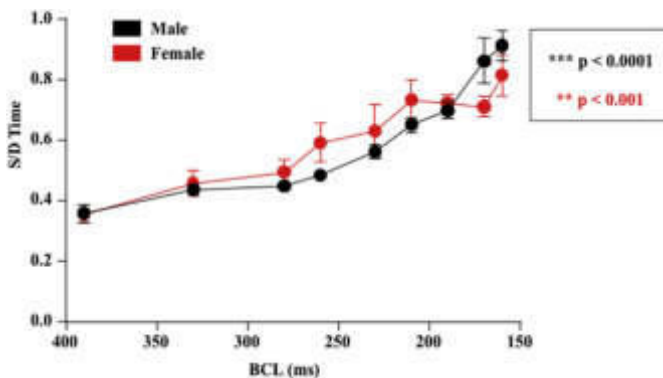


Fig. 6. Mechanical restitution of systolic/diastolic time. Simultaneous plot of systolic/diastolic time (S/D time) in both male (black) and female (red) rat hearts. Data are shown as Mean \pm S.E.M. ** $p < 0.001$, *** $p < 0.0001$.

Acknowledgements

We thank Dr. Cristina Caffarra Malvezzi for the help in the discussion of the manuscript.

Appendix A. Supplementary data

Supplementary data to this article can be found online at <https://doi.org/10.1016/j.pbiomolbio.2019.05.003>.

References

- Ayaz, O., Banga, S.E., Heinze-Milne, S., Rose, R.A., Pyle, W.G., Howlett, S.E., 2019. Long term testosterone deficiency modifies myofilament and calcium handling proteins and promotes diastolic dysfunction in the aging mouse heart. *Am. J. Physiol. Heart Circ. Physiol.* 316 (4), H768–H780.
- Blenck, C.L., Harvey, P.A., Reckelhoff, J.F., Leinwand, L.A., 2016. The importance of biological sex and estrogen in rodent models of cardiovascular health and disease. *Circ. Res.* 118, 1294–1312.
- Bombardini, T., Gemignani, V., Bianchini, E., Venneri, L., Petersen, C., Pisanisi, E., Pratali, L., Alonso-Rodriguez, D., Pianelli, M., Fatta, F., Giannoni, M., Arpesella, G., Picano, E., 2008. Diastolic time - frequency relation in the stress echo lab: filling timing and flow at different heart rates. *Cardiovasc. Ultrasound* 6, 15.
- Buonanno, C., Arbustini, E., Rossi, L., Dander, B., Vassanelli, C., Paris, B., Poppi, A., 1982. Left ventricular function in men and women. Another difference between sexes. *Eur. Heart J.* 3, 525–528.
- Bupha-Intr, T., Laosiripisan, J., Wattanapermpool, J., 2009. Moderate intensity of regular exercise improves cardiac SR Ca²⁺ uptake activity in ovariectomized rats. *J. Appl. Physiol.* 107, 1105–1112.
- Cong, B., Zhu, X., Cao, B., Xiao, J., Wang, Z., Ni, X., 2013. Estrogens protect myocardium against ischemia/reperfusion insult by up-regulation of CRH receptor type 2 in female rats. *Int. J. Cardiol.* 168, 4755–4760.
- Curl, C.L., Wendt, I.R., Canny, B.J., Kotsanas, G., 2003. Effects of ovariectomy and 17 beta-oestradiol replacement on [Ca²⁺]_i in female rat cardiac myocytes. *Clin. Exp. Pharmacol. Physiol.* 30, 489–494.
- Dworatzek, E., Mahmoodzadeh, S., Schriever, C., Kusumoto, K., Kramer, L., Santos, G., Fliegner, D., Leung, Y.K., Ho, S.M., Zimmermann, W.H., Lutz, S., Regitz-Zagrosek, V., 2019. Sex-specific regulation of collagen I and III expression by 17beta-Estradiol in cardiac fibroblasts: role of estrogen receptors. *Cardiovasc. Res.* 115, 315–327.
- Er, F., Michels, G., Brandt, M.C., Khan, I., Haase, H., Eicks, M., Lindner, M., Hoppe, U.C., 2007. Impact of testosterone on cardiac L-type calcium channels and Ca²⁺ sparks: acute actions antagonize chronic effects. *Cell Calcium* 41, 467–477.
- Farrell, S.R., Ross, J.L., Howlett, S.E., 2010. Sex differences in mechanisms of cardiac excitation-contraction coupling in rat ventricular myocytes. *Am. J. Physiol. Heart Circ. Physiol.* 299, H36–H45.
- Fassina, L., Di Grazia, A., Naro, F., Monaco, L., De Angelis, M.G., Magenes, G., 2011. Video evaluation of the kinematics and dynamics of the beating cardiac synchytium: an alternative to the Langendorff method. *Int. J. Artif. Organs* 34, 546–558.
- Fassina, L., Rozzi, G., Rossi, S., Scacchi, S., Galetti, M., Lo Muzio, F.P., Del Bianco, F., Colli Franzone, P., Petrilli, G., Faggian, G., Miragoli, M., 2017. Cardiac kinematic parameters computed from video of in situ beating heart. *Sci. Rep.* 7, 46143.
- Franz, M.R., Schaefer, J., Schottler, M., Seed, W.A., Noble, M.I., 1983. Electrical and mechanical restitution of the human heart at different rates of stimulation. *Circ. Res.* 53, 815–822.
- Goliasch, G., Goscinska-Bis, K., Caracciolo, G., Nakabo, A., Smolka, G., Pedrizzetti, G., Narula, J., Sengupta, P.P., 2013. CRT improves LV filling dynamics: insights from echocardiographic particle imaging velocimetry. *JACC Cardiovasc. Imaging* 6, 704–713.
- Gori, M., Lam, C.S., Gupta, D.K., Santos, A.B., Cheng, S., Shah, A.M., Claggett, B., Zile, M.R., Kraigher-Krainer, E., Pieske, B., Voors, A.A., Packer, M., Bransford, T., Lefkowitz, M., McMurray, J.J., Solomon, S.D., Investigators, P., 2014. Sex-specific cardiovascular structure and function in heart failure with preserved ejection fraction. *Eur. J. Heart Fail.* 16, 535–542.
- Grandy, S.A., Howlett, S.E., 2006. Cardiac excitation-contraction coupling is altered in myocytes from aged male mice but not in cells from aged female mice. *Am. J. Physiol. Heart Circ. Physiol.* 291, H2362–H2370.
- Kerr, K.F., Avery, C.L., Lin, H.J., Raffield, L.M., Zhang, Q.S., Browning, B.L., Browning, S.R., Conomos, M.P., Gogarten, S.M., Laurie, C.C., Sofer, T., Thornton, T.A., Hohensee, C., Jackson, R.D., Kooperberg, C., Li, Y., Mendez-Giraldez, R., Perez, M.V., Peters, U., Reiner, A.P., Zhang, Z.M., Yao, J., Sotoodehnia, N., Taylor, K.D., Guo, X., Lange, L.A., Soliman, E.Z., Wilson, J.G., Rotter, J.I., Heckbert, S.R., Jain, D., Whitset, E.A., 2017. Genome-wide association study of heart rate and its variability in Hispanic/Latino cohorts. *Heart Rhythm* 14, 1675–1684.
- Makkar, R.R., Fromm, B.S., Steinman, R.T., Meissner, M.D., Lehmann, M.H., 1993. Female gender as a risk factor for torsades de pointes associated with cardiovascular drugs. *J. Am. Med. Assoc.* 270, 2590–2597.
- McCulloch, A.D., Smail, B.H., Hunter, P.J., 1989. Regional left ventricular epicardial deformation in the passive dog heart. *Circ. Res.* 64, 721–733.

- Mehta, L.S., Beckie, T.M., DeVon, H.A., Grines, C.L., Krumholz, H.M., Johnson, M.N., Lindley, K.J., Vaccarino, V., Wang, T.Y., Watson, K.E., Wenger, N.K., American Heart Association Cardiovascular Disease in, W, Special Populations Committee of the Council on Clinical Cardiology, C.o.E, Prevention, C.o.C, Stroke, N, Council on Quality of, C. and Outcomes, R., 2016. Acute myocardial infarction in women: a scientific statement from the American heart association. *Circulation* 133, 916–947.
- Mehta, P.K., Wei, J., Wenger, N.K., 2015. Ischemic heart disease in women: a focus on risk factors. *Trends Cardiovasc. Med.* 25, 140–151.
- Meraviglia, V., Wen, J., Piacentini, L., Campostrini, G., Wang, C., Florio, M.C., Azzimato, V., Fassina, L., Langes, M., Wong, J., Miragoli, M., Gaetano, C., Pompilio, G., Barbuti, A., DiFrancesco, D., Mascalonzi, D., Pramstaller, P.P., Colombo, G.I., Chen, H.S., Rossini, A., 2016. Higher cardiogenic potential of iPSCs derived from cardiac versus skin stromal cells. *Front. Biosci. (Landmark Ed)* 21, 719–743.
- Milerova, M., Drahota, Z., Chytilova, A., Tauchmannova, K., Houstek, J., Ostadal, B., 2016. Sex difference in the sensitivity of cardiac mitochondrial permeability transition pore to calcium load. *Mol. Cell. Biochem.* 412, 147–154.
- Parks, R.J., Howlett, S.E., 2013. Sex differences in mechanisms of cardiac excitation-contraction coupling. *Pflügers Archiv* 465, 747–763.
- Petre, R.E., Quaile, M.P., Rossman, E.I., Ratcliffe, S.J., Bailey, B.A., Houser, S.R., Margulies, K.B., 2007. Sex-based differences in myocardial contractile reserve. *Am. J. Physiol. Regul. Integr. Comp. Physiol.* 292, R810–R818.
- Raddino, R., Poli, E., Pela, G., Manca, C., 1989. Action of steroid sex hormones on the isolated rabbit heart. *Pharmacology* 38, 185–190.
- Ravens, U., 2018. Sex differences in cardiac electrophysiology. *Can. J. Physiol. Pharmacol.* 96, 985–990.
- Ren, J., Hintz, K.K., Roughead, Z.K., Duan, J., Colligan, P.B., Ren, B.H., Lee, K.J., Zeng, H., 2003. Impact of estrogen replacement on ventricular myocyte contractile function and protein kinase B/Akt activation. *Am. J. Physiol. Heart Circ. Physiol.* 284, H1800–H1807.
- Rosenkranz-Weiss, P., Tomek, R.J., Mathew, J., Eghbali, M., 1994. Gender-specific differences in expression of mRNAs for functional and structural proteins in rat ventricular myocardium. *J. Mol. Cell. Cardiol.* 26, 261–270.
- Sarnari, R., Kamal, R.Y., Friedberg, M.K., Silverman, N.H., 2009. Doppler assessment of the ratio of the systolic to diastolic duration in normal children: relation to heart rate, age and body surface area. *J. Am. Soc. Echocardiogr.* 22, 928–932.
- Schwartz, D.W., Beck, J.M., Kowalski, J.M., Ross, J.D., 2004. Sex differences in the response of rat heart ventricle to calcium. *Biol. Res. Nurs.* 5, 286–298.
- Shaw, L.J., 2016. Sex differences in cardiovascular imaging. *JACC Cardiovasc. Imaging* 9, 494–497.
- Tadros, R., Ton, A.T., Fiset, C., Nattel, S., 2014. Sex differences in cardiac electrophysiology and clinical arrhythmias: epidemiology, therapeutics, and mechanisms. *Can. J. Cardiol.* 30, 783–792.
- Tan, T.P., Gao, X.M., Krawczynsyn, M., Feng, X., Kiriazis, H., Dart, A.M., Du, X.J., 2003. Assessment of cardiac function by echocardiography in conscious and anesthetized mice: importance of the autonomic nervous system and disease state. *J. Cardiovasc. Pharmacol.* 42, 182–190.
- Wainstein, R.V., Sasson, Z., Mak, S., 2012. Frequency-dependent left ventricular performance in women and men. *Am. J. Physiol. Heart Circ. Physiol.* 302, H2363–H2371.
- Weerateerangkul, P., Shinlapawittayatorn, K., Palee, S., Apajjai, N., Chattipakorn, S.C., Chattipakorn, N., 2017. Early testosterone replacement attenuates intracellular calcium dyshomeostasis in the heart of testosterone-deprived male rats. *Cell Calcium* 67, 22–30.
- Williams, A.M., Shave, R.E., Cheyne, W.S., Eves, N.D., 2017. The influence of adrenergic stimulation on sex differences in left ventricular twist mechanics. *J. Physiol.* 595, 3973–3985.
- Wingate, S., 1997. Cardiovascular anatomy and physiology in the female. *Crit. Care Nurs. Clin.* 9, 447–452.

Cite this article as: Rozzi G, Lo Muzio FP, Sandrini C, Rossi S, Fassina L, Faggian G *et al.* Real-time video kinematic evaluation of the *in situ* beating right ventricle after pulmonary valve replacement in patients with tetralogy of Fallot: a pilot study. *Interact CardioVasc Thorac Surg* 2019;29:625–31.

Real-time video kinematic evaluation of the *in situ* beating right ventricle after pulmonary valve replacement in patients with tetralogy of Fallot: a pilot study

Giacomo Rozzi^{a,b,†}, Francesco P. Lo Muzio ^{a,b,†}, Camilla Sandrini ^a, Stefano Rossi^b, Lorenzo Fassina^c,
Giuseppe Faggian^a, Michele Miragoli^{b,d,‡} and Giovanni Battista Luciani^{a,*,‡}

^a Department of Surgery, Dentistry, Pediatrics and Gynaecology, University of Verona, Verona, Italy

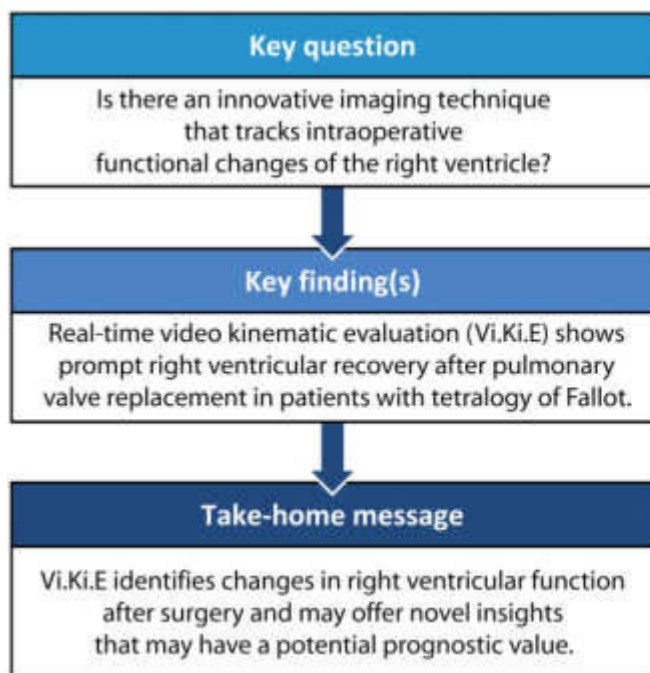
^b Department of Medicine and Surgery, University of Parma, Parma, Italy

^c Department of Electrical, Computer and Biomedical Engineering, University of Pavia, Pavia, Italy

^d Humanitas Clinical and Research Center, Rozzano, Italy

* Corresponding author. Section of Cardiac Surgery, Department of Surgery, Dentistry, Pediatrics and Gynaecology, University of Verona, O.C.M. Piazzale Stefani 1, 37126 Verona, Italy. Tel: +39-45-8123303; fax: +39-45-8123308; e-mail: giovanni.luciani@univr.it (G.B. Luciani).

Received 15 October 2018; received in revised form 1 April 2019; accepted 14 April 2019



Abstract

OBJECTIVES: The timing for pulmonary valve replacement (PVR) after tetralogy of Fallot repair is controversial, due to limitations in estimating right ventricular dysfunction and recovery. Intraoperative imaging could add prognostic information, but transoesophageal echocardiography is unsuitable for exploring right heart function. Right ventricular function after PVR was investigated in real time using a novel video-based contactless kinematic evaluation technology (Vi.Ki.E.), which calculates cardiac fatigue and energy consumption.

[†]Both authors contributed equally to this work.

[‡]Both authors jointly supervised this work.

METHODS: Six consecutive patients undergoing PVR at 13.8 ± 2.6 years (range 6.9–19.8) after the repair of tetralogy of Fallot were enrolled. Mean right ventricular end-diastolic and end-systolic volume at magnetic resonance imaging were 115.6 ± 16.2 ml/m² and 61.5 ± 14.6 ml/m², respectively. Vi.Ki.E. uses a fast-resolution camera placed 45 cm above the open chest, recording cardiac kinematics before and after PVR. An algorithm defines cardiac parameters, such as energy, fatigue, maximum contraction velocity and tissue displacement.

RESULTS: There were no perioperative complications, with patients discharged in satisfactory clinical conditions after 7 ± 2 days (range 5–9). Vi.Ki.E. parameters describing right ventricular dysfunction decreased significantly after surgery: energy consumption by 45% [$271\,125 \pm 94\,222$ (mm/s)² vs $149\,202 \pm 11\,980$ (mm/s)², $P=0.0001$], cardiac fatigue by 12% ($292\,671 \pm 29\,369$ mm/s² vs $258\,755 \pm 42\,750$ mm/s², $P=0.01$), contraction velocity by 54% (3412 ± 749 mm/s vs 1579 ± 400 mm/s, $P=0.0007$) and displacement by 23% (27 ± 4 mm vs 21 ± 4 mm, $P=0.01$). Patients undergoing PVR at lower end-diastolic volumes, had greater functional recovery of Vi.Ki.E. parameters.

CONCLUSIONS: Intraoperative Vi.Ki.E shows immediate recovery of right ventricular mechanics after PVR with less cardiac fatigue and energy consumption, providing novel insights that may have a prognostic relevance for functional recovery.

Keywords: Tetralogy of Fallot • Pulmonary valve replacement • Cardiac kinematics • Magnetic resonance imaging

INTRODUCTION

Pulmonary regurgitation (PR) is the most common sequela late after repair of tetralogy of Fallot (ToF) [1]. The resulting chronic right ventricle (RV) volume overload leads to varying degrees of ventricular dilatation and dysfunction, which are associated with arrhythmias, cardiac failure and premature death [1]. While pulmonary valve replacement (PVR) has been shown to be effective in resolving PR [2], late results after surgery have not been uniformly associated with clinical improvement [3]. Although to some clinicians, this observation would suggest that the current indications for PVR may be excessively conservative, leading to intervention when irreversible RV dysfunction has ensued [4], others object that a prognosis without PVR may be better in select patient cohorts, due to the additional morbidity associated with PVR surgery [5]. Therefore, the indication and timing for PVR remain a matter of debate.

The current international guidelines for PVR after ToF repair focus on RV functional deterioration, even in asymptomatic patients [6].

However, there is mounting evidence that load-dependent and load-independent indices of RV function assessed by cardiac magnetic resonance (CMR), may be instrumental in guiding indication and timing for PVR [7]. Accordingly, both RV end-diastolic volume (EDV) and RV end-systolic volume (ESV), including ejection fraction, are currently utilized to assess the correct timing of PVR [8]. However, controversy remains on threshold values due to often unpredictable outcomes after PVR. This has stimulated a quest for alternative clinical and experimental methods to investigate the RV function, in patients with chronic PR after ToF repair [9–11]. Theoretically, a technology able to evaluate RV performance during PVR may track functional changes, and ultimately aid in determining the best timing for PVR, in the future. We recently described an original method to elaborate high temporal and spatial resolution parameters of ventricular function in real time during open-chest surgery, using video kinematic recordings [12]. Briefly, this innovative technique was validated in our previous work [12], in which its algorithm efficiency and quality were evaluated by comparing the data obtained from: the cardiac electro-mechanical coupling model; the pendulum harmonic motion; the spatial and temporal resolution and longitudinal assessment of the kinematic parameters and the contraction force by placing a known mass onto the epicardium of a beating rat heart. This pilot study aims to assess safety and efficacy of

intraoperative kinematic evaluation to describe acute RV functional changes in patients undergoing PVR late after ToF repair.

MATERIALS AND METHODS

The study was approved by the Institutional Review Board (# 847CESC Protocol # 13371), and all patients signed an informed consent. Selection criteria for the study were (i) PR after transannular patch repair of ToF with pulmonary stenosis; (ii) symptomatic patients with severe PR or asymptomatic patients with evidence of progressive severe RV dilatation or dysfunction [6]; (iii) PVR using stented bioprostheses; and (iv) feasibility of PVR normothermic cardiopulmonary bypass on the beating heart. The latter criterion was introduced to eliminate the influence of intraoperative myocardial ischaemia on postoperative cardiac kinematics. Furthermore, this criterion was also adopted to closely replicate potential advantages of transcatheter PVR, when no additional myocardial ischaemia was involved. Between November 2016 and February 2018, 6 consecutive patients were enrolled.

Table 1: Demographic and laboratory variables

	N = 6	Mean	Median	Range
Gender (male/female)	3/3			
BSA (m ²)		1.3 ± 0.2	1.4	0.7–1.7
Age at PVR (years)		13.0 ± 2.3	12.2	6.9–20.1
Age at ToF repair (months)		3.0 ± 0.6	2	1–5
Time to PVR (years)		13.8 ± 2.6	12.5	6.9–19.8
NYHA class II–III	4/6			
SR, complete RBBB (EKG)	4/6			
QRS duration (ms)		156.5 ± 8.7	162	128–174
Severe PR (ECHO)	5/6			
Preoperative CMR				
RVEDVi (ml/m ²)		115.6 ± 16.2	108.5	62.5–183.0
RVESVi (ml/m ²)		61.5 ± 14.6	53.7	12.5–104.0
RVEF (%)		55.1 ± 5.5	53.8	42.0–79.0
PR fraction (%)		49.0 ± 6.9	49.0	22.0–73.0
LVEF (%)		56.0 ± 1.7	54.5	51.0–62.0

BSA: body surface area; CMR: cardiac magnetic resonance; LVEF: left ventricular ejection fraction; NYHA: New York Heart Association; PR: pulmonary regurgitation; PVR: pulmonary valve replacement; RBBB: right bundle branch block; RVEDVi: right ventricular end-diastolic volume index; RVEF: right ventricular ejection fraction; RVESVi: right ventricular end-systolic volume index; SR: sinus rhythm; ToF: tetralogy of Fallot.

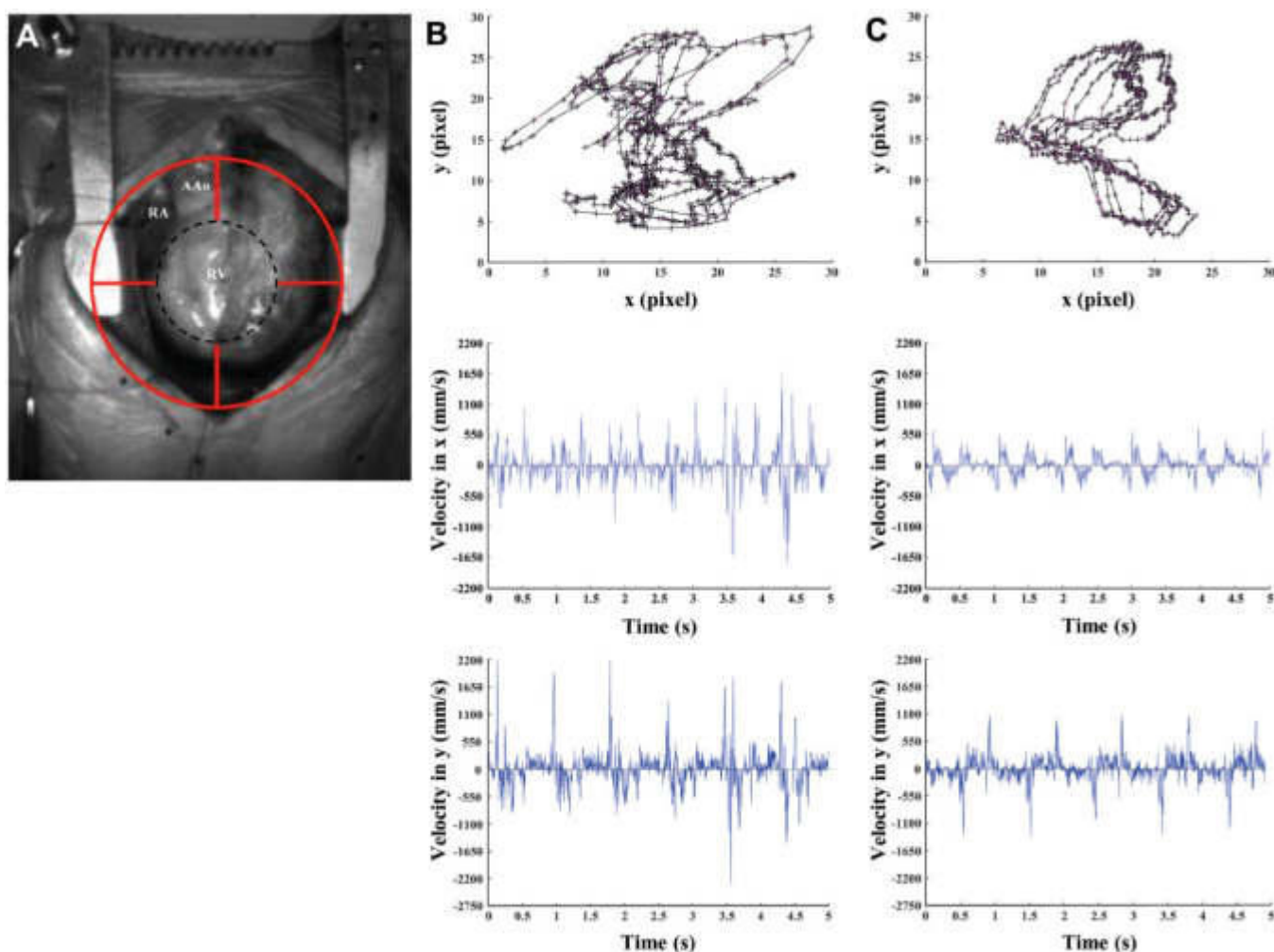


Figure 1: Video kinematic results obtained pre- and post-pulmonary valve replacement (PVR). **(A)** Marker position (red circle) on the patient's heart (RV) during open-chest surgery. **(B)** Upper panel, marker trajectories (black lines with ticks) and acceleration (pink arrows) pre-PVR. Middle panel, video cardiogram in x-axis pre-PVR. Lower panel, video cardiogram in y-axis pre-PVR. **(C)** Same as **(B)** but post-PVR. AAo: ascending aorta; Black dashed circle: effective area of analysis; RA: right atrium; RV: right ventricle.

All patients underwent preoperative CMR and transthoracic echocardiographic evaluation. Demographic and laboratory variables are reported in Table 1.

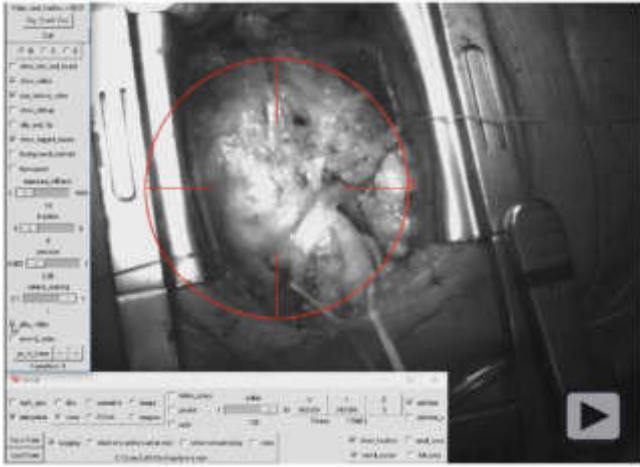
Surgical methods

All PVR procedures were performed by 1 surgeon (G.B.L.). Patients underwent PVR via repeat median sternotomy, using aortic and bicaval cannulation and under normothermic (36°C) cardiopulmonary bypass on the beating heart. Video kinematic recordings were focused on the apical trabecular component of the RV, in line with previous evidence showing this portion as the one bearing most of the chronic volume overload [13] (Fig. 1A). All patients underwent postoperative transthoracic echocardiographic evaluation.

Experimental protocol

For each patient, a high-speed camera (Basler acA1300-200um USB 3.0 with the ON Semiconductor PYTHON 1300 CMOS sensor, Ahrensburg, Germany, equipped with Edmund Optics

6 mm compact fixed focal length lens, Barrington, NJ, USA) was placed approximately 0.4 m above the heart during ToF surgery and 4 videos of 5 s at 200 FPS with a resolution of 1280 × 1024 and a quality of 10p were recorded at 2 time points. Compared to the previous study [12], this camera and the lenses were specifically chosen for human hearts with the intention of increasing the field of view and assessing the RV kinematics globally. The first recording (pre-PVR) was after chest opening, the second one (post-PVR) around 30 min after weaning from cardiopulmonary bypass exit. In the post-PVR recording, great care was taken to reproduce the same haemodynamic conditions observed in the pre-PVR, including central venous pressure, systolic arterial blood pressure, heart rate and identical ventilator settings. No patient required inotropic support and only one required intravenous antiarrhythmic therapy, as specified below (case #3). The videos were acquired on a high-performance PC (Intel core i7-6700HQ 3.5 GHz, 16GB DDR4 2133 MHz SDRAM, 1TB HDD 7200 RPM With 128GB SSD PCIE ×4) by using an USB 3.0 cable through the camera's own software (Pylon 5 Camera Software Suite 5.0.5 for Microsoft Windows, Ahrensburg, Germany).



Video 1: Intraoperative video recording of cardiac kinematics of the right ventricular outflow tract. A virtual target (red) allows to focus the virtual marker. The virtual marker (yellow) on the first frame of the video follows the light spots on the epicardial surface, tracking the spatial-temporal coordinates x , y and t of that marker in each frame.

Video kinematic evaluation of right ventricle function

The videos were evaluated by using the Video Spot Tracker software (VST, CISMM, Computer Integrated Systems for Microscopy and Manipulation, UNC Chapel Hill, NC, USA), allowing a virtual marker to be placed on the first frame of the video, which follows the light spots on the epicardial surface, tracking the spatial-temporal coordinates x , y and t of that marker in each frame (Fig. 1A and Video 1). Afterwards, a custom-made algorithm [14] implemented with MATLAB Programming Language (The MathWorks, Inc., Natick, MA, USA) analyses these coordinates, evaluates video cardiograms (ViCGs) and presents the following physical quantities:

- Displacement: estimates instantaneous movement of the cardiac tissue;
- Contraction velocity: estimates instantaneous velocity of the cardiac tissue;
- Force: estimates cardiac fatigue (instantaneous acceleration);
- Energy: estimates the kinetic energy during cardiac cycle (it follows the classical and Hamiltonian mechanics for kinetic energy $\frac{1}{2} mv^2$) [12].

The algorithm presents the raw data in pixels and we reported these in SI-accepted unit (m) to provide useful information to surgeons. In the laboratory, we reconstructed a transformation pixel-to-mm curve ($r^2 = 0.9977$) by placing the camera at different heights, from 0.05 to 0.6 m with 0.05 m step, above a millimetre paper (Supplementary Material, Table).

Of note, all scientists involved with experimental data acquisition and interpretation were blinded to preoperative and postoperative clinical and laboratory data.

Statistical analysis

Data are presented as mean \pm SEM. The normality of the data was assessed with the Kolmogorov–Smirnov test. The Student's t -test with Welch's correction and cumulative distribution with the

Kolmogorov–Smirnov test were performed. A value of $P < 0.05$ was considered significant. The programme GraphPad v.6 (GraphPad Software, Inc., La Jolla, CA, USA) was used for analysis and results.

RESULTS

Clinical outcome

All patients underwent surgical PVR on the beating heart: 4 patients received a 23-mm, 1 patient a 21-mm and 1 patient a 25-mm stented bioprosthesis. There were no perioperative complications, except for 1 patient experiencing reversible subclinical hepatic dysfunction. Patients were discharged after a mean of 7.0 ± 2.0 days (5–9 days) of hospitalization. Transthoracic echocardiogram prior to discharge documented the recovery of normal RV dimensions in 5 out of 6 patients (83%), preserved ($>50\%$) right ventricular ejection fraction (RVEF) in 3 out of 6 patients and mildly reduced ($>40\%$) RVEF in 3 out of 6 patients. On Doppler examination there was absence of PR in all patients and a mean peak trans-prosthetic pulmonary valve gradient of 16.5 ± 7.1 mmHg. During a mean follow-up of 8.5 ± 4.5 months (2–15 months), all patients were in New York Heart Association (NYHA) I, except 1 patient in NYHA II. No patient experienced adverse cardiovascular events and all were in regular sinus rhythm, free from oral anticoagulation. The follow-up echocardiogram was similar to that taken before discharge, with a mean peak trans-prosthetic pulmonary valve gradient of 14.5 ± 7.9 mmHg and preserved RVEF in 5 out of 6 patients.

Intraoperative video kinematic evaluation of right ventricle function in patients with tetralogy of Fallot

The qualitative and quantitative results of the 6 patients were extremely homogeneous, except for 1 patient (#3), who exhibited counterintuitive experimental outcomes. Intraoperatively, this patient showed atrial ectopic tachycardia after PVR, which was initially refractory to antiarrhythmic therapy and eventually subsided 6 h after surgery.

From a qualitative point of view, trajectories and ViCGs differed between pre- and post-PVR condition in all patients (Fig. 1). In detail, all trajectories showed irregular and chaotic patterns (Fig. 1B, upper panel) prior to PVR. The same occurred for ViCGs, where systolic and diastolic phases were difficult to differentiate because of background noise in both x and y axes (Fig. 1B, middle and lower panels). On the contrary, trajectories showed regular, overlapped and well-preserved patterns after PVR (Fig. 1C, upper panel). The ViCGs displayed both systolic and diastolic phases and we identified less noise in both x and y axes (Fig. 1C, middle and lower panels). Moreover, marker displacement in trajectories and ViCGs amplitude decreased after PVR when compared to before PVR.

From a quantitative point of view, all kinematic parameters significantly decreased (Fig. 2A) after PVR when compared to before PVR. On an average, displacement decreased by 23%, maximum contraction velocity by 54%, force by 12% and energy by 45% (Fig. 2A). Regarding the mechanical performances of individual patients, we noted (Fig. 2B) that all patients showed a decreasing trend for all parameters, except for patient #3 who

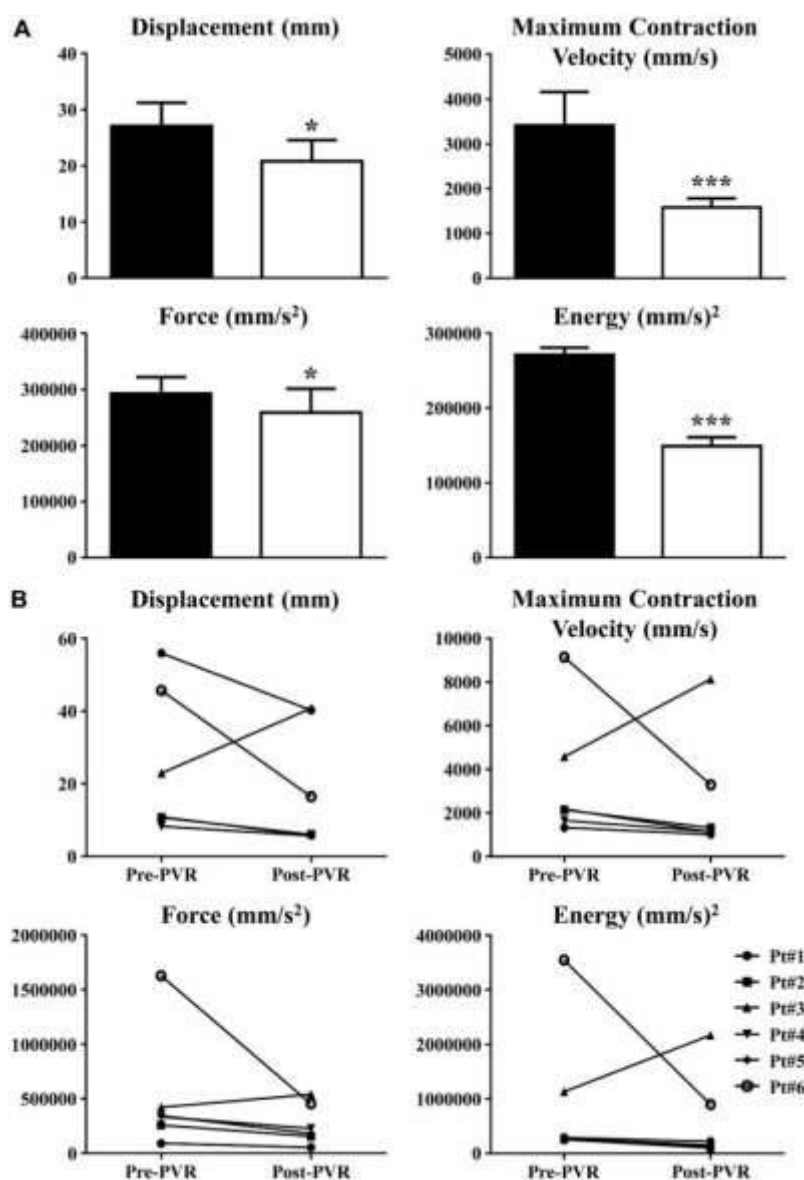


Figure 2: Kinematic parameters in tetralogy of Fallot patients. (A) Pre-PVR (black columns) was recorded at the chest opening before aortic cannulation. Post-PVR (white columns) was recorded after the surgery and protamine sulphate infusion. Data are shown as mean \pm SEM. * $P < 0.05$ versus pre-PVR, *** $P < 0.001$ versus pre-PVR. (B) Visual representation of video kinematic evaluation parameters, trends for each patient pre- and post-PVR. PVR: pulmonary valve replacement; SEM: standard error of the mean.

exhibited an increasing trend. Prior to PVR, patient #6 showed the highest values for each parameter and the greatest percentage decrease after PVR. In particular, patient #6 values after PVR were greater than the rest of the study population, and, even though these exhibited the greatest decrease, the final parameter values remained 2-fold higher than pre-PVR values from the rest of the study population.

To suggest possible clinical correlations, the acquired RV kinematics parameters were compared with CMR, the gold standard RV imaging technique. Thus, we plotted RVEDV index (RVEDVi) versus energy (Fig. 3, upper panel) and force, a surrogate for cardiac fatigue (Fig. 3, lower panel), because these kinematic parameters exhibit the strongest clinical implications. In both graphs, patients undergoing surgery with an RVEDVi below 129 ml/m² showed a consistent decrease in parameter values after PVR, in line with recovery of minimal contraction energy and cardiac fatigue. Patient #6, who underwent PVR with an RVEDVi of

183 ml/m² (a value currently representing standard indication for surgery) also displayed lower values after PVR with the greatest decrease by far. However, after PVR, energy and force (cardiac fatigue) values in this patient remained higher than the corresponding parameters prior to PVR in the remainder of the study population.

DISCUSSION

Although PVR leads to prompt resolution of PR occurring after ToF repair [2], clinical improvement after PVR is not always predictable [3, 5, 7], leading to controversy over indications and timing for surgery.

Therefore, in addition to clinical observations using meta-analyses [2], propensity matched [5] and prospective [4] studies, efforts have been made to devise experimental models [9–11] able to unravel pathophysiology of the RV following PVR.

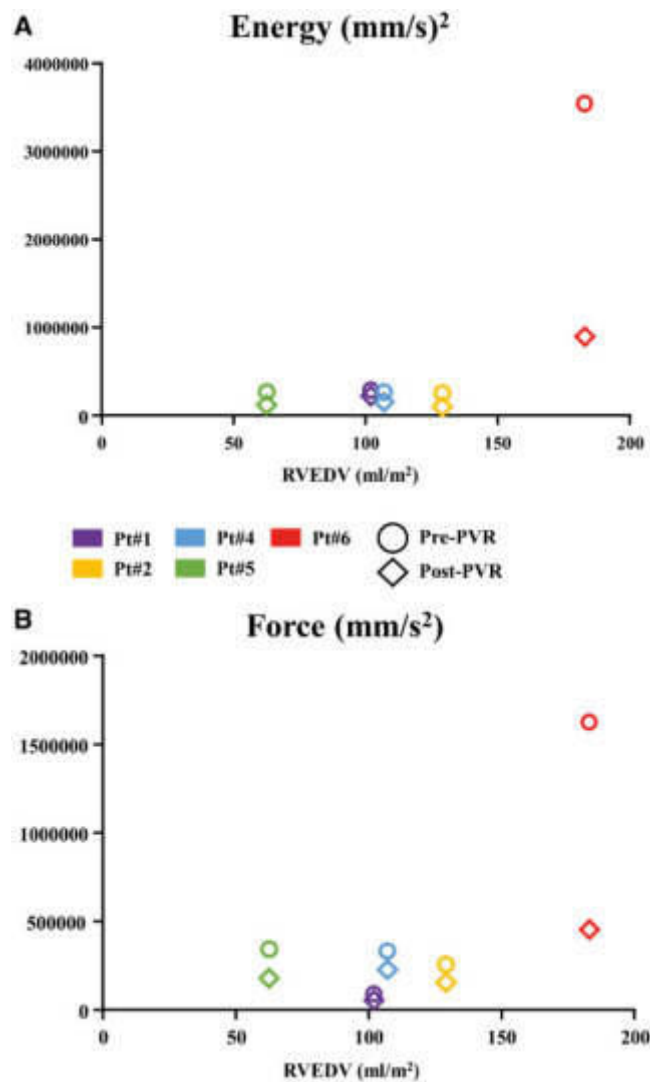


Figure 3: Correlation between cardiac magnetic resonance and right ventricle kinematic parameters. **(A)** Graph displaying the relation between RVEDV and energy. Colours represent different patients (see legend), circle is pre-PVR and diamond is post-PVR. **(B)** Same as **(A)** but for force. PVR: pulmonary valve replacement; RVEDV: right ventricular end-diastolic volume.

In this pilot study, a novel method to describe real time *in vivo* cardiac kinematics was experimentally applied to offer insight into acute changes of RV properties associated with resolution of volume overload by surgical PVR. This technique was previously applied, in patients undergoing surgical myocardial revascularization [12].

The original experimental approach is a video-based and contactless technique, which can describe precise cardiac kinematic information during open-chest procedures. This technology is versatile, as it may be applied for both basic and clinical research, in conjunction with standard monitoring procedures, without interfering with open-chest cardiac surgery. In patients undergoing surgical myocardial revascularization [12], this technique was able to detect fine contraction of the ischaemic/reperfused cardiac tissue areas, which are poorly explored by conventional transoesophageal echocardiography. In this study, we focused our attention on RV pathophysiology.

The results of the current experimental study, demonstrate that in patients with previously operated ToF, RV preload reduction by PVR allows: (i) decrease of contraction force (cardiac

fatigue) by 12%; (ii) decrease of energy by 45%; and (iii) decrease of maximum contraction velocity and displacement (instantaneous velocity and instantaneous movement of the cardiac tissue, respectively), because the reduction of force and energy leads to less RV epicardial movement and velocity. One plausible and expected mechanism that could explain this trend is related to the Frank-Starling law: a decrease in RV preload generates a decrease in myocardium stretch (less tension development) and, consequently, a decrease in actin-myosin crossbridge activity leading to less cardiac force and kinetic energy [15].

The pilot study herein provides, for the first time, evidence that PVR may afford immediate recovery of RV functional properties in children and young adults late after ToF repair. Therefore, this work allows one to take the recent findings by Heng *et al.* [4] on very early (on average 10 days) RV volume recovery at CMR in adults undergoing PVR for chronic PI after ToF on step further. It is noteworthy that when applying standard CMR criteria for PVR, early and late mortality are not negligible and the rate of adverse cardiovascular events (death, VT) does not correlate with either EDV or ESV indices [4, 5]. This suggests that current RV threshold volumes at preoperative CMR will not reliably predict clinical outcome, whereas decline in systolic function (RVEF) may [4, 5, 8]. Surprisingly, the same observations have been made even when using more proactive criteria to refer for PVR [5]. The latter finding may lead one to consider conservative management preferable rather than PVR in patients with PR after repaired ToF. Alternatively, it can be hypothesized that even the use of proactive CMR criteria to refer ToF patients for PVR may be too restrictive to favourably influence late prognosis.

Indeed, evidence by Frigiola *et al.* [16] suggests that PVR, when performed in children and adolescents (younger than 18 years old) and with more aggressive CMR indications (RVEDVi <150 ml/m²), may be associated with negligible early and late mortality. Furthermore, their surgical referral policy may allow normalization of RV volumes, improvement in biventricular function and normalization of V_E/V_{CO_2} , a parameter of exercise capacity, which best reflects everyday requirements [16].

Our patient population differs in many ways from most large clinical series on PVR late after ToF repair [2–5, 7, 8]. First and foremost, the average age at primary ToF repair was in the first 3 months of life, representing current standard timing for infant repair, and the average age at PVR was in the early teenage years. On the other hand, most published series report on patients in the third and fourth decade of life undergoing PVR 20–30 years after originally having had ToF repair at a preschool or school age. Therefore, exposure to the consequences of chronic RV overload had significantly shorter duration in our series. Furthermore, the underlying diagnosis in this study was restricted to ToF with pulmonary stenosis, whereas prior series encompassed a variety of cardiac defects, associated with ToF, including pulmonary atresia. The latter often imply more complex surgery, repair using a period of myocardial ischaemia and the use of extra-cardiac conduits, all factors that may adversely affect RV function. In addition, average RV volumes at preoperative CMR in our series were well below even proactive criteria for PVR in older ToF patients, although closer to the ones reported by Frigiola *et al.* [16] on PVR in adolescent ToF patients. Finally, and most importantly, unlike most other series, we selected only patients who could undergo beating heart PVR on normothermic cardiopulmonary bypass. Therefore, the additional influence of RV dysfunction due to myocardial ischaemia was eliminated in our study. It is noteworthy, that the series with clinical and CMR variables similar to ours also

resorted to routine beating heart PVR [16]. The feasibility of beating heart PVR is important, as prior studies have surmised that failure of PVR to affect mid-term clinical outcome might also be due to the additional surgical trauma incurred during the procedure [2, 3, 5], thus advocating wider use of transcatheter PVR. Based on this hypothesis, we are witnessing a trend towards recommending the lowering of CMR thresholds for PVR when transcatheter intervention is possible [17].

This study suggests a correlation between RV volumes at CMR and contraction force, index of cardiac fatigue, and energy even in patients with preoperative RVEDVi lower than current 'proactive' recommendations for surgery (115 vs 152 ml/m²). This observation is in line with prior experimental findings using cardiac catheterization and CMR, where a rapid decline in RV power and efficiency are seen at critical values of 139 ml/m² RVEDV and 75 ml/m² RVESV index [18].

Limitations

As a pilot study, the current work is limited by the small cohort size. We focused our attention on young patients with ToF undergoing PVR in a single centre. Moreover, our observations were restricted to the intraoperative acute phase of RV changes following PVR. Both circumstances hamper the ability of this study to generate experimental indices, which may reflect its prognostic clinical value. A 6-month postoperative CMR is currently underway to ascertain whether video kinematic parameters may predict late RV remodelling.

A technical limitation of video kinematic evaluation is related to the use of a 2-dimensional camera (for which depth is obviously missing) in acquiring the 3-dimensional cardiac phenomenon. Nevertheless, the algorithm is already implemented for the 3-dimensional motion. Employing a second camera in the operating room will be the next upgrade.

Finally, although video kinematic evaluation may display limited acute prognostic ability in ToF patients undergoing elective PVR, as the perioperative course of these patients is generally uncomplicated, this novel technology is currently being tested in other operative settings, far more commonly exposed to acute perioperative RV failure, such as staged palliation of single RVs (i.e. aortic or mitral atresia) and LVAD implantation in cardiomyopathies.

CONCLUSIONS

Video kinematic analysis is a safe, contactless and valid intraoperative technique, which demonstrates prompt improvement of RV functional properties through the reduction of cardiac fatigue and kinetic energy in select ToF patients after PVR.

SUPPLEMENTARY MATERIAL

Supplementary material is available at *ICVTS* online.

Funding

This study was supported by the Institutional funds of the University of Verona and of the University of Parma [FFBR-MIUR-2017 to M.M.].






Conflict of interest: none declared.

REFERENCES

- [1] Gatzoulis MA, Balaji S, Webber SA, Siu SC, Hokanson JS, Poile C *et al.* Risk factors for arrhythmia and sudden cardiac death late after repair of tetralogy of Fallot: a multicentre study. *Lancet* 2000;356:975–81.
- [2] Ferraz Cavalcanti PE, Sâ MP, Santos CA, Esmeraldo IM, de Escobar RR, de Menezes AM *et al.* Pulmonary valve replacement after operative repair of tetralogy of Fallot: meta-analysis and meta-regression of 3,118 patients from 48 studies. *J Am Coll Cardiol* 2013;62:2227–43.
- [3] Harrild DM, Berul CI, Cecchin F, Geva T, Gauvreau K, Pigula F *et al.* Pulmonary valve replacement in tetralogy of Fallot: impact on survival and ventricular tachycardia. *Circulation* 2009;119:445–51.
- [4] Heng EL, Gatzoulis MA, Uebing A, Sethia B, Uemura H, Smith GC *et al.* Immediate and midterm cardiac remodeling after surgical pulmonary valve replacement in adults with repaired tetralogy of Fallot: a prospective cardiovascular magnetic resonance and clinical study. *Circulation* 2017;136:1703–13.
- [5] Bokma JP, Geva T, Sleeper LA, Babu Narayan SV, Wald R, Hickey K *et al.* A propensity score-adjusted analysis of clinical outcomes after pulmonary valve replacement in tetralogy of Fallot. *Eur Heart J* 2016;37: 829–35.
- [6] Warnes CA, Williams RG, Bashore TM, Child JS, Connolly HM, Dearani JA *et al.* ACC/AHA 2008 Guidelines for the Management of Adults with Congenital Heart Disease: a report of the American College of Cardiology/American Heart Association Task Force on Practice Guidelines (writing committee to develop guidelines on the management of adults with congenital heart disease). *Circulation* 2008;118: 2395–451.
- [7] Bokma JP, Winter MM, Oosterhof T, Vliegen HW, van Dijk AP, Hazekamp MG *et al.* Preoperative thresholds for mid-to-late haemodynamic and clinical outcomes after pulmonary valve replacement in tetralogy of Fallot. *Eur Heart J* 2016;37:829–35.
- [8] Geva T, Mulder B, Gauvreau K, Babu-Narayan SV, Wald RM, Hickey K *et al.* Preoperative predictors of death and sustained ventricular tachycardia after pulmonary valve replacement in patients with repaired tetralogy of Fallot enrolled in the INDICATOR cohort. *Circulation* 2018; 138:2106–15.
- [9] Tang D, Del Nido PJ, Yang C, Zuo H, Huang X, Rathod RH *et al.* Patient-specific MRI-based right ventricle models using different zero-load diastole and systole geometries for better cardiac stress and strain calculations and pulmonary valve replacement surgical outcome predictions. *PLoS One* 2016;11:e0162986.
- [10] Shibata M, Itatani K, Hayashi T, Honda T, Kitagawa A, Miyaji K *et al.* Flow energy loss as a predictive parameter for right ventricular deterioration caused by pulmonary regurgitation after tetralogy of Fallot repair. *Pediatr Cardiol* 2018;39:731–42.
- [11] Kopic S, Stephensen SS, Heiberg E, Arheden H, Bonhoeffer P, Ersbøll M *et al.* Isolated pulmonary regurgitation causes decreased right ventricular longitudinal function and compensatory increased septal pumping in a porcine model. *Acta Physiol* 2017;221:163–73.
- [12] Fassina L, Rozzi G, Rossi S, Scacchi S, Galetti M, Lo Muzio FP *et al.* Cardiac kinematic parameters computed from video of in situ beating heart. *Sci Rep* 2017;7:46143.
- [13] Bodhey NK, Beerbaum P, Sarikouch S, Kropf S, Lange P, Berger F *et al.* Functional analysis of the components of the right ventricle in the setting of tetralogy of Fallot. *Circ Cardiovasc Imaging* 2008;1:141–7.
- [14] Fassina L, Di Grazia A, Naro F, Monaco L, De Angelis MG, Magenes G. Video evaluation of the kinematics and dynamics of the beating cardiac syncytium: an alternative to the Langendorff method. *Int J Artif Organs* 2011;34:546–58.
- [15] Amiad Pavlov D, Landesberg A. The cross-bridge dynamics is determined by two length-independent kinetics: implications on muscle economy and Frank-Starling Law. *J Mol Cell Cardiol* 2016;90:94–101.
- [16] Frigiola A, Tsang V, Bull C, Coats L, Khambadkone S, Derrick G *et al.* Biventricular response after pulmonary valve replacement for right ventricular outflow tract dysfunction: is age a predictor of outcome? *Circulation* 2008;118:S182–90.
- [17] Tretter JT, Friedberg MK, Wald RM, McElhinney DB. Defining and refining indications for transcatheter pulmonary valve replacement in patients with repaired tetralogy of Fallot: contributions from anatomical and functional imaging. *Int J Cardiol* 2016;221:916–25.
- [18] Fogel MA, Sundareswaran KS, de Zelicourt D, Dasi LP, Pawlowski T, Rome J *et al.* Power loss and right ventricular efficiency in patients after tetralogy of Fallot repair with pulmonary insufficiency: clinical implications. *J Thorac Cardiovasc Surg* 2012;143:1279–85.

Cite this article as: Rozzi G, Lo Muzio FP, Fassina L, Rossi S, Statello R, Sandrini C *et al.* Right ventricular functional recovery depends on timing of pulmonary valve replacement in tetralogy of Fallot: a video kinematic study. *Eur J Cardiothorac Surg* 2021;59:1329–36.

Right ventricular functional recovery depends on timing of pulmonary valve replacement in tetralogy of Fallot: a video kinematic study

Giacomo Rozzi^{a,b,c,†}, Francesco Paolo Lo Muzio ^{a,b,†}, Lorenzo Fassina^d, Stefano Rossi ^b, Rosario Statello^{b,e},
Camilla Sandrini ^f, Maira Laricchiuta^a, Giuseppe Faggian ^a, Michele Miragoli^{b,c,‡} and
Giovanni Battista Luciani ^{a,*}

^a Department of Surgery, Dentistry, Pediatrics and Gynecology, University of Verona, Verona, Italy

^b Department of Medicine and Surgery, University of Parma, Parma, Italy

^c Department of Molecular Cardiology, Humanitas Clinical and Research Center, IRCCS, Rozzano, Italy

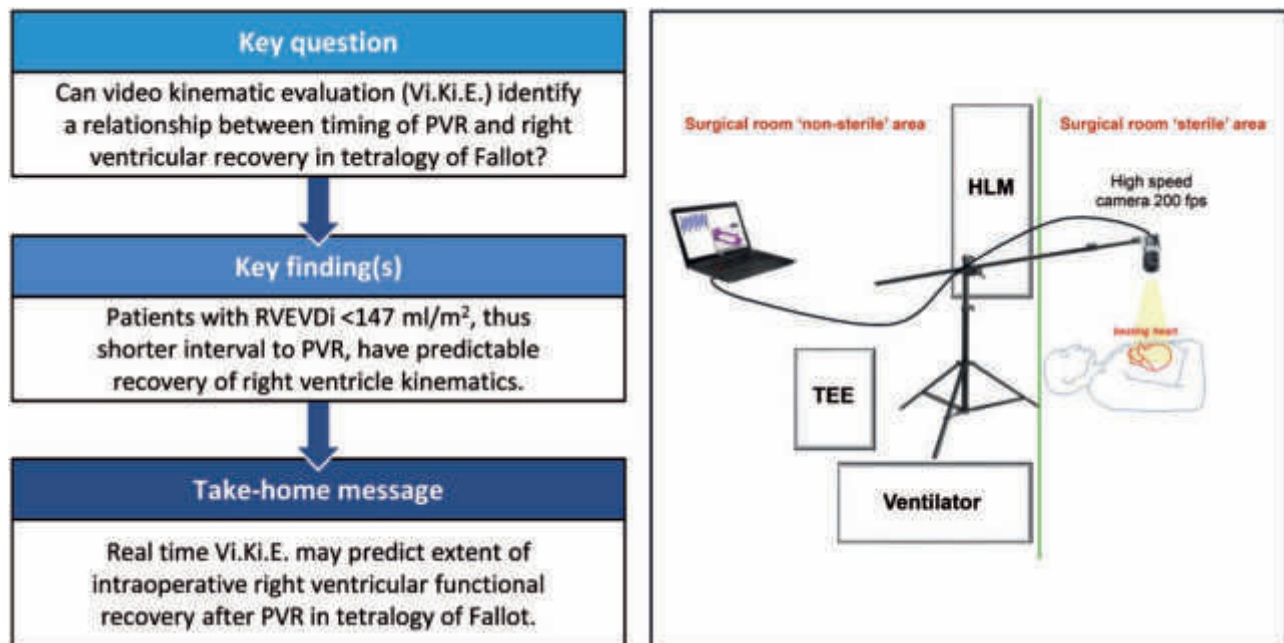
^d Department of Electrical, Computer and Biomedical Engineering, University of Pavia, Pavia, Italy

^e Department of Medical Sciences and Public Health, University of Cagliari, Cagliari, Italy

^f Department of Medicine, University of Verona, Verona, Italy

* Corresponding author. Section of Cardiac Surgery, Department of Surgery, Dentistry, Pediatrics and Gynecology, University of Verona, O.C.M. Piazzale Stefani 1, 37126 Verona, Italy. Tel: +39-045-8123303; e-mail: giovanni.luciani@univr.it (G.B. Luciani).

Received 31 August 2020; received in revised form 19 November 2020; accepted 7 December 2020



[†]The first two authors contributed equally to this work.

[‡]Co-last senior author.

Presented at the 34th Annual Meeting of the European Association for Cardio-Thoracic Surgery, Barcelona, Spain, 8–10 October 2020.

Abstract

OBJECTIVES: Indications for and timing of pulmonary valve replacement (PVR) after tetralogy of Fallot repair are controversial. Among magnetic resonance imaging indices proposed to time valve replacement, a right ventricular (RV) end-diastolic volume index greater than 160 ml/m² is often used. Recent evidence suggests that this value may still identify patients with irreversible RV dysfunction, thus hindering recovery. Our goal was to define, using intraoperative video kinematic evaluation, whether a relationship exists between timing of PVR and early functional recovery after surgery.

METHODS: Between November 2016 and November 2018, a total of 12 consecutive patients aged 27.1 ± 19.1 years underwent PVR on average 22.2 ± 13.3 years after tetralogy of Fallot repair. Mean RV end-diastolic volume evident on the magnetic resonance images was 136.9 ± 35.7 ml/m². Intraoperative cardiac kinematics were assessed by video kinematic evaluation via a high-speed camera acquiring videos at 200 fps before and after valve replacement.

RESULTS: Patients presenting with RV end-diastolic volume <147 ml/m² were significantly younger (11.2 ± 5.0 vs 38.4 ± 17.0; *P* = 0.005) and had a shorter time interval to valve replacement (11.0 ± 5.2 vs 30.1 ± 11.3; *P* = 0.03). The entire population showed a moderate correlation among energy expenditure, cardiac fatigue, perimeter of contraction and preoperative RV end-diastolic volume index. Both groups showed a reduction in all kinematic parameters after PVR, but those with end-diastolic volume >147 ml/m² showed an unpredictable outcome.

CONCLUSIONS: Video kinematic evaluation provides insight into intraoperative RV recovery in patients with tetralogy of Fallot undergoing PVR. Accordingly, functional recovery can be expected in patients with preoperative end-diastolic volume <147 ml/m².

Keywords: Tetralogy of Fallot • Pulmonary valve replacement • Video kinematic evaluation • Magnetic resonance imaging

ABBREVIATIONS

ANOVA	Analysis of variance
MRI	Magnetic resonance imaging
NYHA	New York Heart Association
PR	Pulmonary regurgitation
PVR	Pulmonary valve replacement
RV	Right ventricular
RVEDVi	RV end-diastolic volume index
RVEF	RV ejection fraction
RVESVi	RV end-systolic volume index
ToF	Tetralogy of Fallot
Vi.Ki.E	Video kinematic evaluation

INTRODUCTION

Indications for and timing of pulmonary valve replacement (PVR) in repaired tetralogy of Fallot (ToF) are debated due to limitations in estimating right ventricular (RV) dysfunction and predicting its recovery [1, 2]. Moreover, clinical outcomes assessed both subjectively and objectively by cardiopulmonary exercise testing have not been uniformly consistent concerning a beneficial effect of PVR [2]. Whereas consensus exists on indications for PVR in symptomatic patients with severe pulmonary regurgitation (PR), the debate continues on predictive diastolic and systolic indices of RV functional recovery [1–3]. Among the parameters proposed in the current guidelines to define the timing of PVR are the RV end-diastolic volume index (RVEDVi) and the RV end-systolic volume index (RVESVi) determined from magnetic resonance imaging (MRI). Accordingly, values above 160 ml/m² or 80 ml/m², respectively, would lead us to recommend PVR in patients with ToF with at least moderate PR [3]. However, recent studies suggest that these cut-off values may still preclude a significant portion of patients from recovering RV function [4–6], suggesting that the thresholds for PVR should be lowered even further. The debate stems from the paucity of prospective studies [5] and from the limitations inherent in retrospective analyses, in which

patients surviving from the pioneering era of ToF repair are mixed with those from the current era. This situation has stimulated the quest for alternative methods, including experimental ones, to investigate RV function during PVR [7–9].

Previous pilot work from our group assessed the safety and efficacy of video kinematic evaluation (Vi.Ki.E.), an original contactless experimental technology [10], to define RV functional changes in patients with ToF before and after PVR [11].

The goal of the present study was to establish whether Vi.Ki.E. can be used to assess intraoperative RV functional recovery after surgery, possibly offering prognostic insight into the timing of PVR in patients with ToF.

PATIENTS AND METHODS

Patients

The study was approved by our institutional review board (#847CESC Protocol # 13371), and all patients signed an informed consent form. Between November 2016 and November 2018, a total of 12 consecutive patients aged 27.1 ± 19.1 years undergoing PVR 22.1 ± 13.2 years after ToF repair were enrolled. Per institutional protocol, all patients undergoing surgical PVR, including the 12 herein, were initially assessed for transcatheter pulmonary valve implants. When deemed not suitable for catheter-based intervention, patients were referred for surgical PVR. The first 6 patients in this series were the object of a previous pilot study designed to assess the safety and efficacy of the Vi.Ki.E. technique [11].

The inclusion criteria for the current study were (i) isolated PR after transannular patch repair of ToF with pulmonary stenosis; (ii) symptomatic patients with severe PR or asymptomatic patients with evidence of progressive severe RV dilatation or dysfunction; and (iii) feasibility of PVR normothermic cardiopulmonary bypass on the beating heart. Patients with associated septal defects, aortic valve or root disease, pulmonary artery branch stenosis or acquired coronary artery disease were excluded from this study. The entire population underwent preoperative MRI

Table 1: Demographic and magnetic resonance imaging variables of patients with tetralogy of Fallot

	N = 12	Mean ± SD	Median	Range
Gender (male/female)	7/5			
BSA (m ²)		1.6 ± 0.41	1.7	0.73–1.97
Age at PVR (years)		27.1 ± 19.1	20	6–64
ToF to PVR (years)		22.2 ± 13.3	19.5	6–48
RVEDVi (ml/m ²)		136.9 ± 35.7	147.5	62.5–183
RVESVi (ml/m ²)		74.0 ± 30.1	81	12.5–104
RVEF (%)		50.1 ± 12.0	51	37–79
LVEF (%)		54.3 ± 5.9	54	42–62

BSA: body surface area; LVEF: left ventricular ejection fraction; PVR: pulmonary valve replacement; RVEDVi: right ventricular end-diastolic volume index; RVEF: right ventricular ejection fraction; RVESVi: right ventricular end-systolic volume index; ToF: tetralogy of Fallot.

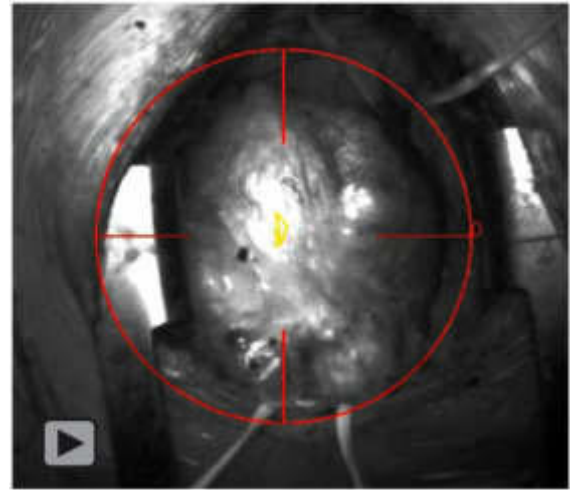
and transthoracic echocardiographic evaluation. The demographic and MRI variables of the patient population are shown in Table 1.

Surgical methods

All surgical procedures were performed by 1 surgeon (G.B.L.) via repeat median sternotomy, using aortic and bicaval cannulation, under normothermic (36°C) cardiopulmonary bypass on the beating heart. Video kinematic recordings were focused on the apical trabecular component of the right ventricle, in line with previous evidence showing this portion as the one taking most of the chronic volume overload [12]. The camera and the tripod were sterilized before being brought into the operating room and between every recording.

Intraoperative video kinematic evaluation

The video recordings were performed as previously described by our group [10]. Briefly, Vi.Ki.E. comprises placing a high-speed camera (Basler acA1300-200um USB 3.0 with the ON Semiconductor PYTHON 1300 CMOS sensor, Ahrensburg, Germany, equipped with Edmund Optics 6-mm compact fixed focal length lens, Barrington, NJ, USA) approximately 0.45 m above the patient during open-heart surgery to acquire videos of the beating heart at high temporal and spatial resolution. Four videos of 5 s each were recorded before and after PVR for each patient. The pre-PVR time point was at chest opening after freeing pericardial adhesions, whereas the post-PVR recording was performed 30 min after protamine sulfate was administered. In the post-PVR recording, care was taken to re-establish the same haemodynamic conditions observed in the pre-PVR recording, including central venous pressure, systolic arterial blood pressure, heart rate and ventilator settings. Right after completing the recordings, the tracking software Video Spot Tracker (Computer Integrated Systems for Microscopy and Manipulation, UNC, Chapel Hill, NC, USA) was used to process the videos because it placed a virtual marker on the epicardium on the first frame of the video. The virtual marker was positioned and optimized on the light spots present on the epicardial surface through a kernel (mathematical function). The frame-by-frame movement of the marker was recorded as a list of coordinates in x and y (Video 1).



Video 1: Video reproduces the tracking function in a patient with tetralogy of Fallot, head down. Red circle: virtual marker attached to the light on the epicardium; yellow line: the epicardial trajectory obtained by the marker movement.

Then, a custom-made algorithm, implemented in MATLAB[®] and based on Hamiltonian mechanics, elaborated those coordinates and provided the following cardiac kinematic parameters:

- Displacement: frame-by-frame estimate of the virtual marker movement. It is used to calculate the instantaneous movement of the epicardial tissue.
- Perimeter: the sum of all the virtual marker displacements during the cardiac cycles. It represents the entire movement of the epicardial tissue during the video recording and is used as an index of the ventricular compliance.
- Contraction velocity: the frame-by-frame estimation of the virtual marker velocity during the contraction phase. It estimates the instantaneous velocity of the epicardial tissue during the contraction phase.
- Cardiac fatigue: the mean acceleration of the virtual marker (of unitary mass) over all the cardiac cycles following the Hamiltonian mechanics. It calculates the epicardial tissue acceleration during the cardiac cycles.
- Energy: the mean kinetic energy of the virtual marker over all the cardiac cycles following the Hamiltonian mechanics. It estimates the heart energy expenditure during the video recording.

In this work, the perimeter of contraction was used instead of the displacement [10], because it estimates the ventricular compliance, which is clinically more relevant. As in the previous work [10], these parameters were converted from the pixel unit, the raw unit derived from the algorithm, to the SI-accepted unit (m).

Statistical analyses

The Pearson correlation was performed to evaluate the correlation between kinematic parameters and RVEDVi at MRI. After observation of a relationship between preoperative RVEDVi and intraoperative kinematic parameters recorded prior to PVR, the population was divided into 2 groups based on the RVEDVi

threshold of 147 ml/m^2 , the median value of the parameter ($<147 \text{ ml/m}^2$ for group 1 vs $>147 \text{ ml/m}^2$ for group 2). Therefore, after checking the normality of the data for each parameter with the Kolmogorov–Smirnov test, the Wilcoxon matched pairs signed rank test or a two-way analysis of variance (ANOVA) for repeated measures with ‘time’ as the within-subject factor (2 levels: pre-PVR and post-PVR) and ‘group’ as the between-subject factor (2 levels: group 1 and group 2) was performed. A *post hoc* analysis was conducted using the Student’s *t*-test with a Bonferroni correction for multiple comparisons where necessary. The Wilcoxon matched pairs signed-rank test or the paired *t*-test was used only for the parameters for which the two-way ANOVA for repeated measures could not be performed. A value of $P < 0.05$ was considered significant. The programme SPSS version 26 (IBM, Armonk, NY, USA) was used for the statistical analyses and GraphPad v.6 (GraphPad Software, Inc., La Jolla, CA, USA) was used to display the results.

RESULTS

Clinical outcome

All patients underwent surgical PVR on the beating heart: 5 patients received 23-mm stented bioprostheses; 2 patients, 25 mm; 2 patients, 21 mm; and 3 patients received a pulmonary homograft (size 27 mm in 2, and 25 mm in 1), respectively. A brief period of cardioplegic cardiac arrest was necessary to complete a right-sided Maze procedure using cryoablation catheters in 3 patients with a history of paroxysmal atrial fibrillation. There were no perioperative complications, except for 1 patient who experienced reversible subclinical hepatic dysfunction and 1 patient who required 2 days of inotropic support in the intensive care unit. Patients were discharged after a mean of 7.2 ± 2.4 days (5–12 days) of hospitalization, all in regular sinus rhythm. Transthoracic echocardiography prior to discharge documented the recovery of normal RV dimensions in 8 patients (67%) and moderate dilation in 4 (33%). Preserved ($>50\%$) RV ejection fraction (RVEF) was found in 7 (58%) patients, mildly reduced ($>40\%$) in 4 and severely reduced in 1 patient, who was 64 years old at PVR and the oldest in this series. Doppler studies showed the absence of PR in all patients and a mean peak trans-prosthetic pulmonary valve gradient of $16.5 \pm 7.1 \text{ mmHg}$. During a mean follow-up of 24.6 ± 12.5 months (13–39 months), all patients were in New York Heart Association (NYHA) functional class I, except for 1 patient who was in NYHA functional class II. No patient experienced adverse cardiovascular events, and all were in regular sinus rhythm, free from oral anticoagulation, except for 1, who developed complete atrioventricular block 6 months after PVR and the Maze procedure, requiring a permanent pacemaker implant. The information from the follow-up echocardiogram was similar to that from the evaluation prior to discharge, with a mean peak trans-prosthetic pulmonary valve gradient of $18.5 \pm 7.9 \text{ mmHg}$, preserved RVEF in 8 (67%) patients and mildly reduced RVEF in 3. RV dilation was absent or mild in 11 (92%) patients, whereas 1 patient in NYHA functional class II maintained moderate RV dilation and reduced RVEF.

Intraoperative cardiac kinematics

As previously observed [11], the pre-PVR Vi.Ki.E. parameters that yield the strongest clinical implications, namely energy and

cardiac fatigue, along with the perimeter, were plotted against preoperative RVEDVi to investigate the degree of correlation. Figure 1 shows the correlation coefficient *r* for energy expenditure ($r = 0.59$), cardiac fatigue ($r = 0.62$) and the perimeter of contraction ($r = 0.64$) in the whole population. For the 3 kinematic parameters, a cut-off value of 147 ml/m^2 emerged, whereafter the curve describes an exponential relationship. Plotting of pre-PVR kinematic parameters against preoperative RVESVi, an index also recently proposed to guide PVR timing, did not depict a moderate-to-good correlation (data not shown).

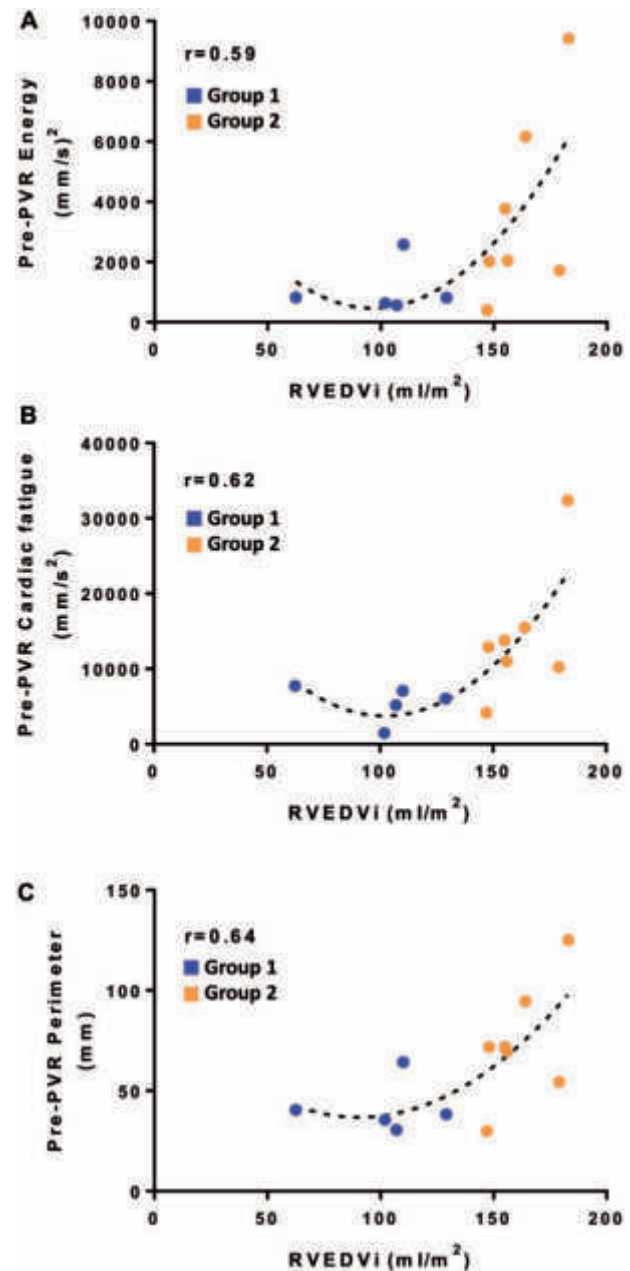


Figure 1: Correlation between video kinematic evaluation parameters and RVEDVi during pre-PVR in patients with tetralogy of Fallot. (A) Correlation between the average energy expenditure parameter against RVEDVi at pre-PVR. (B and C) Same as A but for cardiac fatigue and perimeter of contraction, respectively. Blue: patients with $\text{RVEDVi} < 147 \text{ ml/m}^2$; orange: patients with $\text{RVEDVi} > 147 \text{ ml/m}^2$. The dashed line represents the best fitting curve, which is an exponential with the correlation coefficient (*r*) displayed. PVR: pulmonary valve replacement; RVEDVi: right ventricular end-diastolic volume index.

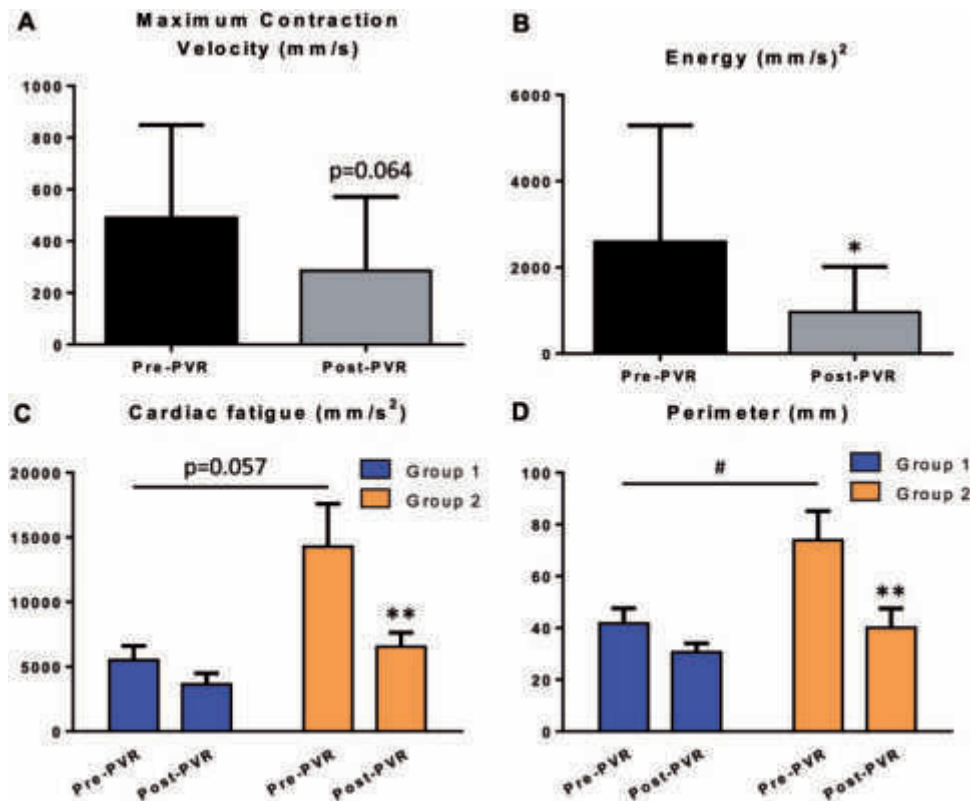


Figure 2: Kinematic parameters in patients with tetralogy of Fallot before and after PVR. (A) Maximum contraction velocity in patients with tetralogy of Fallot ($N = 12$) at both pre-PVR (black) and post-PVR (grey) time points. (B) Same as A but for the energy parameter. (C) Cardiac fatigue for group 1 (blue, $N = 5$) and group 2 (orange, $N = 7$). (D) Same as C but for the perimeter. Data are shown as mean \pm SEM. * $P < 0.05$; ** $P < 0.01$ versus pre-PVR. # $P < 0.05$ versus group 1. PVR: pulmonary valve replacement.

In Fig. 2A–D, the kinematic parameters of the 12 patients are displayed. All parameters examined decreased significantly after PVR. In detail, the maximum contraction velocity (Fig. 2A) decreased from 486.8 ± 104.2 to 285.4 ± 82.4 mm/s ($P = 0.064$) and the energy expenditure (Fig. 2B), from $2.55 \times 10^3 \pm 7.84 \times 10^2$ to $9.65 \times 10^2 \pm 3.03 \times 10^2$ mm²/s² ($P = 0.016$). The two-way ANOVA for repeated measures yielded a main effect of both ‘time’ ($F[1,10] = 6.810$; $P = 0.026$) and ‘group’ ($F[1,10] = 5.635$; $P = 0.039$) on cardiac fatigue, reflecting a significant difference between pre-PVR and post-PVR (9900.86 ± 2039.27 vs 5090.30 ± 748.87) and between group 1 and group 2 (4578.30 ± 1877.18 vs 10412.86 ± 1586.51). Similarly, the two-way ANOVA revealed a main effect of ‘time’ ($F[1,10] = 13.13$; $P = 0.005$) on the perimeter, reflecting a significant difference between pre-PVR and post-PVR (57.84 ± 7.21 vs 35.40 ± 4.64). *Post hoc* analysis also revealed that group 2 showed almost significantly higher pre- ($P = 0.057$) and post-PVR ($P = 0.082$) cardiac fatigue compared to group 1. In addition, the average pre-PVR value of perimeter was higher ($P = 0.05$) in group 2 than in group 1. Finally, within group 2, we observed a significant decrease between pre- and post-PVR values of both cardiac fatigue ($P = 0.009$) and perimeter ($P = 0.002$). Therefore, all patients showed prompt recovery, whether partial or complete, of RV functional parameters.

Cardiac kinematics and right ventricular end-diastolic volume index

The patient population was thus stratified based on the relationship between pre-PVR kinematic parameters and preoperative

RVEDVi, around a threshold value of 147 ml/m^2 (Fig. 1). Thereafter, significant differences emerged, showing that patients in group 1 were younger ($P = 0.005$), had a shorter time interval from ToF repair to PVR ($P = 0.03$), presented with greater RVESVi ($P = 0.054$) and had greater RVEF and left ventricular ejection fraction, albeit the difference was not significant (Table 2). To investigate possible differences in intraoperative experimental results based on timing of PVR (i.e. age at PVR, time interval of ToF repair and PVR), the kinematic parameters were also compared within the 2 groups for maximum contraction velocity and energy expenditure because they were not suitable for a two-way ANOVA comparison (see Statistical analyses). In group 1, a counterintuitive increasing trend for the maximum contraction velocity (from $3.20 \times 10^2 \pm 77.4$ to $3.44 \times 10^2 \pm 189$ mm/s) (Fig. 3A) and a decreasing trend for the energy expenditure (from $1.08 \times 10^3 \pm 3.78 \times 10^2$ to $9.65 \times 10^2 \pm 5.97 \times 10^2$) (Fig. 3C) emerged. The maximum contraction velocity result was probably influenced by 1 patient experiencing reversible atrial tachycardia after PVR. In group 2, the maximum contraction velocity significantly decreased from $6.07 \times 10^2 \pm 159.8$ to $2.43 \times 10^2 \pm 60.18$ mm/s ($P = 0.037$) (Fig. 3B) and the energy expenditure from $3.65 \times 10^3 \pm 1.19 \times 10^3$ to $9.65 \times 10^2 \pm 3.47 \times 10^2$ mm²/s² ($P = 0.024$) (Fig. 3D).

When comparing the post-PVR kinematics between the 2 groups, we found that only cardiac fatigue was significantly higher in group 2 ($P = 0.001$) (data not shown).

Finally, in order to offer prognostic insight about the timing for PVR, the difference of the recovery between pre- and post-PVR for the parameters that yield the strongest clinical implication

Table 2: Demographic and magnetic resonance imaging variables stratified by right ventricular end-diastolic volume index at pre-operative assessment

	RVEDVi < 145 ml/m ²			RVEDVi > 145 ml/m ²			P-value
	Mean ± SD	Median	Range	Mean ± SD	Median	Range	
BSA (m ²)	1.2 ± 0.4	1.3	0.73–1.61	1.8 ± 0.1	1.86	1.64–1.97	0.025
Age at PVR (years)	11.2 ± 5.0	10	6.0–19.0	38.4 ± 17.0	39	20.0–64.0	0.005
ToF to PVR (years)	11.0 ± 5.2	10	6.0–19.0	30.1 ± 11.3	25	18.0–48.0	0.03
RVESVi (ml/m ²)	53.0 ± 32.4	48	12.5–102.0	91.5 ± 12.7	94.5	72–104	0.054
RVEF (%)	57.5 ± 13.6	55	42–79	44.0 ± 6.3	43	37–52	0.1
LVEF (%)	56.4 ± 4.5	55	51–62	52.5 ± 6.8	54	42–62	0.18

BSA: body surface area; LVEF: left ventricular ejection fraction; PVR: pulmonary valve replacement; RVEDVi: right ventricular end-diastolic volume index; RVEF: right ventricular ejection fraction; RVESVi: right ventricular end-systolic volume index; ToF: tetralogy of Fallot.

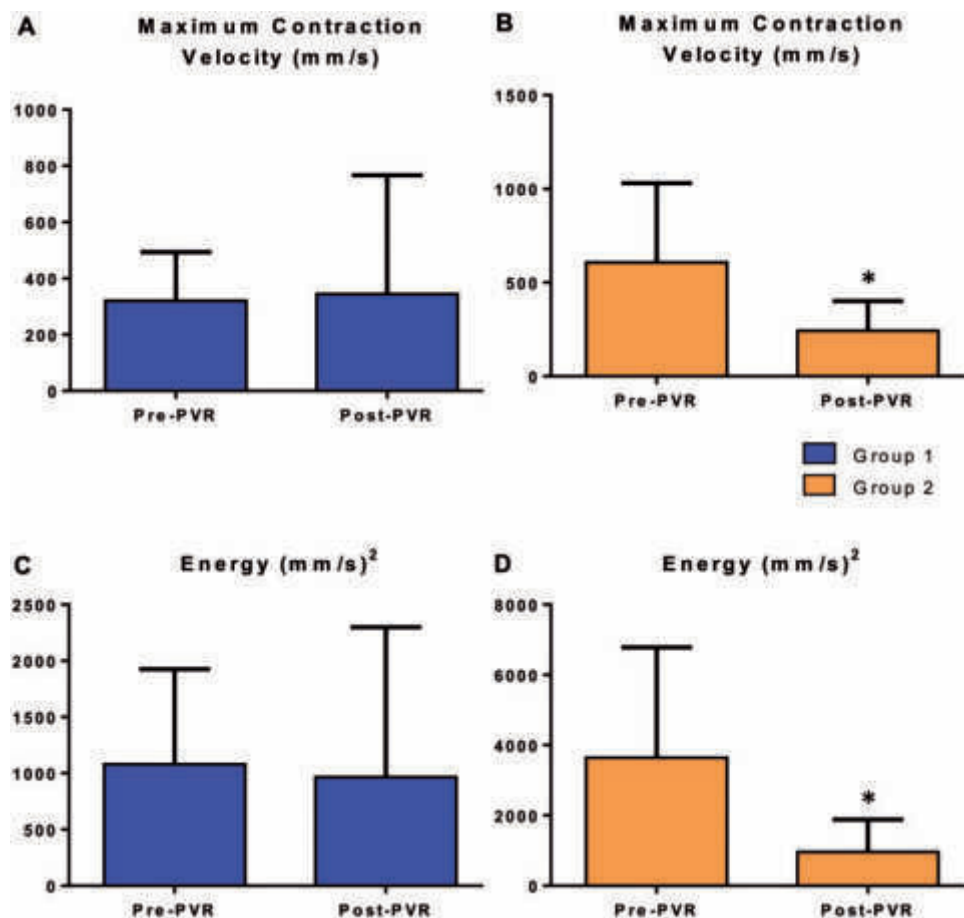


Figure 3: Maximum contraction velocity and energy in groups 1 and 2 before and after PVR. (A) Maximum contraction velocity in group 1 (blue, N = 5) before and after PVR (pre- and post-PVR time points, respectively). (B) Same as A but for group 2 (orange, N = 7) at pre- and post-PVR. (C and D) Same as A and B but for the energy parameter. Data are shown as mean ± SEM. *P < 0.05 versus pre-PVR. PVR: pulmonary valve replacement.

was compared in the 2 groups (Fig. 4A–C). Patients in group 2 showed greater relative recovery compared to those in group 1. In detail, the energy expenditure decreased by 58% vs 31%, cardiac fatigue by 45% vs 35% and perimeter of contraction by 41% vs 25%. However, patients referred later for PVR (group 2) showed greater variability in postoperative outcomes (Fig. 4).

DISCUSSION

This experimental study shows that intraoperative video kinematics can describe early RV functional recovery after PVR in patients with ToF. Furthermore, the current results provide insight into factors influencing prompt ventricular recovery. Accordingly,

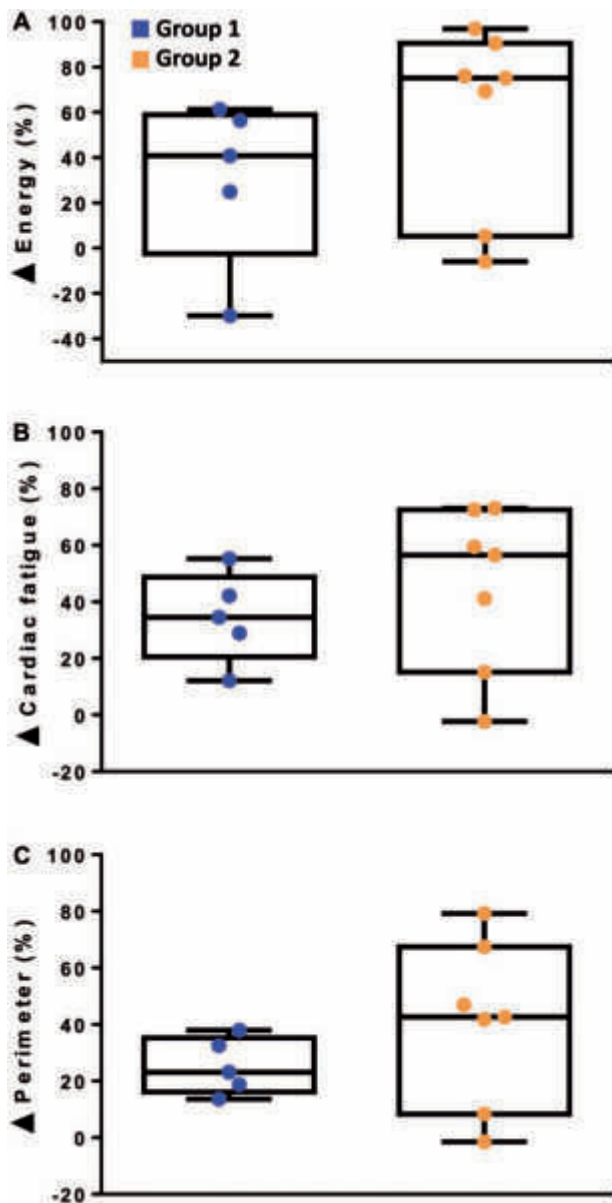


Figure 4: Distribution of percentage changes (Δ) in energy, cardiac fatigue and perimeter for both group 1 and group 2. (A) The percentage changes (Δ) were calculated as the difference between the values of energy at pre-PVR and post-PVR for both group 1 and group 2. (B and C) same as A but for cardiac fatigue and perimeter. PVR: pulmonary valve replacement.

RVEDVi lower than 147 ml/m^2 at preoperative MRI, a surrogate for earlier timing of PVR in the present work, is associated with intraoperative RV functional recovery.

Our experience allowed us to corroborate the preliminary observation from a safety and efficacy study, whereby a correlation was suggested between preoperative RVEDVi at MRI and the kinematic parameters of cardiac fatigue and energy expenditure in patients with preoperative RV volumes lower than those that are the current 'proactive' recommendations for surgery [11]. It is evident that long-standing RV volume overload due to PR is directly correlated with preoperative RV dysfunction, as assessed by intraoperative video kinematic analysis (Fig. 1). Interestingly, the correlation with cardiac fatigue, energy expenditure and ventricular compliance presents with a dichotomous behaviour with a watershed around an RVEDVi of 150 ml/m^2 .

Our entire patient population showed prompt improvement in all kinematic parameters after PVR with a significant decrease in maximum contraction velocity, cardiac fatigue, energy consumption and, indirectly, increase in ventricular compliance (reduction of perimeter of contraction). These changes may be explained by the Frank-Starling law, which asserts that a decrease in ventricular preload is followed by a reduction of the force generated [13], in line with the reduction of cardiac fatigue and of energy consumption. The acute preload reduction right after PVR leads to a less stretched ventricle and indirectly improves ventricular compliance, herein measured using the perimeter of contraction. Finally, the maximum contraction velocity is reduced because of the force-velocity relationship of the Frank-Starling law, which states that, after a decrease in preload, cardiac muscle fibres will have a lower velocity of shortening. The decrease in preload after PVR not only affects the right ventricle but, indirectly, also the left ventricle [14]. The interventricular interactions are regulated by the changes in chamber pressure and volume and anatomically by the pericardium, interventricular septum and myocardial tracts linking the ventricles [15]. In the open-chest setting, the interaction between ventricles is important in determining the position of the interventricular septum during diastole. Physiologically, the position of the septum is determined by the difference in the pressures on both sides. Hence, pathological conditions like ToF characterized by increased RV end-diastolic pressure and chamber enlargement determine a septal shift towards the left ventricle, thereby hampering its mechanical performance. Therefore, any decrease in RV end-diastolic pressure after PVR may also lead to an improvement in the mechanics of the left ventricle.

However, patients presenting with RVEDVi greater than 147 ml/m^2 undoubtedly had a distinct behaviour compared with those with lower RV volume overload. This situation was evidenced not only by the worse kinematic performance prior to PVR, but also by the observation that recovery of baseline kinematic functional parameters was not always complete and was, most notably, less predictable. Considering that the RVEDVi threshold value clearly separated younger patients with a shorter time interval between ToF repair and PVR, from our experimental study, we infer that recovery of the RV functional parameter directly depends on the timing of the PVR. The present results agree with prior experimental findings using cardiac catheterization and MRI, where rapid decline in RV power and efficiency were shown at cut-off values of 139 ml/m^2 RVEDV and 75 ml/m^2 RVESVi [8].

Retrospective studies and meta-analyses have been unable to unravel the issue of benefits and timing of PVR after ToF repair, possibly due to limitations inherent with study design such as the heterogeneity of the patient population, overlap of historical and current patients, variability in operative techniques and outcome [1, 2, 16]. Although the issue of PVR timing in current clinical practice depends on a variety of parameters, including symptoms, exercise testing, RV and left ventricular function and RV volumes at MRI, previous clinical studies support the present experimental analysis. One prospective study has identified thresholds for complete RV remodelling at MRI (RVEDVi $< 158 \text{ ml/m}^2$; RVESVi $< 82 \text{ ml/m}^2$), which closely mirror our findings [5]. Furthermore, a previous observational study reporting on a patient population comparable to the one herein (relative to age at PVR, time of original repair and preoperative MRI profile) has shown how more proactive indications (RVEDVi $< 150 \text{ ml/m}^2$) may afford negligible early and late mortality, recovery of RV volumes, improvement in biventricular function and normalization of V_E/V_{CO_2} [4]. Finally, there is more recent evidence supporting

the inference that earlier timing of PVR may reduce the risk of malignant arrhythmias and death after PVR [17, 18].

Limitations

This study has some limitations. The patient cohort size is partly due to the stringent selection criteria. In addition, 3 patients in group 2 required a brief period of myocardial ischaemia so we could perform a right-sided Maze procedure. Although the kinematic results in the latter patients did not diverge significantly from those in patients having a completely beating heart operation (data not shown), an influence on the experimental results cannot be ruled out. Furthermore, a limitation of the Vi.Ki.E. evaluation is the use of a single 2-dimensional camera to record the 3-dimensional movement of the heart. Therefore, the present results may represent a simplification of kinematics analysis, albeit necessary to derive translational inferences on the impact of surgery on RV functional properties.

Conversely, the present technique may offer some advantages over echocardiography and MRI when assessing patients undergoing PVR. Compared with MRI, PVR allows real-time, cost-effective patient evaluation during the acute phase. Compared with transoesophageal echocardiography, it is non-invasive, contactless and less operator-dependent due to the algorithm-driven evaluation. Other advantages compared to both techniques are the higher spatial and temporal resolutions, the image quality and the RV mechanical quantitative assessment. Future developments related to the current observations include follow-up MRI and exercise testing to assess late clinical implications of intraoperative findings.

CONCLUSIONS

Vi.Ki.E. is an experimental technique able to describe intraoperative RV functional changes in patients with ToF undergoing PVR. The results herein offer further insight into the extent of RV recovery. Accordingly, prompt recovery can be expected in patients with preoperative end-diastolic volume less than 147 ml/m², suggesting earlier timing of PVR.

Funding

The current study was supported by institutional funds from the University of Verona and the University of Parma FFBR-MIUR-2017, FIL-2018 to M.M.

Conflict of interest: none declared.

Author contributions

Giacomo Rozzi: Data curation; Formal analysis; Investigation; Writing—original draft. **Francesco Paolo Lo Muzio:** Data curation; Formal analysis; Investigation; Writing—original draft. **Lorenzo Fassina:** Methodology; Validation. **Stefano Rossi:** Validation; Visualization. **Rosario Statello:** Data curation; Formal analysis. **Camilla Sandrini:** Data curation; Formal analysis. **Maira Laricchiuta:** Data curation; Formal analysis. **Giuseppe Faggian:** Funding acquisition; Project administration. **Michele Miragoli:** Funding acquisition; Supervision; Writing—review & editing. **Giovanni Battista Luciani:** Conceptualization; Investigation; Supervision; Writing—original draft; Writing—review & editing.

Reviewer information

European Journal of Cardio-Thoracic Surgery thanks Hitendu Hasmukhlal Dave, Martin M. Kostolny, James A. Quintessenza and the other, anonymous reviewer(s) for their contribution to the peer review process of this article.

REFERENCES

- [1] Bokma JP, Geva T, Sleeper LA, Babu Narayan SV, Wald R, Hickey K *et al.* A propensity score-adjusted analysis of clinical outcomes after pulmonary valve replacement in tetralogy of Fallot. *Heart* 2018;104:738–44.
- [2] Ferraz Cavalcanti PE, Sá MP, Santos CA, Esmeraldo IM, de Escobar RR, de Menezes AM *et al.* Pulmonary valve replacement after operative repair of tetralogy of Fallot: meta-analysis and meta-regression of 3,118 patients from 48 studies. *J Am Coll Cardiol* 2013;62:2227–43.
- [3] Stout KK, Daniels CJ, Aboulhosn JA, Bozkurt B, Broberg CS, Colman JM *et al.* 2018 AHA/ACC Guideline for the management of adults with congenital heart disease: a report of the American College of Cardiology/American Heart Association Task Force on Clinical Practice Guidelines. *J Am Coll Cardiol* 2019;73:e81–192.
- [4] Frigiola A, Tsang V, Bull C, Coats L, Khambadkone S, Derrick G *et al.* Biventricular response after pulmonary valve replacement for right ventricular outflow tract dysfunction: is age a predictor of outcome? *Circulation* 2008;118:S182–90.
- [5] Heng EL, Gatzoulis MA, Uebing A, Sethia B, Uemura H, Smith GC *et al.* Immediate and midterm cardiac remodeling after surgical pulmonary valve replacement in adults with repaired tetralogy of fallot: a prospective cardiovascular magnetic resonance and clinical study. *Circulation* 2017;136:1703–13.
- [6] Lee C, Choi ES, Lee CH. Long-term outcomes of pulmonary valve replacement in patients with repaired tetralogy of Fallot. *Eur J Cardiothorac Surg* 2020;58:246–52.
- [7] Tang D, Del Nido PJ, Yang C, Zuo H, Huang X, Rathod RH *et al.* Patient-specific MRI-based right ventricle models using different zero-load diastole and systole geometries for better cardiac stress and strain calculations and pulmonary valve replacement surgical outcome predictions. *PLoS One* 2016;11:e0162986.
- [8] Fogel MA, Sundareswaran KS, de Zelicourt D, Dasi LP, Pawlowski T, Rome J *et al.* Power loss and right ventricular efficiency in patients after tetralogy of Fallot repair with pulmonary insufficiency: clinical implications. *J Thorac Cardiovasc Surg* 2012;143:1279–85.
- [9] Kopic S, Stephensen SS, Heiberg E, Arheden H, Bonhoeffer P, Ersbøll M *et al.* Isolated pulmonary regurgitation causes decreased right ventricular longitudinal function and compensatory increased septal pumping in a porcine model. *Acta Physiol (Oxf)* 2017;221:163–73.
- [10] Fassina L, Rozzi G, Rossi S, Scacchi S, Galetti M, Lo Muzio FP *et al.* Cardiac kinematic parameters computed from video of *in situ* beating heart. *Sci Rep* 2017;7:46143.
- [11] Rozzi G, Lo Muzio FP, Sandrini C, Rossi S, Fassina L, Faggian G *et al.* Real-time video kinematic evaluation of the *in situ* beating right ventricle after pulmonary valve replacement in patients with tetralogy of Fallot: a pilot study. *Interact CardioVasc Thorac Surg* 2019;29:625–31.
- [12] Bodhey NK, Beerbaum P, Sarikouch S, Kropf S, Lange P, Berger F *et al.* Functional analysis of the components of the right ventricle in the setting of tetralogy of Fallot. *Circ Cardiovasc Imaging* 2008;1:141–7.
- [13] Amiad Pavlov D, Landesberg A. The cross-bridge dynamics is determined by two length-independent kinetics: implications on muscle economy and Frank-Starling Law. *J Mol Cell Cardiol* 2016;90:94–101.
- [14] Belenkie I, Smith ER, Tyberg JV. Ventricular interaction: from bench to bedside. *Ann Med* 2001;33:236–41.
- [15] Friedberg MK. Imaging right-left ventricular interactions. *JACC Cardiovasc Imaging* 2018;11:755–71.
- [16] Geva T, Mulder B, Gauvreau K, Babu-Narayan SV, Wald RM, Hickey K *et al.* Preoperative predictors of death and sustained ventricular tachycardia after pulmonary valve replacement in patients with repaired tetralogy of fallot enrolled in the INDICATOR cohort. *Circulation* 2018;138:2106–15.
- [17] Romeo JLR, Takkenberg JJM, Cuyppers JAAE, de Groot NMS, van de Woestijne P, Bruining N *et al.* Timing of pulmonary valve replacement in patients with corrected Fallot to prevent QRS prolongation. *Eur J Cardiothorac Surg* 2020;58:559–66.
- [18] Dorobantu DM, Sharabiani MTA, Taliotis D, Parry AJ, Tulloh RMR, Bentham JR *et al.* Age over 35 years is associated with increased mortality after pulmonary valve replacement in repaired tetralogy of Fallot: results from the UK National Congenital Heart Disease Audit database. *Eur J Cardiothorac Surg* 2020;58:825–31.



Article

Artificial Intelligence Supports Decision Making during Open-Chest Surgery of Rare Congenital Heart Defects

Francesco Paolo Lo Muzio ^{1,2,†}, Giacomo Rozzi ^{1,2,3,†}, Stefano Rossi ², Giovanni Battista Luciani ¹, Ruben Foresti ², Aderville Cabassi ^{2,‡}, Lorenzo Fassina ^{4,*} and Michele Miragoli ^{2,3,*}

- ¹ Department of Surgery, Dentistry, Pediatrics and Gynecology, University of Verona, 37134 Verona, Italy; francescopaolo.lomuzio@univr.it (F.P.L.M.); giacomo.rozzi@univr.it (G.R.); giovanni.luciani@univr.it (G.B.L.)
² Department of Medicine and Surgery, University of Parma, 43126 Parma, Italy; stefano.rossi@univr.it (S.R.); ruben.foresti@univr.it (R.F.); aderville.cabassi@univr.it (A.C.)
³ Humanitas Research Hospital—IRCCS, Via Manzoni 56, 20089 Rozzano, MI, Italy
⁴ Department of Electrical, Computer and Biomedical Engineering (DIII), University of Pavia, 27100 Pavia, Italy
* Correspondence: lorenzo.fassina@univp.it (L.F.); michele.miragoli@univr.it (M.M.); Tel.: +39-0382-98-5352 (L.F.); +39-0521-90-3256 (M.M.)
† Equal contribution.
‡ Co-last Author.



Citation: Lo Muzio, F.P.; Rozzi, G.; Rossi, S.; Luciani, G.B.; Foresti, R.; Cabassi, A.; Fassina, L.; Miragoli, M. Artificial Intelligence Supports Decision Making during Open-Chest Surgery of Rare Congenital Heart Defects. *J. Clin. Med.* **2021**, *10*, 5330. <https://doi.org/10.3390/jcm10225330>

Academic Editors: Francesco Onorati and Teruhiko Imamura

Received: 12 October 2021

Accepted: 10 November 2021

Published: 16 November 2021

Publisher's Note: MDPI stays neutral with regard to jurisdictional claims in published maps and institutional affiliations.



Copyright: © 2021 by the authors. Licensee MDPI, Basel, Switzerland. This article is an open access article distributed under the terms and conditions of the Creative Commons Attribution (CC BY) license (<https://creativecommons.org/licenses/by/4.0/>).

Abstract: The human right ventricle is barely monitored during open-chest surgery due to the absence of intraoperative imaging techniques capable of elaborating its complex function. Accordingly, artificial intelligence could not be adopted for this specific task. We recently proposed a video-based approach for the real-time evaluation of the epicardial kinematics to support medical decisions. Here, we employed two supervised machine learning algorithms based on our technique to predict the patients' outcomes before chest closure. Videos of the beating hearts were acquired before and after pulmonary valve replacement in twelve Tetralogy of Fallot patients and recordings were properly labeled as the “unhealthy” and “healthy” classes. We extracted frequency-domain-related features to train different supervised machine learning models and selected their best characteristics via 10-fold cross-validation and optimization processes. Decision surfaces were built to classify two additional patients having good and unfavorable clinical outcomes. The k-nearest neighbors and support vector machine showed the highest prediction accuracy; the patients' class was identified with a true positive rate $\geq 95\%$ and the decision surfaces correctly classified the additional patients in the “healthy” (good outcome) or “unhealthy” (unfavorable outcome) classes. We demonstrated that classifiers employed with our video-based technique may aid cardiac surgeons in decision making before chest closure.

Keywords: supervised machine learning; right ventricle kinematics; Tetralogy of Fallot; surgery decision making; prognosis prediction

1. Introduction

Artificial intelligence (AI) has been heralded in the family of “disruptive” technology and as a promising tool to assist clinicians in making better clinical decisions [1,2]. AI implementations can discover and use information hidden in the massive amounts of data usually available for clinical decision making [3–5]. Moreover, AI systems aim to reduce diagnostic and therapeutic errors, unavoidable in routine clinical practice, using any sensor or available data to improve the prediction. Among the AI systems that have been tested, there is the Medical Decision Support System which improved clinical decision making in both diagnosis and therapy selection, especially in cases of uncertainty or incomplete information [6].

AI promisingly showed to surpass diagnoses obtained from repetitive human tasks by merging digital imaging with all other data coming from different fields of research [7,8]. Regarding cardiac imaging, AI has been proposed for analyzing CT-scan [9], MRI [10,11] and transthoracic echocardiography data [12].

Recently, AI has been implemented to reduce the number of observations needed to achieve both prognostic and diagnostic robust results [13–16] with a limited number of patients.

Several AI-related tools, especially for rare disease diagnoses, have shown progress in determining the risk score and in screening areas such as genomics [17], histopathology [18] and radiology [19]. Although all of them are certain to revolutionize our concept of prognosis and diagnosis, AI-related cardiac imaging is currently not employed during open-chest surgery.

Transesophageal echocardiography is the gold standard imaging technique to monitor the left ventricular mechanics during cardiac surgery, but there is still the absence of real-time intraoperative imaging techniques for the evaluation of the right ventricle (RV). This is critical, especially for complex congenital heart diseases in which RV dysfunctions are common features [20]. Hence, AI algorithms are still not employed or developed for this specific task. As for the intraoperative evaluation of the RV, our group has introduced and validated an innovative and contactless imaging technique named Vi.Ki.E. (Video Kinematic Evaluation) [21]. Briefly, the technique consists of recording high-temporal resolution videos of the epicardial movement of the exposed beating heart to calculate kinematic parameters before and after surgery. We applied Vi.Ki.E. in the field of myocardial ischemia [21] and complex congenital heart diseases such as Tetralogy of Fallot (ToF) [22,23], which is the most common RV pathology representing 7–10% of the congenital cardiac defects [24]. Interestingly, in our most recent work on ToF [23], we observed a promising correlation between the before surgery Vi.Ki.E. parameters and preoperative RVEDVI measured by cardiac magnetic resonance (the gold standard for RV evaluation in congenital patients).

In the present work, two supervised machine learning (SML) models were selected and trained with data extracted from twelve consecutive ToF patients undergoing pulmonary valve replacement (PVR). We opted for SML over unsupervised machine learning due to its capability to consider not only the data but also the patient's documented clinical outcome, reducing the classification error and providing more clinically relevant results [24]. In the operating room, the success and prediction of the outcome of the surgical intervention are still based on the medical team's experience. Our intraoperative approach allows us to compare the heart kinematic parameters before and after surgery and postulate on the intervention success, but the implementation of SML would allow us to predict the outcome upon chest closure. Therefore, to develop suitable SML models, we extracted features from the frequency domain [25–28] of the RV epicardial movement recorded with our imaging technique.

This monocentric study aimed to develop Vi.Ki.E.-based SML models to provide an important decision-making tool supporting the medical team during open-chest surgery.

2. Materials and Methods

2.1. Surgical Methods

The surgical methods and selection criteria of our study were described in our previous work [22]. Briefly, all surgical procedures were performed by one surgeon (G.B.L.) via repeat median sternotomy, using aortic and bicaval cannulation, under normothermic cardiopulmonary bypass on the beating heart. The latter criterion was implemented to exclude the effects of myocardial ischemia/stunning on the kinematic parameters and, thus, the whole recording. Anesthetic was administered only once at the beginning of the surgery. Finally, apart from one patient who had an intraoperative tachycardia that was assessed in our pilot study [21], the heart rate of all patients was the same between the two timepoints.

2.2. Right Ventricle Video Recording

The study was approved by the Institutional Review Board (# 847CESC Protocol # 13371) and all patients signed an informed consent agreement. Between November 2016 and November 2018, a total of twelve consecutive ToF patients undergoing PVR were studied accordingly with our previous works [20] and used to train the classifiers. Briefly, three to four videos lasting five seconds were recorded at 200 fps in two surgical phases: before the beginning of the surgical procedure and at the end of the surgery (PVR), circa 30 min after protamine sulphate infusion. The timing of the second surgery was implemented to obtain the same blood density of the before-surgery phase. Consequently, the open source tracking software Video Spot Tracker (VST, CISMM, Computer Integrated Systems for Microscopy and Manipulation, UNC Chapel Hill, NC, USA) was used to track the right ventricle epicardial movement using a virtual video marker (Figure 1a). Then, a custom algorithm implemented in MATLAB® (Release R2020a, The MathWorks, Inc., Natick, MA, USA) extracted the x and y coordinates versus the time of the RV movement (Figure 1b), which were used as a source of information for the SML classifiers.

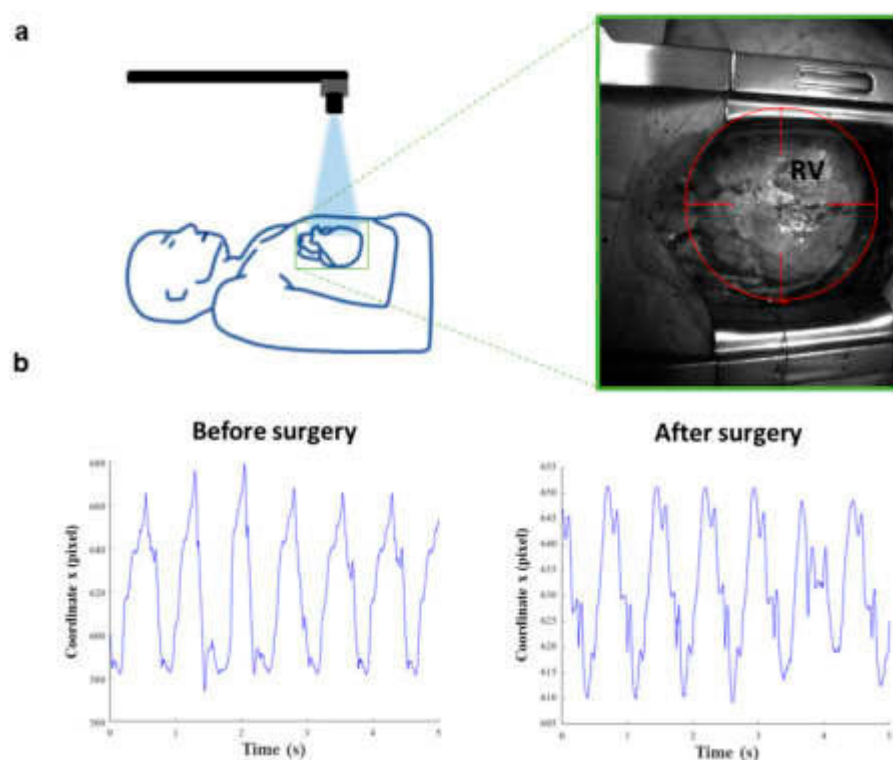


Figure 1. Vi.Ki.E. workflow and coordinates of a representative ToF patient. (a) Schematic representation of the Vi.Ki.E. surgical setup (left). The green square surrounding the heart is magnified in the right panel displaying the virtual marker position on the right ventricle (RV) epicardium. (b) The x coordinates extracted from a 5 s video recording before and after surgery phases.

As concerns the Vi.Ki.E. data, the algorithm provides the following parameters, as described in [21]:

- Maximum contraction velocity: estimates the instantaneous maximal velocity of the cardiac tissue during systole;
- Force: estimates the instantaneous acceleration;
- Energy: estimates the kinetic energy during cardiac cycles;
- Perimeter: estimates the ventricular compliance.

In detail, we have recorded and analyzed a total of 86 videos of beating hearts, subdivided into 43 before and 43 after PVR surgery.

Moreover, we tested our classifiers on two additional patients, with known clinical outcomes and not used for the models' training, via the decision surface method. One ToF patient undergoing PVR who had a favorable outcome (discharged after 7 days of hospitalization) and one patient undergoing PVR for isolated congenital pulmonary valve regurgitation who had an unfavorable hospital course (death two weeks after surgery).

2.3. Features/Predictors

For each video, we extracted numeric features/predictors (Table 1) that are an overall measure of the "trait" of the periodic mechanical x and y coordinates representing the cardiac cycle.

Table 1. Set of features/predictors extracted from the periodic movement of the RV. A total of 7 features/predictors are calculated for both x and y coordinates. A citation for each feature is shown in the table (each link was accessed on 1 August 2021).

Feature/Predictor	MATLAB [®] Function
Band power [pixel]: it returns the 'average power' or average l_2 norm (average Euclidean norm) of the input signal [pixel]	bandpower https://it.mathworks.com/help/signal/ref/bandpower.html
Power bandwidth [Hz]: it returns the 3 dB (half-power) bandwidth of the input signal	powerbw https://it.mathworks.com/help/signal/ref/powerbw.html
Occupied bandwidth [Hz]: it returns the 99% occupied bandwidth of the input signal	obw https://it.mathworks.com/help/signal/ref/obw.html
Spurious free dynamic range [dB]: it returns the SFDR of the real sinusoidal-like input signal	sfdr https://it.mathworks.com/help/signal/ref/sfdr.html
Signal to noise and distortion ratio [dB]: it returns the SINAD of the real sinusoidal-like input signal	sinad https://it.mathworks.com/help/signal/ref/sinad.html
Signal to noise ratio [dB]: it returns the SNR of the input signal	SNR https://it.mathworks.com/help/signal/ref/snr.html
Spectral entropy (information content) of the input signal	pentropy https://it.mathworks.com/help/signal/ref/pentropy.html

In detail, Table 1 showed the seven MATLAB[®] functions (Release R2020a, The MathWorks, Inc., Natick, MA, USA) to calculate the features/predictors for each of the 86 video recordings. Furthermore, the known clinical outcome was used to label the patient video recording as unhealthy (before surgery) or healthy (after surgery) class.

2.4. Models' Training and Optimization

The two classifiers showing the highest classification accuracy were trained and optimized with the abovementioned matrix. In detail:

1. Optimizable KNN (k-nearest neighbor classifier), via the "fitcknn" function (<https://it.mathworks.com/help/stats/fitcknn.html>, accessed on 1 August 2021) with a total of 100 optimization iterations and no standardization of the input features;
2. Optimizable SVM (support vector machine classifier), via the "fitsvm" function (<https://it.mathworks.com/help/stats/fitsvm.html>, accessed on 1 August 2021) with a total of 100 optimization iterations and no standardization of the input features.

Both models were optimized via the minimization of the classification error and, also, 10-fold cross-validated: for 10 times, a new 10% of the patients were not used to train but to blindly validate the models. Cross-validation is a good practice to avoid over-fitting, which is undesired memorization of the training data reducing the model predictive ability.

2.5. Decision Surface

The cross-validated and optimized classifiers were used to build 2D simplified classification models for both x and y coordinates. This simplified 2D approach allowed to build the so-called decision surface where every point of the Cartesian plane is classified using, as a representative feature of the patient status, the SNR of the kinematic periodic movement of the RV.

2.6. Statistical Analysis

To calculate the minimum number of patients to perform the study, we used the formula by Armitage et al. [29] to evaluate the 95% confidence interval for the disease's prevalence, where the amplitude (D) of that confidence interval is established a priori and with $Z(\sigma/2) = 1.96$. Knowing the ToF prevalence is circa 1/3500 live births and establishing $D = 2\%$, the minimum number of patients that should be enrolled to study the disease is $N > 10.97$ [30].

The Vi.Ki.E. parameters are expressed as mean \pm SEM. The normality of the distribution of the data was investigated with Kolmogorov–Smirnov test, and the significance was assessed by Mann–Whitney test. *p* values were considered significant at <0.05 .

3. Results

3.1. Selected Models

The frequency-domain-related features extracted from the epicardial movement of the RV were processed by the Classification Learner Application in MATLAB® to test different classification models.

Table 2 shows that the two ensemble methods, as well as the linear discriminant, the kernel naïve Bayes and the Gaussian naïve Bayes models, displayed a classification accuracy below 75% and therefore were not adopted in this work [31].

Table 2. All tested classifiers ranked in terms of accuracy (%).

Classifier	Accuracy (%)
Boosted trees (ensemble of trees using the AdaBoost (Adaptive Boosting) algorithm) [32]	46.5
RUSBoosted trees (ensemble of trees using the RUSBoost (Random Undersampling Boosting) algorithm) [33]	46.5
Linear discriminant [34]	66.3
Kernel naïve Bayes [35]	68.6
Gaussian naïve Bayes [36]	69.8
Fine Gaussian (Radial Basis) support vector machine (SVM) [37]	79.1
Fine <i>k</i> -nearest neighbor (KNN) [38]	86.0

On the contrary, both KNN and SVM classifiers showed the highest classification accuracy and therefore were elected to be customized and optimized for our specific medical aim.

3.2. Optimized Model Training

At the end of the optimized training we obtained:

- The confusion matrix with the number of truly recognized videos on the diagonal and the number of falsely recognized videos on the antidiagonal (Figures 2a and 3a);
- The preceding confusion matrices were used to compute the corresponding True Positive Rate (TPR), the probability to truly recognize the class, on the diagonal, and False Negative Rate (FNR), the probability to misrecognize the class, on the antidiagonal (Figures 2b and 3b);
- The optimized parameters of the 10-fold cross-validated models (Figures 4a and 5a);

- The Area Under Curve (AUC) or area under ROC (Receiver Operating Characteristic) curve (Figures 4b and 5b);
- The MATLAB®’s script of the optimized model;
- The MATLAB®’s optimized model (as a saved workspace structure array) to employ in the operating room to classify the current patient’s heart movement as unhealthy or healthy.

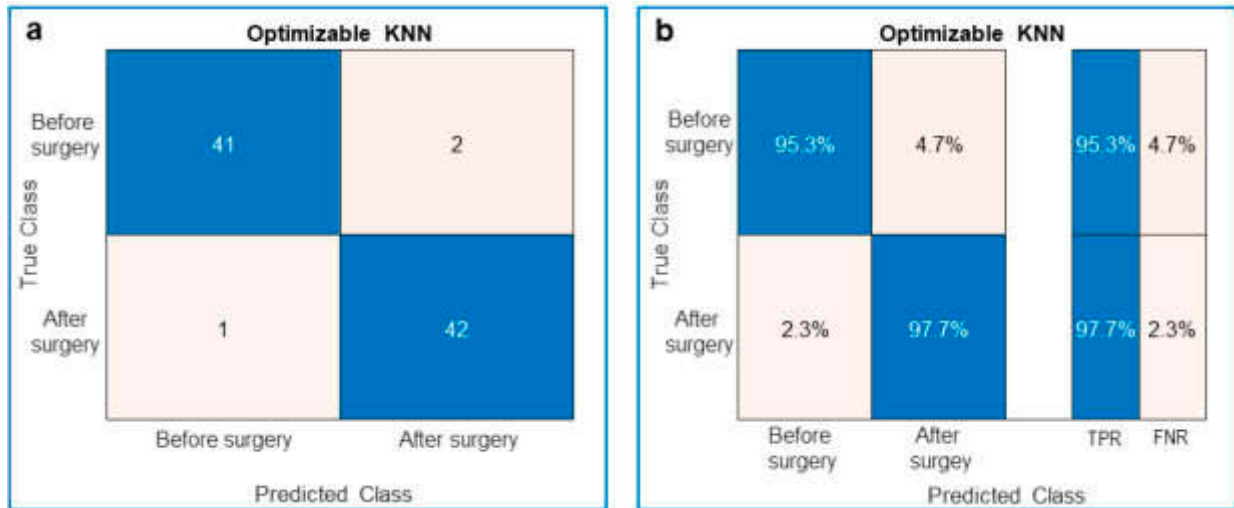


Figure 2. Performance of the trained optimizable k-nearest neighbor (KNN) classifier. (a) Confusion matrix showing the true and predicted classes of the ToF patients’ videos. The blue diagonal is related to the number of videos that were truly recognized (Predicted Class = True Class), whereas the pink antidiagonal is related to the number of videos that were falsely recognized (Predicted Class ≠ True Class). (b) Same as (a) with the True Positive Rate (TPR) in blue and the False Negative Rate (FNR) in pink.

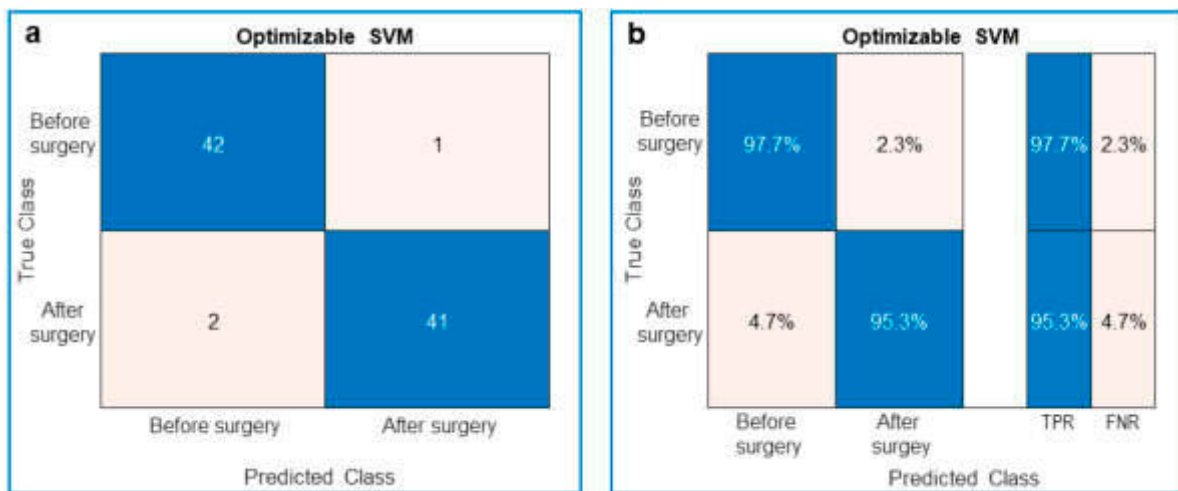


Figure 3. Performance of the trained optimizable support vector machine (SVM) classifier. (a) Confusion matrix showing the true and predicted classes of the ToF patients’ videos. The blue diagonal is related to the number of videos that were truly recognized (Predicted Class = True Class), whereas the pink antidiagonal is related to the number of videos that were falsely recognized (Predicted Class ≠ True Class). (b) Same as (a) the True Positive Rate (TPR) in blue and the False Negative Rate (FNR) in pink.

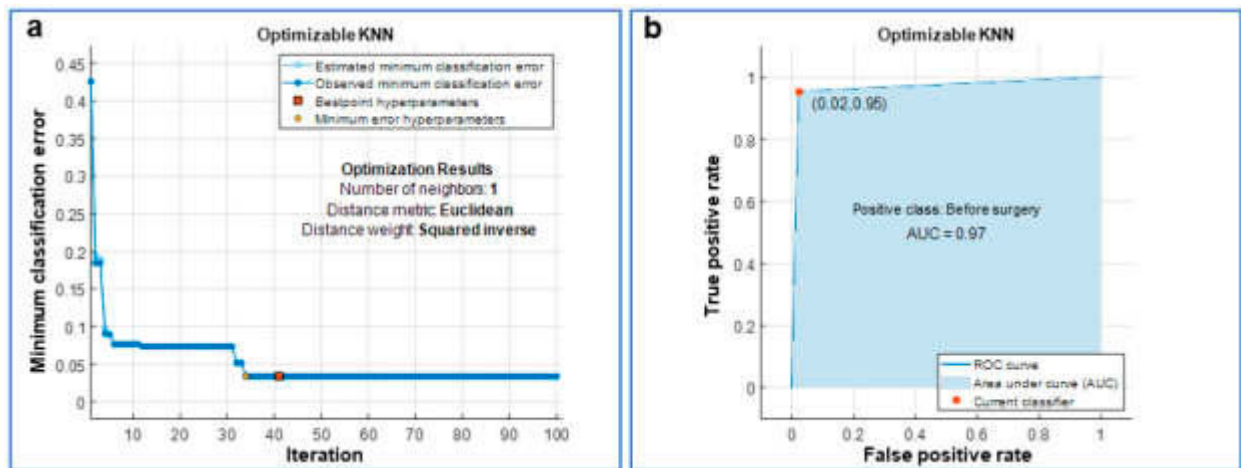


Figure 4. Optimization of the k-nearest neighbor (KNN) classifier. (a) The classifier was optimized over 100 iterations via the minimization of the classification error and its optimized hyperparameters are reported as “Optimization Results”. In detail, for each iteration of the optimization, the classifier was also 10-fold cross-validated. (b) Receiver Operating Characteristic (ROC) curve with the area under the curve (AUC) painted in blue; a value of AUC close to 1 means a very low classification error for the optimized classifier.

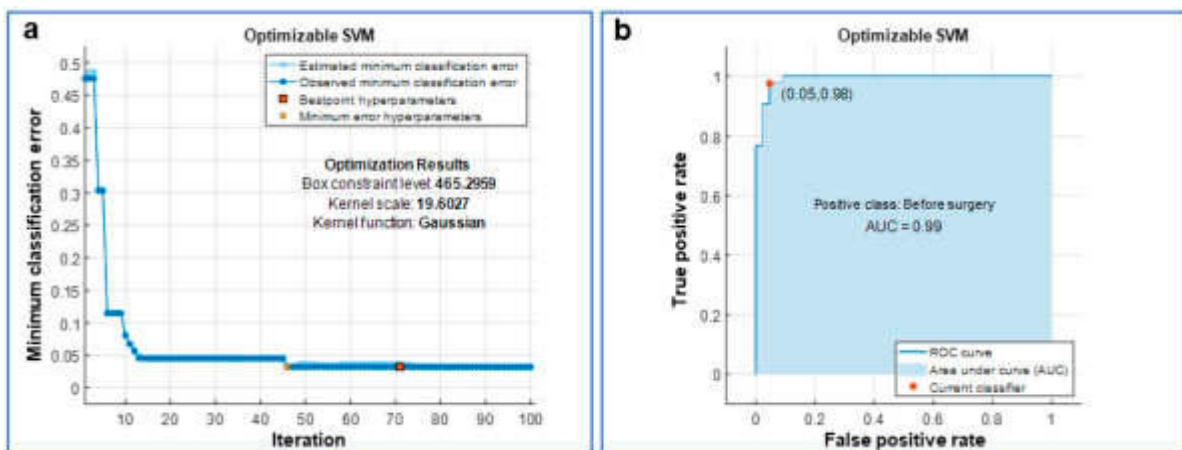


Figure 5. Optimization of the support vector machine (SVM) classifier. (a) The classifier was optimized over 100 iterations via the minimization of the classification error and its optimized hyperparameters are reported as “Optimization Results”. In detail, for each iteration of the optimization, the classifier was also 10-fold cross-validated. (b) Receiver Operating Characteristic (ROC) curve with the area under the curve (AUC) painted in blue; a value of AUC close to 1 means a very low classification error for the optimized classifier.

In detail, the KNN displayed a TPR of 95.3% and an FNR of 4.7% before surgery, whereas after surgery the TPR was 97.7% and the FNR was 2.3% (Figure 2).

Similarly, the SVM showed a TPR of 97.7% and an FNR of 2.3% before surgery, whereas after surgery the TPR was 95.3% and the FNR was 4.7% (Figure 3). When the cross-validated classifier reached the last optimization iteration (the 100th in our study), each iteration was evaluated in terms of classification error and the one with the minimum error provided the so-called “best point hyperparameters”. The estimated and observed minimum classification errors were plotted against the iteration number when they were <0.05. The KNN was optimized for a number of neighbors equal to 1, for the Euclidean distance metric and the squared inverse distance weight (Figure 4). The SVM was optimized considering a Gaussian kernel function, a kernel scale of 19.6027 and a box constraint level of 465.2959 (Figure 5). In addition, for both optimized models, the AUC was close to 1 (0.97 for KNN and 0.99 for SVM), which is the value of a perfect classification (Figures 4 and 5).

3.3. Classifiers' Prediction Ability Tested via Two Additional Patients with Different Outcomes

We sought to investigate the classifiers' prediction skills in two additional patients not considered in the training process. First, we assessed the cardiac kinematics (Figure 6a) in one ToF patient who underwent PVR with a known favorable outcome (discharged after 7 days of hospitalization). As in our previous works [22,23], we observed a decreasing trend for all Vi.Ki.E. parameters, which was significant for the energy and perimeter. Then, the Vi.Ki.E. coordinates of this patient were inputted into our SML models to build the decision surfaces. As a representative feature, we selected the signal-to-noise ratio (dB) (SNR) displayed in Figure 6b. Both before and after surgery, video recordings were correctly classified into the unhealthy and healthy classes by both trained models, respectively.

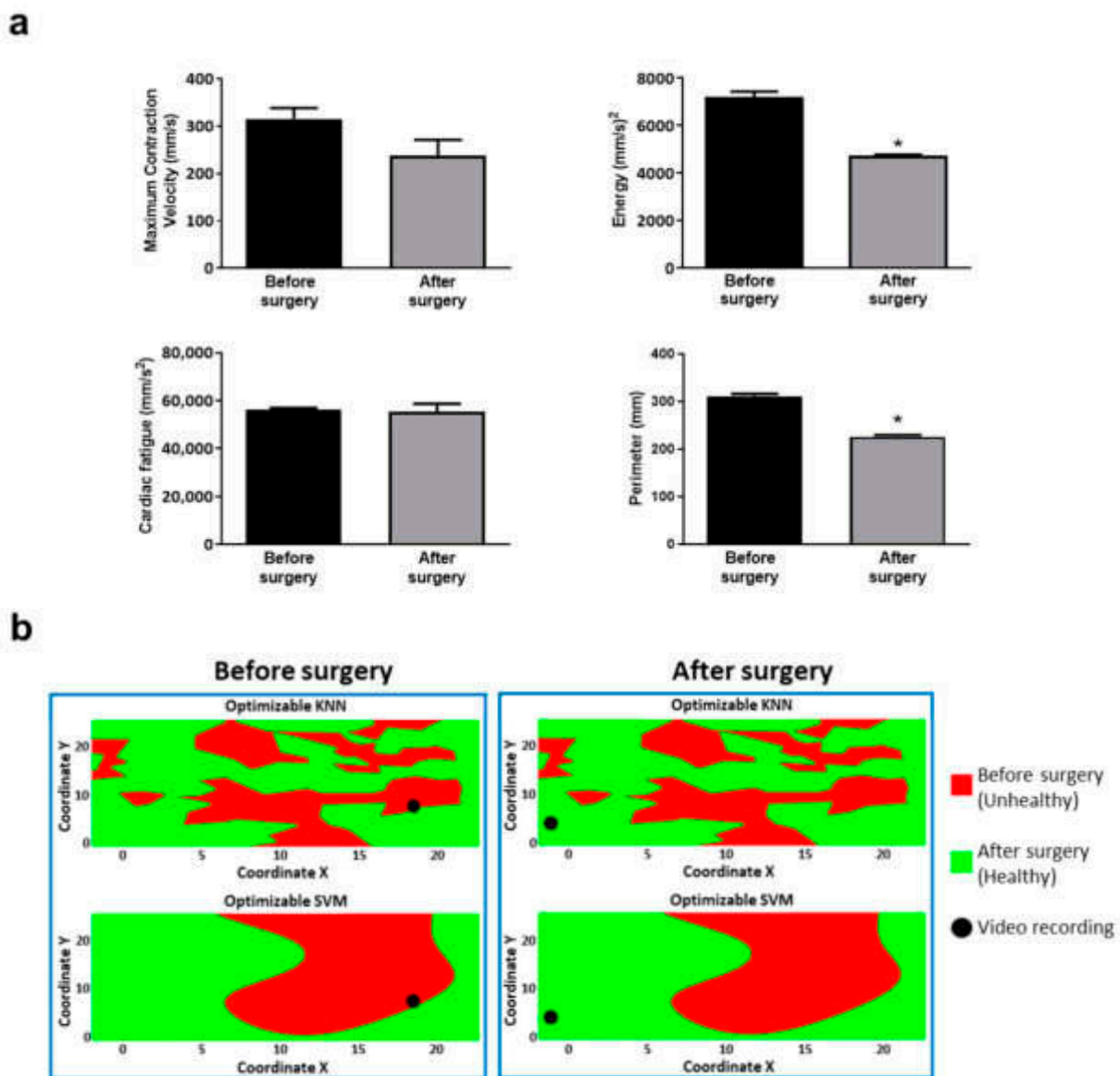


Figure 6. Vi.Ki.E. data and decision surfaces of a ToF patient with a favorable outcome. (a) The average Vi.Ki.E. parameters calculated before (black) and after surgery (grey). Top left: Maximum contraction velocity. Top right: energy. Bottom left: force. Bottom right: perimeter. Data are shown as mean \pm SEM. * $p < 0.05$ versus before surgery. (b) The decision surfaces of the signal-to-noise ratio (SNR) for both our classification models before (left panels) and after surgery (right panels). The black circle represents the classification/prediction of the patient's video according to KNN (top) and SVM (bottom) models. The red area is related to a prediction of unhealthy, whereas the green area to a prediction of healthy.

Likewise, we assessed the cardiac kinematics (Figure 7a) in a patient undergoing PVR for isolated congenital pulmonary valve regurgitation who had an unfavorable hospital course (death two weeks after surgery). We observed an increasing trend for all the Vi.Ki.E. parameters, which is in contrast with our previous work. The Vi.Ki.E. coordinates of this patient were used to build the decision surfaces for the SNR feature (Figure 7b). In detail, the before-surgery video recordings were correctly classified into the unhealthy class by both trained models (Figure 7: left panels, top and bottom). On the contrary, the after-surgery video recordings were still classified into the unhealthy class (instead of healthy) by both trained models (Figure 7: right panels, top and bottom), thus correctly predicting the documented unfavorable outcome.

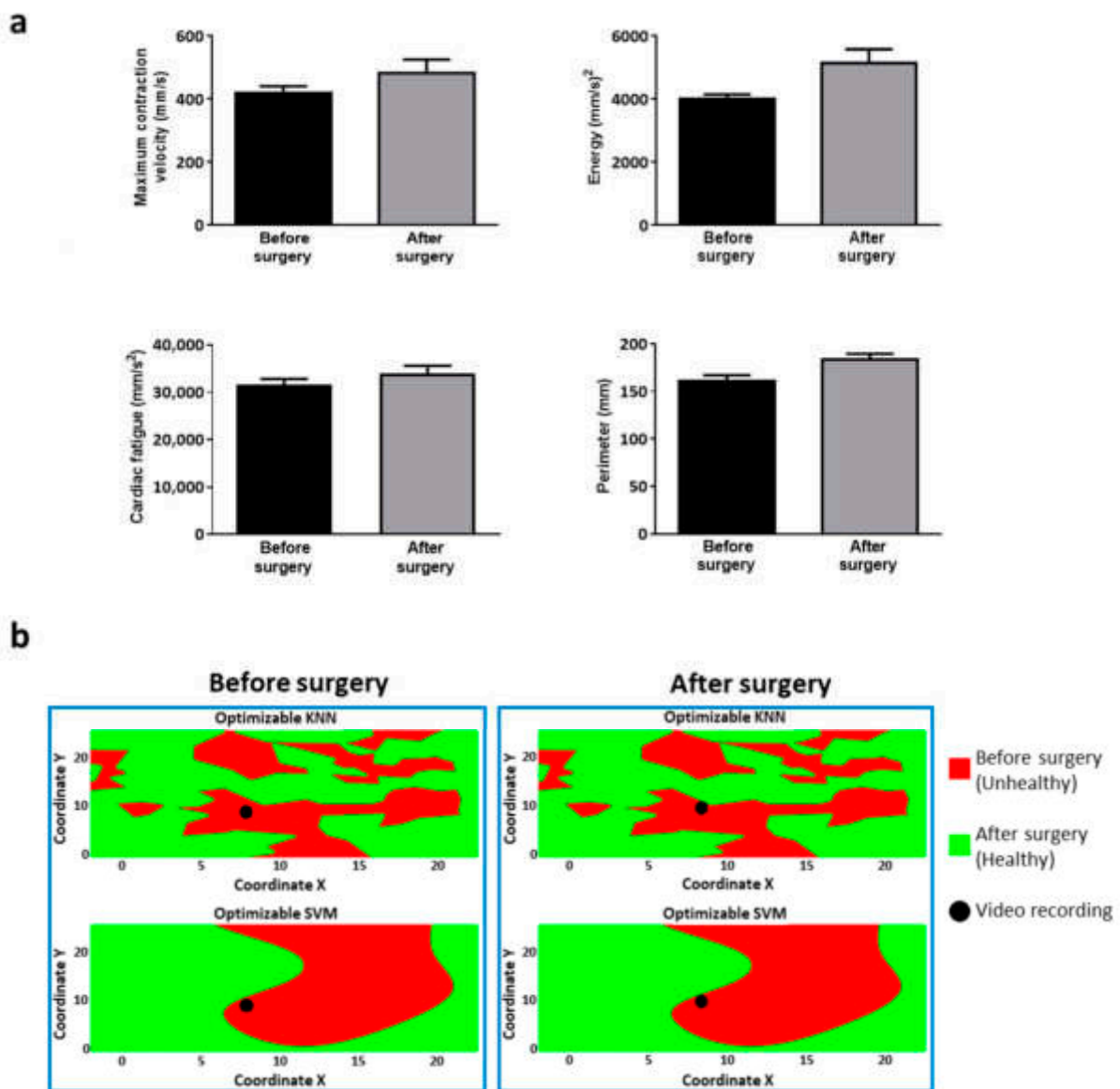


Figure 7. Vi.Ki.E. data and decision surfaces of a patient with pathophysiology similar to ToF and an unfavorable outcome. (a) The Vi.Ki.E. parameters calculated for every recording before (black) and after surgery (grey). Top left: Maximum contraction velocity. Top right: energy. Bottom left: force. Bottom right: perimeter. Data are shown as mean ± SEM. (b) The decision surfaces of the signal-to-noise ratio (SNR) for both our classification models before (left panel) and after surgery (right panel). The black circle represents the classification/prediction of the patient’s video according to KNN (top) and SVM (bottom) models. The red area is related to a prediction of unhealthy, whereas the green area is related to a prediction of being healthy.

4. Discussion

In this work, we employed supervised classifiers capable of correctly predicting outcomes on a set of patients affected by ToF and undergoing PVR. Tetralogy of Fallot is a rare congenital heart disease, which requires repair in early infancy and is associated with excellent survival into adulthood. Later on, most patients will develop chronic pulmonary valve regurgitation, which is characterized by the impairment of the right ventricular mechanical function [39]. The lack of imaging techniques for the intraoperative evaluation of the RV does not allow a precise assessment of its mechanical function during surgery, comparable to the information provided by MRI outside the operating room setting [40]. Moreover, the kinematics of the RV are extremely complex and there are emblematic cases in which its movement could be very atypical [41].

Predictive outcomes based on conventional technologies require a vast dataset of patients; conditions that, for rare diseases, entail multi-center investigations [42]. To overcome this limitation, a promising tool could be SML classifiers due to their ability to merge data coming from different research fields.

In this study, we trained two SML classifiers based on Vi.Ki.E., a contactless imaging technology developed by our laboratories to evaluate the RV kinematics [21–23,43]. We used the Vi.Ki.E. coordinates to extract frequency-domain-related features/predictors from the sinusoidal-like movement of the heart. The outputs of the trained classifiers are two classes, named either unhealthy (before surgery) or healthy (after surgery). The two models with the highest classification accuracy were the KNN and the SVM (>75%), which were optimized for our specific medical aim. Interestingly, both KNN and SVM classifiers are widely used in cardiology/cardiac surgery. For example, KNN has been recently employed for the accurate delineation of the QRS complex [44] and as predictive analytics for the postoperative length of stay after isolated coronary artery bypass grafting [45]. Likewise, SVM has been extensively used for predicting the development of complications after cardiac surgery [46,47]. Indeed, Moghaddasi et al. employed the SVM model to classify the severity of mitral regurgitation via transthoracic echocardiography [48].

Despite the limited number of cases, as shown in the power analysis consistent with the rarity of ToF, we optimized and 10-fold cross-validated the SMLs, obtaining good results in terms of TPR, FNR and AUC for both KNN and SVM models.

The usefulness of both classifiers was tested with an additional ToF patient undergoing PVR who had a favorable outcome. The Vi.Ki.E. assessment showed a decreasing trend for all kinematic parameters in line with our previous studies on right ventricular unloading [22,23]. We used the signal-to-noise ratio (SNR) predictor as a representative feature to build a simplified 2D classification model, named “decision surface”, for both coordinates. Both KNN and SVM decision surfaces correctly recognized the patient’s before and after surgery status in the respective unhealthy and healthy classes, which is thus in line with his prognosis.

We also used our classifiers on another patient who died two weeks after PVR for isolated congenital pulmonary valve regurgitation. The intraoperative Vi.Ki.E. parameters showed the opposite trend to that of our ToF population, denoting a still fatigued heart, although supported by inotropic drugs. As shown by the decision surfaces, the two classification models classified the after surgery heart movement as unhealthy (instead of healthy), thus correctly highlighting the still complex clinical condition. In conclusion, both KNN and SVM models classified the dead patient in line with his adverse prognosis.

The intraoperative clinical situation of the patient with an unfavorable outcome demonstrated the necessity of a real-time classification tool, directly applicable in the operating room [49], that could be useful to surgeons for prognostic assessment [50]. It is conceivable that the patient who did not benefit from PVR had since developed irreversible right ventricular dysfunction, due to longstanding RV hypertrophy and dilation, ultimately resulting in myocardial scarring (replacement of muscle with connective tissue). The quantification of scar tissue deposition relies on preoperative cardiac MRI. However,

the extent of myocardial scarring, which may predict irreversible right ventricular dysfunction, is presently unclear. Therefore, any additional tool which may aid in predicting postoperative recovery, including intraoperative technology integrated with AI elaboration, is potentially applicable and beneficial.

This study aimed to create ready-to-use classifiers to support surgeons during open-chest surgery. As both Vi.Ki.E. and classifiers' algorithms were implemented in MATLAB[®], the SMLs can be employed within the operating room right after the video-kinematic evaluation, providing insights for the intraoperative prognosis. Another strength of our classifiers is their customizable and optimizable nature, given that the proposed framework could be applied in other cardiac pathological conditions after training with specific patients' datasets. Moreover, the models can be improved over time as new patients are followed up and included in the training dataset. Our single-center pilot study demonstrated that, in the context of rare congenital heart diseases, predictive classification can be achieved with a minimal number of patients by resorting to artificial intelligence tools.

Author Contributions: F.P.L.M.: writing—original draft; designed the video recording protocol; data acquisition. G.R.: writing—original draft; designed the video recording protocol; data acquisition. S.R.: writing—review and editing. G.B.L.: performed all the surgeries; writing—review and editing. R.F.: writing—review and editing. A.C.: funding acquisition; writing—review and editing. L.F.: conceptualization; feature extraction and machine learning; writing—review and editing. M.M.: conceptualization; funding acquisition; project supervision; writing—review and editing. All authors have read and agreed to the published version of the manuscript.

Funding: FIL-2018–2021 (Quota incentivante di Ateneo) to M.M. and A.C. This work was also supported by a PRIN grant (2017AXL54F_002) to L.F.P.

Institutional Review Board Statement: The study was approved by the Institutional Review Board of AOUI of Verona (IT) (# 847CESC Protocol # 13371) and all patients signed an informed consent agreement.

Informed Consent Statement: Informed consent was obtained from all subjects involved in the study.

Data Availability Statement: Data will be provided upon request.

Acknowledgments: We thank Cristina Caffarra Malvezzi, Rosario Statello and Amparo Guerrero Gerbolés for their helpful discussion regarding the manuscript.

Conflicts of Interest: The authors declare no conflict of interest.

References

1. Jiang, F.; Jiang, Y.; Zhi, H.; Dong, Y.; Li, H.; Ma, S.; Wang, Y.; Dong, Q.; Shen, H.; Wang, Y. Artificial intelligence in healthcare: Past, present and future. *Stroke Vasc. Neurol.* **2017**, *2*, 230–243. [[CrossRef](#)] [[PubMed](#)]
2. Foresti, R.; Rossi, S.; Magnani, M.; Lo Bianco, C.G.; Delmonte, N. Smart Society and Artificial Intelligence: Big Data Scheduling and the Global Standard Method Applied to Smart Maintenance. *Engineering* **2020**, *6*, 835–846. [[CrossRef](#)]
3. Haleem, A.; Javaid, M.; Khan, I.H. Holography applications toward medical field: An overview. *Indian J. Radiol. Imaging* **2020**, *30*, 354–361. [[CrossRef](#)] [[PubMed](#)]
4. Jayaraman, P.P.; Forkan, A.R.M.; Morshed, A.; Haghighi, P.D.; Kang, Y.-B. Healthcare 4.0: A review of frontiers in digital health. *WIREs Data Min. Knowl. Discov.* **2020**, *10*, e1350. [[CrossRef](#)]
5. Poli, R.; Obrst, L. The Interplay Between Ontology as Categorical Analysis and Ontology as Technology. In *Theory and Applications of Ontology: Computer Applications*; Poli, R., Healy, M., Kameas, A., Eds.; Springer: Dordrecht, The Netherlands, 2010; pp. 1–26.
6. Bal, M.; Amasyali, M.F.; Sever, H.; Kose, G.; Demirhan, A. Performance evaluation of the machine learning algorithms used in inference mechanism of a medical decision support system. *Sci. World J.* **2014**, *2014*, 137896. [[CrossRef](#)]
7. Chen, Y.; McElvain, L.E.; Tolpygo, A.S.; Ferrante, D.; Friedman, B.; Mitra, P.P.; Karten, H.J.; Freund, Y.; Kleinfeld, D. An active texture-based digital atlas enables automated mapping of structures and markers across brains. *Nat. Methods* **2019**, *16*, 341–350. [[CrossRef](#)]
8. Feeny, A.K.; Chung, M.K.; Madabhushi, A.; Attia, Z.I.; Cikes, M.; Firouznia, M.; Friedman, P.A.; Kalscheur, M.M.; Kapa, S.; Narayan, S.M.; et al. Artificial Intelligence and Machine Learning in Arrhythmias and Cardiac Electrophysiology. *Circ. Arrhythm. Electrophysiol.* **2020**, *13*, e007952. [[CrossRef](#)]

9. Oikonomou, E.K.; Siddique, M.; Antoniadou, C. Artificial intelligence in medical imaging: A radiomic guide to precision phenotyping of cardiovascular disease. *Cardiovasc. Res.* **2020**, *116*, 2040–2054. [[CrossRef](#)]
10. Knott, K.D.; Seraphim, A.; Augusto, J.B.; Xue, H.; Chacko, L.; Aung, N.; Petersen, S.E.; Cooper, J.A.; Manisty, C.; Bhuva, A.N.; et al. The Prognostic Significance of Quantitative Myocardial Perfusion An Artificial Intelligence-Based Approach Using Perfusion Mapping. *Circulation* **2020**, *141*, 1282–1291. [[CrossRef](#)]
11. Dawes, T.J.W.; de Marvao, A.; Shi, W.; Fletcher, T.; Watson, G.M.J.; Wharton, J.; Rhodes, C.J.; Howard, L.; Gibbs, J.S.R.; Rueckert, D.; et al. Machine Learning of Three-dimensional Right Ventricular Motion Enables Outcome Prediction in Pulmonary Hypertension: A Cardiac MR Imaging Study. *Radiology* **2017**, *283*, 381–390. [[CrossRef](#)]
12. Genovese, D.; Rashedi, N.; Weinert, L.; Narang, A.; Addetia, K.; Patel, A.R.; Prater, D.; Goncalves, A.; Mor-Avi, V.; Lang, R.M. Machine Learning-Based Three-Dimensional Echocardiographic Quantification of Right Ventricular Size and Function: Validation Against Cardiac Magnetic Resonance. *J. Am. Soc. Echocardiogr.* **2019**, *32*, 969–977. [[CrossRef](#)]
13. Deo, R.C. Machine Learning in Medicine. *Circulation* **2015**, *132*, 1920–1930. [[CrossRef](#)] [[PubMed](#)]
14. Fralick, M.; Colak, E.; Mamdani, M. Machine Learning in Medicine. *N. Engl. J. Med.* **2019**, *380*, 2588–2589. [[CrossRef](#)]
15. Mukherjee, P.; Cintra, M.; Huang, C.; Zhou, M.; Zhu, S.; Colevas, A.D.; Fischbein, N.; Gevaert, O. CT-based Radiomic Signatures for Predicting Histopathologic Features in Head and Neck Squamous Cell Carcinoma. *Radiol. Imaging Cancer* **2020**, *2*, e190039. [[CrossRef](#)]
16. Fassina, L.; Faragli, A.; Lo Muzio, F.P.; Kelle, S.; Campana, C.; Pieske, B.; Edelmann, F.; Alogna, A. A Random Shuffle Method to Expand a Narrow Dataset and Overcome the Associated Challenges in a Clinical Study: A Heart Failure Cohort Example. *Front. Cardiovasc. Med.* **2020**, *7*, 599923. [[CrossRef](#)]
17. Rockowitz, S.; LeCompte, N.; Carmack, M.; Quitadamo, A.; Wang, L.; Park, M.; Knight, D.; Sexton, E.; Smith, L.; Sheidley, B.; et al. Children’s rare disease cohorts: An integrative research and clinical genomics initiative. *NPJ Genom. Med.* **2020**, *5*, 29. [[CrossRef](#)]
18. Guthridge, J.M.; Lu, R.; Tran, L.T.; Arriens, C.; Aberle, T.; Kamp, S.; Munroe, M.E.; Dominguez, N.; Gross, T.; DeJager, W.; et al. Adults with systemic lupus exhibit distinct molecular phenotypes in a cross-sectional study. *EClinicalMedicine* **2020**, *20*, 100291. [[CrossRef](#)] [[PubMed](#)]
19. Cohen, A.M.; Chamberlin, S.; Deloughery, T.; Nguyen, M.; Bedrick, S.; Meninger, S.; Ko, J.J.; Amin, J.J.; Wei, A.H.; Hersh, W. Detecting rare diseases in electronic health records using machine learning and knowledge engineering: Case study of acute hepatic porphyria (vol 15, e0235574, 2020). *PLoS ONE* **2020**, *15*, e0238277. [[CrossRef](#)]
20. Hinton, R.B.; Ware, S.M. Heart Failure in Pediatric Patients With Congenital Heart Disease. *Circ. Res.* **2017**, *120*, 978–994. [[CrossRef](#)]
21. Fassina, L.; Rozzi, G.; Rossi, S.; Scacchi, S.; Galetti, M.; Lo Muzio, F.P.; Del Bianco, F.; Colli Franzone, P.; Petrilli, G.; Faggian, G.; et al. Cardiac kinematic parameters computed from video of in situ beating heart. *Sci. Rep.* **2017**, *7*, 46143. [[CrossRef](#)] [[PubMed](#)]
22. Rozzi, G.; Lo Muzio, F.P.; Sandrini, C.; Rossi, S.; Fassina, L.; Faggian, G.; Miragoli, M.; Luciani, G.B. Real-time video kinematic evaluation of the in situ beating right ventricle after pulmonary valve replacement in patients with tetralogy of Fallot: A pilot study. *Interact. Cardiovasc. Thorac. Surg.* **2019**, *29*, 625–631. [[CrossRef](#)] [[PubMed](#)]
23. Rozzi, G.; Lo Muzio, F.P.; Fassina, L.; Rossi, S.; Statello, R.; Sandrini, C.; Laricchiuta, M.; Faggian, G.; Miragoli, M.; Luciani, G.B. Right ventricular functional recovery depends on timing of pulmonary valve replacement in tetralogy of Fallot: A video kinematic study. *Eur. J. Cardio-Thorac. Surg. Off. J. Eur. Assoc. Cardio-Thorac. Surg.* **2021**, *59*, 1329–1336. [[CrossRef](#)]
24. Villafane, J.; Feinstein, J.A.; Jenkins, K.J.; Vincent, R.N.; Walsh, E.P.; Dubin, A.M.; Geva, T.; Towbin, J.A.; Cohen, M.S.; Fraser, C.; et al. Hot topics in tetralogy of Fallot. *J. Am. Coll. Cardiol.* **2013**, *62*, 2155–2166. [[CrossRef](#)]
25. Sevakula, R.K.; Au-Yeung, W.M.; Singh, J.P.; Heist, E.K.; Isselbacher, E.M.; Armoundas, A.A. State-of-the-Art Machine Learning Techniques Aiming to Improve Patient Outcomes Pertaining to the Cardiovascular System. *J. Am. Heart Assoc.* **2020**, *9*, e013924. [[CrossRef](#)] [[PubMed](#)]
26. Lin, C.H. Frequency-domain features for ECG beat discrimination using grey relational analysis-based classifier. *Comput. Math. Appl.* **2008**, *55*, 680–690. [[CrossRef](#)]
27. Kinoshita, O.; Fontaine, G.; Rosas, F.; Elias, J.; Iwa, T.; Tonet, J.; Lascault, G.; Frank, R. Time-Domain and Frequency-Domain Analyses of the Signal-Averaged Ecg in Patients with Arrhythmogenic Right-Ventricular Dysplasia. *Circulation* **1995**, *91*, 715–721. [[CrossRef](#)]
28. Taye, G.T.; Hwang, H.J.; Lim, K.M. Application of a convolutional neural network for predicting the occurrence of ventricular tachyarrhythmia using heart rate variability features (vol 10, 6769, 2020). *Sci. Rep.* **2020**, *10*, 6769. [[CrossRef](#)]
29. Armitage, P.B.G.; Berry, G.; Matthews, J.N.S. Clinical Trials. In *Statistical Methods in Medical Research*; Wiley Blackwell: Hoboken, NJ, USA, 2002; pp. 591–647.
30. Liu, Y.; Chen, S.; Zuhlke, L.; Black, G.C.; Choy, M.K.; Li, N.; Keavney, B.D. Global birth prevalence of congenital heart defects 1970–2017: Updated systematic review and meta-analysis of 260 studies. *Int. J. Epidemiol.* **2019**, *48*, 455–463. [[CrossRef](#)]
31. Gould, K.A. The Elements of Statistical Learning (2nd edition): Data Mining, Inference, and Prediction. *Dimens Crit. Care Nur.* **2016**, *35*, 52.
32. Freund, Y.; Schapire, R.E. A decision-theoretic generalization of on-line learning and an application to boosting. *J. Comput. Syst. Sci.* **1997**, *55*, 119–139. [[CrossRef](#)]

33. Seiffert, C.; Khoshgoftaar, T.M.; Van Hulse, J.; Napolitano, A. RUSBoost: Improving Classification Performance when Training Data is Skewed. In Proceedings of the 2008 19th International Conference on Pattern Recognition, Tampa, FL, USA, 8–11 December 2008; pp. 3650–3653.
34. Melillo, P.; Fusco, R.; Sansone, M.; Bracale, M.; Pecchia, L. Discrimination power of long-term heart rate variability measures for chronic heart failure detection. *Med. Biol. Eng. Comput.* **2011**, *49*, 67–74. [[CrossRef](#)]
35. Melillo, P.; Izzo, R.; Orrico, A.; Scala, P.; Attanasio, M.; Mirra, M.; De Luca, N.; Pecchia, L. Automatic Prediction of Cardiovascular and Cerebrovascular Events Using Heart Rate Variability Analysis. *PLoS ONE* **2015**, *10*, e0118504. [[CrossRef](#)]
36. Ali, L.; Khan, S.U.; Golilarz, N.A.; Yakubu, I.; Qasim, I.; Noor, A.; Nour, R. A Feature-Driven Decision Support System for Heart Failure Prediction Based on chi 2 Statistical Model and Gaussian Naive Bayes. *Comput. Math. Methods Med.* **2019**, *2019*, 6314328. [[CrossRef](#)] [[PubMed](#)]
37. Dutta, S.; Chatterjee, A.; Munshi, S. Correlation technique and least square support vector machine combine for frequency domain based ECG beat classification. *Med. Eng. Phys.* **2010**, *32*, 1161–1169. [[CrossRef](#)]
38. Liu, G.Z.; Wang, L.; Wang, Q.; Zhou, G.M.; Wang, Y.; Jiang, Q. A New Approach to Detect Congestive Heart Failure Using Short-Term Heart Rate Variability Measures. *PLoS ONE* **2014**, *9*, e93399. [[CrossRef](#)]
39. Frigiola, A.; Tsang, V.; Bull, C.; Coats, L.; Khambadkone, S.; Derrick, G.; Mist, B.; Walker, F.; van Doorn, C.; Bonhoeffer, P.; et al. Biventricular response after pulmonary valve replacement for right ventricular outflow tract dysfunction: Is age a predictor of outcome? *Circulation* **2008**, *118*, S182–S190. [[CrossRef](#)]
40. Mercier-Rosa, L.; Yang, W.; Kutty, S.; Rychik, J.; Fogel, M.; Goldmuntz, E. Quantifying pulmonary regurgitation and right ventricular function in surgically repaired tetralogy of Fallot: A comparative analysis of echocardiography and magnetic resonance imaging. *Circ. Cardiovasc. Imaging* **2012**, *5*, 637–643. [[CrossRef](#)]
41. Pedrotti, P.; Peritore, A.; Cereda, A.; Giannattasio, C.; Imazio, M. Total pericardial agenesis mimicking arrhythmogenic right ventricular dysplasia. *J. Cardiovasc. Med.* **2016**, *17*, e216–e217. [[CrossRef](#)]
42. Bokma, J.P.; Geva, T.; Sleeper, L.A.; Babu Narayan, S.V.; Wald, R.; Hickey, K.; Jansen, K.; Wassall, R.; Lu, M.; Gatzoulis, M.A.; et al. A propensity score-adjusted analysis of clinical outcomes after pulmonary valve replacement in tetralogy of Fallot. *Heart* **2018**, *104*, 738–744. [[CrossRef](#)] [[PubMed](#)]
43. Lo Muzio, F.P.; Rozzi, G.; Rossi, S.; Gerboles, A.G.; Fassina, L.; Pela, G.; Luciani, G.B.; Miragoli, M. In-situ optical assessment of rat epicardial kinematic parameters reveals frequency-dependent mechanic heterogeneity related to gender. *Prog. Biophys. Mol. Biol.* **2020**, *154*, 94–101. [[CrossRef](#)] [[PubMed](#)]
44. Saini, I.; Singh, D.; Khosla, A. QRS detection using K-Nearest Neighbor algorithm (KNN) and evaluation on standard ECG databases. *J. Adv. Res.* **2013**, *4*, 331–344. [[CrossRef](#)] [[PubMed](#)]
45. Alshakhs, F.; Alharthi, H.; Aslam, N.; Khan, I.U.; Elasheri, M. Predicting Postoperative Length of Stay for Isolated Coronary Artery Bypass Graft Patients Using Machine Learning. *Int. J. Gen. Med.* **2020**, *13*, 751–762. [[CrossRef](#)]
46. Tseng, P.Y.; Chen, Y.T.; Wang, C.H.; Chiu, K.M.; Peng, Y.S.; Hsu, S.P.; Chen, K.L.; Yang, C.Y.; Lee, O.K. Prediction of the development of acute kidney injury following cardiac surgery by machine learning. *Crit. Care* **2020**, *24*, 478. [[CrossRef](#)]
47. Fernandes, M.P.B.; Armengol de la Hoz, M.; Rangasamy, V.; Subramaniam, B. Machine Learning Models with Preoperative Risk Factors and Intraoperative Hypotension Parameters Predict Mortality After Cardiac Surgery. *J. Cardiothorac. Vasc. Anesth.* **2021**, *35*, 857–865. [[CrossRef](#)] [[PubMed](#)]
48. Moghaddasi, H.; Nourian, S. Automatic assessment of mitral regurgitation severity based on extensive textural features on 2D echocardiography videos. *Comput. Biol. Med.* **2016**, *73*, 47–55. [[CrossRef](#)] [[PubMed](#)]
49. Bellini, V.; Guzzon, M.; Bigliardi, B.; Mordonini, M.; Filippelli, S.; Bignami, E. Artificial Intelligence: A New Tool in Operating Room Management. Role of Machine Learning Models in Operating Room Optimization. *J. Med. Syst.* **2019**, *44*, 20. [[CrossRef](#)] [[PubMed](#)]
50. Bartek, M.A.; Saxena, R.C.; Solomon, S.; Fong, C.T.; Behara, L.D.; Venigandla, R.; Velagapudi, K.; Lang, J.D.; Nair, B.G. Improving Operating Room Efficiency: Machine Learning Approach to Predict Case-Time Duration. *J. Am. Coll. Surg.* **2019**, *229*, 346–354.e3. [[CrossRef](#)]